frontiers | Research Topics

Imaging and functional imaging of the lung

Edited by
Joseph M. Reinhardt and Sam Bayat

Published in
Frontiers in Physiology

ISSN 1664-8714
ISBN 978-2-8325-4797-7
DOI 10.3389/978-2-8325-4797-7

About Frontiers

Frontiers is more than just an open access publisher of scholarly articles: it is a pioneering approach to the world of academia, radically improving the way scholarly research is managed. The grand vision of Frontiers is a world where all people have an equal opportunity to seek, share and generate knowledge. Frontiers provides immediate and permanent online open access to all its publications, but this alone is not enough to realize our grand goals.

Frontiers journal series

The Frontiers journal series is a multi-tier and interdisciplinary set of open-access, online journals, promising a paradigm shift from the current review, selection and dissemination processes in academic publishing. All Frontiers journals are driven by researchers for researchers; therefore, they constitute a service to the scholarly community. At the same time, the *Frontiers journal series* operates on a revolutionary invention, the tiered publishing system, initially addressing specific communities of scholars, and gradually climbing up to broader public understanding, thus serving the interests of the lay society, too.

Dedication to quality

Each Frontiers article is a landmark of the highest quality, thanks to genuinely collaborative interactions between authors and review editors, who include some of the world's best academicians. Research must be certified by peers before entering a stream of knowledge that may eventually reach the public - and shape society; therefore, Frontiers only applies the most rigorous and unbiased reviews. Frontiers revolutionizes research publishing by freely delivering the most outstanding research, evaluated with no bias from both the academic and social point of view. By applying the most advanced information technologies, Frontiers is catapulting scholarly publishing into a new generation.

What are Frontiers Research Topics?

Frontiers Research Topics are very popular trademarks of the *Frontiers journals series*: they are collections of at least ten articles, all centered on a particular subject. With their unique mix of varied contributions from Original Research to Review Articles, Frontiers Research Topics unify the most influential researchers, the latest key findings and historical advances in a hot research area.

Find out more on how to host your own Frontiers Research Topic or contribute to one as an author by contacting the Frontiers editorial office: frontiersin.org/about/contact

Imaging and functional imaging of the lung

Topic editors
Joseph M. Reinhardt – The University of Iowa, United States
Sam Bayat – Université Grenoble Alpes, France

Citation
Reinhardt, J. M., Bayat, S., eds. (2024). *Imaging and functional imaging of the lung*. Lausanne: Frontiers Media SA. doi: 10.3389/978-2-8325-4797-7

Table of contents

frontiers | Frontiers in Physiology

TYPE Original Research
PUBLISHED 17 October 2022
DOI 10.3389/fphys.2022.1008526

OPEN ACCESS

EDITED BY
Lars Knudsen,
Hannover Medical School, Germany

REVIEWED BY
Rui Carlos Sá,
University of California, San Diego,
United States
Sam Bayat,
Université Grenoble Alpes, France

*CORRESPONDENCE
Antonia E. Wuschner,
antonia.wuschner@wisc.edu

SPECIALTY SECTION
This article was submitted to Respiratory Physiology and Pathophysiology, a section of the journal Frontiers in Physiology

RECEIVED 31 July 2022
ACCEPTED 05 October 2022
PUBLISHED 17 October 2022

CITATION
Wuschner AE, Flakus MJ, Wallat EM, Reinhardt JM, Shanmuganayagam D, Christensen GE, Gerard SE and Bayouth JE (2022), CT-derived vessel segmentation for analysis of post-radiation therapy changes in vasculature and perfusion.
Front. Physiol. 13:1008526.
doi: 10.3389/fphys.2022.1008526

CT-derived vessel segmentation for analysis of post-radiation therapy changes in vasculature and perfusion

Antonia E. Wuschner[1]*, Mattison J. Flakus[1], Eric M. Wallat[1], Joseph M. Reinhardt[2], Dhanansayan Shanmuganayagam[3], Gary E Christensen[4,5], Sarah E. Gerard[2] and John E. Bayouth[6]

[1]Department of Medical Physics, University of Wisconsin, Madison, WI, United States, [2]Roy J. Carver Department of Biomedical Engineering, University of Iowa, Iowa, IA, United States, [3]Department of Animal Science, University of Wisconsin, Madison, WI, United States, [4]Department of Electrical and Computer Engineering, University of Iowa, Iowa, IA, United States, [5]Department of Radiation Oncology, University of Iowa, Iowa, IA, United States, [6]Department of Radiation Medicine, Oregon Health Sciences University, Portland, OR, United States

Vessel segmentation in the lung is an ongoing challenge. While many methods have been able to successfully identify vessels in normal, healthy, lungs, these methods struggle in the presence of abnormalities. Following radiotherapy, these methods tend to identify regions of radiographic change due to post-radiation therapytoxicities as vasculature falsely. By combining texture analysis and existing vasculature and masking techniques, we have developed a novel vasculature segmentation workflow that improves specificity in irradiated lung while preserving the sensitivity of detection in the rest of the lung. Furthermore, radiation dose has been shown to cause vascular injury as well as reduce pulmonary function post-RT. This work shows the improvements our novel vascular segmentation method provides relative to existing methods. Additionally, we use this workflow to show a dose dependent radiation-induced change in vasculature which is correlated with previously measured perfusion changes ($R^2 = 0.72$) in both directly irradiated and indirectly damaged regions of perfusion. These results present an opportunity to extend non-contrast CT-derived models of functional change following radiation therapy.

KEYWORDS

lung perfusion, post-RT vascular change, pulmonary vasculature segmentation, radiation-induced damage, ct-derived perfusion

1 Introduction

Vascular segmentation is an ongoing challenge. Several groups have attempted to develop robust vasculature segmentation algorithms. Of these, most models rely on knowledge about the features of vessels such as intensity, curvature, tubularity, centerline, and smoothness but all methods thus far face their own challenges (Jerman et al., 2015) (Sato et al., 1998) (Krissian et al., 2000) (Aylward and Bullitt, 2002) (Zhang et al., 2010)

(Lavi et al., 2004) (Metz et al., 2007) (Buelow et al., 2005) (Agam et al., 2005) (Medical Imaging 2008: Image Processing, 2008).

In lung images, there is a natural contrast seen on CT imaging due to the high density difference between vessels and the lung parenchyma. Segmenting vessels in the lungs specifically has been addressed by various groups (Agam et al., 2005) (Xiao et al., 2011) (Shikata et al., 2004) (Medical Imaging 2008: Image Processing, 2008). However, all these methods struggle to address the issue that other structures besides vessels can have similar Hounsfield Unit (HU) intensities such as tumor nodules or dense lesions resulting from fibrosis, mucous, etc. Particularly, in regions of damaged lung, previous work has indicated that the algorithm struggles to distinguish damaged lung from vessel (Rudyanto et al., 2014).

Texture analysis presents an opportunity to identify particular radiographic abnormalities caused by medical intervention e.g. radiation therapy. These methods are robust and can identify several different textures in lung parenchyma such as ground glass, honeycombing, emphysema, consolidated, bronchovascular, and ground glass reticular (Uppaluri et al., 1997). In this work we use these texture analysis methods to improve upon existing vascular segmentation methods to produce a workflow capable of identifying vasculature accurately in the presence of damaged or abnormal lung tissue. Furthermore, we use this workflow to show a dose dependent radiation-induced change in vasculature which correlated with measured perfusion changes in both directly irradiated and indirectly damaged regions.

2 Methods

2.1 Swine model subject description

Previous studies have used the Wisconsin Miniature Swine (WMS) and detail their unique characteristics that make them an ideal model as well as show strong correlations between WMS and human response (Wallat et al., 2021) (Reed et al., 2010) (Wuschner et al., 2021a). In this work, two groups of five WMS (ten total) each received CT imaging and RT treatment. The swine ranged from 70–100 kg and were 14.4 ± 1.7 months of age. These two groups will be referred to as group A and group B, with differences between the groups described in the current section. All WMS were sedated to eliminate motion artifacts and mechanically ventilated to a consistent tidal volume of 1 L and respiratory rate of 15 breaths per minute matching the average tidal volume and respiratory rate of human subjects in a prospective clinical trial studying functional avoidance in the lung (NCT02843568). The animal care practices and all experimental procedures were approved by the University of Wisconsin Institutional Animal Care and Use Committee (IACUC). The drugs and methods of anesthesia and euthanasia were approved in compliance with American Veterinary Medical Association (AVMA) guidelines for anesthesia and euthanasia of swine. Both committees assured that all procedures were in compliance with ARRIVE guidelines.

2.1.1 Treatment schemes and imaging schedule

For all ten swine in groups A and B, CT images were acquired both pre- and 3 months post-RT. At each time point, subjects received a four-dimensional CT (4DCT) and dynamic contrast-enhanced perfusion scans. The dynamic perfusion scans were performed following the procedure detailed in Wuschner et al. (Wuschner et al., 2021a).

All subjects underwent a five fraction stereotactic body RT (SBRT) course of 12 Gy per fraction totaling 60 Gy, however the two groups of swine were treated with two different forms of image-guided radiation therapy, as described below. The differences in delivery system were due to clinical availability at the time of the study. Figure 1 shows a representative dose distribution that was delivered to subjects in each group. For all subjects, the contralateral lung did not receive dose above 5 Gy.

In group A, the treatment planning target volume (PTV) was designated as the bifurcation of a vessel in the posterior base, near the left lateral chest wall, of the left lung. Treatment delivery was executed using an MRI-guided LINAC system (ViewRay, Cleveland Ohio) in order to maximize dose conformity and reduce the uncertainty of dose delivery due to respiratory motion. The ViewRay system continually monitors and gates treatment by acquiring 0.35 T MRI images and stopping treatment when the target is outside of the threshold view set.

For subjects in group B, the PTV was centered on a vessel and airway in the right upper lobe of the subject. This target location was selected to enable treatment response analysis to the directly irradiated vessels and distal pulmonary vasculature receiving moderate to low radiation doses. Treatments were delivered on the Radixact®linear accelerator with motion Synchrony treatment system (Accuray Incorporated, Sunnyvale, CA) in order to maximize dose conformity and reduce the uncertainty of dose delivery due to respiratory motion. Radixact®is a helical tomotherapy radiation therapy delivery system that contains an intrafraction motion management system called Synchrony®, which has been adapted from CK Synchrony (Schnarr et al., 2018). On the system, an x-ray tube and flat-panel kV imager are offset 90° from the megavoltage (MV) imager and beam. The kV imaging subsystem is used to periodically localize the target during treatment. For monitoring respiratory motion, light-emitting diodes (LEDs) were placed on the swines' chest and identified with a camera mounted to the treatment table to provide the phase of respiration. The target can then be localized without implanted fiducials near the target using a motion correlation model. Further details of the model are described in Schnarr et al. (Schnarr et al., 2018).

For all swine, treatment fractions were delivered following a standard clinical SBRT schedule receiving each fraction with a day in between each delivery during weekdays and 2 days over

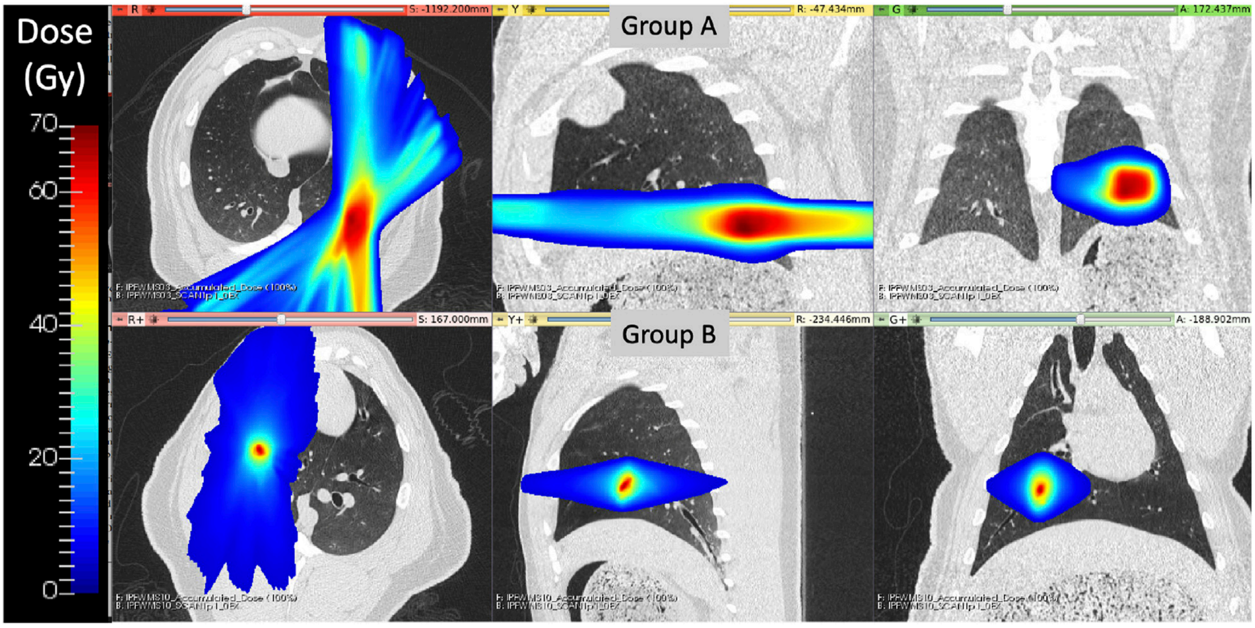

FIGURE 1
Delivered radiation dose distributions for WMS groups **(A)** and **(B)** show treatment differences. Group B had a more medial and cranial dose distribution with a smaller region of targeted high dose values.

the weekend. Subjects were mechanically ventilated to eight breaths per minute during treatments with inverted breathing to hold inhale longer than exhale.

2.2 Image analysis tools used

2.2.1 Feature-learning vascular segmentation

In the 2012 VESSEL12 Grand Challenge run in conjunction with the IEEE International Symposium on Biomedical Imaging, several different approaches to vascular segmentation on non-contrast CT were proposed (Rudyanto et al., 2014). The top scoring approach by Kiros et al. utilized multi-scale patch-based feature-learning and implements the sparse coding principles described by Coates et al. (Coates and Ng, 2011) (Kiros et al., 2014). Since this method does not require joint learning, features are learned efficiently and quickly (Kiros et al., 2014). Since the conclusion of the challenge, Konopczynski et al. have improved upon the work of Kiros et al. by extending the method to learn 3D features in an unsupervised manner in a multi-scale scheme using dictionary learning *via* least angle regression (Konopczynski et al., 2016). Their method improved upon the accuracy achieved by Kiros et al. from 96.66 ± 1.10% to 97.24 ± 0.90% on the principle VESSEL12 data set (Konopczynski et al., 2016). The VESSEL12 challenge separately evaluated the ability of segmentation methods to distinguish several types of dense abnormalities from vessels. The datasets for these categories consisted of non-contrast CT images that contained vessels in the presence of dense lesions, which include atelectasis, fibrosis, and adhesive straining, as well as mucus-filled bronchi, which are airways that instead of being clear, are filled with liquid such as mucus (Rudyanto et al., 2014). Many of these are characteristic of the radiographic change that is seen in post-RT radiotherapy patients. In these categories, the methods of Konopczynski et al. achieved a sensitivity of 0.95, but struggled in specificity (achieved 0.13) meaning it classified several things as vessels that were not. This code is open-source and is code that was used in the “Vessel Segmentation” step shown in Figure 3 (Rudyanto et al., 2014). The output of this code is a probability map that indicates the probability of a given voxel containing a vessel.

2.2.2 Texture analysis

To improve the specificity of the resulting vessel segmentation from the Konopczynski method described above, texture analysis was used to identify and remove false positives. The texture analysis method used is the Adaptive Multi-Feature Method (AMFM) developed by Uppaluri et al. at the University of Iowa (Uppaluri et al., 1997). This method classifies voxels of an input lung CT as one of seven textures: normal, ground glass, ground glass reticular, honeycombing, bronchvascular, emphysema, or consolidated.

The general procedure for performing the analysis is as follows. First, lung regions are identified on the CT scan using a multi-resolution convolutional neural network lung

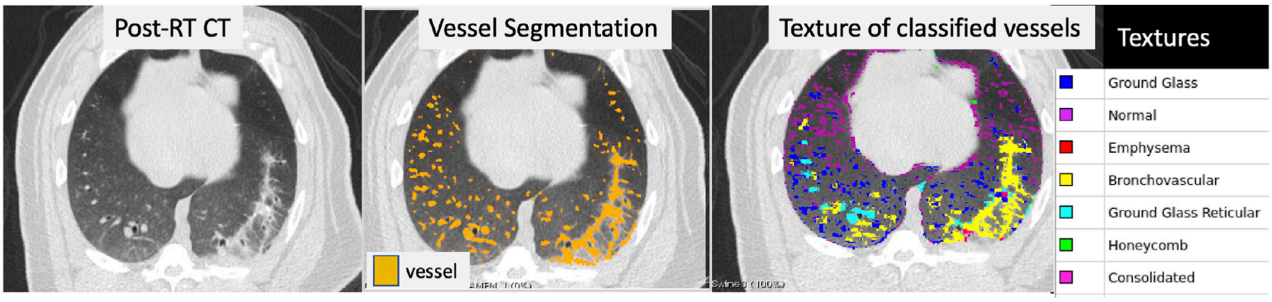

FIGURE 2
Example of a post-RT CT scan showing radiographic damage (left frame), the resulting vessel segmentation (middle frame), and the texture classification for each voxel (right frame) that was classified as a vessel. The vessel segmentation classifies several voxels in the area of the CT showing radiographic change as vessel that are likely false positives. Texture analysis was performed over the entire lung and is shown masked by the voxels that were identified as vessel in the third panel. The textures of the voxels in the region of false-positives are bronchovascular, consolidated, or ground-glass reticular which are expected radiation-induced textures.

segmentaiton approach proposed by Gerard et al. (Gerard et al., 2020) (Gerard et al., 2021). Next, preprocessing was performed on the masked CT image using edgementation (Uppaluri et al., 1997). This method merges pixels in regions where the difference between the grey levels of adjacent pixels is small. From there, feature extraction is performed. The features extracted can be grouped into three categories; first order, second order, and the geometric fractal dimension. The first-order features were mean, variance, skewness, kurtosis, and grey-level entropy as described in Ferdeghini et al. (Ferdeghini et al., 1991). Eleven second order features were calculated. Five of these were derived from the run length matrix (short-run emphasis, long-run emphasis, grey-level non-uniformity, run-length non-uniformity, and run percentage) and the remaining six were derived from the co-occurrence matrix (angular second moment, entropy, inertia, contrast, correlation, and inverse difference moment) (Fleagle et al., 1994). The details of the geometric fractal dimension are detailed in Uppaluri et al. (Uppaluri et al., 1995). Each calculated feature is normalized for the size of the pixel and lung prior to optimal feature extraction. Optimal feature extraction is performed using the divergence method and correlation analysis with labeled training data that is classified as 1 of the seven textures by an experienced radiologist (Andrews and Swartzlander, 1973). Finally, classification is performed using a Bayesian classifier (Sonka et al., 1993).

Figure 2 shows the result of applying the AMFM texture analysis to a post-RT CT and masking it by voxels that were classified as vessels using the method described above. The vessel segmentation classifies several voxels in the area of the CT showing radiographic change as vessel that are likely false positives. Texture analysis shows that the voxels in this region are bronchovascular, consolidated, or ground-glass reticular which are expected radiation-induced textures. Therefore, by removing any voxels that are both classified as a vessel and classified by one of these textures, we can remove the false positives in the vessel segmentation.

However it can also be seen that voxels that are clearly vessels in the right lung are classified as ground glass reticular. This is because the AMFM technique is designed to classify lung parenchyma, not vasculature. When the vasculature is large enough, the features of the vasculature are similar to that of ground glass reticular and thus they are classified as such. This does not occur with the smaller vasculature that are small enough such that their normalized do not classify as one of the removed textures. To address this, a third image processing step is needed to add back in the larger vasculature.

2.2.3 Lung and large vessel segmentation

To add in the larger vasculature, two lung masking techniques are used. The first is a multi-resolution convolutional neural network proposed by Gerard et al.to perform lung segmentation (Gerard et al., 2020) (Gerard et al., 2021). The lung segmentation produced by this generates a smooth boundary at the mediastinum which includes the large vessels filled in (see Figure 3). The second method is an optimal thresholding method which is utilized to generate a mask of well-aerated regions. The aerated mask is subsequently smoothed and small holes are filled using morphological operations thus leaving the large vasculature unmasked. The difference image between the lung segmentation and the aerated segmentation is used to identify large vasculature (Gerard, 2018).

2.3 Vascular segmentation workflow

The full vascular segmentation workflow is detailed in Figure 3. The 4DCT image is input into the vascular segmentation, AMFM texture, CNN lung segmentation, and aerated segmentation codes. The AMFM texture map is

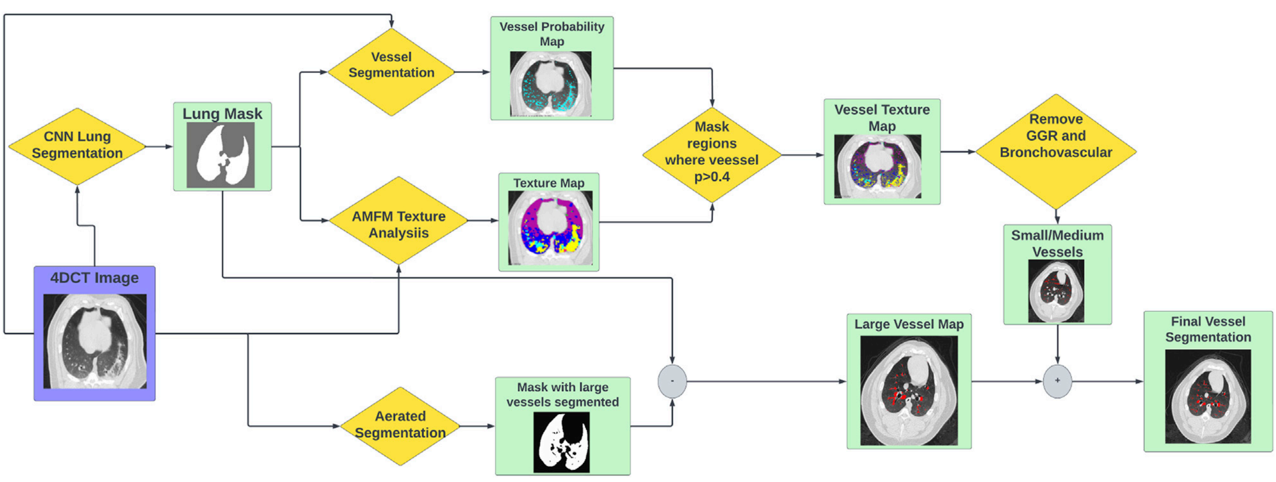

FIGURE 3
Flowchart showing the workflow to produce vascular segmentations using the tools described.

masked by the vessel segmentation such that only vessel classified voxels remain (determined using a threshold of $p > 0.4$). Additionally, any voxels classified as vessel that are also identified as ground glass reticular or bronchovascular are removed. This produces the a map of the small and medium vasculature. Separately, the aerated segmentation is subtracted from the CNN lung segmentation to produce the large vasculature map. Finally, the large and small/medium vessel maps are added together to produce the final vessel segmentation.

2.4 Analysis of post-RT change

2.4.1 Group A

All post-RT scans were deformably registered to the pre-RT scan using a B-spline registration algorithm (Cao et al., 2012) (Yin et al., 2009). The transformation matrix produced in the registration was then applied to the post-RT vessel segmentation to allow for voxel-wise comparisons. Analysis was performed in four dose bins; voxels receiving “no dose” (< 5 Gy), “low dose” (5–20 Gy), “medium dose” (20–40 Gy), and “high dose” (above 40 Gy). In each dose bin, the volume of vasculature was calculated by summing the number of voxels classified as a vessel and multiplying by the voxel size. The percent change in vessel volume from pre to post-RT was then calculated using equation 1. Additionally student paired two-tailed t-tests were used to compare the pre and post-RT volumes of vasculature in each dose bin across the five swine.

$$\Delta VesselVolume\,(\%) = \frac{Volume_{post} - Volume_{pre}}{Volume_{pre}} * 100\% \tag{1}$$

2.4.2 Group B

For the subjects in Group B, analysis was performed similarly to the subjects in Group A with the addition of analysis being split into direct and indirect change. The process for this analysis is summarized in Figure 4. Similarly to Group A, the pre and post-RT CTs are registered and the transformation matrix is used to bring the post-RT vessel map into the frame of reference of the pre-RT scan and dose distribution. However, in addition to masking by dose bin, the analysis is masked as being in either a “fed”, “not fed”, or “contralateral” region. Here “contralateral” refers to the left lung (left entirely unirradiated below 5 Gy), “fed” refers to regions that contain vasculature that branch from the vessel irradiated to the prescription dose, and “not fed” refers to regions that do not contain vasculature that branch from the vessel irradiated to the prescription dose. This results in 7 separate analysis regions (no, low, and medium dose in both the fed and not fed regions and the contralateral region). In each of these regions the percent change in volume of vasculature was calculated as described for group A using Eq. 1.

Additionally for these subjects, the perfusion change in each of the seven contours analyzed in the group B subjects was calculated from the contrast-CTs using the methodology described in Wuschner et al. (Wuschner et al., 2022).

3 Results

3.1 Improved vascular segmentation

An example of the vessel segmentation algorithm is shown in Figure 5. The post-RT original vessel segmentation classifies regions of radiographic change as vessel. When removing the ground glass reticular and bronchovascular voxels, in both the pre and post-RT

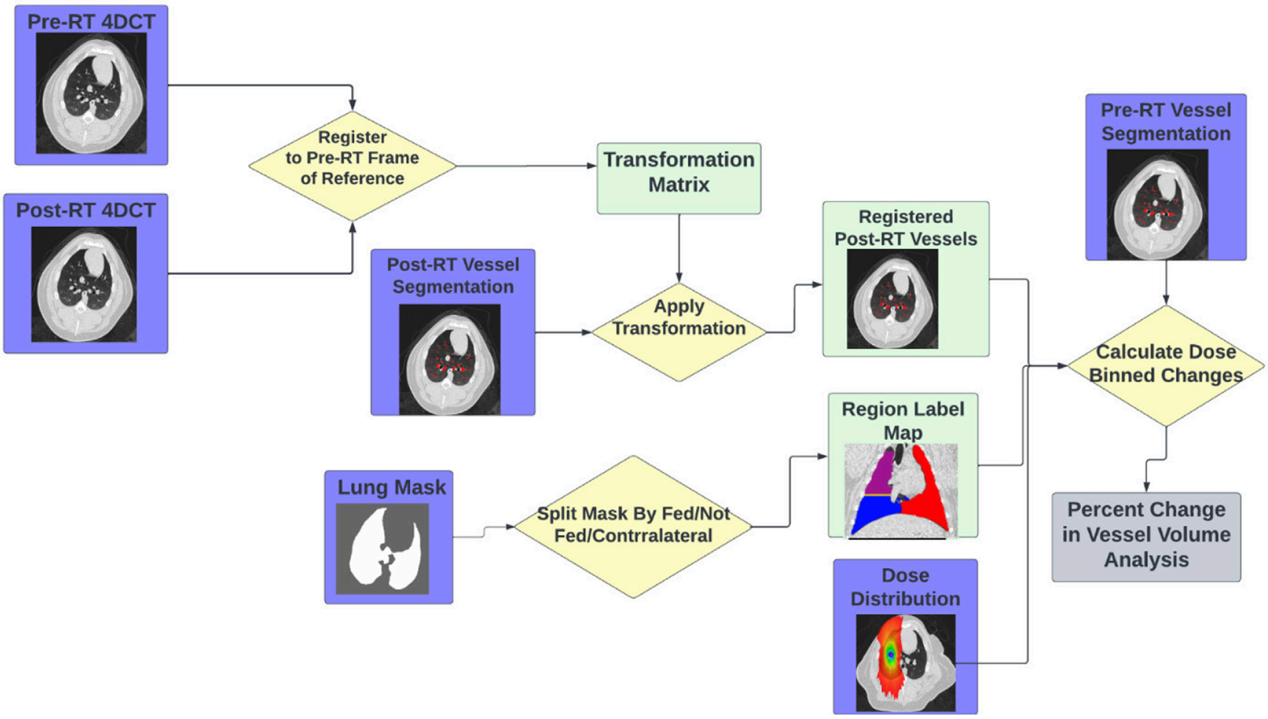

FIGURE 4
Flowchart showing the workflow to perform the indirect vascular change analysis using the tools described.

examples it is observed that the larger vessels are no longer segmented. In the post-RT case it can also be seen that the radiographic change region is no longer classified as vessel. When large vasculature is added back in both pre and post-RT resultant vessel maps appear to be consistent with the vessels observed on the original CTs. Figures 6, 7 show the improvements made by the novel vessel segmentation in an axial slice of all of the subjects used in this work. In all subjects, it is clear that radiographic change is falsely classified as vessel in the original vessel segmentation method. This is further highlighted in Figure 8 where a side by side 3D rendering shows the effect of this false classification. The conventional method, in the regions denoted as having radiographic change, are so over-segmented that you cannot distinguish the true vasculature in this region and it just appears as a large condensed structure. However, when using the novel segmentation workflow presented in this work, we see that it appears specificity is improved in those regions of radiographic change while preserving the sensitivity of the segmentation in the rest of the lung. The improved workflow 3D rendering shows a connected vascular tree in these regions. In the group B swine, the result is more subtle but this is due to the fact that the radiographic change in these swine was not as drastic as the group A swine in a single axial slice. This is due to the differences in dose distribution delivered as well as differences in the size of vasculature irradiated.

3.2 Post-RT changes in vasculature

Figure 9 and Table 1 show a summary of the percent changes in volume of vessel in each of the dose bins. For the group B subjects, analysis is not split into fed and not fed regions in this figure. Each point on the graph is plotted at the center of the dose bin it represents and is the average percent change of the five subjects analyzed (Group A or Group B) or 10 subjects analyzed (All Swine). All data sets show strong linear correlation with dose where the reduction in vascular volume increases with increasing dose. However, there is a difference in behavior between Group A and Group B where Group A shows minimal change in the unirradiated dose bin (-3.3 ± 3.8%) while Group B shows a large change (-17.8 ± 5.3%).

Figure 10 and Table 2 show a summary of the percent changes in volume of vessel in each of the dose bins with the additional group B analysis. All data sets still show strong linear correlation with dose where the reduction in vascular volume increases with increasing dose. The percent changes in the not fed regions are very similar to the group A percent changes while the fed regions show significantly higher magnitudes of change.

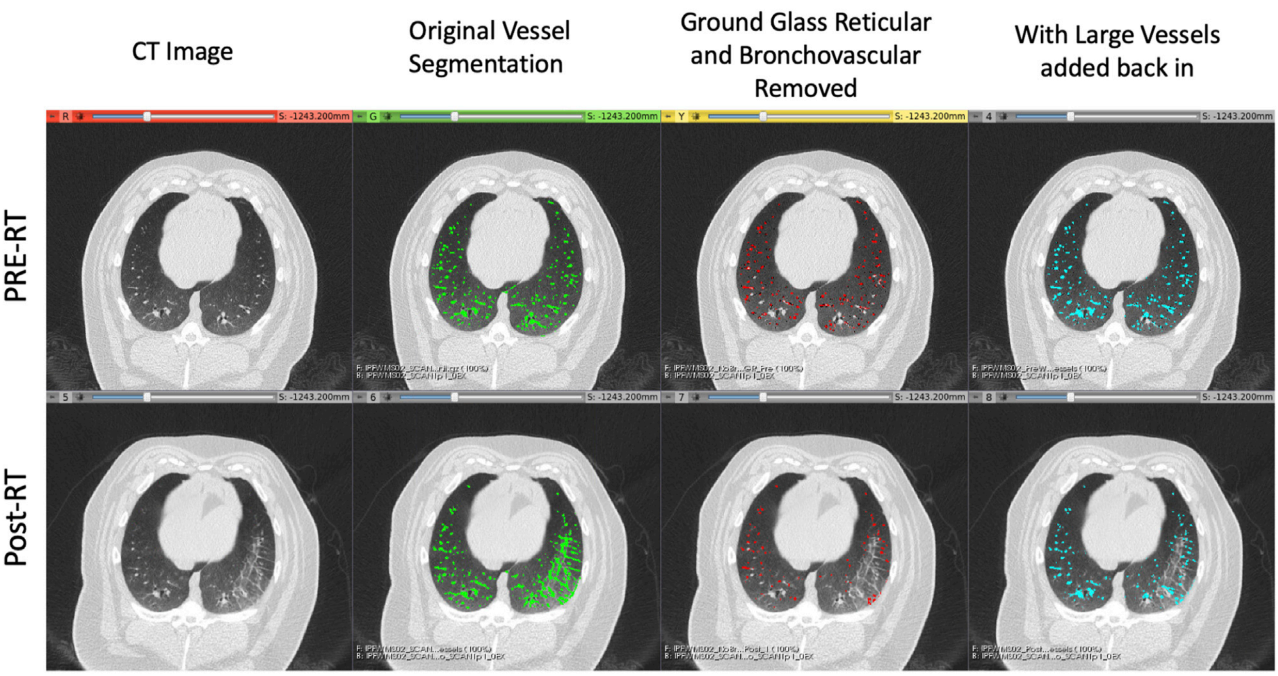

FIGURE 5
Example of the vessel segmentation algorithm results for a pre-RT (top row) and post-RT (bottom row) example. From left to right: the original CT, the vessel segmentation denoting voxels classified as vessels in green, the result of removing voxels that were classified as both vessels and either ground glass reticular or bronchovascular (red), and finally the result of adding back in the large vessels (blue).

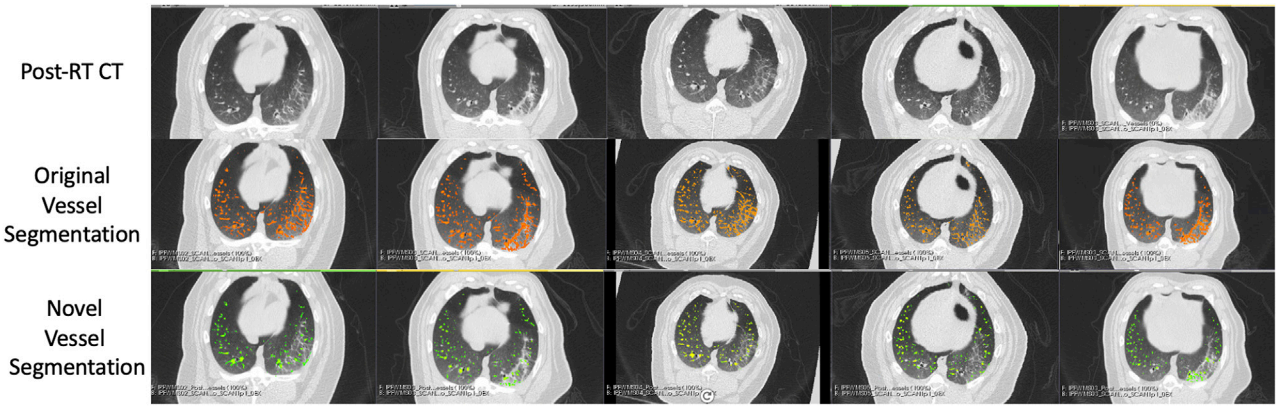

FIGURE 6
Segmentation results in the five Group **(A)** swine. Each column represents a subject where the top row shows the post-RT CT image in an axial slice showing the post-RT radiographic change. The middle row shows the original vessel segmentation overlayed on the CT in red which in all subjects classified damaged regions of the lung as vessel. The bottom row shows the result of the novel vessel segmentation workflow overlayed on the CT in green. In all subjects, the apparent quality of the vessel segmentation improves in the regions of radiographic change as indicated by the reduction in large connected regions being identified. The resulting segmentation appears to align with vessels that can be observed in the CT in both irradiated and non-irradiated regions.

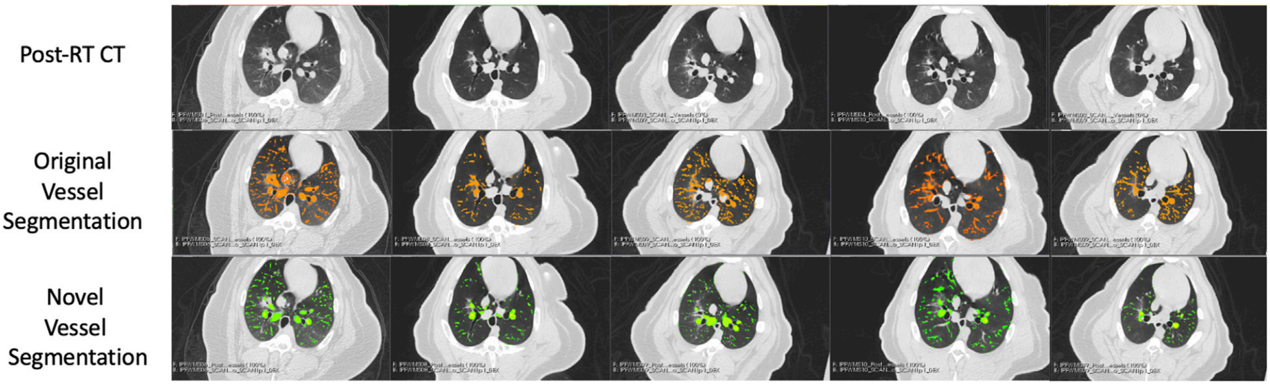

FIGURE 7
Segmentation results in the five Group **(B)** swine. Each column represents a subject where the top row shows the post-RT CT image in an axial slice showing the post-RT radiographic change. The middle row shows the original vessel segmentation overlayed on the CT in red which in all subjects classified damaged regions of the lung as vessel. The bottom row shows the result of the novel vessel segmentation workflow overlayed on the CT in green. In all subjects, the apparent quality of the vessel segmentation improves in the regions of radiographic change as indicated by the reduction in large connected regions being identified. The resulting segmentation appears to align with vessels that can be observed in the CT in both irradiated and non-irradiated regions.

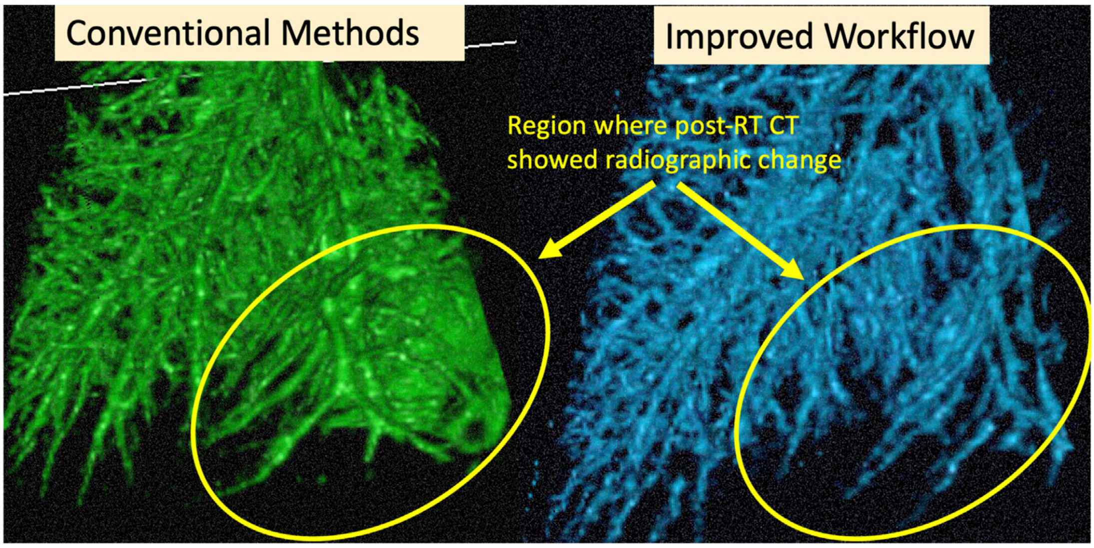

FIGURE 8
Example cropped 3D Rendering of an example subject. Circled regions show where the CT showed radiographic change post-RT. We see the result of the over-segmentation in the conventional method and the improvement on this using the proposed method.

3.3 Correlation of vasculature and perfusion change

Figure 11 and Table 3 show the relation between the percent change in vessel volume and the percent change in perfusion with each analysis contour labeled. The percent change in perfusion values were analyzed on the same subjects and same contours and were previously reported in Wuschner et al. (Wuschner et al., 2022). The perfusion study showed an indirect effect where the fed vessels, regardless of dose, experienced large, statistically significant compared to pre-RT, perfusion reductions. However, the not fed vessels did not experience statistically significant changes except in the mid dose vessels indicating that the perfusion reduction was dose dependent (in the case of not fed regions) but also dependent on location relative to highly irradiated regions (fed regions). The contralateral lung in the

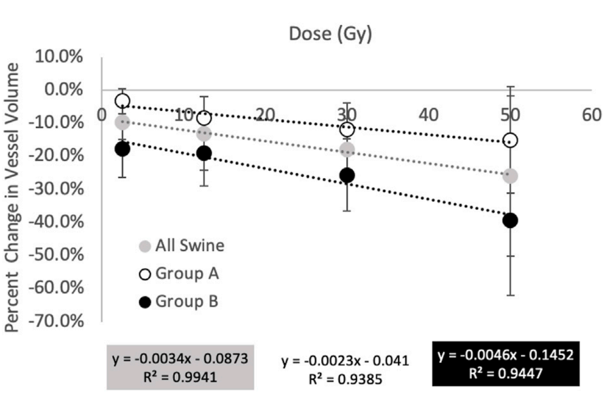

FIGURE 9
Summary of percent changes in vessel volume as a function of dose. All groups show increasing reductions in vessel volume with increasing dose however the magnitude of the changes differs in behavior between groups **(A)** and **(B)**. Group **(A)** shows minimal change in the unirradiated dose bin while Group **(B)** shows a large change.

TABLE 1 Summary of percent changes in vessel volume. Values in table are entered as average (standard deviation) of the 10 swine (all swine) or of the five swine (Group A or Group B). Statistically significant values ($p < 0.05$) are denoted with a *.

Dose (Gy)	All swine	Group a swine	Group B swine
2.5	-9.7% (8.7%)*	-3.35% (3.8%)	-17.8% (5.3%)*
12.5	-13.1% (10%)	-8.4% (6.5%)*	-19.1% (11.1%)
30	-18% (10.9%)*	-11.8% (7.9%)	-25.7% (9.4%)*
50	-25.9% (22.7%)*	-15.1% (16.1%)	-39.4% (24.2%)*

perfusion study experienced no statistically significant perfusion change. A line of best fit is drawn on Figure 11 and shows good correlation ($R^2 = 0.726$) between the perfusion study results from our previous study, and the vascular change results in this study.

4 Discussion

4.1 Improvements of vessel segmentation method

It can be noted that the results presented in this section are all qualitative. While the qualitative results are convincing and encouraging, we recognize that future work should involve further validation of this method using a quantitative analysis. To our knowledge however, there is no publicly available labeled ground-truth data-set for vascular segmentation in the presence of radiation-induced radiographic change or other similar high density lung damage that could be confused as vessel using standard segmentation methods. The only available ground-truth we are aware of only labels vasculature in normal healthy lungs which will not test the novelty of our segmentation workflow.

With this acknowledged, Figure 5 shows a clear qualitative improvement in accuracy in the segmentation. In the post-RT scan there is clear radiographic change in the slice shown in the right lung. The original vessel segmentation shown in green identifies this radiographic change as vasculature. This misclassification was consistent across subjects and highlights the limitations to using the vessel segmentation method developed by Konopczynski et al. (Konopczynski et al., 2016) alone.

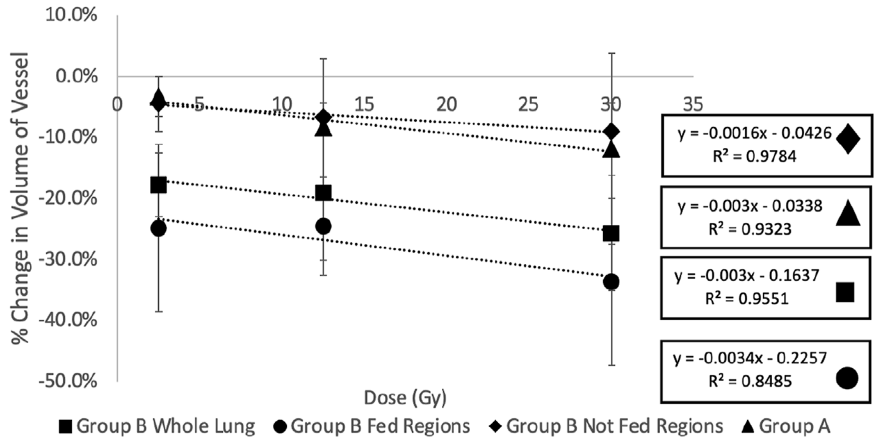

FIGURE 10
Summary of the percent changes in volume of vessel in each of the dose bins for the group **(A)** swine (all not fed), group **(B)** swine, and split group **(B)** swine results masked by being in a fed or not fed region. All data sets show strong linear correlation with dose where the reduction in vascular volume increases with increasing dose. The percent changes in the not fed regions are very similar to the group **(A)** percent changes while the fed regions show significantly higher magnitudes of change.

TABLE 2 Summary of percent changes in vessel volume. Values in table are entered as average (standard deviation) of the five swine in each group. Statistically significant values ($p < 0.05$) are denoted with a *.

Dose (Gy)	Group a swine	Group B not fed regions	Group B fed regions	Group B whole lung
2.5	-3.4% (3.8%)	-4.4% (3.3%)	-24.9% (13.7%)	-17.8% (5.3%)*
12.5	-8.4% (6.5%)*	-24.6% (8.1%)	-6.7% (11.2%)	-19.1% (11.1%)
30	-11.8% (7.9%)	-33.7% (13.7%)*	-9.1% (15.6%)	-25.7% (9.4%)*

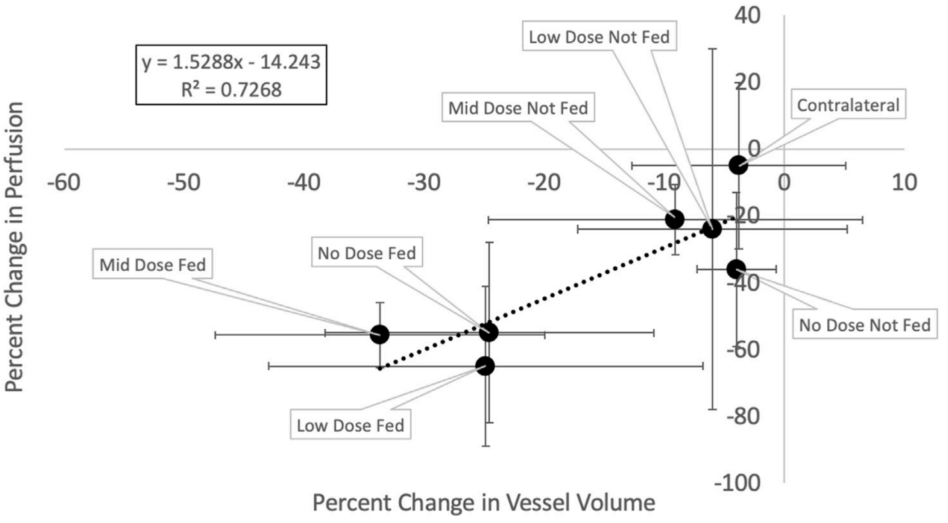

FIGURE 11
Change in vessel volume vs change in perfusion. Each point represents a different analysis contour and is the average of the five swine subjects with error bars representing the standard deviations in each metric.

In Figure 2 another example of this mis-classification is shown in the middle pane where the regions denoted in orange pick up radiographic damage in the left lung. This figure further shows the texture correspondence in these regions using the AMFM texture analysis where it is clear that the dorsal regions of the left lung, where the radiographic change and false vessel classification is observed, is comprised of ground glass reticular and bronchovascular textures. The effect of removing vessels of this classification is shown in the third pane from the left in Figure 5. It appears through qualitative inspection that the specificity is improved in the region showing radiographic change but in both the pre and post-RT cases the sensitivity is reduced in the detection of large vessels. Finally, the final pane shows the result of the third step where large vessels are added back in. Here we see the apparent quality of the vessel segmentation improves in both irradiated and non-irradiated regions and is now consistent with the observable vessels on the CT image.

Particularly to note, is that in the pre-RT scan, the original and final segmentations appear identical. This confirms for us that the step of removing textures is only necessary to reduce the false positives in the case of abnormal radiographic features. In this work where the swine lungs were healthy at pre-RT this serves to remove radiation-induced damage, but in the case of human subjects who may have lungs with pre-existing disease, this could be extended for use in pre-RT scans as well.

4.2 Changes in vasculature

All results show a linear relation between increasing dose and decreasing vessel volume suggesting that radiation dose causes vascular volume reduction. Potential mechanisms of this include constriction and atrophy. Vascular atrophy has already been observed in the Group A swine and the direct effects of this atrophy on perfusion were reported previously (Wuschner et al., 2021a). Pathological analysis on these swine has confirmed a loss

TABLE 3 Summary of vessel volume percent change and perfusion percent change in each contour analyzed. Data in the table is the same as the data shown in Figure 11. Entries are written as the average (standard deviation) of the five subjects. Perfusion results are as reported in Wuschner et al. (Wuschner et al., 2022). Statistically significant values ($p < 0.05$) are denoted with a *.

Contour	Vessel volume change	Perfusion change
No Dose Fed 0–5 Gy	-24.6% (13.7%)	-55% (27%)*
Low Dose Fed 5–20 Gy	-24.9% (18.1%)*	-65% (24%)*
Mid Dose Fed 20–40 Gy	-33.7% (13.7%)*	-55.7% (9.7%)*
No Dose Not Fed 0–5 Gy	-4% (3.3%)	-36 (23%)
Low Dose Not Fed 5–20 Gy	-6% (11.2%)	-24% (54%)
Mid Dose Not Fed 20–40 Gy	-9.1% (15.6%)	-21.2% (10.5%)*
Contralateral	-3.8% (8.9%)	-5% (25%)

of structure in the vascular wall in addition to reporting additional mechanisms of constriction as well as confirming the intraparenchymal hemorrhage hypotheses reported in (Wuschner et al., 2021a), (Wuschner et al., 2022), and (Marks et al., 2003) where vascular leakage was observed as a result of radiation dose delivered (Wuschner et al., 2021b).

However, there are a few differences between analysis groups that suggest unique physiological characteristics. Figure 10 shows the difference between the fed and not fed regions that received the same dose. The "fed" region receiving the same dose as the corresponding "not fed" region showed significantly larger magnitudes of reduction in vessel volume. We believe this to be indication of an "indirect effect" where regions receiving no or minimal dose experience large functional declines. This effect has been observed previously in several studies (Wallat et al., 2021) (Vicente et al., 2020) (Thomas et al., 2019) (Farr et al., 2018).

Furthermore, the results of the "not fed" regions agree closely with the results of the group A swine who were irradiated in an inferior region of the lung. This means the region irradiated in the group A swine was centered on a small vessel that did not bifurcate multiple times to feed additional vasculature. These swine did not even have regions that were "fed" and received no dose and some did not have vessels irradiated that were "fed" and irradiated to low dose. These swine therefore, only experienced direct damage where the damage to the region is dependent primarily to the dose it received. This is also true of the "not fed" regions in the group B swine. However, the "fed" regions of the group A swine are also dependent on the dose to feeding vasculature; meaning if there is morphological change in the anatomy of a vessel that feeds the region, there will be downstream reduction in perfusion.

4.3 Correlation between vessel and perfusion change

Figure 11 shows a strong correlation exists between the observed reductions in vasculature and the observed reductions in perfusion ($R^2 = 0.72$). These results suggest that the change in vessel volume (a metric derived from a standard simulation 4DCT), is related to the change in perfusion to a region. Physiologically, this makes sense. Perfusion refers to the flow of blood through the capillary network surrounding the alveolar sacs. If the vascular tree is atrophied and blood cannot reach these capillaries, perfusion will reduce. Furthermore, the indirect effect will be magnified in the fed regions if blood leaks out of the vasculature several bifurcations prior to additional vasculature which supports why the percent changes in vessel volume are smaller than the percent changes in perfusion.

This combined with the dose dependency results shown in this work as well as our previous work (Wuschner et al., 2022) suggests that with enough subjects, a dose response model could be developed using the vascular tree as an input to predict the decline in perfusion to a region based on the dose it receives and the proximity of it to other locations receiving high dose on the vascular tree. This would allow for predictions in functional perfusion information to be made without the need for contrast.

This is a benefit for many reasons. The first benefit is for ease of integration into clinical workflow. Lung radiotherapy patients already receive a 4DCT in order to track lung motion and perform treatment planning. Previous perfusion studies have used methods such as SPECT or PET which require an additional scan and an injection of a radio-pharmaceutical (Ireland et al., 2007) (Farr et al., 2015a) (Thomas et al., 2019) (Marks et al., 2003) (Hopkins et al., 2012). The vascular maps can be derived from the same scans that are already used for treatment. While there are CT-derived perfusion scans, these all require the administration of iodine contrast. While being an additional step in clinical workflow, iodine can also be damaging to patient's kidneys which is particularly important in the case of cancer patients who may already have compromised baseline renal function. Finally, these perfusion scans have limited field of view which limits the region of analysis and the number of vessels that can be analyzed. This leads to a large degree of variability in the perfusion derived measurements. This can be observed in Table 3 where the vessel change measurements have smaller standard deviations than the perfusion change measurements due to being able to analyze more vessels in the regions.

4.4 Comment on variability

There was a large degree of variability in these measurements as shown by the error bars on the plot in Figure 11 and those listed in Table 3. It is important to note that the sample size of this study was limited to only five subjects for this particular analysis since only the Group B swine were irradiated with enough distal vasculature and tissue to allow for this analysis. Notes on variations in response between subjects and potential causes for the large standard deviations in the perfusion work have previously been described by Wuschner et al. (Wuschner et al., 2022) and are applicable here as well. Future work should include extending this analysis to a larger pool of subjects to minimize the sensitivity of the average measurement to a single subject. Additionally, the new workflow, while it appears to yield a promising improvement, does still contain minor error which could contribute to some variability as well. Some of these errors can be visualized in Figure 5 where in the sub-pleural regions there are small regions segmented that do not look like vessels in the CT. This is likely due to errors in the aerated masking technique that struggles with damage that is so peripheral in the lung.

4.5 Application to functional avoidance radiation therapy

Lung cancer is one of the most commonly diagnosed cancers and is currently responsible for the highest percentage of cancer related deaths (American Cancer Society, 2022). A significant portion of these patients receive radiation therapy (RT) as part of their treatment depending on the stage of their cancer (American Cancer Society, 2022). However, many of these patients experience radiation-induced lung injuries as a result of treatment which decrease patient quality of life and can even be fatal (Marks et al., 2003).

Conventional methods use volumetric dose constraints to minimize toxicities, however these methods do not consider the local function of the lung which has been reported to be locally dependent and different by individual (Siva et al., 2015) (Farr et al., 2015b) (Faught et al., 2017) (Bates et al., 2009) (Vinogradskiy et al., 2013) (Yamamoto et al., 2011) (Shioyama et al., 2007).

Functional avoidance in RT treatment planning aims to do consider these personalized local dependencies by selectively avoiding high functioning regions of the lung. To do this, detailed dose response models are required. In recent years, multiple groups have begun developing these models and some have tested their efficacy in clinical trials (McDonald et al., 1995) (Mah and Dyk, 1988) (Mehta, 2005) (Graves et al., 2010) (Patton et al., 2018) (Koike et al., 2015) (Hopkins et al., 2012) (Zhang et al., 2010) (Vinogradskiy et al., 2013) (Wallat et al., 2020) (Wallat et al., 2021) (Bates et al., 2009) (Hoover et al., 2014) (Ireland et al., 2016) (Vicente et al., 2020). To date, the only prospective clinical trials using these techniques have been ventilation-based (Bayouth et al., 2019) and all non-contrast CT-derived methods have been exclusively ventilation based (Patton et al., 2018) (Vinogradskiy et al., 2013) (Vicente et al., 2020) (Castillo et al., 2021). This does not create a comprehensive model to accurately model the function regions that need avoidance. Perfusion based trials have been performed, however they have all been retrospective and utilized scans outside of normal clinical workflow which poses challenges as described previously (Ireland et al., 2007) (Siva et al., 2015) (Farr et al., 2015a) (Thomas et al., 2019). Having a bio-marker that can derive perfusion information from the same standard of care CT would allow for a more comprehensive model of function to be developed and tested in prospective clinical trials. Future work should involve performing these measurements on a large cohort of subjects to build a model then testing that model in a prospective clinical trial.

5 Conclusion

In this work we present a novel vascular segmentation workflow that shows significant observable improvements. Through qualitative inspection, it appears there is an improvement in accuracy in the presence of damage or abnormal radiographic features on a CT. Additionally we use this method to demonstrate a strong dose-response relationship on the morphology of segmented vasculature post-RT. Finally, we show that these measurements correlate with previously reported perfusion changes in the same subject cohort which presents an opportunity for this method to be a non-contrast CT-derived bio-marker for functional perfusion change. While future work should fully validate the method proposed *via* quantitative analysis, this work presents numerous potential benefits towards the advancement of functional avoidance treatment planning.

Data availability statement

The original contributions presented in the study are included in the article/supplementary material, further inquiries can be directed to the corresponding author.

Ethics statement

The animal study was reviewed and approved by University of Wisconsin Institutional Animal Care and Use Committee.

Author contributions

Conceptualization, AW, J.R, GC, MF, EW, JB; methodology, AW, DS, JB; software, GC, EW, SG;

validation, AW; formal analysis, AW; resources,JB.; data curation, AW, MF, EW, SG; writing—original draft preparation, AW; writing—review and editing, JB, MF, EW, JR, GC, SG; supervision, JB.; project administration, JB.; funding acquisition, JB. All authors have read and agreed to the published version of the manuscript.

Funding

This research was funded by the National Institutes of Health grant CA166703.

Acknowledgments

The authors would like to thank the following people: Jen Meudt and the students of the University Wisconsin Veterinary school for their assistance with animal husbandry, Accuray for providing a Radixact system for research purposes and assisting with technical support on the system throughout the swine treatments, and Jessica Miller and Michael Lawless for their assistance in developing the Dynamic Contrast CT protocol.

Conflict of interest

JR is a shareholder in VIDA Diagnostics, Inc., GC receives licensing fees from VIDA Diagnostics, Inc., and JB has ownership interest in MR Guidance, LLC.

MR Guidance has business activity with ViewRay, Inc., and while this project was not sponsored in any way by ViewRay, data were collected on the ViewRay MRIdian system.

Data were collected on a Radixact system (Accuray, Inc.) provided to UW-Madison under a research agreement (JB, PI)

The remaining authors declare that the research was conducted in the absence of any commercial or financial relationships that could be construed as a potential conflict of interest.

Publisher's note

References

Agam, G., Armato, S., and Wu, C. (2005). Vessel tree reconstruction in thoracic CT scans with application to nodule detection. *IEEE Trans. Med. Imaging* 24, 486–499. doi:10.1109/TMI.2005.844167

American Cancer Society (2022). *2022-cancer-facts-and-figures*. American Cancer Society.

Andrews, H. C., and Swartzlander, E. E. (1973). Introduction to mathematical techniques in pattern recognition. *IEEE Trans. Syst. Man, Cybern.* SMC-3, 302. doi:10.1109/TSMC.1973.4309231

Aylward, S., and Bullitt, E. (2002). Initialization, noise, singularities, and scale in height ridge traversal for tubular object centerline extraction. *IEEE Trans. Med. Imaging* 21, 61–75. doi:10.1109/42.993126

Bates, E. L., Bragg, C. M., Wild, J. M., Hatton, M. Q., and Ireland, R. H. (2009). Functional image-based radiotherapy planning for non-small cell lung cancer: A simulation study. *Radiother. Oncol.* 93, 32–36. doi:10.1016/j.radonc.2009.05.018

Bayouth, J., Wallat, E., Wuschner, A., Flakus, M., Patton, T., Shao, W., et al. (2019). *Longitudinal changes in lung tissue elasticity following radiation therapy*. San Antonio, Tx: AAPM Annual Meeting.

Buelow, T., Wiemker, R., Blaffert, T., Lorenz, C., and Renisch, S. (2005). "Automatic extraction of the pulmonary artery tree from multi-slice CT data," in Proceeding of the Medical Imaging 2005: Physiology, Function, and Structure from Medical Images (SPIE), San Diego, California, United States, April 2005, 730. vol. 5746. doi:10.1117/12.595286

Cao, K., Ding, K., Reinhardt, J. M., and Christensen, G. E. (2012). Improving intensity-based lung CT registration accuracy utilizing vascular information. *Int. J. Biomed. Imaging* 2012, 1–17. doi:10.1155/2012/285136

Castillo, E., Nair, G., Turner-Lawrence, D., Myziuk, N., Emerson, S., Al-Katib, S., et al. (2021). Quantifying pulmonary perfusion from non-contrast computed tomography. *Med. Phys.* 48, 1804–1814. doi:10.1002/mp.14792

Coates, A., and Ng, A. Y. (2011). "The importance of encoding versus training with sparse coding and vector quantization," in Proceedings of the 28th International Conference on International Conference on Machine Learning, Bellevue, Washington, USA (Bellevue, WA: OmniPress), 921–928.

Farr, K. P., Kallehauge, J. F., Møller, D. S., Khalil, A. A., Kramer, S., Bluhme, H., et al. (2015). Inclusion of functional information from perfusion SPECT improves predictive value of dose–volume parameters in lung toxicity outcome after radiotherapy for non-small cell lung cancer: A prospective study. *Radiother. Oncol.* 117, 9–16. doi:10.1016/j.radonc.2015.08.005

Farr, K. P., Møller, D. S., Khalil, A. A., Kramer, S., Morsing, A., and Grau, C. (2015). Loss of lung function after chemo-radiotherapy for NSCLC measured by perfusion SPECT/CT: Correlation with radiation dose and clinical morbidity. *Acta Oncol.* 54, 1350–1354. doi:10.3109/0284186X.2015.1061695

Farr, K. P., Khalil, A. A., Møller, D. S., Bluhme, H., Kramer, S., Morsing, A., et al. (2018). Time and dose-related changes in lung perfusion after definitive radiotherapy for NSCLC. *Radiother. Oncol.* 126, 307–311. doi:10.1016/j.radonc.2017.11.008

Faught, A. M., Miyasaka, Y., Kadoya, N., Castillo, R., Castillo, E., Vinogradskiy, Y., et al. (2017). Evaluating the toxicity reduction with computed tomographic ventilation functional avoidance radiation therapy. *Int. J. Radiat. Oncol. Biol. Phys.* 99, 325–333. doi:10.1016/j.ijrobp.2017.04.024

Ferdeghini, E. M., Pinamonti, B., Picano, E., Lattanzi, F., Bussani, R., Slavich, G., et al. (1991). Quantitative texture analysis in echocardiography: Application to the diagnosis of myocarditis. *J. Clin. Ultrasound* 19, 263–270. doi:10.1002/jcu.1870190503

Fleagle, S. R., Stanford, W., Burns, T., and Skorton, D. J. (1994). *Feasibility of quantitative texture analysis of cardiac magnetic resonance imagery: Preliminary results*, 23–32. doi:10.1117/12.174416

Gerard, S. E. (2018). *Multi-scale convolutional neural networks for segmentation of pulmonary structures in computed tomography*. Ph.D. thesis. Iowa City: University of Iowa.

Gerard, S. E., Herrmann, J., Kaczka, D. W., Musch, G., Fernandez-Bustamante, A., and Reinhardt, J. M. (2020). Multi-resolution convolutional neural networks for fully automated segmentation of acutely injured lungs in multiple species. *Med. Image Anal.* 60, 101592. doi:10.1016/j.media.2019.101592

Gerard, S. E., Herrmann, J., Xin, Y., Martin, K. T., Rezoagli, E., Ippolito, D., et al. (2021). CT image segmentation for inflamed and fibrotic lungs using a multi-resolution convolutional neural network. *Sci. Rep.* 11, 1455. doi:10.1038/s41598-020-80936-4

Graves, P. R., Siddiqui, F., Anscher, M. S., and Movsas, B. (2010). Radiation pulmonary toxicity: From mechanisms to management. *Semin. Radiat. Oncol.* 20, 201–207. doi:10.1016/j.semradonc.2010.01.010

Hoover, D. A., Capaldi, D. P., Sheikh, K., Palma, D. A., Rodrigues, G. B., Dar, A. R., et al. (2014). Functional lung avoidance for individualized radiotherapy (FLAIR): Study protocol for a randomized, double-blind clinical trial. *BMC Cancer* 14, 934. doi:10.1186/1471-2407-14-934

Hopkins, S. R., Wielpütz, M. O., and Kauczor, H. U. (2012). Imaging lung perfusion. *J. Appl. Physiol.* 113, 328–339. doi:10.1152/japplphysiol.00320.2012

Ireland, R. H., Bragg, C. M., McJury, M., Woodhouse, N., Fichele, S., van Beek, E. J., et al. (2007). Feasibility of image registration and intensity-modulated radiotherapy planning with hyperpolarized helium-3 magnetic resonance imaging for non–small-cell lung cancer. *Int. J. Radiat. Oncol. Biol. Phys.* 68, 273–281. doi:10.1016/j.ijrobp.2006.12.068

Ireland, R., Tahir, B., Wild, J., Lee, C., and Hatton, M. (2016). Functional image-guided radiotherapy planning for normal lung avoidance. *Clin. Oncol.* 28, 695–707. doi:10.1016/j.clon.2016.08.005

Jerman, T., Pernuš, F., Likar, B., and Špiclin, Z. (2015). *Beyond frangi: An improved multiscale vesselness filter*. doi:10.1117/12.2081147

Kiros, R., Popuri, K., Cobzas, D., and Jagersand, M. (2014). "Stacked multiscale feature learning for domain independent medical image segmentation," in *International workshop on machine learning in medical imaging*, 25–32. doi:10.1007/978-3-319-10581-9-4

Koike, H., Sueyoshi, E., Sakamoto, I., and Uetani, M. (2015). Quantification of lung perfusion blood volume by dual-energy CT in patients with and without chronic obstructive pulmonary disease. *J. Belg. Soc. Radiol.* 99, 62–68. doi:10.5334/jbr-btr.865

Konopczynski, T., Kroger, T., Zheng, L., Garbe, C. S., and Hesser, J. (2016). "Automated multiscale 3D feature learning for vessels segmentation in Thorax CT images," in Proceedings of the 2016 IEEE Nuclear Science Symposium, Medical Imaging Conference and Room-Temperature Semiconductor Detector Workshop (NSS/MIC/RTSD), Strasbourg, France, October 2016 (IEEE). doi:10.1109/NSSMIC.2016.8069570

Krissian, K., Malandain, G., Ayache, N., Vaillant, R., and Trousset, Y. (2000). Model-based detection of tubular structures in 3D images. *Comput. Vis. Image Underst.* 80, 130–171. doi:10.1006/cviu.2000.0866

Lavi, G., Lessick, J., Johnson, P. C., and Khullar, D. (2004). Single-seeded coronary artery tracking in CT angiography. *IEEE Nucl. Sci. Symposium Conf. Rec.* 5, 3308–3311. doi:10.1109/nssmic.2004.1466397

Mah, K., and Dyk, V. (1988). Quantitative measurement of changes in human lung density following irradiation. *Radiotherapy Oncol.* 11, 169–179. doi:10.1016/0167-8140(88)90253-8

Marks, L., Yu, X., Vujaskovic, Z., Smalljr, W., Folz, R., and Anscher, M. (2003). Radiation-induced lung injury. *Semin. Radiat. Oncol.* 13, 333–345. doi:10.1016/S1053-4296(03)00034-1

McDonald, S., Rubin, P., Phillips, T. L., and Marks, L. B. (1995). Injury to the lung from cancer therapy: Clinical syndromes, measurable endpoints, and potential scoring systems. *Int. J. Radiat. Oncol. Biol. Phys.* 31, 1187–1203. doi:10.1016/0360-3016(94)00429-O

Medical Imaging 2008: Image Processing (2008). *Medical Imaging 2008: Image Processing*, 6914. San Diego, CA: Society of Photo-Optical Instrumentation Engineers (SPIE) Conference Series.

Mehta, V. (2005). Radiation pneumonitis and pulmonary fibrosis in non-small-cell lung cancer: Pulmonary function, prediction, and prevention. *Int. J. Radiat. Oncol. Biol. Phys.* 63, 5–24. doi:10.1016/j.ijrobp.2005.03.047

Metz, C., Schaap, M., Van Der Giessen, A., Van Walsum, T., and Niessen, W. (2007). "Semi-automatic coronary artery centerline extraction in computed tomography angiography data," in Proceeding of the 2007 4th IEEE International Symposium on Biomedical Imaging: From Nano to Macro - Proceedings, Arlington, VA, USA, April 2007 (IEEE), 856–859. doi:10.1109/ISBI.2007.356987

Patton, T. J., Bayouth, J. E., Bednarz, B. P., Fain, S. B., Reinhardt, J. M., and Smilowitz, J. (2018). *Quantifying and modeling radiation therapy-induced ventilation changes and investigating the robustness of 4DCT-based functional avoidance*. Madison, WI: Tech. rep.

Reed, J., Krueger, C., Shanmuganayagam, D., Crenshaw, T., Reichert, J., and Parrish, J. (2010). *Wisconsin miniature swine*. Madison, WI: Tech. rep.

Rudyanto, R. D., Kerkstra, S., van Rikxoort, E. M., Fetita, C., Brillet, P. Y., Lefevre, C., et al. (2014). Comparing algorithms for automated vessel segmentation in computed tomography scans of the lung: The VESSEL12 study. *Med. Image Anal.* 18, 1217–1232. doi:10.1016/j.media.2014.07.003

Sato, Y., Nakajima, S., Shiraga, N., Atsumi, H., Yoshida, S., Koller, T., et al. (1998). Three-dimensional multi-scale line filter for segmentation and visualization of curvilinear structures in medical images. *Med. Image Anal.* 2, 143–168. doi:10.1016/S1361-8415(98)80009-1

Schnarr, E., Beneke, M., Casey, D., Chao, E., Chappelow, J., Cox, A., et al. (2018). Feasibility of real-time motion management with helical tomotherapy. *Med. Phys.* 45, 1329–1337. doi:10.1002/mp.12791

Shikata, H., Hoffman, E. A., and Sonka, M. (2004). "Automated segmentation of pulmonary vascular tree from 3D CT images," in Proceeding of the Medical Imaging 2004: Physiology, Function, and Structure from Medical Images (SPIE), San Diego, California, United States, April 2004, 107. vol. 5369. doi:10.1117/12.537032

Shioyama, Y., Jang, S. Y., Liu, H. H., Guerrero, T., Wang, X., Gayed, I. W., et al. (2007). Preserving functional lung using perfusion imaging and intensity-modulated radiation therapy for advanced-stage non–small cell lung cancer. *Int. J. Radiat. Oncol. Biol. Phys.* 68, 1349–1358. doi:10.1016/j.ijrobp.2007.02.015

Siva, S., Thomas, R., Callahan, J., Hardcastle, N., Pham, D., Kron, T., et al. (2015). High-resolution pulmonary ventilation and perfusion PET/CT allows for functionally adapted intensity modulated radiotherapy in lung cancer. *Radiother. Oncol.* 115, 157–162. doi:10.1016/j.radonc.2015.04.013

Sonka, M., Hlavac, V., and Boyle, R. (1993). *Image processing analysis and machine vision chapman*. Iowa City, IA: Hall Computing, 112–178.

Thomas, H. M. T., Zeng, J., Lee, H. J., Jr, Sasidharan, B. K., Kinahan, P. E., Miyaoka, R. S., et al. (2019). Comparison of regional lung perfusion response on longitudinal MAA SPECT/CT in lung cancer patients treated with and without functional tissue-avoidance radiation therapy. *Br. J. Radiol.* 92, 20190174. doi:10.1259/bjr.20190174

Uppaluri, R., Mitsa, T., and Galvin, J. R. (1995). *Fractal analysis of high-resolution CT images as a tool for quantification of lung diseases*, 133. doi:10.1117/12.209685

Uppaluri, R., Mitsa, T., Sonka, M., Hoffman, E. A., and Lennan, G. M. C. (1997). Quantification of pulmonary emphysema from lung computed tomography images. *Am. J. Respir. Crit. Care Med.* 156, 248–254. doi:10.1164/ajrccm.156.1.9606093

Vicente, E., Modiri, A., Kipritidis, J., Hagan, A., Yu, K., Wibowo, H., et al. (2020). Functionally weighted airway sparing (FWAS): A functional avoidance method for preserving post-treatment ventilation in lung radiotherapy. *Phys. Med. Biol.* 65, 165010. doi:10.1088/1361-6560/ab9f5d

Vinogradskiy, Y., Diot, Q., Kavanagh, B., Schefter, T., Gaspar, L., and Miften, M. (2013). Spatial and dose-response analysis of fibrotic lung changes after stereotactic body radiation therapy. *Med. Phys.* 40, 081712. doi:10.1118/1.4813916

Wallat, E., Flakus, M., Wuschner, A., Shao, W., Christensen, G., Reinhardt, J., et al. (2020). Modeling the impact of out-of-phase ventilation on normal lung tissue response to radiation dose. *Med. Phys.* 47, 3233–3242. doi:10.1002/mp.14146

Wallat, E. M., Wuschner, A. E., Flakus, M. J., Christensen, G. E., Reinhardt, J. M., Shanmuganayagam, D., et al. (2021). Radiation-induced airway changes and downstream ventilation decline in a swine model. *Biomed. Phys. Eng. Express* 7, 065039. doi:10.1088/2057-1976/ac3197

Wuschner, A. E., Wallat, E. M., Flakus, M. J., Shanmuganayagam, D., Meudt, J., Christensen, G. E., et al. (2021). Radiation-induced Hounsfield unit change correlates with dynamic CT perfusion better than 4DCT-based ventilation measures in a novel-swine model. *Sci. Rep.* 11, 13156. doi:10.1038/s41598-021-92609-x

Wuschner, A., Wallet, E., Flakus, M., Reinhardt, J., Christensen, G., Bayouth, J., et al. (2021). "Measuring radiation-induced changes in perfusion with dynamic contrast-enhanced 4DCT and non-contrast lung density analysis in a novel swine model," in *Medical PHYSICS* (Hoboken: Wiley).

Wuschner, A. E., Flakus, M. J., Wallat, E. M., Reinhardt, J. M., Shanmuganayagam, D., Christensen, G. E., et al. (2022). Measuring indirect radiation-induced perfusion change in fed vasculature using dynamic contrast CT. *J. Pers. Med.* 12, 1254. doi:10.3390/jpm12081254

Xiao, C., Staring, M., Shamonin, D., Reiber, J. H., Stolk, J., and Stoel, B. C. (2011). A strain energy filter for 3D vessel enhancement with application to pulmonary CT images. *Med. Image Anal.* 15, 112–124. doi:10.1016/j.media.2010.08.003

Yamamoto, T., Kabus, S., Klinder, T., Lorenz, C., von Berg, J., Blaffert, T., et al. (2011). Investigation of four-dimensional computed tomography-based pulmonary ventilation imaging in patients with emphysematous lung regions. *Phys. Med. Biol.* 56, 2279–2298. doi:10.1088/0031-9155/56/7/023

Yin, Y., Hoffman, E. A., and Lin, C. L. (2009). Mass preserving nonrigid registration of CT lung images using cubic B-spline. *Med. Phys.* 36, 4213–4222. doi:10.1118/1.3193526

Zhang, J., Ma, J., Zhou, S., Hubbs, J. L., Wong, T. Z., Folz, R. J., et al. (2010). Radiation-induced reductions in regional lung perfusion: 0.1-12 Year data from a prospective clinical study. *Int. J. Radiat. Oncol. Biol. Phys.* 76, 425–432. doi:10.1016/j.ijrobp.2009.02.005

frontiers | Frontiers in Physiology

TYPE Review
PUBLISHED 03 November 2022
DOI 10.3389/fphys.2022.986422

OPEN ACCESS

EDITED BY
Joseph M. Reinhardt,
The University of Iowa, United States

REVIEWED BY
Gaetano Scaramuzzo,
University of Ferrara, Italy
Stephen Littleton,
United States Department of Veterans Affairs, United States
Savino Spadaro,
University of Ferrara, Italy

*CORRESPONDENCE
Xia Zheng,
zxicu@zju.edu.cn
Qiang Fang,
1183005@zju.edu.cn

†These authors have contributed equally to this work and share last authorship

SPECIALTY SECTION
This article was submitted to Respiratory Physiology and Pathophysiology,
a section of the journal
Frontiers in Physiology

RECEIVED 05 July 2022
ACCEPTED 25 October 2022
PUBLISHED 03 November 2022

CITATION
Jiang H, Han Y, Zheng X and Fang Q (2022), Roles of electrical impedance tomography in lung transplantation.
Front. Physiol. 13:986422.
doi: 10.3389/fphys.2022.986422

Roles of electrical impedance tomography in lung transplantation

Hui Jiang, Yijiao Han, Xia Zheng*† and Qiang Fang*†

Department of Critical Care Medicine, The First Affiliated Hospital, Zhejiang University School of Medicine, Hangzhou, China

Lung transplantation is the preferred treatment method for patients with end-stage pulmonary disease. However, several factors hinder the progress of lung transplantation, including donor shortages, candidate selection, and various postoperative complications. Electrical impedance tomography (EIT) is a functional imaging tool that can be used to evaluate pulmonary ventilation and perfusion at the bedside. Among patients after lung transplantation, monitoring the graft's pulmonary function is one of the most concerning issues. The feasible application of EIT in lung transplantation has been reported over the past few years, and this technique has gained increasing interest from multidisciplinary researchers. Nevertheless, physicians still lack knowledge concerning the potential applications of EIT in lung transplantation. We present an updated review of EIT in lung transplantation donors and recipients over the past few years, and discuss the potential use of ventilation- and perfusion-monitoring-based EIT in lung transplantation.

KEYWORDS

electrical impedance tomography, lung transplantation, lung functional imaging, mechanical ventilation, lung perfusion

1 Introduction

Since Hardy et al. (1963) successfully performed the first human lung transplantation, lung transplantation has continued to develop for several decades. Lung transplantation has become the first-choice treatment for chronic, end-stage lung disease patients in whom medical therapy was ineffective (DeFreitas et al., 2021). For patients with severe functional impairments caused by respiratory diseases, lung transplantation can substantially improve quality of life and prolong survival (Arcasoy and Kotloff, 1999). There has been steady growth in the annual incidence of lung transplantations, with approximately 4,500 single and bilateral lung transplantations performed annually in adults since 2017 (Chambers et al., 2019). Based on records from the International Society for Heart and Lung Transplantation (ISHLT) International Thoracic Organ Transplant (TTX) Registry, a total of 67,493 adult recipient transplants were reported from January 1992 to June 2018 (Chambers et al., 2021). Despite progress in surgical techniques, immunosuppressive agents, and perioperative care, many early complications, such as primary graft dysfunction (PGD), threaten the pulmonary function and viability of the allograft. Delayed onset complications, such as chronic lung allograft dysfunction

TABLE 1 Summary on research of EIT in lung transplantation.

Researchers	Research types	Subjects	Main findings of the research	Indications for EIT in lung transplantation	Limitations of the research
Caruana et al. (2010)	Case report	A patient treated with single lung transplantation for idiopathic pulmonary fibrosis	Pendelluft was detected using EIT between lungs after single lung transplantation during mechanical ventilation.	Pendelluft phenomenon detection	The finding lacked the confirmation of a randomized controlled trial
Jr et al. (2010)	Cohort study	Sixteen lung transplantation patients (6 bilateral, 5 unilateral for emphysema and 5 unilateral for fibrosis)	EIT can show dynamic lung images and be used to assess the regional ventilation in patients submitted to lung transplantation.	Regional ventilation assessment	The sample size of the study was small
Camargo et al. (2014)	Case report	A patient with bronchiolitis obliterans syndrome after bilateral lung transplantation	EIT seems to be helpful in differentiating bronchiolitis obliterans syndrome from a decrease in FEV_1 caused by other reasons after lung transplantation.	Bronchial anastomosis stenosis evaluation	The finding lacked the confirmation of a randomized controlled trial
Guerin and Frerichs (2014)	Case report	A patient with lymphangioleiomyomatosis treated with single lung transplantation	A better picture of the correlation between lung function and structure can be obtained using EIT. EIT tends to provide images closer to the truth than X-rays and CT.	Functional lung imaging	The use was not confirmed
Ramanathan et al. (2016)	Case report	Six patients treated with single lung transplantation	Changes in regional ventilation may be associated with changes in position between transplanted and native lung. Ventilation of transplanted lung was observed to be better than that of native lung, especially in lateral positions	Position-dependent changes in regional ventilation in single lung transplantation	The study involved patients with spontaneous breathing only, and the results cannot be translated to those under mechanical ventilation
Romero et al. (2016)	Case report	A single left lung transplantation recipient with emphysema-type COPD.	Recruitment maneuver was performed under EIT, and enabled the tidal volume distribution and the pressures required to ventilate the transplanted lung to be observed.	Recruitment maneuver responsiveness	The finding lacked the confirmation of a randomized controlled trial
Hart (2016)	Cohort study	Fifty lung transplantation patients	EIT is valid for the diagnosis of chronic lung allograft dysfunction in lung transplantation recipients.	Chronic lung allograft dysfunction diagnosis	No results of the study were disclosed
Sella et al. (2021a)	Cohort study	Six patients after bilateral lung transplantation (4 for pulmonary fibrosis, 1 for bronchiectasis and 1 for BOS)	EIT is a reliable tool for individualized PEEP setting in lung transplantation recipients, with similar to PEEP titration based on the best respiratory system static compliance.	PEEP titration	The finding lacked the confirmation of a randomized controlled trial
Son et al. (2021)	Case report	A lung donor after brain death	Prone positioning using EIT acutely improved the oxygenation of a brain-dead donor's lungs with atelectasis. It may be a feasible strategy to improve the pulmonary function of a marginal lung donor.	Intervention during donor care before lung transplantation	The use was not confirmed

(Continued on following page)

TABLE 1 (*Continued*) Summary on research of EIT in lung transplantation.

Researchers	Research types	Subjects	Main findings of the research	Indications for EIT in lung transplantation	Limitations of the research
Zarantonello et al. (2021)	Case report	A single lung transplantation recipient with pulmonary artery stenosis	EIT has a potential role in identifying ventilation-perfusion mismatch caused by postoperative vascular complications and allows for noninvasive bedside detection and follow-up.	Bedside detection and follow-up of pulmonary artery stenosis	Locations of stenosis cannot be precisely positioned

EIT, electrical impedance tomography; FEV_1, forced expiratory volume in one second; CT, computed tomography; COPD, chronic obstructive pulmonary disease; BOS, bronchiolitis obliterans syndrome; PEEP, positive end-expiratory pressure.

(CLAD), adversely impact the mortality and long-term outcomes of recipients (Meyer, 2018). As lung transplantation continues to develop, success will be determined by the ability to overcome obstacles, including donor shortage, appropriate candidate selection, PGD, and CLAD (Young and Dilling, 2019). They all concern lung function without exception, and assessing pulmonary function is an indispensable part (Tejwani et al., 2016).

After lung transplantation, patients usually require postoperative care and mechanical ventilation in an intensive care unit (ICU). Therefore, one of the most concerning issues for physicians is monitoring the graft's pulmonary function (Fuehner et al., 2016). The conventional lung function imaging techniques may be inconvenient or impossible for critically ill patients in the ICU. Fortunately, a new technique has been developed. Electrical impedance tomography (EIT), a radiation-free, noninvasive, and real-time imaging tool, utilizes the changes in bioelectrical impedance to extract information and provides dynamic images of ventilation at the bedside (Frerichs et al., 2017). Since EIT allows frequent adjustment of ventilator settings, it is particularly useful in assessing heterogeneous gas distribution during mechanical ventilation (Shono and Kotani, 2019). The technique has proven to be useful in ventilator parameter optimization (Bachmann et al., 2018). Various studies have reported that EIT can be used for recruitment maneuvers (RM), positive end-expiratory pressure (PEEP) titration, lung volume estimation, and pulmonary perfusion (Zhao et al., 2010; Ambrósio et al., 2021; Xu et al., 2021). Since EIT was first available commercially in Europe in 2011, clinical research and case reports have been successively conducted all over the world (Shono and Kotani, 2019). However, few studies and cases have reported the practice of EIT in lung transplantation. In this review, we present an updated clinical review of EIT in lung transplantation donors and recipients over the past few years (Table 1) and discuss the potential use of ventilation and perfusion monitoring-based EIT in lung transplantation (Figure 1).

2 Basic principle and parameters of EIT

2.1 Basic principle

Different tissues possess distinct impedance characteristics, which are determined by specific compositions, such as fat, water, and electrolytes in the extracellular fluid (Lobo et al., 2018). Thoracic bioimpedance is significantly influenced by two cyclic procedures: ventilation and perfusion. Chest impedance varies on a large scale from residual capacity to total lung volume. However, perfusion causes a relatively small change from diastole to systole compared to ventilation (Bodenstein et al., 2009). To perform bioimpedance measurements, the electrode belt of EIT is tied around the thorax. The instrument determines the distribution of bioimpedance by injecting small alternating currents through surface electrodes and measuring potential differences between pairs of passive electrodes (Muders et al., 2010). According to Ohm's law, the bioelectrical impedance between the injecting and measuring electrode pairs is obtained from the known applied current and the measured voltages. This process is repeated constantly around the entire thorax during a current cycle, and a series of results are used to reconstruct one cross-sectional EIT image (Maciejewski et al., 2021).

EIT can be used to assess lung perfusion distribution. The pulsatility method and the saline bolus injection method are the two methods of EIT used to assess lung perfusion. The pulsatility method is used to estimate pulmonary perfusion based on the measurement of pulsatile variation in pulmonary blood volume (Grant et al., 2011). Continuous information on pulmonary perfusion is retrieved by using cardiac and ventilation EIT signal separating techniques involving frequency-domain filtering, electrocardiogram (ECG) gating, and respiratory pause (Vonk Noordegraaf et al., 1998; Frerichs et al., 2009). The saline injection method reflects regional pulmonary perfusion by bolus injection of a high-conductivity contrast agent that causes changes in thoracic electrical impedance.

After saline injection, impedance is significantly decreased in a certain lung region, thus suggesting that there is more contrast agent flow and indicating adequate perfusion. To reduce the interference of respiration with impedance, it must be implemented during respiratory pause. At present, the global thoracic impedance remains relatively unchanged, which better reflects the effect of saline angiography (Xu et al., 2021).

2.2 Basic parameters

The main view in EIT displays the following three parts: The pulmonary images, the impedance waveforms, and the digital panel. The pulmonary image is divided into dynamic image and end-expiratory image of the impedance variation. A dynamic image shows an animated EIT image that represents impedance changes against the baseline. The cross-section image can be set to four different regions of interest (ROI) according to the relative position in the thorax. Global impedance waveform shows the relative impedance changes over time, while regional impedance waveforms represent relative impedance changes of the defined ROI. At the right side of waveforms, regional tidal variations (TV) in percentage of the global TV occurring in each ROI are displayed as numeric values. The general parameters of EIT can be classified into the spatial and temporal distribution parameters. For the spatial distribution parameters, global tidal impedance variation (TV global) describes the global impedance change between beginning and end of inspiration in the breath. Likewise, regional tidal variation describes the regional impedance change within the corresponding ROI. End-expiratory lung impedance (EELI) infers the relative change in end-expiratory lung volume (Eronia et al., 2017). The center of ventilation (COV) describes the weighted geometric ventilation center, and a high level indicates that ventilation shifts to the dorsal side (Frerichs et al., 2020). The global inhomogeneity index (GI) reflects the extent of heterogeneous gas distribution in ventilation (Zhao et al., 2010). In the temporal distribution parameters, regional ventilation delay (RVD) and regional ventilation delay inhomogeneity (RVDI) contain regional pulmonary mechanics information derived from EIT. RVD associated with atelectasis areas shows a delayed time in the distribution of inspired air during the respiratory cycle (Muders et al., 2012). The delayed time required for the regional time-impedance curve to reach a certain threshold of its maximum impedance change. The RVDI is the standard deviation of the RVD in all pixels, which quantifies the time heterogeneity of the regional ventilation time course (Muders et al., 2010). Moreover, some EIT derived parameters indicate respiratory physiology and pathophysiology. For each breathing cycle, silent spaces are defined as pixels with impedance change of less than 10% of the maximum impedance change. Based on the relative position of the pixels to the COV, the silent spaces are divided into dependent silent space and non-dependent silent space (Spadaro et al., 2018). During ventilation, flow and airway pressure are recorded using a pneumotachograph, along with the EIT signal. Each regional pressure-volume (PV) curve corresponds to a row of pixels in the EIT image. The regional PV curve is fitted using the sigmoidal equation and the regional inflection points of each curve are mathematically determined (Scaramuzzo et al., 2019). Moreover, regional hysteresis was calculated as the difference between the expiratory and inspiratory limbs of the EIT-based regional PV curve (Scaramuzzo et al., 2020b).

3 The use of EIT in lung transplantation

3.1 Donor care in pretransplant preparation

In recent years, an overwhelming majority of transplanted lungs have come from brain-dead (BD) patients (Wong and Liu, 2021). If a BD donor has sustained injury due to inflammatory responses, catecholamine storms, and ischemia-reperfusion, then the lungs are usually unusable for transplantation (Avlonitis et al., 2003). There has been a lack of appropriate donor care, and a considerable number of potential donors do not meet ideal lung donor criteria. When lungs from insufficient-quality donors, also known as marginal donors, are transplanted and the overall mortality is adversely affected (Chaney et al., 2014). The ratio of the arterial partial pressure of oxygen to the fraction of inspired oxygen (PaO_2/FiO_2), as one of the main criteria for ideal lung donor, needs to be more than 300 mmHg (Van Raemdonck et al., 2009). However, atelectasis and hypoxemia are more likely to occur in BD donors due to the absence of spontaneous breathing and a cough response (Marklin et al., 2020). Therefore, active pulmonary management strategies, including RM, bronchoscopy, and lung-protective ventilation, could be used to reverse atelectasis and improve the utilization rate of donors (Marklin et al., 2021). Son et al. (2021) reported that use of the EIT-guided prone position converted an ineligible donor to a qualified donor. The PaO_2/FiO_2 of the patient was 342 mmHg when she was selected as a potential donor and later dropped to 49 mmHg due to severe atelectasis. The donor's lung was unsuitable for transplantation. Within 4 h of being placed in the prone position, the atelectasis improved significantly. Tidal images on EIT showed that the status of ventral and dorsal ventilation returned to uniform, with matching bilateral ventilation. The donor's lung was finally successfully transplanted due to gradual PaO_2/FiO_2 recovery. Another study similarly found that the prone position acutely improved the oxygenation of a hypoxemic BD donor's lungs with atelectasis and resulted in more lungs being transplanted (Marklin et al., 2021). The prone position might be a feasible option for improving the condition of a marginal lung and enabling transplantation. Meanwhile, EIT can be used to observe the efficacy of the prone position in terms of improving of lung ventilation and perfusion (Zarantonello et al., 2020).

Improvement in PaO_2/FiO_2 has been considered a significant goal for restoring marginal lungs to the donor pool before transplantation. The common mechanisms leading to hypoxemia include ventilation/perfusion mismatch, hypoventilation and abnormal oxygen diffusion (Powner et al., 2005). The combined measurement of ventilation and perfusion by EIT could identify probable etiologies of acute respiratory failure at the bedside (He et al., 2021). EIT may be an available tool in etiology diagnosis and dynamic assessment in interventions during donor care before lung transplantation. Due to the prolonged supine position, atelectasis is common in cadaveric donors. Recruitment maneuvers are an important part of donor optimization, especially when oxygenation is lower than normal (Van Raemdonck et al., 2009). Yun et al. (2016) observed a discrepancy between regional lung reopening based EIT and oxygenation improvement after RM. EIT has the potential to evaluate the efficacy of RM by combining oxygenation measurements. These studies indicate that EIT can be used to assess the efficacy of donor maintenance dynamically to meet the ideal criteria before graft extraction. Moreover, EIT is a real-time evaluation imaging technique and does not require frequent patient transfer compared to X-ray and computed tomography. It has been suggested that EIT may be useful for ensuring the suitability of donor lungs; however, its use has not been confirmed.

3.2 Ventilation monitoring in posttransplant care

3.2.1 Pulmonary functional image

Lobar torsion, bronchial anastomosis fistula, and various airway complications will most likely lead to inhomogeneous ventilation, hypoxia and/or dyspnea (Santacruz and Mehta, 2009; Lin et al., 2013). Whether in single or bilateral lung transplantation, it is essential to routinely monitor pulmonary ventilation during the postoperative period (Yeung and Keshavjee, 2014). EIT as a promising alternative for pulmonary functional imaging has recently attracted increasing attention. A case presented that EIT assessed the ventilation heterogeneity between the native and transplanted lung after single lung transplantation in a female recipient (Guerin and Frerichs, 2014). The recipient underwent single left lung transplantation in 2004 for lymphangioleiomyomatosis and developed CLAD with chronic respiratory failure requiring long-term home oxygen therapy. Ten years later, there was an acute deterioration in her condition. After progressing to acute respiratory distress, the patient underwent endotracheal intubation and ventilator connection with a low tidal volume strategy in the intensive care unit. The anteroposterior chest radiograph and the computed tomography scan showed a lack of ventilation in the left transplanted lung and overdistension in the right native lung. However, the waveforms of EIT showed the variation in thoracic impedance occurring almost exclusively on the left side of the chest, which meant there was no gas exchange in the right lung. Combining lung functional images of EIT (finding low ventilation in the native lung) and lung morphological images allowed the therapy team to identify the crux of the problem, namely treating the still ventilated transplanted lung. In this case, the main benefit of the EIT was the functional status information obtained regarding the native and transplanted lungs.

3.2.2 Recruitment maneuver monitoring

Several complications of lung transportation, including PGD, acute rejection, and CLAD, adversely affect the prognosis of the recipient during the perioperative period (Whitson et al., 2007). PGD refers to a specific syndrome with acute lung injury comparable to acute respiratory distress syndrome (ARDS) within the first 72 h following transplantation (Snell et al., 2017; Swaminathan et al., 2021). In the case reported by Romero et al. (2016), a patient received left single lung transplantation for emphysema chronic obstructive pulmonary disease. To alleviate stage 3 PGD during the postoperative period, mechanical ventilation was performed using the Biphasic Positive Airway Pressure (BIPAP) model, which was set at a low tidal volume (290 ml) and a PEEP level of 8 cm H_2O to avoid lung overdistension. Subsequently, it was observed during ventilation monitoring using EIT that most of the gas was distributed in the native lung, and the ventilation of the left transplanted lung was insufficient. Recruitment maneuvers were performed under EIT to observe the tidal volume distribution and the alveolar opening pressure required to maintain ventilation of the transplanted lung. Although EIT cannot identify all disorders caused by insufficient ventilation, it can observe RM responsiveness directly and achieve a more homogeneous gas distribution.

3.2.3 Regional ventilation inhomogeneity

The compliance of the transplanted lung is different from that of the native lung. The relative compliance depends on the damage to the transplanted lung and the underlying lung pathology characteristics (Anantham et al., 2005). Heterogeneity in ventilation after lung transplantation is common. Obviously, uneven ventilation distribution usually exists in single lung transplantation because the donor lungs from different individuals possess different respiratory mechanics (Lee et al., 2012). Likewise, bilateral lung transplantation may also lead to heterogeneous ventilation due to lung injury caused by PGD and acute rejection (Barnes et al., 2015). Jr et al. (2010) performed EIT in five single lung emphysema patients. Compared with the transplanted lung, different impedance variations and regional air trapping were observed in the native lungs. When adopting with conventional strategy, most of the tidal volume is transferred to the normal, more compliant lungs, which are disproportionately inflated (Anantham et al., 2005). This will lead to ventilator-induced lung injury and abnormal perfusion diversion. Hence, it is essential to set an appropriate PEEP to diminish ventilator-induced lung injury after lung transplantation. A decremental PEEP trial using EIT was performed in six bilateral lung transplantation patients (Sella et al., 2021a). The optimal PEEP was the most appropriate compromise between lung overdistension and collapse. After statistical analysis, the PEEP setting had a similar influence in EIT as in PEEP titration in achieving the best static compliance of the respiratory system.

It is well known that a pendelluft phenomenon refers to the transfer of gas from nondependent to dependent regions without changing the tidal volume. Nevertheless, it is assumed that pendelluft does not usually occur, except in two situations: violent spontaneous breathing efforts in ARDS and postinspiratory pause in heterogeneous lung units (Yoshida et al., 2013). Pendelluft leads to selective overdistension of the dependent lung regions and fails to efficiently contribute to gas exchange (Enokidani et al., 2021). Caruana et al. (2010) reported that a single lung transplant recipient with idiopathic pulmonary fibrosis was ventilated on synchronized intermittent mandatory ventilation with volume control (SIMV-VC). There was a significant difference between the filling time of the native and transplanted lung, determined as 1.07 s ($p < 0.01$, 95% confident internal: 0.90, 1.24) by EIT during SIMV-VC. The difference was greater than one second, which is considered clinically significant in filling times, indicating that the transplanted lung is filling while the native lung is emptying, known as the pendelluft phenomenon. EIT was used to determine the effectiveness of the ventilator mode and ventilation inhomogeneity in this study.

In addition, Ramanathan et al. (2016) assessed EELI and TIV in each lung in five different positions (the supine position, left lying position, right lying position, sitting, and standing) in six patients with single lung transplantation. The study showed that ventilation in the transplanted lung was significantly better than in the native lung, despite whether the transplanted lung was dependent in the lateral position. Firstly, it was a small sample study in which the pendelluft phenomenon in one patient's lung strongly affected the results. When the outlier date from this subject was deleted, the difference in tidal variation became statistically significant for the most evaluated locations. Secondly, the above study only involved spontaneously breathing patients, and the results could not be translated into patients who underwent mechanical ventilation. Therefore, the findings of this study remain to be confirmed by the further studies.

3.2.4 Complications detection

CLAD, a late complication in lung transplantation, is often characterized by a continuous decline in forced expiratory volume in one second (FEV_1) for at least 3 weeks, limiting the 5-year survival to approximately 55% (Verleden et al., 2014). CLAD can be divided into two phenotypes: bronchiolitis obliterans syndrome (BOS) and restrictive graft syndrome (RAS) (Sato et al., 2013). Camargo et al. reported that the percentages of each lung ventilation in EIT were consistent with a bronchoscopy's impression in bronchial anastomosis stenosis, suggesting that EIT might be useful in the differential diagnosis of BOS (Camargo et al., 2014). Moreover, Hart (2016) registered an intervention clinical trial to evaluate the diagnostic value of EIT in chronic rejections of lung transplantation. The study aimed to provide an accurate diagnostic method capable of distinguishing BOS from RAS compared to the current gold standard, FEV_1, which can accurately stage BOS (Meyer et al., 2014). Furthermore, the study investigators considered providing EIT-based physiological data on lung transplant recipients with chronic rejection. The registered trial (Hart, 2016) was completed in 2018, but the corresponding published results have not been found.

3.3 Lung perfusion evaluation in posttransplant care

Ventilation/perfusion (V/Q) mismatch may occur after reperfusion in lung transplantation. The native lung is preferentially perfused because of the constricted vascular system of the transplanted lung, and it is preferentially ventilated due to its lower pulmonary compliance (Soluri-Martins et al., 2015). The assessment of lung perfusion is of valuable in posttransplant care. However, the variation in thoracic impedance from diastole to systole caused by perfusion is much smaller than that caused by ventilation (Bodenstein et al., 2009). EIT can be used to assess lung perfusion distribution by a distinct impedance comparison method. Zarantonello et al. (2021) reported EIT-based detection and follow-up of pulmonary artery stenosis in lung transplantation. A middle-aged male developed severe acute respiratory failure early after undergoing bilateral lung transplantation for idiopathic pulmonary fibrosis. EIT assessment showed a mismatch between ventilation and perfusion in the left graft due to reduced and delayed perfusion. The poor perfusion of the left lung led the researchers to focus on potential vessel stenosis. Severe left anastomotic pulmonary artery stenosis was confirmed by computed tomography pulmonary angiography. During the follow-up in the latter 5 days, EIT showed improvement in ventilation-perfusion matching with a resolution of the anastomotic stricture. According to the results of the literature search, this was the first report on the evaluation of lung perfusion in posttransplant lung care using EIT. Compared to the role of computed tomography pulmonary angiography in pulmonary artery stenosis, EIT allows repeated, nonradiative, and noninvasive bedside assessments. Therefore, EIT can potentially play a role in identifying ventilation-perfusion mismatch caused by postoperative vascular complications.

4 The future of EIT in lung transplantation

4.1 Personalized ventilation

The specific mechanical ventilation strategy for a lung transplant is still unclear, and there are no large-scale clinical randomized trials to confirm it. The mainstream view is to adopt a lung-protective strategy similar to ARDS patients (Barnes et al., 2015). It is believed that a higher level of PEEP is beneficial for ARDS patients (Amato et al., 2015). Nevertheless, it has been challenging to determine the optimal PEEP for mechanical ventilation of lung transplant recipients (Diamond and Ahya, 2014). A previous study showed that the low, medium and high tidal volumes had similar effects on short- and medium-term prognoses in lung transplantation recipients (Thakuria et al., 2016). Although a high PEEP level is associated with a high risk of pneumothorax and bronchial anastomotic complications, it is also associated with increased bronchial blood flow. Low PEEP may be associated with a higher driving pressure, and a high pressure will lead to poor physiological function, clinical prognosis, and pulmonary function (Thakuria et al., 2017). Therefore, a postoperative personalized PEEP setting is desirable to reduce ventilator-induced lung injury and minimize pulmonary complications in lung transplantation. Fortunately, EIT-guided PEEP titration at the bedside provides the possibility of individualized ventilation for recipients (Sella et al., 2021b). The first and most frequently used method monitors changes in regional lung compliance during a decremental PEEP trial. The optimal PEEP level is indicated by the best compromise between lung overdistension and collapse (Costa et al., 2009). The second method increases PEEP levels in maintaining EELI for assessing alveolar recruitment maneuvers (Eronia et al., 2017). The studies identified that EIT seems to be a promising bedside tool for personalized PEEP selection. The P-V curve has been suggested as a PEEP setting tool to explore changes in respiratory system compliance. However, it shows the global behavior of the lung without providing information on the regional lung mechanics. Additionally, it has been shown that regional inflection points derived from EIT reflect the heterogeneity of the lung and regional P-V curves obtained by EIT convey more sensitive information than global lung mechanics (Scaramuzzo et al., 2019). Compared with P-V curve PEEP titration, EIT-guided titration based on regional lung compliance is associated with improved driving pressure and survival rate in moderate to severe ARDS (Hsu et al., 2021). Based on the proportion of poorly or nonventilated lung units (silent spaces), the PEEP level suggested by EIT determines more ventilation homogeneity. It minimizes dorsal hypo-ventilated regions compared to transpulmonary pressure guided titration (Scaramuzzo et al., 2020a). The variation in EIT-derived dependent silent spaces induced by PEEP correlates well with lung recruitment measured by the P-V curve and could be used to set a personalized PEEP level. The deterioration of regional nondependent lung compliance suggests the potential role of EIT in identifying overdistention (Spadaro et al., 2018). Studies also described the optimal PEEP level as the value representing the lowest GI or the lowest RVD (Zhao et al., 2010; Muders et al., 2012).

Since asymmetrical lung disease leads to different airway resistance and lung compliance, the different ventilator strategies used in each lung are an innovative approach (Anantham et al., 2005). Once, researchers tried to apply different ventilation modes to each lung, designated differential lung ventilation (DLV) or one-lung ventilation (OLV). DLV is favorable to homogeneously distributed ventilation, V/Q mismatch decrease, and oxygenation improvement (Kremer et al., 2019). However, a feasibility study reported that EIT could play a role in immediately recognizing double-lumen tube misplacement in the contralateral main bronchus and the real-time assessment of DLV (Steinmann et al., 2008). Due to difficulties in catheter fixation, airway management, and sedation, DLV is burdensome to achieve in clinical practice.

For years, there has been the hypothesis that position affects lung region ventilation. In particular, the prone position has been considered an easy, inexpensive, and effective option for treating patients with ARDS (Pelosi et al., 2002). Moreover, the prone position to improve regional ventilation provides a novel alternative for reducing inhomogeneous ventilation after single lung transplantation (Marklin et al., 2020, 2021). A prospective study showed that EIT could dynamically assess the physiologic effects of the prone position using the tidal volume distribution and respiratory system compliance in dependent and nondependent regions, alveolar overdistension and collapse, and the increase in end-expiratory lung volume. With the above items, EIT might help identify patients who are more likely to obtain improved lung protection early by turning the prone position in ARDS (Dalla Corte et al., 2020). The study included severe ARDS patients and revealed that the prone position impacted global and regional ventilation using EIT monitoring during extracorporeal membrane oxygenation. This was reflected in the gradual redistribution of tidal volume and EELI from ventral to dorsal after the prone position (Franchineau et al., 2020).

4.2 Weaning

Prolonged mechanical ventilation is associated with an increased risk of in-hospital death in lung transplant recipients (Hadem et al., 2016). The ventilator weaning process should be attempted as soon as possible in recipients with hemodynamically stable and improved oxygenation (Kim et al., 2018). A spontaneous breathing trial (SBT) is usually performed to assess a patient's eligibility for extubation. Arterial blood gas is used to determine the outcome of SBT in conventional SBT methods (Boles et al., 2007). Moreover, the possibility of weaning failure was low in patients with well-distributed ventral and dorsal ventilation, which was monitored by EIT-based regional intertidal gas distribution (Zhao et al., 2017). SBT failure was characterized in the early course of SBT by a more significant reduction in EELI and a higher level of GI in ventilation distribution than in patients who succeeded in SBT (Longhini et al., 2019). Bickenbach et al. (2017) recorded GI, TIV, EELI, and RVD at three points in time on SBT in patients with delayed weaning. It was shown that in patients with an initial GI > 41.5, an SBT was more likely to fail, with a sensitivity of 87.5% and a specificity of 60.9%, which suggested that EIT could predict the failure of weaning. Wang *et al.* found that the EIT may be a useful adjunctive tool for evaluating ventilator weaning using pre-SBT GI and SBT ROI_2 (four ROIs were divided from the ventral to dorsal, with ROI_2 being the second region) as predictors (Wang et al., 2021). In addition to weaning failure due to pulmonary system dysfunction, phrenic nerve injury can also lead to atelectasis, difficult weaning, and prolonged ventilation in lung transplantation (Hernández-Hernández et al., 2022). Moon et al. (2021) revealed that dynamic inhomogeneity of ventilation along the vertical axis of lungs using EIT could predict weaning failure regardless of diaphragm dysfunction. As a monitor to assess regional ventilation heterogeneity and its variations, EIT could be used to guide weaning and predict weaning failure in lung transplant recipients.

4.3 Perfusion monitoring

EIT can also be used to assess lung perfusion distribution, but the interference of cardiac perfusion needs to be ruled out. The pulsatility method is used to analyze the impedance variation in pulmonary vascular blood volume pulsatility to reflect pulmonary perfusion. However, pulsatility impedance does not directly reflect actual forward lung blood flow (Bluth et al., 2019). The accuracy of this method for assessing pulmonary perfusion has been questioned (Hellige and Hahn, 2011). It is susceptible to cardiac systolic and diastolic activities, airway pressure and distensibility of the small pulmonary vessels (Borges et al., 2012; Nguyen et al., 2012). Moreover, multiple animal experiments have indicated that saline bolus injection in EIT has a good correlation and consistency with single-photon emission computed tomography (SPECT) in pulmonary perfusion imaging (Fagerberg et al., 2009; Hentze et al., 2018). In recent years, growing attention has been given to the application of saline bolus EIT method in pulmonary perfusion imaging. Saline bolus injection for EIT perfusion imaging can be utilized for evaluating the V/Q matching condition in lung transplantation (He et al., 2020a). In recent years, growing attention has been given to the application of EIT in pulmonary perfusion imaging. Saline bolus injection for EIT perfusion imaging can evaluate the V/Q matching condition in lung transplantation (He et al., 2020a). Lung transplant recipients own an increased risk of pulmonary embolism (PE) compared to other hospitalized and postoperative patients (Krivokuca et al., 2011). He et al. showed that EIT-based ventilation and perfusion measures, including dead space, V/Q match, and intrapulmonary shunt percentage, could discriminate patients with acute PE from other patients with acute respiratory failure. The study suggested that contrast-enhanced EIT was potentially a promising bedside approach with good efficiency in PE diagnosis (He et al., 2020b). Idiopathic pulmonary arterial hypertension, a severe pulmonary vascular disease that does not respond to drug treatment, is one of the main indications for lung transplantation (Lordan and Corris, 2011). Meanwhile, rare pulmonary arterial hypertension (PAH) recurrence cases have been reported after lung transplantation (Soriano et al., 1999; Izbicki et al., 2005; Narula et al., 2014). Studies have shown that the impedance variation in lung perfusion is reduced in PAH in comparison with the normopressoric group. As it is closely related to hemodynamic characteristics, disease severity, and survival rate in patients with PAH, EIT might be a promising noninvasive technique for PAH diagnosis (Smit et al., 2006; Hovnanian et al., 2021). The potential validity of EIT in pulmonary perfusion assessment helps to identify and diagnose transplant complications from stenosis of pulmonary vascular anastomoses, such as PAH and PE.

The investigation of EIT in pulmonary perfusion imaging may reveal a new pathophysiological feature of ARDS. Pixels were classified as nonventilated if ventilation was less than 10% of the highest pixel-level value measured in the patient, and nonperfused was also defined as a similar method. The fraction of dead space and shunt corresponds to the percentage of nonventilated and nonperfused pixels in the total. The V/Q mismatch representation as to the sum of the dead space fraction and shunt fraction. Spinelli et al. (2021) found that V/Q mismatch was an independent predictor of death in ARDS patients with mechanical ventilation. Another study showed that a high dead space fraction could be a specific characteristic in patients with ARDS from coronavirus disease 2019 (Mauri et al., 2020). In recent years, Pavlovsky et al. (2022) developed a new EIT-based algorithm that resembles the multiple inert gas elimination technique (MIGET). The algorithm can be used to quantify V/Q mismatch and PEEP response, which may be a sensitive marker of ARDS severity.

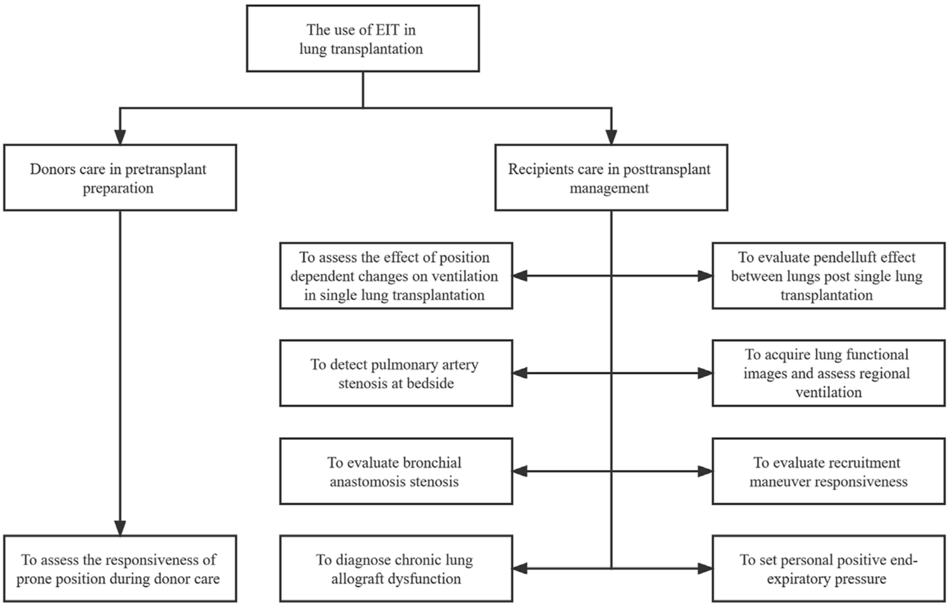

FIGURE 1
The illustrative figure on the use of EIT in lung transplantation. EIT: electrical impedance tomography.

4.4 Others aspects

Pneumothorax can occur spontaneously after lung transplantation and/or arise in patients receiving long-term mechanical ventilation (Slebos et al., 2001; Yuzuak et al., 2021). The use of EIT can be used to diagnose pneumothorax that occurs during recruitment maneuvers. Pneumothorax was manifested by a sudden increase in impedance in the affected region and a disproportionate amount of ventilation to the increase in PEEP. Since the technique only shows a variation in impedance, the affected area was no longer ventilated after pneumothorax, and the ventilation image was lost (Morais et al., 2017). Pleural effusions are prevalent phenomena after transplantation (Joean et al., 2021). Moreover, the validity in evaluating pleural effusion and emptying was also presented in EIT (Omer et al., 2021). The regional out-of-phase impedance changes are associated with the occurrence of pleural effusions (Becher et al., 2018). The out-of-phase impedance changes were characterized by a decrease in the impedance of certain areas during inspiration, followed by an increase during exhalation, which was contrary to normal conditions. After pleural effusion evacuating, an increase in end-expiratory impedance can be observed using EIT (Rara et al., 2020).

5 Limitations

For decades, imaging techniques have been used to detect abnormalities, monitor function, and diagnose diseases. Advances and the wide availability in lung imaging techniques have provided new insights into pulmonary structure and function and their alterations. More recently, functional lung imaging has been performed using positron emission tomography (PET), SPECT, and hyperpolarized gas magnetic resonance imaging (MRI) (Mirsadraee and van Beek, 2015; Bajc et al., 2019). PET and SPECT have higher image resolution than EIT, their application in lung transplantation is limited by radiation. The current protocols of hyperpolarized gas MRI rely on a fixed breath-holding movement, which depends on the patient's cooperation (Fain, 2020). Whether radionuclides or hyperpolarized inert gases, these have been regarded as costly and hard-to-obtain materials. Moreover, it is unrealistic that transferring the patients, who received a lung transplant and connecting a ventilator, to the CT or MRI rooms. Because of its small size, portability, no need for radiation, and dynamic imaging ability, the EIT device is especially suitable for ventilation monitoring at the bedside in patients who are mechanically ventilated after lung transplantation. However, the limitations and constraints of this technique need to be expressly noted. First, the spatial resolution in EIT remains low because each pixel contains information about many alveolar unit impedances. An electric current is applied to the body through the electrodes, and then the voltage generated between the other electrodes is measured and recorded. Since the current is not limited to a horizontal plane, EIT obtains an image of an impedance change of approximately 5 cm cross-section of the thorax. One of the limitations of this principle is the low resolution. To improve this resolution, the number of bound electrodes could be increased (Tang et al., 2002). However, the standard available electrode belt on the market is 16 or 32 electrodes, and circumventing this issue requires more breakthroughs in design. Second, modifying the electrode belt position could lead to inconsistencies between the considered lung regions in multiple measurements. To reliably assess the ventilation and perfusion distribution, the belt should always be bound in a fixed position on the thorax (Sella et al., 2021b). The electrode belt should not be attached to damaged and inflamed skin. It is noted that the incision of the lung transplant coincides with the suggested binding region of the EIT electrode band, especially for double lung transplantation. The fractured state of the surgical incision affects the extraction of the electrical signal from the electrode band. Long periods of bondage or the application of conductive gels may lead to incision infection with delayed healing. Strict disinfection of the electrode belt at each operation may be beneficial for this problem. It is common for lung transplant recipients to have a drainage tube placed in the chest in the postoperative period (Joean et al., 2021). Excessive pleural effusion and severe pneumothorax may limit ventilation and affect the accuracy of ventilation assessment in EIT imaging of lung transplantation (Becher et al., 2018; Rara et al., 2020). However, as the chest tube drainage amount gradually decreases, this adverse impact may be alleviated with the appropriate timing of EIT operations. More reliable studies are needed to confirm EIT's ability to distinguish between atelectasis, pleural effusion, and pneumothorax after lung transplantation (Zhou et al., 2022). Furthermore, other situations deserve attention to avoid adverse effects. The image quality obtained by EIT is poor in morbidly obese patients with a body mass index greater than 50. In addition, EIT is sensitive to body movement, and it may be unreliable to apply it to lung recipients with chaotic body movements. If lung transplant recipients is equipped with a pacemaker or need to defibrillate in the rescue, the use of EIT should be carefully considered, and its validity will be compromised (Lobo et al., 2018).

6 Conclusion

In summary, the application of EIT in lung transplantation, including lung donor care, pulmonary functional imaging, recruitment maneuvers and ventilation heterogeneity monitoring, postoperative complication detection and lung perfusion evaluation, has gradually increased. EIT may be a valuable technique that will be especially useful in lung transplantation, including but not limited to personalized ventilation, weaning, and perfusion monitoring. Indeed, the practice of EIT is still in its infancy, and the further studies are needed to further determine the potential use of EIT in lung transplantation.

Author contributions

HJ, XZ, and QF contributed to design of the review. HJ wrote the first draft of the manuscript. YH wrote and refined several important sections of the manuscript. XZ and QF revised the manuscript. All authors read and approved the final submitted manuscript.

Funding

This study was supported by National Science and Technology Major Project of Ministry of Science and Technology (2017ZX10204401) and Zhejiang Province Health Major Science and Technology Program of National Health Commission Scientific Research Fund (WKJ-ZJ-2110).

Conflict of interest

The authors declare that the research was conducted in the absence of any commercial or financial relationships that could be construed as a potential conflict of interest.

Publisher's note

References

Amato, M. B., Meade, M. O., Slutsky, A. S., Brochard, L., Costa, E. L., Schoenfeld, D. A., et al. (2015). Driving pressure and survival in the acute respiratory distress syndrome. *N. Engl. J. Med.* 372 (8), 747–755. doi:10.1056/NEJMsa1410639

Ambrósio, A. M., Sanchez, A. F., Pereira, M. A. A., Andrade, F., Rodrigues, R. R., Vitorasso, R. L., et al. (2021). Assessment of regional ventilation during recruitment maneuver by electrical impedance tomography in dogs. *Front. Vet. Sci.* 8, 815048. doi:10.3389/fvets.2021.815048

Anantham, D., Jagadesan, R., and Tiew, P. E. (2005). Clinical review: Independent lung ventilation in critical care. *Crit. Care* 9 (6), 594–600. doi:10.1186/cc3827

Arcasoy, S. M., and Kotloff, R. M. (1999). Lung transplantation. *N. Engl. J. Med.* 340 (14), 1081–1091. doi:10.1056/nejm199904083401406

Avlonitis, V. S., Fisher, A. J., Kirby, J. A., and Dark, J. H. (2003). Pulmonary transplantation: The role of brain death in donor lung injury. *Transplantation* 75 (12), 1928–1933. doi:10.1097/01.Tp.0000066351.87480.9e

Bachmann, M. C., Morais, C., Bugedo, G., Bruhn, A., Morales, A., Borges, J. B., et al. (2018). Electrical impedance tomography in acute respiratory distress syndrome. *Crit. Care* 22 (1), 263. doi:10.1186/s13054-018-2195-6

Bajc, M., Schümichen, C., Grüning, T., Lindqvist, A., Le Roux, P. Y., Alatri, A., et al. (2019). EANM guideline for ventilation/perfusion single-photon emission computed tomography (SPECT) for diagnosis of pulmonary embolism and beyond. *Eur. J. Nucl. Med. Mol. Imaging* 46 (12), 2429–2451. doi:10.1007/s00259-019-04450-0

Barnes, L., Reed, R. M., Parekh, K. R., Bhama, J. K., Pena, T., Rajagopal, S., et al. (2015). Mechanical ventilation for the lung transplant recipient. *Curr. Pulmonol. Rep.* 4 (2), 88–96. doi:10.1007/s13665-015-0114-8

Becher, T., Bußmeyer, M., Lautenschläger, I., Schädler, D., Weiler, N., and Frerichs, I. (2018). Characteristic pattern of pleural effusion in electrical impedance tomography images of critically ill patients. *Br. J. Anaesth.* 120 (6), 1219–1228. doi:10.1016/j.bja.2018.02.030

Bickenbach, J., Czaplik, M., Polier, M., Marx, G., Marx, N., and Dreher, M. (2017). Electrical impedance tomography for predicting failure of spontaneous breathing trials in patients with prolonged weaning. *Crit. Care* 21 (1), 177. doi:10.1186/s13054-017-1758-2

Bluth, T., Kiss, T., Kircher, M., Braune, A., Bozsak, C., Huhle, R., et al. (2019). Measurement of relative lung perfusion with electrical impedance and positron emission tomography: An experimental comparative study in pigs. *Br. J. Anaesth.* 123 (2), 246–254. doi:10.1016/j.bja.2019.04.056

Bodenstein, M., David, M., and Markstaller, K. (2009). Principles of electrical impedance tomography and its clinical application. *Crit. Care Med.* 37 (2), 713–724. doi:10.1097/CCM.0b013e3181958d2f

Boles, J. M., Bion, J., Connors, A., Herridge, M., Marsh, B., Melot, C., et al. (2007). Weaning from mechanical ventilation. *Eur. Respir. J.* 29 (5), 1033–1056. doi:10.1183/09031936.00010206

Borges, J. B., Suarez-Sipmann, F., Bohm, S. H., Tusman, G., Melo, A., Maripuu, E., et al. (2012). Regional lung perfusion estimated by electrical impedance tomography in a piglet model of lung collapse. *J. Appl. Physiol.* 112 (1), 225–236. doi:10.1152/japplphysiol.01090.2010

Camargo, P., Afonso, J. E., Costa, A. N., Carraro, R. M., Campos, S. V., Abdalla, L. G., et al. (2014). Evaluation of bronchial anastomosis stenosis after lung transplantation with electrical impedance tomography: A case report. *Am. J. Respir. Crit. Care Med.* 189. doi:10.1164/ajrccm-conference.2014.189.1_MeetingAbstracts.A1594

Caruana, L., Corley, A., Tronstad, O., Hopkins, P., and Fraser, J. (2010). Pendelluft exists between lungs post single lung transplant during mechanical ventilation. A pilot study using electrical impedance tomography. *Am. J. Respir. Crit. Care Med.* 1, A3074. doi:10.1164/ajrccm-conference.2010.181.1_MeetingAbstracts.A3074

Chambers, D. C., Cherikh, W. S., Harhay, M. O., Hayes, D., Jr., Hsich, E., Khush, K. K., et al. (2019). The international thoracic organ transplant Registry of the international society for heart and lung transplantation: Thirty-sixth adult lung and heart-lung transplantation report-2019; focus theme: Donor and recipient size match. *J. Heart Lung Transpl.* 38 (10), 1042–1055. doi:10.1016/j.healun.2019.08.001

Chambers, D. C., Perch, M., Zuckermann, A., Cherikh, W. S., Harhay, M. O., Hayes, D., Jr., et al. (2021). The international thoracic organ transplant Registry of the international society for heart and lung transplantation: Thirty-eighth adult lung transplantation report - 2021; focus on recipient characteristics. *J. Heart Lung Transpl.* 40 (10), 1060–1072. doi:10.1016/j.healun.2021.07.021

Chaney, J., Suzuki, Y., Cantu, E., 3rd, and van Berkel, V. (2014). Lung donor selection criteria. *J. Thorac. Dis.* 6 (8), 1032–1038. doi:10.3978/j.issn.2072-1439.2014.03.24

Costa, E. L., Borges, J. B., Melo, A., Suarez-Sipmann, F., Toufen, C., Jr., Bohm, S. H., et al. (2009). Bedside estimation of recruitable alveolar collapse and hyperdistension by electrical impedance tomography. *Intensive Care Med.* 35 (6), 1132–1137. doi:10.1007/s00134-009-1447-y

Dalla Corte, F., Mauri, T., Spinelli, E., Lazzeri, M., Turrini, C., Albanese, M., et al. (2020). Dynamic bedside assessment of the physiologic effects of prone position in acute respiratory distress syndrome patients by electrical impedance tomography. *Minerva Anestesiol.* 86 (10), 1057–1064. doi:10.23736/s0375-9393.20.14130-0

DeFreitas, M. R., McAdams, H. P., Azfar Ali, H., Iranmanesh, A. M., and Chalian, H. (2021). Complications of lung transplantation: Update on imaging manifestations and management. *Radiol. Cardiothorac. Imaging* 3 (4), e190252. doi:10.1148/ryct.2021190252

Diamond, J. M., and Ahya, V. N. (2014). Mechanical ventilation after lung transplantation. It's time for a trial. *Ann. Am. Thorac. Soc.* 11 (4), 598–599. doi:10.1513/AnnalsATS.201403-104ED

Enokidani, Y., Uchiyama, A., Yoshida, T., Abe, R., Yamashita, T., Koyama, Y., et al. (2021). Effects of ventilatory settings on pendelluft phenomenon during mechanical ventilation. *Respir. Care* 66 (1), 1–10. doi:10.4187/respcare.07880

Eronia, N., Mauri, T., Maffezzini, E., Gatti, S., Bronco, A., Alban, L., et al. (2017). Bedside selection of positive end-expiratory pressure by electrical impedance tomography in hypoxemic patients: A feasibility study. *Ann. Intensive Care* 7 (1), 76. doi:10.1186/s13613-017-0299-9

Fagerberg, A., Stenqvist, O., Aneman, A., and AnemAn, A. (2009). Monitoring pulmonary perfusion by electrical impedance tomography: An evaluation in a pig model. *Acta Anaesthesiol. Scand.* 53 (2), 152–158. doi:10.1111/j.1399-6576.2008.01847.x

Fain, S. B. (2020). Hyperpolarized gas MRI Technology breaks through: Advancing our understanding of anti-type 2 inflammation therapies in severe asthma. *Chest* 158 (4), 1293–1295. doi:10.1016/j.chest.2020.07.019

Franchineau, G., Brechot, N., Hekimian, G., Lebreton, G., Bourcier, S., Demondion, P., et al. (2020). Prone positioning monitored by electrical impedance tomography in patients with severe acute respiratory distress syndrome on veno-venous ECMO. *Ann. Intensive Care* 10 (1), 12. doi:10.1186/s13613-020-0633-5

Frerichs, I., Amato, M. B., van Kaam, A. H., Tingay, D. G., Zhao, Z., Grychtol, B., et al. (2017). Chest electrical impedance tomography examination, data analysis, terminology, clinical use and recommendations: Consensus statement of the TRanslational EIT developmeNt stuDy group. *Thorax* 72 (1), 83–93. doi:10.1136/thoraxjnl-2016-208357

Frerichs, I., Pulletz, S., Elke, G., Reifferscheid, F., Schadler, D., Scholz, J., et al. (2009). Assessment of changes in distribution of lung perfusion by electrical impedance tomography. *Respiration.* 77 (3), 282–291. doi:10.1159/000193994

Frerichs, I., Zhao, Z., and Becher, T. (2020). Simple electrical impedance tomography measures for the assessment of ventilation distribution. *Am. J. Respir. Crit. Care Med.* 201 (3), 386–388. doi:10.1164/rccm.201908-1502LE

Fuehner, T., Kuehn, C., Welte, T., and Gottlieb, J. (2016). ICU care before and after lung transplantation. *Chest* 150 (2), 442–450. doi:10.1016/j.chest.2016.02.656

Grant, C. A., Pham, T., Hough, J., Riedel, T., Stocker, C., and Schibler, A. (2011). Measurement of ventilation and cardiac related impedance changes with electrical impedance tomography. *Crit. Care* 15 (1), R37. doi:10.1186/cc9985

Guerin, C., and Frerichs, I. (2014). Getting a better picture of the correlation between lung function and structure using electrical impedance tomography. *Am. J. Respir. Crit. Care Med.* 190 (10), 1186–1187. doi:10.1164/rccm.201405-0812IM

Hadem, J., Gottlieb, J., Seifert, D., Fegbeutel, C., Sommer, W., Greer, M., et al. (2016). Prolonged mechanical ventilation after lung transplantation-A single-center study. *Am. J. Transpl.* 16 (5), 1579–1587. doi:10.1111/ajt.13632

Hardy, J. D., Webb, W. R., Dalton, M. L., Jr., and Walker, G. R., Jr. (1963). Lung homotransplantation in man. *Jama* 186, 1065–1074. doi:10.1001/jama.1963.63710120001010

Hart, N. (2016). *Evaluation of electrical impedance tomography for the diagnosis of chronic rejection in lung transplants recipients (CLAD).* ClinicalTrials.gov. Available: https://clinicaltrials.gov/ct2/show/NCT02863835 (Accessed August 11, 2016).

He, H., Chi, Y., Long, Y., Yuan, S., Frerichs, I., Möller, K., et al. (2020a). Influence of overdistension/recruitment induced by high positive end-expiratory pressure on ventilation-perfusion matching assessed by electrical impedance tomography with saline bolus. *Crit. Care* 24 (1), 586. doi:10.1186/s13054-020-03301-x

He, H., Chi, Y., Long, Y., Yuan, S., Zhang, R., Frerichs, I., et al. (2020b). Bedside evaluation of pulmonary embolism by saline contrast electrical impedance tomography method: A prospective observational study. *Am. J. Respir. Crit. Care Med.* 202 (10), 1464–1468. doi:10.1164/rccm.202005-1780LE

He, H., Chi, Y., Long, Y., Yuan, S., Zhang, R., Yang, Y., et al. (2021). Three broad classifications of acute respiratory failure etiologies based on regional ventilation and perfusion by electrical impedance tomography: A hypothesis-generating study. *Ann. Intensive Care* 11 (1), 134. doi:10.1186/s13613-021-00921-6

Hellige, G., and Hahn, G. (2011). Cardiac-related impedance changes obtained by electrical impedance tomography: An acceptable parameter for assessment of pulmonary perfusion? *Crit. Care* 15 (3), 430. doi:10.1186/cc10231

Hentze, B., Muders, T., Luepschen, H., Maripuu, E., Hedenstierna, G., Putensen, C., et al. (2018). Regional lung ventilation and perfusion by electrical impedance tomography compared to single-photon emission computed tomography. *Physiol. Meas.* 39 (6), 065004. doi:10.1088/1361-6579/aac7ae

Hernández-Hernández, M. A., Sánchez-Moreno, L., Orizaola, P., Iturbe, D., Álvaréz, C., Fernández-Rozas, S., et al. (2022). A prospective evaluation of phrenic nerve injury after lung transplantation: Incidence, risk factors, and analysis of the surgical procedure. *J. Heart Lung Transpl.* 41 (1), 50–60. doi:10.1016/j.healun.2021.09.013

Hovnanian, A. L. D., Costa, E. L. V., Hoette, S., Fernandes, C., Jardim, C. V. P., Dias, B. A., et al. (2021). Electrical impedance tomography in pulmonary arterial hypertension. *PLoS One* 16 (3), e0248214. doi:10.1371/journal.pone.0248214

Hsu, H. J., Chang, H. T., Zhao, Z., Wang, P. H., Zhang, J. H., Chen, Y. S., et al. (2021). Positive end-expiratory pressure titration with electrical impedance tomography and pressure-volume curve: A randomized trial in moderate to severe ARDS. *Physiol. Meas.* 42 (1), 014002. doi:10.1088/1361-6579/abd679

Izbicki, G., Shitrit, D., Schechtman, I., Bendayan, D., Fink, G., Sahar, G., et al. (2005). Recurrence of pulmonary veno-occlusive disease after heart-lung transplantation. *J. Heart Lung Transpl.* 24 (5), 635–637. doi:10.1016/j.healun.2004.02.008

Joean, O., Kayser, M. Z., Valtin, C., Ewen, R., and Gottlieb, J. (2021). Characteristics and clinical implications of pleural effusions after lung transplantation: A retrospective analysis of 195 thoracocenteses in 113 patients. *Clin. Transpl.* 35 (5), e14267. doi:10.1111/ctr.14267

Jr, J., Carvalho, C., and Amato, M. (2010). Assessment of regional ventilation in lung transplantation, using electrical impedance tomography. *Am. J. Respir. Crit. Care Med.* 1, A4328. doi:10.1164/ajrccm-conference.2010.181.1_MeetingAbstracts.A4328

Kim, S. Y., Jeong, S. J., Lee, J. G., Park, M. S., Paik, H. C., Na, S., et al. (2018). Critical care after lung transplantation. *Acute Crit. Care* 33 (4), 206–215. doi:10.4266/acc.2018.00360

Kremer, R., Aboud, W., Haberfeld, O., Armali, M., and Barak, M. (2019). Differential lung ventilation for increased oxygenation during one lung ventilation for video assisted lung surgery. *J. Cardiothorac. Surg.* 14 (1), 89. doi:10.1186/s13019-019-0910-2

Krivokuca, I., van de Graaf, E. A., van Kessel, D. A., van den Bosch, J. M., Grutters, J. C., and Kwakkel-van Erp, J. M. (2011). Pulmonary embolism and pulmonary infarction after lung transplantation. *Clin. Appl. Thromb. Hemost.* 17 (4), 421–424. doi:10.1177/1076029610371474

Lee, J. C., Diamond, J. M., and Christie, J. D. (2012). Critical care management of the lung transplant recipient. *Curr. Respir. Care Rep.* 1 (3), 168–176. doi:10.1007/s13665-012-0018-9

Lin, M.-W., Huang, S.-C., Kuo, S.-W., Huang, P.-M., Hsu, H.-H., and Lee, Y.-C. (2013). Lobar torsion after lung transplantation. *J. Formos. Med. Assoc.* 112 (2), 105–108. doi:10.1016/j.jfma.2012.10.012

Lobo, B., Hermosa, C., Abella, A., and Gordo, F. (2018). Electrical impedance tomography. *Ann. Transl. Med.* 6 (2), 26. doi:10.21037/atm.2017.12.06

Longhini, F., Maugeri, J., Andreoni, C., Ronco, C., Bruni, A., Garofalo, E., et al. (2019). Electrical impedance tomography during spontaneous breathing trials and after extubation in critically ill patients at high risk for extubation failure: A multicenter observational study. *Ann. Intensive Care* 9 (1), 88. doi:10.1186/s13613-019-0565-0

Lordan, J. L., and Corris, P. A. (2011). Pulmonary arterial hypertension and lung transplantation. *Expert Rev. Respir. Med.* 5 (3), 441–454. doi:10.1586/ers.11.21

Maciejewski, D., Putowski, Z., Czok, M., and Krzych Ł, J. (2021). Electrical impedance tomography as a tool for monitoring mechanical ventilation. An introduction to the technique. *Adv. Med. Sci.* 66 (2), 388–395. doi:10.1016/j.advms.2021.07.010

Marklin, G. F., O'Sullivan, C., and Dhar, R. (2020). Prone ventilation in brain-dead organ donors acutely increases oxygenation and results in more lungs transplanted. *J. Heart Lung Transplant.* 39 (4), S375. doi:10.1016/j.healun.2020.01.473

Marklin, G. F., O'Sullivan, C., and Dhar, R. (2021). Ventilation in the prone position improves oxygenation and results in more lungs being transplanted from organ donors with hypoxemia and atelectasis. *J. Heart Lung Transpl.* 40 (2), 120–127. doi:10.1016/j.healun.2020.11.014

Mauri, T., Spinelli, E., Scotti, E., Colussi, G., Basile, M. C., Crotti, S., et al. (2020). Potential for lung recruitment and ventilation-perfusion mismatch in patients with the acute respiratory distress syndrome from coronavirus disease 2019. *Crit. Care Med.* 48 (8), 1129–1134. doi:10.1097/ccm.0000000000004386

Meyer, K. C., Raghu, G., Verleden, G. M., Corris, P. A., Aurora, P., Wilson, K. C., et al. (2014). An international ISHLT/ATS/ERS clinical practice guideline: Diagnosis and management of bronchiolitis obliterans syndrome. *Eur. Respir. J.* 44 (6), 1479–1503. doi:10.1183/09031936.00107514

Meyer, K. C. (2018). Recent advances in lung transplantation. *F1000Res.* 7, 1684. doi:10.12688/f1000research.15393.1

Mirsadraee, S., and van Beek, E. J. (2015). Functional imaging: Computed tomography and MRI. *Clin. Chest Med.* 36 (2), 349–363. x. doi:10.1016/j.ccm.2015.02.014

Moon, D. S., Huh, J. W., Hong, S. B., Koh, Y., and Lim, C. M. (2021). Dynamic inhomogeneity of aeration along the vertical axis of the lung may predict weaning failure regardless of diaphragm dysfunction. *J. Crit. Care* 65, 186–191. doi:10.1016/j.jcrc.2021.06.010

Morais, C. C., De Santis Santiago, R. R., Filho, J. R., Hirota, A. S., Pacce, P. H., Ferreira, J. C., et al. (2017). Monitoring of pneumothorax appearance with electrical impedance tomography during recruitment maneuvers. *Am. J. Respir. Crit. Care Med.* 195 (8), 1070–1073. doi:10.1164/rccm.201609-1780LE

Muders, T., Luepschen, H., and Putensen, C. (2010). Impedance tomography as a new monitoring technique. *Curr. Opin. Crit. Care* 16 (3), 269–275. doi:10.1097/MCC.0b013e3283390cbf

Muders, T., Luepschen, H., Zinserling, J., Greschus, S., Fimmers, R., Guenther, U., et al. (2012). Tidal recruitment assessed by electrical impedance tomography and computed tomography in a porcine model of lung injury. *Crit. Care Med.* 40 (3), 903–911. doi:10.1097/CCM.0b013e318236f452

Narula, T., Farver, C., Erzurum, S., Aldred, M., Lane, C., Budev, M., et al. (2014). Recurrence of idiopathic pulmonary arterial hypertension after lung transplantation. *CHEST* 145 (3), 624A. doi:10.1378/chest.1826554

Nguyen, D. T., Jin, C., Thiagalingam, A., and McEwan, A. L. (2012). A review on electrical impedance tomography for pulmonary perfusion imaging. *Physiol. Meas.* 33 (5), 695–706. doi:10.1088/0967-3334/33/5/695

Omer, N., Abboud, S., and Arad, M. (2021). Diagnosing and monitoring pleural effusion using parametric electrical impedance tomography - a computational 3D model and preliminary experimental results. *Med. Eng. Phys.* 92, 45–53. doi:10.1016/j.medengphy.2021.04.008

Pavlovsky, B., Pesenti, A., Spinelli, E., Scaramuzzo, G., Marongiu, I., Tagliabue, P., et al. (2022). Effects of PEEP on regional ventilation-perfusion mismatch in the acute respiratory distress syndrome. *Crit. Care* 26 (1), 211. doi:10.1186/s13054-022-04085-y

Pelosi, P., Brazzi, L., and Gattinoni, L. (2002). Prone position in acute respiratory distress syndrome. *Eur. Respir. J.* 20 (4), 1017–1028. doi:10.1183/09031936.02.00401702

Powner, D. J., Hewitt, M. J., and Levine, R. L. (2005). Interventions during donor care before lung transplantation. *Prog. Transpl.* 15 (2), 141–148. doi:10.1177/152692480501500206

Ramanathan, K., Mohammed, H., Hopkins, P., Corley, A., Caruana, L., Dunster, K., et al. (2016). Single-lung transplant results in position dependent changes in regional ventilation: An observational case series using electrical impedance tomography. *Can. Respir. J.* 2016, 2471207. doi:10.1155/2016/2471207

Rara, A., Roubik, K., and Tyll, T. (2020). Effects of pleural effusion drainage in the mechanically ventilated patient as monitored by electrical impedance tomography and end-expiratory lung volume: A pilot study. *J. Crit. Care* 59, 76–80. doi:10.1016/j.jcrc.2020.06.001

Romero, A., Alonso, B., Latorre, I., and García, J. (2016). Respiratory monitoring with electrical impedance tomography for lung protective ventilation and alveolar recruitment maneuver in a patient with a single lung transplant and early graft dysfunction. *Rev. Esp. Anestesiol. Reanim.* 63 (6), 347–352. doi:10.1016/j.redar.2015.09.003

Santacruz, J. F., and Mehta, A. C. (2009). Airway complications and management after lung transplantation: Ischemia, dehiscence, and stenosis. *Proc. Am. Thorac. Soc.* 6 (1), 79–93. doi:10.1513/pats.200808-094GO

Sato, M., Hwang, D. M., Waddell, T. K., Singer, L. G., and Keshavjee, S. (2013). Progression pattern of restrictive allograft syndrome after lung transplantation. *J. Heart Lung Transpl.* 32 (1), 23–30. doi:10.1016/j.healun.2012.09.026

Scaramuzzo, G., Spadaro, S., Dalla Corte, F., Waldmann, A. D., Böhm, S. H., Ragazzi, R., et al. (2020a). Personalized positive end-expiratory pressure in acute respiratory distress syndrome: Comparison between optimal distribution of regional ventilation and positive transpulmonary pressure. *Crit. Care Med.* 48 (8), 1148–1156. doi:10.1097/ccm.0000000000004439

Scaramuzzo, G., Spadaro, S., Waldmann, A. D., Böhm, S. H., Ragazzi, R., Marangoni, E., et al. (2019). Heterogeneity of regional inflection points from pressure-volume curves assessed by electrical impedance tomography. *Crit. Care* 23 (1), 119. doi:10.1186/s13054-019-2417-6

Scaramuzzo, G., Spinelli, E., Spadaro, S., Santini, A., Tortolani, D., Dalla Corte, F., et al. (2020b). Gravitational distribution of regional opening and closing pressures, hysteresis and atelectrauma in ARDS evaluated by electrical impedance tomography. *Crit. Care* 24 (1), 622. doi:10.1186/s13054-020-03335-1

Sella, N., Boscolo, A., Zarantonello, F., Bonvecchio, I., Andreatta, G., Pettenuzzo, T., et al. (2021a). Electrical impedance tomography for positive end-expiratory pressure setting after bilateral lung transplantation. *J. Heart Lung Transplant.* 40 (4), S317. doi:10.1016/j.healun.2021.01.897

Sella, N., Pettenuzzo, T., Zarantonello, F., Andreatta, G., De Cassai, A., Schiavolin, C., et al. (2021b). Electrical impedance tomography: A compass for the safe route to optimal PEEP. *Respir. Med.* 187, 106555. doi:10.1016/j.rmed.2021.106555

Shono, A., and Kotani, T. (2019). Clinical implication of monitoring regional ventilation using electrical impedance tomography. *J. Intensive Care* 7 (1), 4. doi:10.1186/s40560-019-0358-4

Slebos, D. J., Elting-Wartan, A. N., Bakker, M., van der Bij, W., and van Putten, J. W. (2001). Managing a bilateral pneumothorax in lung transplantation using single chest-tube drainage. *J. Heart Lung Transpl.* 20 (7), 796–797. doi:10.1016/s1053-2498(00)00220-5

Smit, H. J., Vonk-Noordegraaf, A., Boonstra, A., de Vries, P. M., and Postmus, P. E. (2006). Assessment of the pulmonary volume pulse in idiopathic pulmonary arterial hypertension by means of electrical impedance tomography. *Respiration.* 73 (5), 597–602. doi:10.1159/000088694

Snell, G. I., Yusen, R. D., Weill, D., Strueber, M., Garrity, E., Reed, A., et al. (2017). Report of the ISHLT working group on primary lung graft dysfunction, part I: Definition and grading-A 2016 consensus group statement of the international society for heart and lung transplantation. *J. Heart Lung Transpl.* 36 (10), 1097–1103. doi:10.1016/j.healun.2017.07.021

Soluri-Martins, A., Sutherasan, Y., Silva, P. L., Pelosi, P., and Rocco, P. R. (2015). How to minimise ventilator-induced lung injury in transplanted lungs: The role of protective ventilation and other strategies. *Eur. J. Anaesthesiol.* 32 (12), 828–836. doi:10.1097/eja.0000000000000291

Son, E., Jang, J., Cho, W. H., Kim, D., and Yeo, H. J. (2021). Successful lung transplantation after prone positioning in an ineligible donor: A case report. *Gen. Thorac. Cardiovasc. Surg.* 69 (9), 1352–1355. doi:10.1007/s11748-021-01676-4

Soriano, C. M., Gaine, S. P., Conte, J. V., Fairman, R. P., White, C., and Rubin, L. J. (1999). Anastomotic pulmonary hypertension after lung transplantation for primary pulmonary hypertension: Report of surgical correction. *Chest* 116 (2), 564–566. doi:10.1378/chest.116.2.564

Spadaro, S., Mauri, T., Böhm, S. H., Scaramuzzo, G., Turrini, C., Waldmann, A. D., et al. (2018). Variation of poorly ventilated lung units (silent spaces) measured by electrical impedance tomography to dynamically assess recruitment. *Crit. Care* 22 (1), 26. doi:10.1186/s13054-017-1931-7

Spinelli, E., Kircher, M., Stender, B., Ottaviani, I., Basile, M. C., Marongiu, I., et al. (2021). Unmatched ventilation and perfusion measured by electrical impedance tomography predicts the outcome of ARDS. *Crit. Care* 25 (1), 192. doi:10.1186/s13054-021-03615-4

Steinmann, D., Stahl, C. A., Minner, J., Schumann, S., Loop, T., Kirschbaum, A., et al. (2008). Electrical impedance tomography to confirm correct placement of double-lumen tube: A feasibility study. *Br. J. Anaesth.* 101 (3), 411–418. doi:10.1093/bja/aen166

Swaminathan, A. C., Todd, J. L., and Palmer, S. M. (2021). Advances in human lung transplantation. *Annu. Rev. Med.* 72, 135–149. doi:10.1146/annurev-med-080119-103200

Tang, M., Wang, W., Wheeler, J., McCormick, M., and Dong, X. (2002). The number of electrodes and basis functions in EIT image reconstruction. *Physiol. Meas.* 23 (1), 129–140. doi:10.1088/0967-3334/23/1/312

Tejwani, V., Panchabhai, T. S., Kotloff, R. M., and Mehta, A. C. (2016). Complications of lung transplantation: A roentgenographic perspective. *Chest* 149 (6), 1535–1545. doi:10.1016/j.chest.2015.12.019

Thakuria, L., Davey, R., Romano, R., Carby, M. R., Kaul, S., Griffiths, M. J., et al. (2016). Mechanical ventilation after lung transplantation. *J. Crit. Care* 31 (1), 110–118. doi:10.1016/j.jcrc.2015.09.021

Thakuria, L., Reed, A., Simon, A. R., and Marczin, N. (2017). Mechanical ventilation after lung transplantation. *Chest* 151 (2), 516–517. doi:10.1016/j.chest.2016.10.064

Van Raemdonck, D., Neyrinck, A., Verleden, G. M., Dupont, L., Coosemans, W., Decaluwé, H., et al. (2009). Lung donor selection and management. *Proc. Am. Thorac. Soc.* 6 (1), 28–38. doi:10.1513/pats.200808-098GO

Verleden, G. M., Raghu, G., Meyer, K. C., Glanville, A. R., and Corris, P. (2014). A new classification system for chronic lung allograft dysfunction. *J. Heart Lung Transpl.* 33 (2), 127–133. doi:10.1016/j.healun.2013.10.022

Vonk Noordegraaf, A., Kunst, P. W., Janse, A., Marcus, J. T., Postmus, P. E., Faes, T. J., et al. (1998). Pulmonary perfusion measured by means of electrical impedance tomography. *Physiol. Meas.* 19 (2), 263–273. doi:10.1088/0967-3334/19/2/013

Wang, G., Zhang, L., Li, B., Niu, B., Jiang, J., Li, D., et al. (2021). The application of electrical impedance tomography during the ventilator weaning process. *Int. J. Gen. Med.* 14, 6875–6883. doi:10.2147/ijgm.S331772

Whitson, B. A., Prekker, M. E., Herrington, C. S., Whelan, T. P., Radosevich, D. M., Hertz, M. I., et al. (2007). Primary graft dysfunction and long-term pulmonary function after lung transplantation. *J. Heart Lung Transpl.* 26 (10), 1004–1011. doi:10.1016/j.healun.2007.07.018

Wong, A., and Liu, M. (2021). Inflammatory responses in lungs from donation after brain death: Mechanisms and potential therapeutic targets. *J. Heart Lung Transpl.* 40 (9), 890–896. doi:10.1016/j.healun.2021.03.010

Xu, M., He, H., and Long, Y. (2021). Lung perfusion assessment by bedside electrical impedance tomography in critically ill patients. *Front. Physiol.* 12, 748724. doi:10.3389/fphys.2021.748724

Yeung, J. C., and Keshavjee, S. (2014). Overview of clinical lung transplantation. *Cold Spring Harb. Perspect. Med.* 4 (1), a015628. doi:10.1101/cshperspect.a015628

Yoshida, T., Torsani, V., Gomes, S., De Santis, R. R., Beraldo, M. A., Costa, E. L., et al. (2013). Spontaneous effort causes occult pendelluft during mechanical ventilation. *Am. J. Respir. Crit. Care Med.* 188 (12), 1420–1427. doi:10.1164/rccm.201303-0539OC

Young, K. A., and Dilling, D. F. (2019). The future of lung transplantation. *Chest* 155 (3), 465–473. doi:10.1016/j.chest.2018.08.1036

Yun, L., He, H. W., Möller, K., Frerichs, I., Liu, D., and Zhao, Z. (2016). Assessment of lung recruitment by electrical impedance tomography and oxygenation in ARDS patients. *Med. Baltim.* 95 (22), e3820. doi:10.1097/md.0000000000003820

Yuzuak, E., Aslan, S., and Cakir, I. M. (2021). Pneumothorax in a COVID-19 patient receiving long-term mechanical ventilation. *Rev. Soc. Bras. Med. Trop.* 54, e03762021. doi:10.1590/0037-8682-0376-2021

Zarantonello, F., Andreatta, G., Sella, N., and Navalesi, P. (2020). Prone position and lung ventilation and perfusion matching in acute respiratory failure due to COVID-19. *Am. J. Respir. Crit. Care Med.* 202 (2), 278–279. doi:10.1164/rccm.202003-0775IM

Zarantonello, F., Sella, N., Pettenuzzo, T., Andreatta, G., Dell'Amore, A., Giraudo, C., et al. (2021). Bedside detection and follow-up of pulmonary artery stenosis after lung transplantation. *Am. J. Respir. Crit. Care Med.* 204 (9), 1100–1102. doi:10.1164/rccm.202101-0229IM

Zhao, Z., Peng, S. Y., Chang, M. Y., Hsu, Y. L., Frerichs, I., Chang, H. T., et al. (2017). Spontaneous breathing trials after prolonged mechanical ventilation monitored by electrical impedance tomography: An observational study. *Acta Anaesthesiol. Scand.* 61 (9), 1166–1175. doi:10.1111/aas.12959

Zhao, Z., Steinmann, D., Frerichs, I., Guttmann, J., and Möller, K. (2010). PEEP titration guided by ventilation homogeneity: A feasibility study using electrical impedance tomography. *Crit. Care* 14 (1), R8. doi:10.1186/cc8860

Zhou, R., He, C., Chi, Y., Yuan, S., Tang, B., Li, Z., et al. (2022). Electrical impedance tomography to aid in the identification of hypoxemia etiology: Massive atelectasis or pneumothorax? A case report. *Front. Med.* 9, 970087. doi:10.3389/fmed.2022.970087

frontiers | Frontiers in Physiology

TYPE Original Research
PUBLISHED 14 February 2023
DOI 10.3389/fphys.2023.1040028

OPEN ACCESS

EDITED BY
Gaetano Perchiazzi,
Uppsala University, Sweden

REVIEWED BY
Yidong Yang,
University of Science and Technology of China, China
Mustafa Ghaderzadeh,
Shahid Beheshti University of Medical Sciences, Iran

*CORRESPONDENCE
Mattison J. Flakus,
✉ flakus@wisc.edu

SPECIALTY SECTION
This article was submitted to Respiratory Physiology and Pathophysiology, a section of the journal Frontiers in Physiology

RECEIVED 08 September 2022
ACCEPTED 31 January 2023
PUBLISHED 14 February 2023

CITATION
Flakus MJ, Wuschner AE, Wallat EM, Shao W, Shanmuganayagam D, Christensen GE, Reinhardt JM, Li K and Bayouth JE (2023), Quantifying robustness of CT-ventilation biomarkers to image noise.
Front. Physiol. 14:1040028.
doi: 10.3389/fphys.2023.1040028

Quantifying robustness of CT-ventilation biomarkers to image noise

Mattison J. Flakus[1]*, Antonia E. Wuschner[1], Eric M. Wallat[1], Wei Shao[2], Dhanansayan Shanmuganayagam[3], Gary E. Christensen[4], Joseph M. Reinhardt[5], Ke Li[1] and John E. Bayouth[6]

[1]Department of Medical Physics, University of Wisconsin-Madison, Madison, WI, United States, [2]Department of Medicine, University of Florida, Gainesville, FL, United States, [3]Department of Animal Sciences, University of Wisconsin-Madison, Madison, WI, United States, [4]Department of Electrical and Computer Engineering, University of Iowa, Iowa City, IA, United States, [5]Roy J Carver Department of Biomedical Engineering, University of Iowa, Iowa City, IA, United States, [6]Department of Human Oncology, University of Wisconsin-Madison, Madison, WI, United States

Purpose: To quantify the impact of image noise on CT-based lung ventilation biomarkers calculated using Jacobian determinant techniques.
Methods: Five mechanically ventilated swine were imaged on a multi-row CT scanner with acquisition parameters of 120 kVp and 0.6 mm slice thickness in static and 4-dimensional CT (4DCT) modes with respective pitches of 1 and 0.09. A range of tube current time product (mAs) values were used to vary image dose. On two dates, subjects received two 4DCTs: one with 10 mAs/rotation (low-dose, high-noise) and one with CT simulation standard of care 100 mAs/rotation (high-dose, low-noise). Additionally, 10 intermediate noise level breath-hold (BHCT) scans were acquired with inspiratory and expiratory lung volumes. Images were reconstructed with and without iterative reconstruction (IR) using 1 mm slice thickness. The Jacobian determinant of an estimated transformation from a B-spline deformable image registration was used to create CT-ventilation biomarkers estimating lung tissue expansion. 24 CT-ventilation maps were generated per subject per scan date: four 4DCT ventilation maps (two noise levels each with and without IR) and 20 BHCT ventilation maps (10 noise levels each with and without IR). Biomarkers derived from reduced dose scans were registered to the reference full dose scan for comparison. Evaluation metrics were gamma pass rate (Γ) with 2 mm distance-to-agreement and 6% intensity criterion, voxel-wise Spearman correlation (ρ) and Jacobian ratio coefficient of variation (CoV_{JR}).
Results: Comparing biomarkers derived from low ($CTDI_{vol}$ = 6.07 mGy) and high ($CTDI_{vol}$ = 60.7 mGy) dose 4DCT scans, mean Γ, ρ and CoV_{JR} values were 93% ± 3%, 0.88 ± 0.03 and 0.04 ± 0.009, respectively. With IR applied, those values were 93% ± 4%, 0.90 ± 0.04 and 0.03 ± 0.003. Similarly, comparisons between BHCT-based biomarkers with variable dose ($CTDI_{vol}$ = 1.35–7.95 mGy) had mean Γ, ρ and CoV_{JR} of 93% ± 4%, 0.97 ± 0.02 and 0.03 ± 0.006 without IR and 93% ± 4%, 0.97 ± 0.03 and 0.03 ± 0.007 with IR. Applying IR did not significantly change any metrics (p>0.05).
Discussion: This work demonstrated that CT-ventilation, calculated using the Jacobian determinant of an estimated transformation from a B-spline deformable image registration, is invariant to Hounsfield Unit (HU) variation caused by image noise. This advantageous finding may be leveraged clinically

with potential applications including dose reduction and/or acquiring repeated low-dose acquisitions for improved ventilation characterization.

KEYWORDS

CT, lungs, ventilation, noise, biomarker, registration, 4DCT, Jacobian

1 Introduction

Functional lung biomarkers identify regional variation in lung function, including ventilation and/or perfusion. Ventilation biomarkers have been generated from several medical imaging modalities, including computed tomography (CT) (Simon, 2000; Guerrero et al., 2005; Reinhardt et al., 2008; Kipritidis et al., 2014; Kipritidis et al., 2016; Eslick et al., 2018; Castillo et al., 2019; Shao et al., 2020; Cazoulat et al., 2021). Several methods to derive ventilation information from CT scans have been developed using multiple image acquisition and post-processing techniques. CT-ventilation biomarkers are commonly derived with patient breathing maneuvers of breath-hold CT (BHCT) or free-breathing through four-dimensional CT (4DCT) acquisition. The two primary post-processing techniques that have been implemented are calculating CT-ventilation directly from Hounsfield Units (HU) (Kipritidis et al., 2016) or using the Jacobian determinant of deformable image registration (Reinhardt et al., 2008; Shao et al., 2020). The various methods for calculating regional ventilation from CT scans have been previously reviewed in detail, including descriptions of their uncertainties, validation results and shortcomings (Vinogradskiy, 2019).

One application of ventilation biomarkers is in functional avoidance radiation therapy (RT) in which dose distributions are optimized to reduce dose to functioning lung. Currently being investigated in multiple clinical trials [NCT0252894225 (Yamamoto et al., 2016), NCT0230870926 (Vinogradskiy et al., 2015), NCT0284356827 (Bayouth, 2016)], the goal of functional avoidance RT is to preserve post-RT lung function and mitigate post-RT toxicities. CT-based ventilation biomarkers are particularly advantageous for applications in RT since CT-simulation is routinely acquired for RT treatment planning (Ettinger et al., 2012) and CT has high spatial and temporal resolution. However, CT-ventilation biomarkers have the disadvantage of associated radiation dose, increasing risk to patients (Bagherzadeh et al., 2018). Since there is a direct tradeoff between image dose and image noise in CT imaging, generating biomarkers minimally impacted by image noise would allow for potential dose reduction, broadening clinical applications of the biomarkers. Understanding the relationship between biomarkers and image noise is also critical for evaluating their robustness.

For the purpose of evaluating the impact of image noise on CT-ventilation biomarkers, mitigating the effect of other contributing uncertainties is critical. Mechanically ventilated non-human subjects offer a precisely controlled environment relative to human patients, as demonstrated in previous work (Du et al., 2012; Du et al., 2013; Mistry et al., 2013). Additionally, performing CT imaging in non-human subjects allows greater latitude for increased imaging dose from repeat imaging. Swine models share similarities in genetics, anatomy and bodily function with humans (Schomberg et al., 2016). The novel Wisconsin Miniature Swine (WMS) breed was developed to model human physiology more accurately than conventional breeds (Schomberg et al., 2016). With similar weight and size to humans, WMS are an ideal model for evaluating the relationship between image noise and derived CT-ventilation values. The purpose of this work is to quantify the impact of image noise on CT-ventilation biomarkers calculated using the Jacobian determinant computed directly from the deformable image registration transformation.

2 Materials and methods

2.1 CT imaging

All CT scans were acquired on a Siemens SOMATOM Definition Edge CT scanner (Siemens Healthineers, Erlangen, Germany) at the University of Wisconsin-Madison (UW-Madison, Madison, WI). First, repeated CT acquisitions of a uniform phantom were acquired with varying image noise levels. Next, quantified image noise from phantom imaging was used to guide selection of relevant image noise levels for acquiring CT scans in mechanically ventilated WMS.

For phantom and WMS scans, static (for BHCT) and 4DCT scans were acquired with constant scan parameters currently use in standard of care CT-simulation at UW-Madison. The corresponding parameter values are 120 kV, 0.5 s tube rotation time, 76.8 mm beam collimation and 128 detector rows. Image noise was varied by changing only the tube current time product between acquisitions. The tube current is measured in units of milliamps (mA) and tube rotation time is measured in seconds (s), giving their product units of mA×s or mAs. The tube current time product variable, commonly referred to as mAs, has an inverse relationship with image noise [defined by the standard deviation of Hounsfield Units (HU)], denoted in Eq. **1**, and is proportional to image dose (Eq. **2**).

$$Noise \propto (mAs)^{-0.5} \tag{1}$$

$$Dose \propto mAs \tag{2}$$

2.1.1 Uniform phantom scans

The uniformity region (Module CTP486) of a CATPHAN 504 phantom (The Phantom Laboratory, Salem, NY) was imaged in static and 4DCT acquisition modes. **Figure 1** shows the phantom setup on the CT table and an axial image of the uniformity region. Repeated helical 4DCT scans with a pitch of 0.09 and static scans with a pitch of 1 were acquired with mAs values ranging from 10 to 100 mAs (corresponding to 20–200 mA with 0.5 s); 10 mAs is the minimum mAs value the scanner allows when a 0.5 s rotation time is used

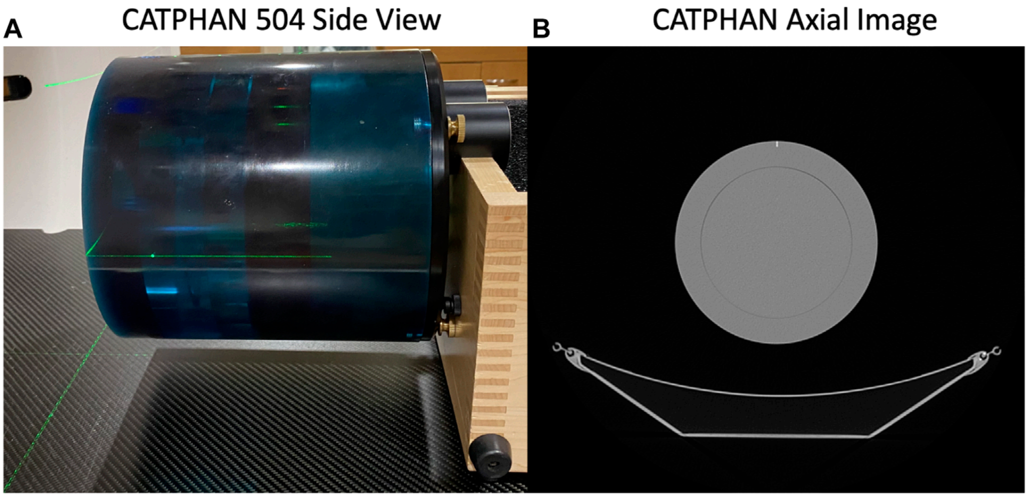

FIGURE 1
The CATPHAN 504 imaged in this study is shown **(A)** setup on the CT table and **(B)** with an axial CT image of the uniformity region.

and 100 mAs is the current mAs value used in standard of care CT-simulation 4DCT scans at UW-Madison.

2.1.2 Image noise calculation and mAs parameter selection

In this work, image noise was calculated as the standard deviation of HU in a centrally-placed circular region of interest (ROI) in axial phantom images acquired with each mAs value. All mAs and corresponding image noise values were fit to an exponential using Microsoft Excel (Microsoft, Inc., Redmond, WA) power-law curve-fitting to identify the relationship between image noise and mAs values with constant scan parameters listed previously for both static and 4DCT acquisitions. Equation 3 shows the general relationship between image noise and 4DCT mAs (mAs_{4D}) with constants A_{4D} and B_{4D}. Similarly, the relationship between BHCT image noise and mAs (mAs_{BH}) is given in Eq. 4 (with constants A_{BH} and B_{BH}). Based on the theoretical relationship between image noise and mAs (Eq. 1), exponential constants B_{4D} and B_{BH} are unitless and expected to have numerical values near 0.5. Since noise is expressed in units of HU, A_{4D} and A_{BH} have units of $HU \times \sqrt{mAs}$.

$$Noise_{4DCT} = A_{4D} \times (mAs_{4D})^{-B_{4D}} \quad [units = HU] \tag{3}$$

$$Noise_{BHCT} = A_{BH} \times (mAs_{BH})^{-B_{BH}} \quad [units = HU] \tag{4}$$

At UW-Madison, 4DCTs are currently used for CT-simulation and CT-ventilation calculation. With a low pitch of 0.09, 4DCT scans are time-consuming to acquire and have high associated dose; these aspects limited feasibility of acquiring several consecutive 4DCTs with unique image noise levels. To address this challenge, 4DCTs were acquired at two noise levels and BHCT scans were acquired at multiple intermediate noise levels. With a pitch of 1, BHCT scans require less dose and time than 4DCT acquisitions. Including BHCT imaging has the added benefit of expanding applicability of the study, since BHCT scans are commonly used for CT-ventilation calculation and the further reduced dose broadens potential clinical uses.

To ensure clinically relevant image noise levels were selected for BHCT imaging, mAs_{BH} values with image noise at and above current practice (mAs_{4D} = 100 mAs/rotation) were chosen. Appropriate mAs_{BH} values were determined by setting Eqs 3, 4 equal to discern mAs_{BH} with an equivalent noise level to mAs_{4D}, as listed in Eq. 5. For WMS imaging, 4DCTs were acquired with reduced (10 mAs) and standard of care (100 mAs) mAs values. BHCT images were acquired at intermediate noise levels equivalent to 4DCTs with 15, 20, 25, 30, 35, 40, 60, 70, 80 and 100 mAs according to Eq. 5. Tighter sampling was used at lower equivalent mAs values (15–40 mAs) since the low noise region is the steepest portion of the exponential curve relating image noise and mAs.

$$mAs_{BH} = \left(\frac{A_{BH}}{A_{4D}} \times (mAs_{4D})^{B_{4D}} \right)^{\frac{1}{B_{BH}}} \tag{5}$$

Beyond varying mAs values, application of iterative reconstruction (IR) was used to evaluate the impact of image noise; IR is commonly used for noise reduction. The commercially available Siemens IR algorithm, SAFIRE, was applied with strength three (out of possible strengths 1–5). All 4DCT and BHCT phantom scans used for noise calculation were reconstructed with 512 mm extended field of view (FOV), 1 mm slice thickness, a medium smooth kernel (Br51f) and both with and without SAFIRE3 IR.

2.1.3 Image dose

Image dose for scans at each mAs level was quantified through the CT dose index volume ($CTDI_{vol}$) for the 32 cm phantom in units of milligray (mGy). For the scan parameters used in this work, 10 and 100 mAs 4DCT scans had corresponding $CTDI_{vol}$ of 6.07 and 60.7 mGy, respectively. Therefore, 4DCT comparisons between 10 and 100 mAs scans represent differences for dose being reduced by 10 times from current standard of care. Since BHCT acquisitions used a higher pitch, they had reduced dose compared to 4DCTs. As stated in the previous section, BHCT mAs values were selected to match image noise, not dose. BHCT $CTDI_{vol}$ values ranged from 1.3 to 7.9 mGy; hence, the lowest dose BHCT scans (1.3 mGy) were acquired with six times less dose than the highest dose BHCT scans (7.9 mGy).

2.1.4 WMS scans

In order to evaluate how image noise affects CT-ventilation biomarkers, CT scans were acquired in live WMS subjects. Schomberg et al. (2016) has detailed the anatomical and physiological similarities between this specific porcine breed and human subjects, including strong respiratory system similarities. For the present study, WMS in early adulthood were used with weight and lung size matching that of human adults. Subject weights ranged from 70 to 100 kg. Our group has previously used WMS for pre-clinical studies (Wallat et al., 2021; Wuschner et al., 2021; Wuschner et al., 2022a; Wuschner et al., 2022b).

Following phantom imaging, five WMS subjects were each imaged on two separate scan dates with breathing precisely controlled by mechanical ventilators and while under general anesthesia, minimizing in-scan subject motion. The animal study was reviewed and approved by the Institutional Animal Care and Use Committee (IACUC). **Supplementary Material** provides details of WMS subject management throughout the imaging study; drug and anesthesia administration methods were approved by the American Veterinary Medical Association (AVMA).

For all subjects on each of the two scan dates, repeated 4DCT and BHCT scans with different levels of image noise were acquired of each subject. Two consecutive 4DCTs were acquired; the first 4DCT was acquired using 100 mAs and the second 4DCT was acquired with 10 mAs, as shown in the top row of **Figure 2**. During 4DCT acquisitions, subjects were ventilated at 15 breaths per minute (BPM) with a 1,000 cubic centimeter (cc) tidal volume (TV). The Varian Real-Time Position Management (RPM) system (Varian Medical Systems, Inc., Palo Alto, CA) was used to track subjects' chest positions during 4DCT acquisitions. RPM respiratory traces were used to reconstruct 4DCT image data into 10 breathing phases classified by their inspiratory (IN) or expiratory (EX) percentage (0EX, 20IN, 40IN, 60IN, 80IN, 100IN, 80EX, 60EX, 40EX, 20EX), as previously described (Han et al., 2011).

BHCTs were also acquired on each scan date at 10 intermediate mAs levels (ranging from equivalent noise to 15–100 mAs 4DCTs). Coronal BHCT images acquired with highest (equivalent to 15 mAs_{4D}) and lowest (equivalent to 100 mAs_{4D}) noise levels are shown in the bottom row of **Figure 2**. BHCT scans were acquired at three distinct lung volumes: maximum expiration (MEBH), maximum inspiration (MIBH) and 80% inspiration (80%Insp) which are analogous to 4DCT 0EX, 100IN and 80IN, respectively. The two different inspiratory volumes (80%Insp and MIBH) were imaged to allow multiple TV options to facilitate equivalent TV (ETV) matching since Jacobian ventilation values are volume dependent (Du et al., 2013). For each of the three BH volumes, the subject held constant pressure to maintain the volume while alternating craniocaudal and caudocranial scans were acquired with decreasing mAs values. This BHCT image acquisition method has been previously described in detail (Flakus et al., 2020). Scans were always acquired in order from highest to lowest dose. All scans were reconstructed with the same parameters used for phantom scans, including both with and without SAFIRE3 IR. **Figure 3** shows an example 10 mAs 4DCT reconstructed with and without IR applied for noise reduction.

2.2 CT-ventilation calculation

CT-Ventilation maps were calculated using the Jacobian determinant of the transformation between inhale and exhale volumes to estimate local tissue expansion as a surrogate for ventilation, as previously described (Reinhardt et al., 2008). The Jacobian-based technique uses image registration between inhale and exhale lung volume images to calculate tissue expansion. Regions of high expansion indicate regions of increased ventilation. Prior to calculating Jacobian values, a deep-learning lung masking segmentation algorithm was used to mask lung volumes (Hofmanninger et al., 2020). Next, all BH and 4DCT breathing phase volumes were calculated from the lung masks. TV were calculated as the difference between inhale volumes and the end exhale volume (MEBH or 0EX) and were used to select ETV between compared scans for effort correction.

When a subject receives consecutive 4DCT scans, their TV may differ, which affects derived CT-ventilation biomarkers. In order to account for this volume effect, effort correction is implemented by selecting inhale phases with the closest matching TV (also referred to as equivalent TV—ETV) between compared scans. As an example, if a subject receives two consecutive 4DCTs and has a much larger full inhale volume on the second scan, the overall TV (i.e., 100IN-0EX) will not match between the two scans. By excluding the full inhale volume of the second scan, the new TV (80IN-0EX) may more closely match the TV of the first scan and be used for ensuing calculation of CT-ventilation biomarkers. Selecting inhale volumes to achieve ETV between scans accommodates for differences in breathing effort that affect lung volumes; this method of effort correction has previously been described in depth (Wallat et al., 2020).

Du et al. (2013) has previously highlighted the importance of effort correction when comparing volume-dependent Jacobian values. Registration of expiratory and ETV-selected inspiratory volumes was achieved using a B-spline deformable image registration with a sum of squared tissue volume differences (SSTVD) metric to account for lung density changes between different volumes (Cao et al., 2012).

For BHCT acquisitions, the ETV-selected inspiratory image (80%Insp or MIBH) was registered to the MEBH image. The Jacobian determinant was calculated directly from the corresponding transformation matrix. Each voxel-level Jacobian value estimates local lung tissue expansion between exhale and inhale BH volumes as a surrogate for ventilation.

For 4DCT acquisitions, the LER-N Jacobian-based ventilation calculation method, initially introduced by Shao et al. (2020), was used to generate ventilation maps. This method involves registering multiple breathing phases included in the ETV to the full expiration phase (0EX). Jacobian determinants are then calculated from all the registrations and combined to determine maximal expansion throughout the breathing cycle. Using image data from more than two breathing phases in LER-N accounts for out-of-phase regions

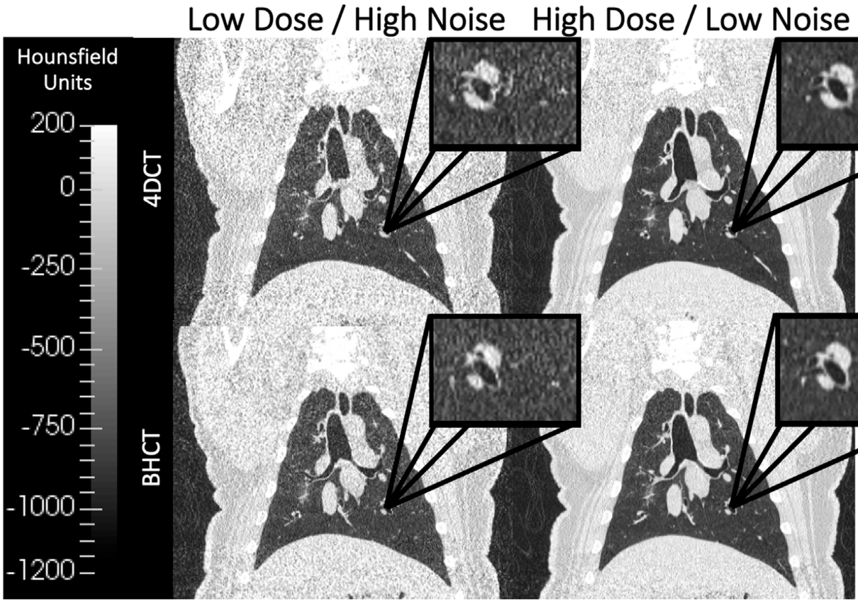

FIGURE 2
Coronal images of scans acquired at multiple dose levels are shown. The top row shows 4DCTs acquired with low dose ($CTDI_{vol}$ = 6.07 mGy) on the left and high dose ($CTDI_{vol}$ = 60.7 mGy) on the right. Similarly, the bottom row shows 4DCTs acquired with low dose ($CTDI_{vol}$ = 1.3 mGy) on the left and high dose ($CTDI_{vol}$ = 7.9 mGy) on the right. Qualitatively, the lower dose images in the left column show increased image noise relative to the high dose images of the right column. All four displayed images were reconstructed without IR applied.

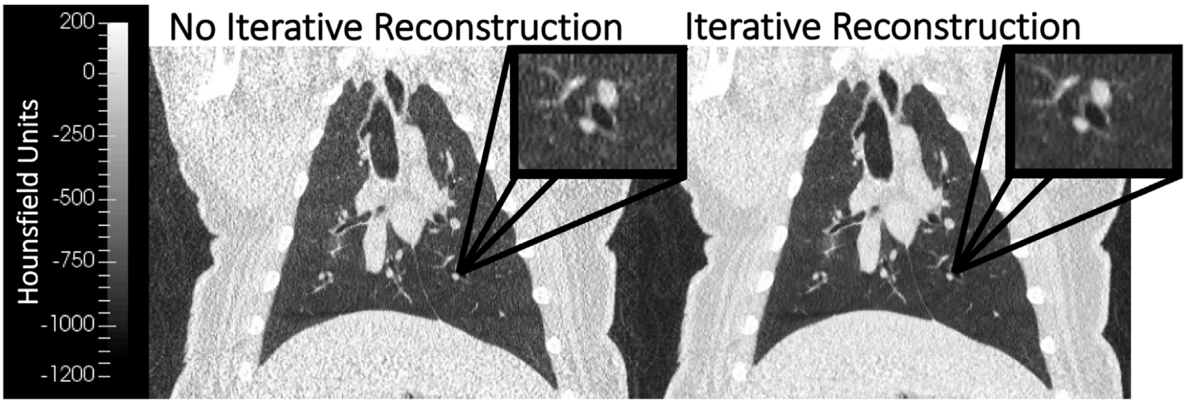

FIGURE 3
Coronal WMS images reconstructed without (left) and with (right) iterative reconstruction (IR) are shown. The image with IR applied demonstrates noise reduction when compared to the image without IR. Both images were acquired with the same image acquisition technique (10 mAs 4DCT).

that do not expand and contract in conjunction with the global lung volume. Previous work has reported that 7.6% of WMS subjects' lung volume is out-of-phase on average (Flakus et al., 2020).

Ventilation maps were generated from scans acquired at all noise levels with and without IR applied. Therefore, 24 CT-ventilation maps were generated per subject per scan date; four 4DCT ventilation maps included two image noise levels each with and without IR and 20 BHCT ventilation maps included 10 image noise levels each with and without IR.

2.3 Quantitative comparison

Comparison of CT-ventilation derived from scans acquired with differing image noise levels was facilitated through deformable image registration (Cao et al., 2012). For each subject, ventilation maps were only compared between those with the same acquisition type (BHCT or 4DCT) acquired on the same day. All reduced mAs (increased noise/decreased dose) scans were registered to the highest mAs (decreased noise/increased dose) scans in order to compare

CT-ventilation maps in the reference frame of the higher mAs scan. Acquisitions with and without IR were compared separately.

Similarity between CT-ventilation biomarkers with different amounts of image noise was quantified using metrics of gamma pass rate (Γ), Spearman correlation coefficient (ρ) and coefficient of variation (CoV_{JR}) of the Jacobian ratio (JR). Higher Γ and ρ values correspond to better consistency between compared CT-ventilation; on the contrary, lower CoV_{JR} values correspond to better consistency. Eqs 6, 8 define two of the three metrics for comparing CT-ventilation values from high and low mAs Jacobians J_1 and J_2, respectively. Γ, defined in Eq. 6 (Low et al., 1998), was evaluated locally with 2 mm distance-to-agreement (DTA) and 6% Jacobian intensity (JI) criterion (C) as has been reported previously in evaluation of CT-ventilation biomarkers (Wallat et al., 2020; Flakus et al., 2020) because it is the standard deviation of Jacobian values when evaluated with repeat scans in human subjects. Spearman correlation was calculated at the voxel level and classified as strong if $\rho \geq 0.8$, following guidelines initially proposed by Zou et al. (2003). Voxel-wise JR is defined in Eq. 7. CoV_{JR} is then calculated from the mean (μ_{JR}) and standard deviation (σ_{JR}) of JR, shown in Eq. 8.

$$\gamma(x_1) = \min_{x_2}\left[\sqrt{\left(\frac{x_2 - x_1}{C_{DTA}}\right)^2 + \left(\frac{J_2(x_2) - J_1(x_1)}{C_{JI}/100\% \times J_1(x_1)}\right)^2}\right] \qquad \forall x_2 \begin{cases} \text{passes if } \gamma \leq 1 \\ \text{fails if } \gamma > 1 \end{cases} \tag{6}$$

$$JR = \frac{J_2}{J_1} \tag{7}$$

$$CoV_{JR} = \frac{\sigma_{JR}}{\mu_{JR}} \tag{8}$$

Since Γ and CoV_{JR} directly compare ventilation values, these metrics are sensitive to significant TV differences between compared scans. To best isolate the effect of image noise, any scans with TV differences > 100 cc were excluded from Γ and CoV_{JR} analysis; this exclusion is consistent with previously reported findings (Reinhardt et al., 2008) regarding volume matching between compared ventilation maps. Since ρ only compares the CT-ventilation magnitude and not direct values, no data was excluded from Spearman correlation analysis.

3 Results

3.1 Image noise relationship to mAs

Based on image noise values calculated from uniform phantom scans, the relationships between image noise and mAs for both 4DCT and BHCT acquisition types are given in Eqs 9, 10. Both fits had R^2 values greater than 0.99. Substituting numerical values for constants A_{4D}, B_{4D}, A_{BH} and B_{BH} fromEqs 9, 10 intoEq. 5 yields Eq. 11 with the numerical relationship between 4DCT and BHCT mAs values that produce the same level of image noise. The right side of Eq. 11 shows an order of magnitude estimate that using approximately 60% of the mAs used in a 4DCT would lead to an equivalent noise level for BHCT scans. This relationship between mAs_{4D} and mAs_{BH} is expected due to a nuance of 4DCT acquisition. For the scanner used in this work, 4DCTs were reconstructed from limited CT angle projections (180°+ fan angle) as opposed to the full 360° used for BHCT reconstructions (Rietzel et al., 2005; Han et al., 2011). Since reduced projection angles leads to increased image noise in CT (Gong et al., 2019) and 4DCTs were acquired with fewer projections than BHCT scans, 4DCTs had higher noise levels than BHCTs when using the same mAs values. Therefore, to achieve equal noise, BHCT scans needed lower mAs values than 4DCT scans. The left side of Eq. 11 was used to calculate BHCT mAs values used to image WMS.

TABLE 1 **Ten mAs_{BH} used in this work are listed. mAs_{BH} were selected using Eq. 11 to find equivalent noise (with units of HU).**

mAs_{BH}	Equivalent noise [HU] mAs_{4D}
10	15
12	20
15	25
18	30
21	35
24	40
36	60
41	70
47	80
59	100

$$Noise_{4DCT} = 405.4 \times (mAs_{4D})^{-0.487} \qquad R^2 > 0.99 \tag{9}$$

$$Noise_{BHCT} = 325.5 \times (mAs_{BH})^{-0.497} \qquad R^2 > 0.99 \tag{10}$$

The 10 mAs_{BH} values used in this work are listed in Table 1 along with mAs_{4D} that produce images with the same image noise level when evaluated in a uniform phantom. Noise levels (with and without IR applied) for all scans acquired in WMS subjects are shown in Figure 4. For 4DCT acquisitions without IR, highest and lowest dose acquisitions had image noise values of 133 and 43 HU, respectively. This corresponds to a 209% image noise increase between acquisitions. For BHCTs, highest and lowest noise values were 103 and 43 HU, corresponding to a 142% increase in image noise.

$$mAs_{BH} = \left(0.8 \times (mAs_{4D})^{0.487}\right)^{\frac{1}{0.497}} \approx 0.6 \times mAs_{4D} \tag{11}$$

3.2 Breathing parameter control

The impact of image noise was studied in mechanically ventilated WMS in part for the ability to tightly control their breathing parameters affecting ventilation. For 4DCT acquisition, TV differences between scans acquired on the same day had mean [range] values of 5 ± 3 [2 13] cc. The 4DCT breathing period had

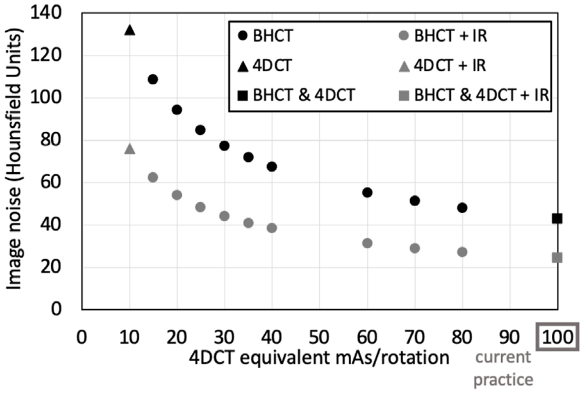

FIGURE 4
Noise levels of scans acquired in WMS.

average coefficient of variation of 0.010 ± 0.009 where a smaller value indicates better agreement. **Figure 5** shows an example of breathing traces between 10 and 100 mAs 4DCTs, demonstrating a highly reproducible breathing pattern while on mechanical ventilation.

Breathing parameter control for BHCT scans was dictated by how consistently subjects held pressure at a given volume. **Figure 6** shows two examples of BHCT volume control: one with consistent volumes across scans and a second showing volume drifting between acquired scans. The volume drift shown on the right in **Figure 6** demonstrates that while uncertainties associated with breathing variability are reduced in WMS imaging, they are not completely eliminated. These examples can be used to contextualize the effect volume differences had on results. For scans on the left plot of **Figure 6** had an average gamma pass rate of 91.5% compared to 89.7% for the scans of the right plot. Specifically, scans with TV differences < 100 cc had average Γ of 94.1% but scans with TV differences > 100 cc had average Γ of 87.5%. Since scans were always acquired in order of lowest to highest dose, any instances of volume drift disproportionately affected low mAs CT-ventilation comparison to full mAs values. Due to volume drift, BHCT TV differences were larger than those of 4DCT with averages of 54 ± 32 cc (range: 1–99) when excluding scans with TV difference > 100 cc and 72 ± 51 cc (range: 1–212) without exclusions.

3.3 4DCT robustness to image noise

For one subject on one scan date, all four CT-ventilation maps generated from 4DCT are shown in the first two columns of **Figure 7**. In these maps, Jacobian values (range 1–1.6) provide an estimation of relative tissue expansion. Values > 1 indicates tissue expansion, which is used as a surrogate for local ventilation in this work. Although non-linear, a Jacobian value of 1.1 roughly corresponds to 10% tissue expansion. Qualitatively, all ventilation maps showed strong similarity, generally identifying the same lung regions as being high or low ventilating. Gamma analysis comparing reduced and standard of care mAs 4DCT biomarkers are shown in the rightmost column of **Figure 7**. Blue-shaded regions passed the analysis, while regions in warm colors (corresponding to $\gamma > 1$) failed the analysis. Γ maps for comparisons with and without IR show spatial similarity. Without IR, 95% of the lung volume passed the Γ analysis between low and high dose 4DCTs for this subject. With IR, the pass rate improved to 96%.

For the same subject and scan date shown in **Figure 7**, visual representations of voxel-wise ρ and CoV_{JR} metrics between low and high dose 4DCTs is shown in **Figure 8**. In the voxel-wise heat map between high and low dose 4DCT Jacobians, voxels are clustered around the $y = x$ diagonal. This clustering shows that the majority of voxels directly agree and many very closely agree. Similarly, the voxel-wise Jacobian ratio (JR) distribution in **Figure 8** has a mean value of nearly one, which would indicate perfect agreement. JR values primarily range from 0.9 to 1.1, indicating that most high and low dose ventilation values agree within 10% at the voxel-level. The JR distribution with IR applied is slightly tighter than without IR, but did not meaningfully change the CoV_{JR} value for the subject.

Average and standard deviation of Γ, ρ and CoV_{JR} values between 10 and 100 mAs 4DCT acquisitions are shown in **Table 2**. The first column of data quantifies similarity when IR was not applied. The second column lists values when comparing CT-ventilation maps from images with IR applied. The listed *p*-values in the final column are from two-sided student's t-tests comparing results with and without IR applied. IR did not make a significant difference for any metric ($p>0.05$), indicating that noise reduction through IR did not increase similarity between derived ventilation maps.

3.4 BHCT robustness to image noise

Since BHCT scans were acquired with 10 different mAs values, biomarker comparison entailed comparing nine reduced dose levels (corresponding to 10–47 mAs) to the full dose level (corresponding to 59 mAs). These comparisons were made both with and without IR applied. **Figure 9** shows all ρ values for BHCT biomarkers between full and reduced dose scans without IR as a function of percent increase in image noise. As demonstrated in the plot, no clear correlation was identified between increased image noise and the Spearman correlation coefficient between full and reduced dose BHCT biomarkers. Summary results combining all reduced dose levels are given in **Table 3**. Similar to 4DCT results, IR application did not significantly affect results ($p>0.05$). When comparing 4DCT and BHCT results, Γ and CoV_{JR} were not significantly different ($p>0.05$) but ρ were ($p<0.001$).

4 Discussion

4.1 WMS model

To our knowledge, this is the first work reporting and quantifying the impact of image noise on CT-ventilation biomarkers. Similar lung size, weight and other physiological attributes between WMS and humans increase the applicability of the results toward clinical implementation. These commonalities suggest that WMS CT-ventilation response to image noise is representative of how CT-ventilation biomarkers derived in humans will be affected. Unlike humans, imaging in WMS allowed reduction

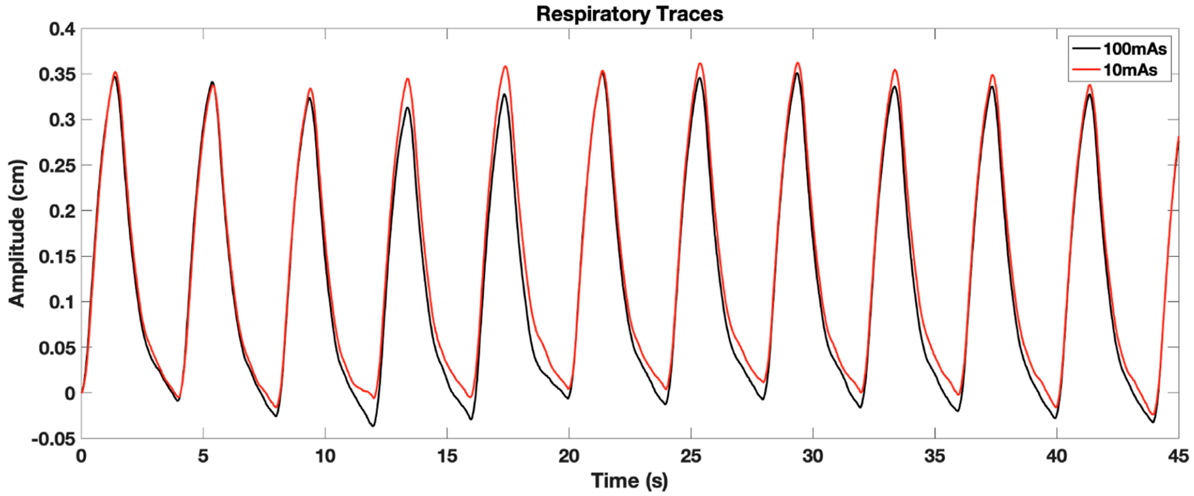

FIGURE 5
RPM breathing traces for consecutively acquired 4DCTs are shown.

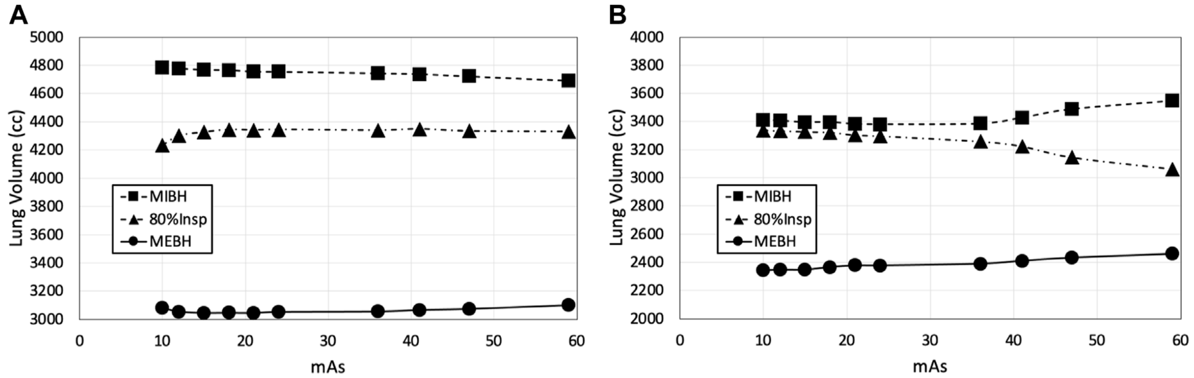

FIGURE 6
BHCT volume control is shown through two examples. In panel **(A)**, volumes remained relatively consistent across all ten scans of all three volumes. In panel **(B)**, clear volume drift is seen across scans. Scans were always acquired in decreasing 59–10 mAs order, so volume drift typically had a larger impact on comparisons involving low mAs biomarkers.

of uncertainties like in-scan subject motion and erratic breathing patterns. **Figures 5**, **6** visually demonstrate small breathing-related uncertainties that remain when imaging WMS, but overall tight control of parameters. WMS also better facilitated the investigation of a wide range of image noise levels due to tolerance of increased CT dose from consecutive scanning.

4.2 Robustness to image noise

Quantitative results presented in **Tables 2**, **3** show overall strong agreement between full and reduced dose biomarkers. Without IR, low and high noise 4DCT scans had corresponding noise values of 43 and 133 HU. When comparing these biomarkers with three times more noise, average Γ and ρ were 93% and 0.88. All Spearman correlations satisfied $\rho > 0.8$, indicating strong agreement as detailed by Zou et al. (2003) Our group previously reported CT-ventilation repeatability in WMS with average Γ and ρ of 89% and 0.92, respectively (Flakus et al., 2020). Those repeatability values compared consecutively acquired 100 mAs 4DCTs with no parameter changes between scans. Of note, breathing parameters affecting ventilation were more tightly controlled in the present study than the previous repeatability study. In that work, 4DCT breathing period CoV and TV differences were 0.004 and 25 cc on average (Flakus et al., 2020), compared to 0.001 and 5 cc in this work. Similar Γ and ρ values from the two studies indicate that image noise is not a driving factor when comparing Jacobian CT-ventilation biomarkers.

BHCT biomarker comparisons between different noise levels also show similar levels of agreement between reduced dose comparisons in the present study (average Γ = 93%, ρ = 0.97) and repeatability comparisons in a previous study (average Γ = 83%, ρ = 0.97) (Flakus et al., 2020). Increased Γ values in this study are consistent with the improved TV control. BHCT scans were used

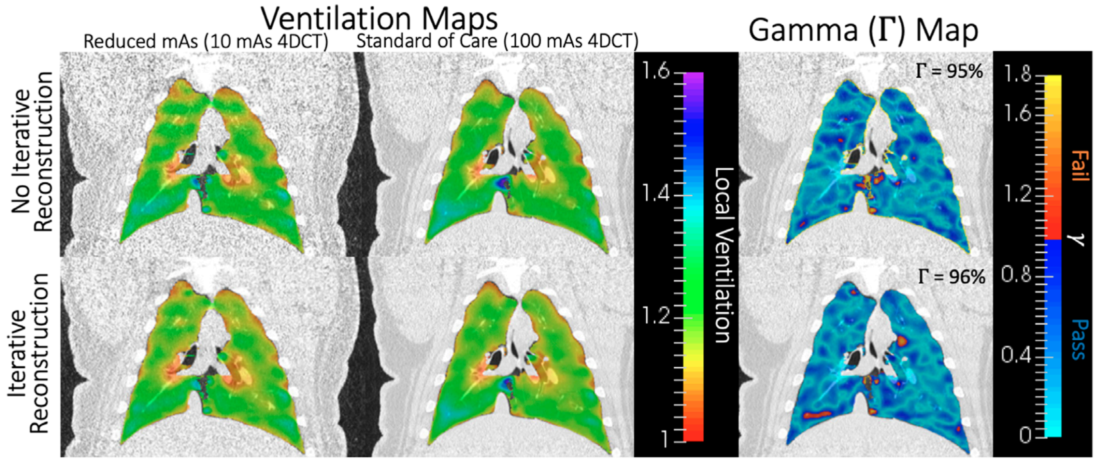

FIGURE 7
For one subject on one scan date, Jacobian values for all four CT-ventilation maps (10 and 100 mAs with and without IR) are shown in the two leftmost columns. On the right, gamma maps are shown for comparing the first two columns without (top) and with (bottom) IR applied. Blue-shaded voxels passed the Γ analysis, which was 95%–96% of the lung volume in this example.

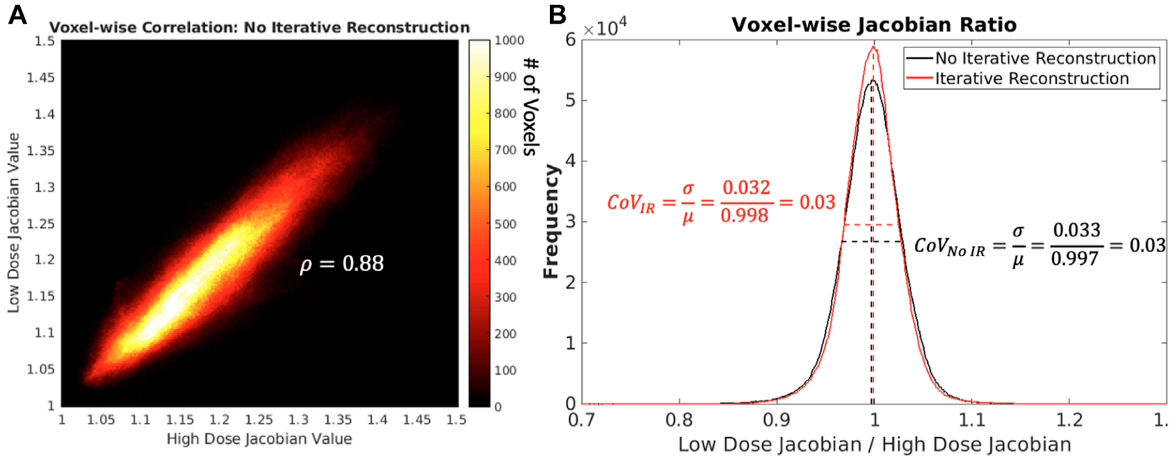

FIGURE 8
In panel **(A)** on the left shows, a heat map comparing low and high dose 4DCT Jacobian values for one subject on one scan date is shown. The colorbar indicates the number of voxels in each Jacobian value bin. In panel **(B)** on the right shows, voxel-wise Jacobian ratios with and without IR are shown. Mean and full width half maximum values are shown as dotted lines to highlight how CoV_{JR} was calculated.

to evaluate several intermediate image noise levels; from Figure 9, there is not a clear trend with the amount of image noise increase and the agreement between biomarkers. All Spearman values are labelled as strong ($\rho > 0.8$) (Zou et al., 2003), with all but two values above 0.9 and most values above 0.94. With noise levels ranging from 43 to 103 HU these results show the effect of increasing noise by up to almost two and a half times. This consistency across nine image noise levels further supports the finding that the Jacobian-based method used in this work is invariant to HU variations caused by image noise.

The minimal impact of image noise on Jacobian values is further validated by the results of comparing biomarkers with IR applied. Although IR reduced image noise (Figure 3), its application did not significantly change resultant quantitative metrics (Tables 2, 3). Figure 7 also shows how closely biomarkers generated from scans with and without IR agree spatially. Since increasing noise through reducing the mAs did not drastically reduce biomarker agreement, it is consistent that decreasing noise by applying IR did not drastically improve biomarker agreement. Maintaining consistent ventilation values in the presence of increased image noise highlights overall robustness of Jacobian-based CT-ventilation biomarkers.

4.3 Dose reduction

Since image noise and dose are inversely related, tolerance of increased image noise indicates a potential for dose reduction. In this work, biomarkers from standard of care 4DCTs were compared to biomarkers from scans with 10 times less dose (60.7 vs. 6.07 mGy

TABLE 2 Quantitative metrics for similarity between ventilation maps derived for 4DCT scans with different noise levels are listed. Results with and without IR are listed separately and were compared using a student's *t*-test and have *p*-values listed in the right most column.

Metric	No iterative reconstruction	Iterative reconstruction	*p*-value
Γ	92.6% ± 2.8%	93.4% ± 4.1%	0.65
ρ	0.88 ± 0.03	0.90 ± 0.04	0.12
CoV_{JR}	0.039 ± 0.009	0.034 ± 0.003	0.13

TABLE 3 Summary quantitative metrics comparing nine reduced dose BHCT biomarkers to full dose biomarkers are given. IR application was compared using a student's *t*-test and did not show a significant difference for any metric (p>0.05).

Metric	No iterative reconstruction	Iterative reconstruction	*p*-value
Γ	92.9% ± 4.3%	92.8% ± 4.4%	0.55
ρ	0.97 ± 0.02	0.97 ± 0.03	0.74
CoV_{JR}	0.034 ± 0.007	0.033 ± 0.006	0.13

$CTDI_{vol}$). For BHCTs, doses ranged from 1.3 to 7.9 mGy $CTDI_{vol}$, allowing for up to six times dose reduction between the highest and lowest dose scans. 4DCTs require higher doses than BHCTs but the value of 4DCT versus BHCT based ventilation is application dependent. Whether acquiring 4DCT or BHCT scans, substantial dose reduction can be realized without sacrificing CT-ventilation quality when using the Jacobian determinant computed directly from the deformable image registration transformation matrix.

4.4 Jacobian-based CT-ventilation

This work focused on a single CT-ventilation post-processing technique, namely computing the Jacobian determinant directly from deformable image registration transformation matrices between inhale and exhale volumes. The robustness to image noise presented here is an advantage of Jacobian-based biomarkers specifically, and does not necessarily apply to other CT-ventilation derivation methods. For example, the commonly used technique of estimating ventilation directly from HU would likely become less reproducible in the presence of increased HU variation.

As a common alternative to the Jacobian-based method presented in this work, HU-based CT-ventilation calculation assumes that HU change between inspiratory and expiratory images is solely due to the addition of air, changing the HU value as air is inhaled throughout the breathing cycle. Regional ventilation is calculated using the difference between voxel-wise inhale and exhale HU values (Kipritidis et al., 2016). The uncertainty in the CT-ventilation value for this method is therefore dependent on the uncertainty of HU values. Based on the standard error propagation formula, the variance of HU-based CT-ventilation is directly proportional to the variance of HU values. Images with increased noise have a larger HU standard deviation (and therefore variance). **Figure 4** shows the standard deviation of HU and how it increases in high noise (and correspondingly low dose) scans. When calculating CT-ventilation using established HU methods, increased image noise would then lead directly to increased uncertainty of derived ventilation biomarkers. Based on the results of this work, invariance to image noise is one advantage that Jacobian-based biomarkers have over those that are directly HU-based. For other CT-ventilation calculation methods beyond using Jacobian determinant or HU-based methods, experiments would need to be performed to quantify image noise dependence.

Since Jacobian-based CT-ventilation can be calculated from 4DCT and BHCT acquisitions, both were evaluated in this work. Both acquisition methods showed similar quantitative agreement

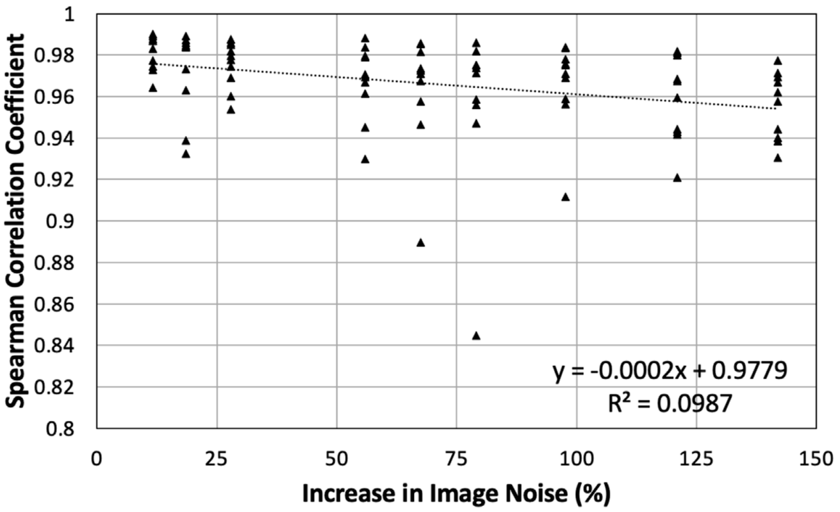

FIGURE 9
All Spearman correlation coefficients between full and reduced dose BHCT biomarkers without IR are plotted. Points are plotted based on the percentage increase in image noise of the reduced dose scan. Compared to 59 mAs, reduced dose scans of 10–47 mAs had increases in image noise of 12%–142%.

between high and low noise based biomarkers. From **Tables 2**, **3**, Γ and CoV_{JR} agree and were not statistically different while ρ was higher for BHCT than 4DCT biomarkers and showed a significant difference. One of three metrics shows that BHCT biomarkers may have stronger agreement in the presence of increased noise; however, both acquisition types showed agreement on par with baseline biomarker repeatability. Whether derived from 4DCT or BHCT scans, Jacobian-based CT-ventilation is advantageously robust to image noise.

4.5 Potential clinical applications

This work identified robustness to image noise as an advantage of Jacobian-based CT-ventilation biomarkers; further consideration is needed to determine how this advantage can be leveraged to be clinically impactful. One way of utilizing this advantage would be to reduce the necessary dose for deriving CT-ventilation biomarkers by acquiring reduced mAs CT scans. In current CT-ventilation uses, this dose reduction would mitigate patient risk associated with CT imaging dose. Additionally, dose reduction may allow CT-ventilation usage in more applications. As a viable low dose option for providing spatial distribution of patients' ventilation, they may be valuable compared to standard of care pulmonary function tests (PFTs); while PFTs have no associated dose, they are only a global measure and have high variance. Diagnostically, spatial ventilation information is relevant in evaluating conditions such as chronic obstructive pulmonary disease (COPD) and emphysema.

For RT applications, reduced imaging dose is minimally meaningful relative to doses delivered during RT. However, the results presented in this work still have potential therapeutic applications. For example, using CT-ventilation to quantify radiation-induced lung damage is an active research area. Acquiring repeated low dose 4DCTs may be advantageous for this application since artifact-ridden 4DCTs often impede the ability to evaluate ventilation changes in response to treatment and/or cause patients to be excluded from clinical studies. Multiple low dose acquisitions can also be valuable for improved characterization of ventilation variance. Further consideration is needed to identify more clinical situations in which the noise invariance advantage of Jacobian-based biomarkers can be best leveraged.

Data availability statement

The raw data supporting the conclusion of this article will be made available by the authors, without undue reservation.

Ethics statement

The animal study was reviewed and approved by Institutional Animal Care and Use Committee.

Author contributions

All authors contributed to conception and design of the study. AW, EW, MF, and JB performed imaging studies. MF performed image and statistical analysis. MF wrote the first draft of the manuscript. All authors contributed to manuscript revision, read, and approved the submitted version.

Funding

This research was funded by the National Institutes of Health grant CA166703.

Acknowledgments

The authors would like to thank Jen Meudt and the students of the University Wisconsin Veterinary school for her assistance with animal management and husbandry.

Conflict of interest

JR is a shareholder in VIDA Diagnostics, Inc. GC receives licensing fees from VIDA Diagnostics, Inc. and is a consultant and owns stock in PowerPollen, Inc., Ames IA. JB has ownership interest in MR Guidance, LLC (MRG), which has performed business with radiation oncology venders.

The remaining authors declare that the research was conducted in the absence of any commercial or financial relationships that could be construed as a potential conflict of interest.

Publisher's note

Supplementary material

The Supplementary Material for this article can be found online at: https://www.frontiersin.org/articles/10.3389/fphys.2023.1040028/full#supplementary-material

References

Bagherzadeh, S., Jabbari, N., and Khalkhali, H. (2018). Estimation of lifetime attributable risks (lars) of cancer associated with abdominopelvic radiotherapy treatment planning computed tomography (ct) simulations. *Int. J. Radiat. Biol.* 94, 454–461. doi:10.1080/09553002.2018.1450536

Bayouth, J. (2016). TU-H-202-03: Spatial distributions of radiation induced pulmonary changes can Be modeled and utilized for image-guided planning and therapy to improve pulmonary function preservation and hence the therapeutic ratio for lung cancer. *Med. Phys.* 43, 3771. doi:10.1118/1.4957635

Cao, K., Ding, K., Reinhardt, J., and Christensen, G. (2012). Improving intensity-based lung ct registration accuracy utilizing vascular information. *Int. J. Biom Imag.* 2012, 285136. doi:10.1155/2012/285136

Castillo, E., Castillo, R., Vinogradskiy, Y., Dougherty, M., Solis, D., Myziuk, N., et al. (2019). Robust ct ventilation from the integral formulation of the jacobian. *Med. Phys.* 46, 2115–2125. doi:10.1002/mp.13453

Cazoulat, G., Balter, J., Matuszak, M., Jolly, S., Owen, D., and Brock, K. (2021). Mapping lung ventilation through stress maps derived from biomechanical models of the lung. *Med. Phys.* 48, 715–723. doi:10.1002/mp.14643

Du, K., Bayouth, J., Cao, K., Christensen, G., Ding, K., and Reinhardt, J. (2012). Reproducibility of registration-based measures of lung tissue expansion. *Med. Phys.* 39, 1595–1608. doi:10.1118/1.3685589

Du, K., Reinhardt, J., Christensen, G., Ding, K., and Bayouth, J. (2013). Respiratory effort correction strategies to improve the reproducibility of lung expansion measurements. *Med. Phys.* 40, 123504. doi:10.1118/1.4829519

Eslick, E., Kipritidis, J., Gradinscak, D., Stevens, M., Bailey, D., Harris, B., et al. (2018). Ct ventilation imaging derived from breath hold ct exhibits good regional accuracy with galligas pet. *Radiother. Oncol.* 127, 267–273. doi:10.1016/j.radonc.2017.12.010

Ettinger, D., Akerley, W., Borghaei, H., Chang, A., Cheney, R., Chirieac, L., et al. (2012). Non-small cell lung cancer. *J. Natl. Comp. Canc Net.* 10, 1236–1271. doi:10.6004/jnccn.2012.0130

Flakus, M. E., Wallat, W., Shao, A., Wuschner, G., Christensen, J., Reinhardt, et al. (2020). Assessing variation in local lung function prior to, during and following radiation therapy. *Med. Phys.* 47, E703.

Gong, C., Zeng, L., and Wang, C. (2019). Image reconstruction model for limited-angle CT based on prior image induced relative total variation. *total Var.* 74, 586–605. doi:10.1016/j.apm.2019.05.020

Guerrero, T., Sanders, K., Noyola-Martinez, J., Castillo, E., Zhang, Y., Tapia, R., et al. (2005). Quantification of regional ventilation from treatment planning ct. *Int. J. Radiat. Oncol. Biol. Phys.* 62, 630–634. doi:10.1016/j.ijrobp.2005.03.023

Han, D., Bayouth, J., Bhatia, S., Sonka, M., and Wu, X. (2011). Characterization and identification of spatial artifacts during 4D-CT imaging. *Med. Phys.* 38, 2074–2087. doi:10.1118/1.3553556

Hofmanninger, J., Prayer, F., Pan, J., Röhrich, S., Prosch, H., and Langs, G. (2020). Automatic lung segmentation in routine imaging is primarily a data diversity problem, not a methodology problem. *Eur. Radiol. Exp.* 4, 50. doi:10.1186/s41747-020-00173-2

Kipritidis, J., Hofman, M., Siva, S., Callahan, J., Roux, P., Woodruff, H., et al. (2016). Estimating lung ventilation directly from 4d ct hounsfield unit values. *Med. Phys.* 43, 33–43. doi:10.1118/1.4937599

Kipritidis, J., Siva, S., Hofman, M., Callahan, J., Hicks, R., and Keall, P. (2014). Validating and improving ct ventilation imaging by correlating with ventilation 4d-pet/ct using 68ga-labeled nanoparticles. *Med. Phys.* 41, 011910. doi:10.1118/1.4856055

Low, D., Harms, W., Mutic, S., and Purdy, J. (1998). A technique for the quantitative evaluation of dose distributions. *Med. Phys.* 25, 656–661. doi:10.1118/1.598248

Mistry, N., Diwanji, T., Shi, X., Pokharel, S., Feigenberg, S., Scharf, S., et al. (2013). Evaluation of fractional regional ventilation using 4dct and effects of breathing maneuvers on ventilation. *Int. J. Radiat. Oncol. Biol.* 87, 825–831. doi:10.1016/j.ijrobp.2013.07.032

Reinhardt, J., Ding, K., Cao, K., Christensen, G., Hoffman, E., and Bodas, S. (2008). Registration-based estimates of local lung tissue expansion compared to xenon ct measures of specific ventilation. *Med. Image Anal.* 12, 752–763. doi:10.1016/j.media.2008.03.007

Rietzel, E., Pan, T., and Chen, G. (2005). Four-dimensional computed tomography: Image formation and clinical protocol. *Med. Phys.* 32, 874–889. doi:10.1118/1.1869852

Schomberg, D., Tellez, A., Meudt, J., Brady, D., Dillon, K., Arowolo, F., et al. (2016). Miniature swine for preclinical modeling of complexities of human disease for translational scientific discovery and accelerated development of therapies and medical devices. *Toxicol. Pathol.* 44, 299–314. doi:10.1177/0192623315618292

Shao, W., Patton, T., Gerard, S., Pan, Y., Reinhardt, J., Durumeric, O., et al. (2020). N-phase local expansion ratio for characterizing out-of-phase lung ventilation. *IEEE Trans. Med. Imaging* 39, 2025–2034. doi:10.1109/TMI.2019.2963083

Simon, B. (2000). Non-invasive imaging of regional lung function using x-ray computed tomography. *J. Clin. Monit. Comput.* 16, 433–442. doi:10.1023/a:1011444826908

Vinogradskiy, Y. (2019). Ct-based ventilation imaging in radiation oncology. *BJR Open* 1, 20180035. doi:10.1259/bjro.20180035

Vinogradskiy, Y., Waxweiler, T., Diot, Q., Kavanagh, B., Schubert, L., Miften, M., et al. (2015). Su-c-bra-06: Developing clinical and quantitative guidelines for a 4dct-ventilation functional avoidance clinical trial. *Med. Phys.* 42, 3196–3197. doi:10.1118/1.4923816

Wallat, E., Flakus, M., Wuschner, A., Shao, W., Christensen, G., Reinhardt, J., et al. (2020). Modeling the impact of out-of-phase ventilation on normal lung tissue response to radiation dose. *Med. Phys.* 47, 3233–3242. doi:10.1002/mp.14146

Wallat, E., Wuschner, A., Flakus, M., Christensen, G., Reinhardt, J., Shanmuganayagam, D., et al. (2021). Radiation-induced airway changes and downstream ventilation decline in a swine model. *Biomed. Phys. Eng. Espress* 7, 065039. doi:10.1088/2057-1976/ac3197

Wuschner, A., Flakus, M., Wallat, E., Reinhardt, J., Shanmuganayagam, D., Christensen, G., et al. (2022a). Ct-derived vessel segmentation for analysis of post-radiation therapy changes in vasculature and perfusion. *Front. Physiol.* 13, 1008526. doi:10.3389/fphys.2022.1008526

Wuschner, A., Flakus, M., Wallat, E., Shanmuganayagam, D., Christensen, G., Reinhardt, J., et al. (2022b). Measuring indirect radiation-induced perfusion change in fed vasculature using dynamic contrast ct. *J. Pers. Med.* 12, 1254. doi:10.3390/jpm12081254

Wuschner, A., Wallat, E., Flakus, M., Shanmuganayagam, D., Meudt, J., Christensen, G., et al. (2021). Radiation-induced hounsfield unit change correlates with dynamic ct perfusion better than 4dct-based ventilation measures in a novel-swine model. *Sci. Rep.* 11, 13156. doi:10.1038/s41598-021-92609-x

Yamamoto, T., Kabus, S., Bal, M., Keall, P., Benedict, S., and Daly, M. (2016). The first patient treatment of computed tomography ventilation functional image-guided radiotherapy for lung cancer. *Radiother. Oncol.* 118, 227–231. doi:10.1016/j.radonc.2015.11.006

Zou, K., Tuncali, K., and Silverman, S. (2003). Correlation and simple linear regression. *Radiology* 227, 3617–3622. doi:10.1148/radiol.2273011499

frontiers | Frontiers in Physiology

TYPE Review
PUBLISHED 21 March 2023
DOI 10.3389/fphys.2023.1142221

OPEN ACCESS

EDITED BY
Joseph M. Reinhardt,
The University of Iowa, United States

REVIEWED BY
Sam Bayat,
Université Grenoble Alpes, France
Abhilash Kizhakke Puliyakote,
University of Alabama at Birmingham,
United States

*CORRESPONDENCE
Lars Knudsen,
✉ knudsen.lars@mh.hannover.de

SPECIALTY SECTION
This article was submitted to
Respiratory Physiology and
Pathophysiology,
a section of the journal
Frontiers in Physiology

RECEIVED 11 January 2023
ACCEPTED 09 March 2023
PUBLISHED 21 March 2023

CITATION
Knudsen L, Hummel B, Wrede C, Zimmermann R, Perlman CE and Smith BJ (2023), Acinar micromechanics in health and lung injury: what we have learned from quantitative morphology. *Front. Physiol.* 14:1142221.
doi: 10.3389/fphys.2023.1142221

Acinar micromechanics in health and lung injury: what we have learned from quantitative morphology

Lars Knudsen[1,2]*, Benjamin Hummel[1], Christoph Wrede[1,3], Richard Zimmermann[1], Carrie E. Perlman[4] and Bradford J. Smith[5,6]

[1]Institute of Functional and Applied Anatomy, Hannover Medical School, Hannover, Germany, [2]Biomedical Research in Endstage and Obstructive Lung Disease Hannover (BREATH), Member of the German Centre for Lung Research (DZL), Hannover, Germany, [3]Research Core Unit Electron Microscopy, Hannover Medical School, Hannover, Germany, [4]Department of Biomedical Engineering, Stevens Institute of Technology, Hoboken, NJ, United States, [5]Department of Bioengineering, College of Engineering Design and Computing, University of Colorado Denver | Anschutz Medical Campus, Aurora, CO, United States, [6]Department of Pediatric Pulmonary and Sleep Medicine, School of Medicine, University of Colorado Anschutz Medical Campus, Aurora, CO, United States

Within the pulmonary acini ventilation and blood perfusion are brought together on a huge surface area separated by a very thin blood-gas barrier of tissue components to allow efficient gas exchange. During ventilation pulmonary acini are cyclically subjected to deformations which become manifest in changes of the dimensions of both alveolar and ductal airspaces as well as the interalveolar septa, composed of a dense capillary network and the delicate tissue layer forming the blood-gas barrier. These ventilation-related changes are referred to as micromechanics. In lung diseases, abnormalities in acinar micromechanics can be linked with injurious stresses and strains acting on the blood-gas barrier. The mechanisms by which interalveolar septa and the blood-gas barrier adapt to an increase in alveolar volume have been suggested to include unfolding, stretching, or changes in shape other than stretching and unfolding. Folding results in the formation of pleats in which alveolar epithelium is not exposed to air and parts of the blood-gas barrier are folded on each other. The opening of a collapsed alveolus (recruitment) can be considered as an extreme variant of septal wall unfolding. Alveolar recruitment can be detected with imaging techniques which achieve light microscopic resolution. Unfolding of pleats and stretching of the blood-gas barrier, however, require electron microscopic resolution to identify the basement membrane. While stretching results in an increase of the area of the basement membrane, unfolding of pleats and shape changes do not. Real time visualization of these processes, however, is currently not possible. In this review we provide an overview of septal wall micromechanics with focus on unfolding/folding as well as stretching. At the same time we provide a state-of-the-art design-based stereology methodology to quantify microarchitecture of alveoli and interalveolar septa based on different imaging techniques and design-based stereology.

KEYWORDS

micromechanics, pulmonary acinus, imaging, electron microscopy, stereology, Alveolar recruitment, interalveolar septa

1 An overview of the functional design of the lung

The design of the mammalian lung is optimized for efficient gas exchange, determined by micro- and ultrastructural properties of the fine lung parenchyma (Weibel et al., 1993). At the level of the gas-exchanger, the alveolus, blood and air are brought together over a large surface area and separated by a very thin leaflet of tissue that is referred to as the blood-gas barrier (Weibel and Knight, 1964; Gehr et al., 1978). At end-inspiration, more than 80% of the human lung is filled with air while blood within the pulmonary vasculature contributes roughly 10% to the lung volume. The remaining 10% of the lung is composed of tissue. In the gas-exchanging region, and above all the blood-gas barrier, the amount of tissue is reduced to a minimum to provide a short diffusion distance for gas exchange. The bulk of the connective tissue within the lung forms a sleeve around the purely conductive airway tree and the accompanying vessels, as well as in pleura and the connected interlobular septa (Knudsen and Ochs, 2018). These regions in which the bulk of connective tissue is located belong to the non-parenchyma of the lung (Ochs et al., 2004). The blood-gas barrier is a crucial part of the lung parenchyma and, in the human lung, has a surface area of 120–140 m^2 and a harmonic mean thickness of less than 1 µm. Even though force bearing connective tissue elements are minimized in lung parenchyma, the large surface area is stable and maintains the precondition for effective gas-exchange during the respiratory cycle.

After entering the lung at the pulmonary hilum, the conductive airways of the human lung follow an irregular, dichotomous inside-out branching pattern. The last purely conducting airway is the terminal bronchiole. After an average of 14–16 branching generations the first airway with excrescent alveoli is termed transitional bronchiole (Haefeli-Bleuer and Weibel, 1988). Subsequent bronchioles with periodic alveoli are respiratory bronchioles. Once alveoli become maximally packed into a sleeve around the airway, the airway is termed an alveolar duct. Alveolar ducts resemble mesh-walled tubes formed of chicken wire. They do not have a continuous wall but are instead circumscribed by a boundary that is formed out of alveolar entrance rings.

Branches of the pulmonary arteries accompany the conductive airways constituting broncho-arterial units (Weibel and Gomez, 1962). The smallest lung unit that is in part bounded by connective tissue is the (secondary) pulmonary lobule (Webb, 2006). Paired bronchioles/arteries enter the center of the lobule; veins and lymphatic vessels are located in the connective tissue of the interlobular septa. The acinus, the functional unit of the gas-exchanging region, starts with a transitional bronchiole (Haefeli-Bleuer and Weibel, 1988). Human, rat, and mouse lungs contain approximately 30,000, 6,000 and 600 acini, respectively (Haefeli-Bleuer and Weibel, 1988; Vasilescu et al., 2012; Barré et al., 2014; Barré et al., 2016). Within the human acinus, the first generations of airways are respiratory bronchioles. The airways continue the dichotomous branching pattern for, on average, eight generation. Within the rodent acinus, in contrast, the airways are nearly all alveolar ducts. Within the acinus, the alveoli are blind-ended while the vessels enable through-flow (König et al., 1993).

The essential consequences of the dichotomous branching pattern of the airways are twofold: first, the airway tree is space filling within the thorax so that air (and blood) can reach every part of the lung efficiently. Secondly, the number of airways increases by a power of two per branching generation which is accompanied by an exponential increase in the cumulative airway cross-sectional area in subsequent airway generations (Weibel and Gomez, 1962). Consequently, the airflow velocity decreases dramatically from the central to the peripheral airways. Gas transport is purely convective from the airway opening—the nose during spontaneous breathing or the trachea during mechanical ventilation—to the terminal bronchiole. There is a combination of both convective and passive diffusive gas transport within the acinar airways (Sapoval et al., 2002; Hogg et al., 2017). During quiet spontaneous breathing, the transport of gases is primarily by convection within the first three branching generations of intra-acinar airways. In the more peripheral branching generations of the acinus, diffusion dominates convection in terms of gas transport. The part of the pulmonary acinus in which diffusion dominates convection has been termed a diffusion cell. A diffusion cell has approximately the size of one-eighth of the acinus during quiet spontaneous breathing in humans (Sapoval et al., 2002). Increasing the tidal volume during exercise or sighing, shifts the location of transition from convection-dominated to diffusion-dominated gas transport to more peripheral generations of the intra-acinar airways.

The pulmonary acini form the fine lung parenchyma. In the human lung, the parenchyma contains an average of 480 million alveoli and contributes roughly 90% to total lung volume. The remaining 10% of the volume is assigned to structures which do not contribute directly to gas exchange and includes purely conductive airways, larger blood-vessels, and the majority of connective tissue which embeds these conductive airways and vessels (Ochs et al., 2004). Alveoli are separated from each other by interalveolar septa and three-dimensional imaging studies have shown that each alveolus in the human lung has 7–9 neighboring alveoli (Reimelt et al., 2023). The interalveolar septa contain a dense network of capillaries composed of capillary segments whose lengths are in the range of their diameter. Hence, the morphology of the alveolar capillary network has been described as sheet-flow around pillars that reach from one side of the interalveolar septa to the other and are filled with cells—principally fibroblasts but also alveolar epithelial cell bodies. Thus, the morphology of the alveolar capillary network differs markedly from that of capillary networks found in the systemic circulation (Fung and Sobin, 1969; Mühlfeld et al., 2010; Grothausmann et al., 2017; Buchacker et al., 2019).

The capillary lumen is separated from the alveolar airspace by the blood-gas barrier. The blood-gas barrier consists of the alveolar epithelium, the interstitial space, and the endothelium and forms a continuous boundary around the air in an alveolus that is interrupted only by the alveolar entrance and by inter-alveolar pores of Kohn. Approximately 50% of the blood-gas barrier of the human lung is termed the "thin side" of the capillary network. Here, the interstitial space contains only a single basement membrane (BM), which is shared by both the alveolar epithelium and the capillary endothelium (Weibel, 2017). The other half is the "thick side" on which the BM of the epithelium is separated from that of the endothelium so that the widened interstitium provides space for stabilizing fiber elements, e.g., collagen fibrils and elastic fibers, and also extensions of interstitial cells such as fibroblasts. The thick side contains elements of a very economically constructed fiber system and other components of the extracellular matrix (Figure 1). This fiber system determines the micromechanical properties of the interalveolar septa (Bou Jawde et al., 2020) and contributes to

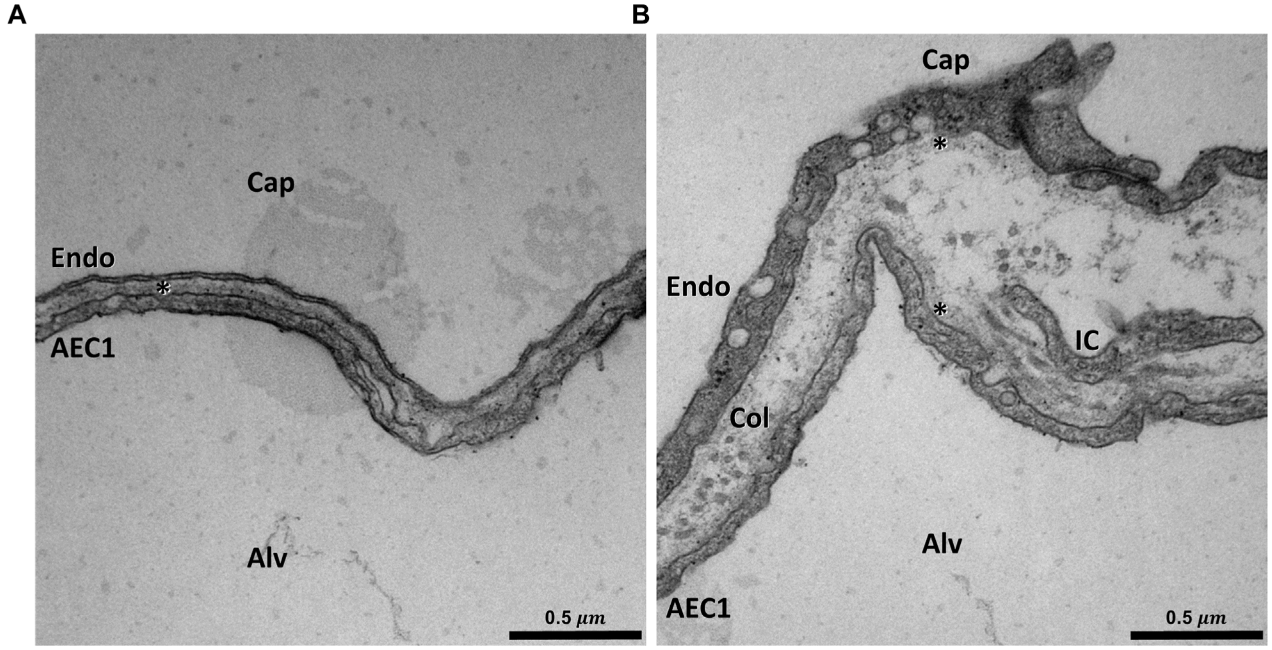

FIGURE 1
Ultrastructure of the blood-gas barrier: Transmission electron micrograph of a rat lung fixed *in vivo* by vascular perfusion *via* the vena cava caudalis at an airway opening pressure of 5 cmH_2O on expiration after two recruitment maneuvers (3 s pause at 30 cmH_2O) (Knudsen et al., 2018). The capillaries (Cap) are open and free from blood cells. In **(A)** an example of the thin part of the blood-gas barrier can be seen. In this area the squamous extension of an alveolar epithelial type 1 cell (ACE1), the basement membrane (asterisk) and the endothelial cell (Endo) form the blood-gas barrier. In **(B)** an example of the thick part of the blood-gas barrier is illustrated. The interstitium between the AEC1 and the endothelium is widened and both AEC1 and the endothelial cell have a basement membrane (asterisk) of its own. Aside from collagen fibrils (Col), cell extensions of interstitial cells (IC), e.g. fibroblasts can be identified.

mechanical stabilization of the gas-exchanging surface area. In addition, the thick side accommodates excess interstitial fluid, thus preserving the gas exchange function of the thin side (Weibel, 2009; Beretta et al., 2021; Mostaco-Guidolin et al., 2021).

The alveolar epithelium contains 2 cell populations in a healthy lung, namely the squamous alveolar epithelial type 1 (AE1) and the more cube-shaped alveolar epithelial type 2 (AE2) cells. Based on single cell RNA-sequencing, a third population, termed alveolar epithelial type 0 (AE0) cell has recently been described in the human lung in those interalveolar septa that are attached to the respiratory bronchioles. This morphologically not yet well characterized cell population has been suggested to fulfill functions in lung regeneration (Kadur Lakshminarasimha Murthy et al., 2022). The AE1 cells minimize the thickness of the blood-gas barrier. AE1 cells cover the capillary network on the air side with planar cellular extensions attached to the underlying BM. The bodies of the AE1 cells, which contain the nucleus and most of the organelles, are usually located in the pillars between the meshwork of the alveolar capillary network. These pillars allow the AE1 cells to traverse the interalveolar septum and form further planar cellular extensions on the other side of the interalveolar septum so that an AE1 cell usually faces more than one alveolar airspace (Schneider et al., 2019). The population of AE1 cells covers approximately 95% of the epithelial BM in both human (Gehr et al., 1978) and mouse lungs (Ruhl et al., 2019; Engelmann et al., 2021). The remaining 5% of the epithelial BM is covered by the cube-shaped, secretory AE2 cells, which are twice as numerous as AE1 cells (Crapo et al., 1982). The AE2 cells synthesize, store, and secrete pulmonary surfactant into the alveolar airspace, where the surfactant dynamically reduces surface tension of the alveolar liquid lining layer. In addition, AE2 cells have stem cell properties. They have the potential for self-renewal and are able to transdifferentiate into AE1 cells so that AE2 cells are responsible for the regeneration of the alveolar epithelium under physiological and pathophysiological conditions (Barkauskas et al., 2013; Jansing et al., 2017). The AE2 cells are usually located in the corners of the alveoli or in niches between segments of the alveolar capillary network, and thus tend not to interfere with the gas-exchanging function. Like the AE1 cells, AE2 cells also traverse the interalveolar septa and are part of the pillars located between the segments of the alveolar capillary network. Thereby, AE2 cells are in direct contact with more than one alveolus (Figure 2). This configuration strategically positions one AE2 cell to be able to supply surfactant to and regenerate the alveolar epithelium in multiple alveoli *via* its multipolar apical domains (Konkimalla et al., 2022).

2 Stabilization of the pulmonary acinus: Balance between distending inflation pressure, retracting fiber elasticity, and surface tension

The sole distending stress applied to the lungs is the transpulmonary pressure, which can be separated into the

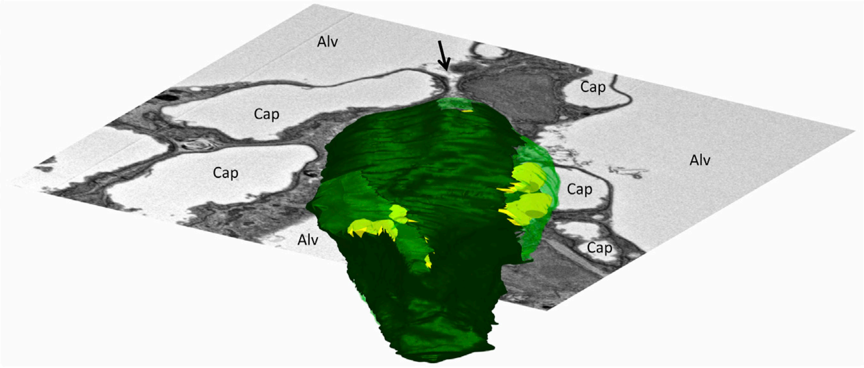

FIGURE 2
Three-dimensional model of an alveolar epithelial type 2 (AE2) cell: The mouse lung was fixed *in situ* by vascular perfusion *via* the right ventricle at an airway opening pressure of 2 cmH_2O on expiration after two recruitment maneuvers (3 s pause at 30 cmH_2O) (Ruhl et al., 2019). Tissue was processed for serial block face scanning electron microscopy (SBF-SEM) as described in Buchacker et al., 2019. The EM image stack was used for segmentation of an AE2 cell, located within a junction of three interalveolar septa. On a three-dimensional representation of the AE2 cell surface, apical portions of the plasma membrane are shown in light green and basolateral portions that are attached to the epithelial basement membrane are shown in dark green. Lamellar bodies located below the plasma membrane are shown in yellow. The AE2 cell is, further, shown inserted into a two-dimensional electron microscopic image of the surrounding environment. The AE2 cell shows multipolarity with four apical domains being in contact with three alveolar airspaces (Alv). The arrow points into a pleat filled with protein containing fluid (hypophase). The bottom of the pleat is formed in part by one of the apical domains of the AE2 cell.

resistive pressure drop along the airways and the pressure across the pleural surface (Mead et al., 1970). The latter equals alveolar pressure minus pleural pressure and is known as the elastic recoil pressure because it is countered by inwardly-directed stresses due to fiber elasticity and interfacial surface tension. The fiber network of the lungs comprises three distinct systems (Wagner et al., 2015; Weibel, 2017; Mostaco-Guidolin et al., 2021). Located most centrally is the *axial system*, which enters the lung at the pulmonary hilum and follows the run of the dichotomous branching of the conducting airways. It reaches the acinus with the terminal bronchiole and ends with fibers forming a lattice around the alveolar entrances, thereby providing a boundary for the alveolar duct. In essence, the axial system enters the acinus centrally and wraps the intra-acinar airways, particularly the alveolar ducts. Located most distally is the *peripheral system*, which originates from the pleura and continues into the interlobular septa. Located in between, and linking, the axial and peripheral systems is the delicate *septal fiber system*, which occurs in the thick parts of the blood-gas barrier and interlaces the capillary network. It is less stiff than either the axial or the peripheral fiber system. Thus, the three fiber systems are arranged roughly in series. Surface tension acts along the alveolar septa, thus in parallel with the septal fiber system. Overall, the balance between distending inflation pressure and retracting fiber elasticity and surface tension comprises a self-stabilizing tensegrity structure (Ingber, 2003).

The effect of surface forces on the lung microarchitecture was elucidated with the development of appropriate tissue processing for electron microscopic investigation (Weibel and Gil, 1968; Untersee et al., 1971). Studies employing these techniques revealed that the alveolar space is not dry. Instead, the alveolar epithelium is covered by a thin liquid lining layer. The liquid layer is aqueous with some protein content, harbors macrophages and is coated by a surface layer of phospholipids (Weibel and Gil, 1968; Reifenrath and Zimmermann, 1973). Quantitative electron microscopic investigations of lung parenchyma from rats following chemical-free cryo-fixation demonstrated that the thickness of this liquid lining layer (= hypophase) varies dramatically (Bastacky et al., 1995). On top of the planar, squamous extensions of the AE1 cells the average thickness of the hypophase is 140 nm and the air-liquid interface is close to planar. In the corners of the alveoli, where alveolar walls converge and AE2 cells are located, the hypophase has a height of up to 890 nm and the interface is curved. With the presence of an air-liquid interface, surface tension forces must act in the lungs. The magnitude of lung surface tension, however, is reduced by the presence of the pulmonary surfactant.

Pulmonary surfactant is a mixture of phospholipids, neutral lipids and surfactant-associated proteins. The most essential components of surfactant for reducing surface tension are palmitoylated phospholipids and surfactant proteins B and C (Notter et al., 2002; Schürch et al., 2010; Knudsen et al., 2012; Ruwisch et al., 2020). Most, but not all components of the pulmonary surfactant are stored in specialized, lysosome-derived organelles, the lamellar bodies (Schmiedl et al., 2005; Ochs, 2010). Lamellar bodies are sheathed by a limiting membrane and contain very densely packed biomembranes with an onionskin-like morphology. Upon stimulus, e.g., stretch during a sigh, the limiting membrane fuses with the apical plasma membrane of the AE2 cell and the surfactant is released into the alveolar space (Wirtz and Dobbs, 1990). Here, the content of the lamellar body unfurls and forms a network of membranes termed tubular myelin, characterized by piles of parallel-organized membranes connected by intersecting membrane planes (Lettau et al., 2022). Tubular myelin or, alternatively, sub-interfacial stacks of surfactant bilayers form reservoirs of active surfactant within the alveolar space (Schürch et al., 2001; Bachofen et al., 2005; Dietl and Haller, 2005). The reduction in surface tension that surfactant achieves is dramatic, particularly with near-maximal interfacial surfactant density at end-expiration. With increasing lung volume towards total lung capacity (TLC) surface tension increases due to reduced interfacial surfactant density, but that density is still high. At about 80% TLC, interfacial surfactant is still in the liquid-condensed state, such that surface tension is still relatively low (Schürch et al., 1976; Nag et al., 1998; Nguyen and Perlman, 2020). Alveolar surface tension cannot, presently, be determined *in vivo* but has been determined *in situ* in excised lungs by two micropuncture-based methods—one employing deposition of surface tension-sensitive liquid droplets and one combining servo-nulling measurement of alveolar liquid phase pressure, confocal microscopic determination of interfacial radius, and application of the Laplace relation (Schürch, 1982; Kharge et al., 2014). At a given lung inflation pressure, these methods showed that surface tension is the same between different-sized alveoli and between aerated and flooded alveoli. Neither method is capable of revealing if surface tension varies between the planar interface, along most of the alveolar septum, and the curved interface in the alveolar corners. Regardless of whether there is intra-alveolar variation in surface tension, however, the intra-alveolar variation in interfacial curvature has profound effects.

The physiological effects of surface tension on the microarchitecture of lung parenchyma were first seen more than 40 years ago by Gil and coworkers. Comparison of air- and saline-filled lungs fixed by vascular perfusion at the same lung volumes (given as percentage of TLC) revealed dramatic differences in the microscopic appearance of the acinar microarchitecture (Gil et al., 1979). The pressures needed to achieve a defined lung volume were much lower in the saline compared to air-filled lungs. At low volume in saline-filled lungs, in the absence of surface tension, septal capillaries bulge into the lumen such that septa have an uneven surface area and markedly varied thickness along their length. The central splines of many septa follow an undulating, unconstrained, path. At high volume above 80% TLC, the capillaries remain bulging but forces transmitted through the septa tend to straighten their central splines. In the normal air-filled lung surface tension is present and the tendency of surface tension is to minimize interfacial surface area. Even the low surface tension present at low lung volume has a marked effect. Surface tension reduces interfacial surface area by flattening capillaries and, through imposition of septal pleating, reducing septal undulation. Septal pleats are small folds in the alveolar septa where the adjacent epithelial surfaces are in contact with each other instead of exposed to air and are detailed in section 3.3, below. But surface tension effects vary along the lengths of the septa. Along most of the septal length, where the air-liquid interface is planar, there is not, according to the Laplace relation, any pressure drop across the interface. With full pulmonary inflation (100% TLC), capillaries are flattened and no pleats are present; there is a single layer of capillaries and the septal spline is linear, suggesting it is in tension. In the alveolar corners, the air-liquid interface is curved such that, according to Laplace, there is a pressure drop across the interface and liquid pressure is less than air pressure. With a lung inflation pressure of 15 cmH_2O, corner liquid pressure was measured and found to be a mere 2 cmH_2O (Kharge et al., 2014). With reduced liquid pressure acting on the septal tissue, capillaries remain patent. Further, the lower liquid pressure in the alveolar corners may draw septal tissue toward the corners and be responsible for septal pleating that is observed at septal junctions. Consequently, in the alveolar corners, there are piles of well-perfused capillaries (Figure 3). At high lung volumes, along most of the septal length, capillaries are further flattened into a slit-like morphology but at the alveolar corners capillaries are still patent. Also, with increasing lung volume there is progressive unfolding of septal pleats and, as detailed below, the septal fibers bear more stress. Overall, the effect of surface tension is to straighten the septal spline; compress the septal tissue—albeit less so near alveolar corners such that septal thickness tends to increase toward septal endpoints; and smooth the septal surface. The liquid lining layer, which fills crevices and has a variable height along the full lengths of the septa (Bastacky et al., 1995), also contributes to the smoothing of the septal surface. The distribution and the mean thickness of the hypophase appear to be subject to dynamic changes during breathing and depend on the lung volume (Ruhl et al., 2019). Since the hypophase, including intra-alveolar surfactant, plays a central role with regard to the pulmonary microarchitecture, studies designed to investigate aspects of the acinar micromechanics need to be performed in air-filled lungs under well controlled conditions, e.g., pressures at the airway opening, lung volume history, and pulmonary vascular pressure.

It is well accepted that low surface tension at low lung volume prevents destabilization of the gas-exchanging surface area (Bachofen and Schürch, 2001). Although an alternative analysis suggests that low surface tension may not be a prerequisite for end-expiratory lung stability (Reifenrath, 1975), the importance of low surface tension is supported by the observation that increased surface tension destabilizes the gas-exchanging surface area, particularly at low lung volumes where the alveoli are small and interfacial radius is low (Mercer et al., 1987; Knudsen et al., 2018; Smith et al., 2020). Destabilization could be attributable to the curved interface in the alveolar corner. According to the Laplace relation, a smaller than normal interfacial radius in the corner of the alveolus would lead to a lower than normal liquid pressure in the corner which should cause more septal folding than normal in the corner. One could imagine that as septa crumple more than usual at their ends, septal length would decrease, the low corner liquid pressure would be translated toward the centers of the septa and positive feedback could lead to alveolar collapse.

At the acinar level, an important effect of lung inflation is to increase alveolar duct volume relative to alveolar volume. Consequently, inflation increases alveolar surface area less than it would if alveolar volume increased proportionately with lung volume (Bachofen et al., 1987; Mercer et al., 1987). Based on the organization of the lung fiber system and the reported morphological features of air- and saline-filled lungs (Gil and Weibel, 1972; Gil et al., 1979; Bachofen et al., 1987), Wilson and Bachofen created a much-appreciated model that explained the mechanical interdependence between alveolar duct and alveoli (Wilson and Bachofen, 1982). The model is valid for lung volumes up to 80% of TLC, which include the physiological range of spontaneous breathing (Wilson and Bachofen, 1982). Recalling that the three lung fiber systems are arranged roughly in series, they can be thought of as three springs connected in series. Applying an inflation pressure to the lung is analogous to applying a constant tension to the three springs, and causes greatest distension of the least-stiff spring. Thus, in healthy lungs at low volume, the stiff axial fibers keep the duct relatively small while, due to distension of

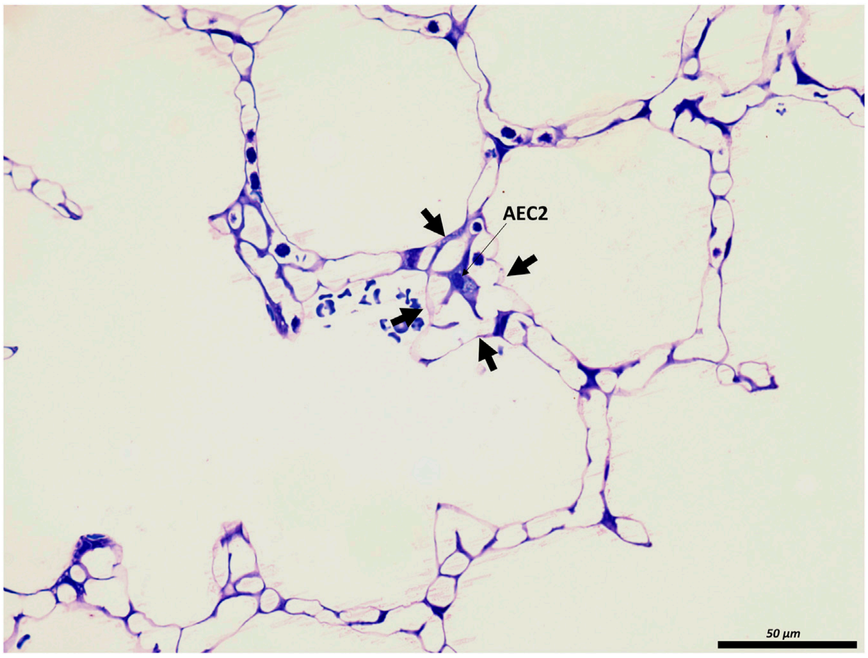

FIGURE 3
The junction of inter-alveolar septa: A healthy rat lung was fixed *in vivo* by vascular perfusion *via* the vena cava caudalis at an airway opening pressure of 10 cmH_2O on expiration after two recruitment maneuvers (3 s pause at 30 cmH_2O) (Knudsen et al., 2018). In the middle of the septal junction (arrows), an alveolar epithelial type II cell (AEC2) is present. While most of the interalveolar septa contain a single layer of the alveolar capillary network, there appear to be two layers at this junction surrounding the AEC2, most likely due to pleating that causes piling up of the interalveolar septa.

compliant septal fibers, the alveoli are stretched relatively large. But the septal fiber system serves largely as a support for the alveolar liquid lining layer and its associated surface tension, such that the stiffness of the septal system is affected by surface tension (Wilson and Bachofen, 1982). Lung inflation reduces interfacial surfactant which increases surface tension thus increasing the stiffness of the septa relative to that of the axial fibers. It is due to the increase in surface tension, thus in septal stiffness, that inflation shifts the duct/alveolus border outward, enlarging ducts and diminishing alveoli.

Under unphysiological conditions, surface tension effects can be more pronounced. In saline-filled lungs, Wilson and Bachofen showed that in the absence of surface tension, septa were both undulating and, due to low stiffness, expanded as the relatively stiff axial fiber system shifted the duct/alveolus border inward and reduced duct caliber. Thus, alveolar surface area has been shown by design-based stereology to be greater in saline-filled lungs lacking surface tension than in air-filled lungs with surface tension acting along the septa (Gil et al., 1979). Following removal of surfactant by lavage the high surface tension, by increasing septal stiffness relative to axial fiber stiffness, caused the duct/alveolus border to move outward such that ducts were expanded and alveoli, with essentially maximally retracted septa, very small. Accordingly, high surface tension has been shown by design-based stereology to reduce alveolar surface area (Gil et al., 1979; Bachofen and Schürch, 2001; Lutz et al., 2015; Lopez-Rodriguez et al., 2016; Knudsen et al., 2018). In lung diseases such as fibrosis and the acute respiratory distress syndrome, surface tension is elevated (Günther et al., 1999; Lutz et al., 2015; Lopez-Rodriguez et al., 2016; Nguyen and Perlman, 2020; Smith et al., 2020). Sufficiently high surface tension can dominate the axial fiber system and cause alveolar collapse and microatelectases as well as pulmonary edema (Nieman et al., 1981; Knudsen et al., 2018; Smith et al., 2020).

2.1 Acinar micromechanics and the glycocalyx

Recent studies draw the attention to a further structure found in the alveolar hypophase that may also influence acinar micromechanics, namely the alveolar epithelial glycocalyx observed also in co-localization with freshly secreted lamellar body-like structures and tubular myelin (Ochs et al., 2020). The epithelial glycocalyx consists of glycoproteins, proteoglycans and hyaluronan. While the proteoglycans and glycoproteins have a transmembrane domain, hyaluronan is anchored at the apical plasma membrane of the alveolar epithelial cells *via* the CD44 receptor. Targeted destruction of the alveolar epithelial glycocalyx by intratracheal heparinase in an animal model provided evidence that the interaction between surfactant and components of the glycocalyx are of relevance for the proper function of the pulmonary surfactant. The loss of the integrity of the glycocalyx led to a reduction in the surface tension lowering capacity of pulmonary surfactant as assessed *in vitro*. While simultaneous adsorption of surfactant and potential surface-tension-raising contaminants can cause artifacts during *in vitro* testing (Holm et al., 1988; Holm et al., 1999; Nguyen and Perlman, 2020; Perlman, 2020), elevated surface tension in this study was supported by a finding of decreased pulmonary compliance and the observation of instability of distal airspaces at the light microscopic level (Rizzo et al., 2022). Thus, glycocalyx degradation products should be added to the list of substances (Nguyen and Perlman, 2020) purported to raise surface tension in lung injury. Clinical investigations accentuate the relevance of glycocalyx degradation. In samples collected in filters integrated in the expiratory limb of the respirator from acute respiratory distress syndrome (ARDS) patients, Rizzo and colleagues detected increased concentrations of cleavage products of the alveolar epithelial glycocalyx such as heparan or chondroitin sulfate, particularly in patients with ARDS caused by direct lung injury. Aside from a role with regard to proper surfactant function and thus acinar micromechanics, the glycocalyx has also been suggested to be involved in regulation of the volume and viscous properties of the hypophase (Ochs et al., 2020), and mediation of inflammatory processes and regeneration (Jiang et al., 2005; Liang et al., 2016).

2.2 Effects of aging on the acinar microarchitecture

Alterations in the fiber network and surfactant system might be responsible for aging effects on the acinar microarchitecture and mechanics. Using hyperpolarized ^{3}He gas and magnetic resonance imaging (MRI) quantitative morphological data of the pulmonary acini can be calculated in living individuals based on the model of the pulmonary acinus published by Haefeli-Bleuer and Weibel (Haefeli-Bleuer and Weibel, 1988; Osmanagic et al., 2010). In healthy non-smoking humans the diameters of the alveolar duct lumen have been shown to increase while the lengths of the interalveolar septa decrease, resulting in shallowing of the alveoli with age (Quirk et al., 2016). These finding are also referred to as ductectasia. Similar observations have been reported in aging mouse and rat lungs (Mizuuchi et al., 1994; Schulte et al., 2019). Schulte et al. described a marked increase in alveolar duct volume in 18 months compared to 12 months old mice while Ruwisch et al. (2020) observed considerable ductektasia already in much younger mice suffering from surfactant protein C (SP-C) deficiency. Quantitative data showed age dependent reorganization of the collagen and elastin fibers within the interalveolar septa such as an increase it the width of fibers combined with enlarged alveolar entrance rings, and an altered distribution within the interalveolar septa (Sobin et al., 1988). Based on computational modelling these alterations in the architecture of the fiber system can explain ductectasia, and the resulting alterations in the geometric configuration can explain the reduction in the pulmonary elastic recoil pressure due to reduced elastance of alveolar entrance rings even in the presence of stiffer septa (Subramaniam et al., 2017). The mechanisms resulting in a reorganization of the fiber system are not clear but it has been suggested to reflect adaptation. In old mouse lungs senescence markers are above all upregulated in AE2 cells and lipofibroblasts (Angelidis et al., 2019; Schiller et al., 2019). These findings are linked with data based on captive bubble surfactometer measurements providing evidence that alveolar surfactant from aged mice has an impaired ability to reduce surface tension (Yazicioglu et al., 2020). As outlined above, higher surface tension results in increased stiffness of alveolar septa, which causes septa to retract and increases septal pleating. The increased septal retraction, which reduces septal tensile load, might induce adaptation of the fiber network, and finally result in ducectasia. The observation that in SP-C knockout mice ductactasia occurs much earlier in life and before AE2 cell senescence supports this notion (Ruwisch et al., 2020).

3 Respiration related deformation of the lung parenchyma: Visualization and quantification

The act of breathing requires that physical forces are repetitively transmitted to the lung structures (Mead et al., 1970). These forces result in deformations, which are quantified in one, two or three-dimensions, e.g., in length, area or volume by referencing to a lower deformation state. This relative deformation is similar but not identical to strain, since the latter is referenced to an unstressed condition, which corresponds to the lung volume at zero transpulmonary pressure. The three-dimensional relative volumetric deformation of the lung is accordingly the ratio of end-inspiratory to end-expiratory lung volume (Vlahakis and Hubmayr, 2005). The stresses acting on the respiratory system result from a pressure differential between the alveolar opening and the pleural surface also referred to as the transpulmonary pressure (Mead, 1961; Mead et al., 1970; Loring et al., 2016). Forces acting on lung parenchyma are a consequence of the elastic recoil pressure. The elastic recoil pressure is caused by the surface tension at the air liquid-interface and the properties of the pulmonary fiber system consisting of elastic fibers and collagen fibrils. It has been estimated that at low lung volumes two-third of the elastic recoil pressure is due to surface tension at the air-liquid interface (Stamenović, 1990). The fiber system transmits the distending inflation pressure during inspiration to the interalveolar septa. The elastic fibers have a linear stress-strain relationship over a wide range of linear deformation so that even after doubling their baseline length the elasticity remains consistent. Elastic fibers therefore create tissue tension at low and high lung volumes. On the other hand, the collagen fibrils within the interalveolar septa have a ‘curly’ configuration at low lung volumes. With pulmonary inflation these fibrils are progressively straightened and become stress bearing, bringing their rigid mechanical properties into play to limit distension. Therefore, collagen fibrils become stress bearing at larger lung volumes, e.g., above 80% of TLC (Suki et al., 2005; Bou Jawde et al., 2020). A similar micromechanical behavior has been proposed for the BM located in the blood-gas barrier (Maina and West, 2005). Among others, the BM is composed of type IV collagen, proteoglycans, laminin, integrins and other anchoring fibers involved in producing cell-matrix junctions, e.g., with the alveolar epithelial cells. The type IV collagen located within the lamina densa appears to be of high relevance to the micromechanical properties of the BM. Here, it has been suggested that dimers of type IV collagen molecules form a network of rhombic meshes with an edge length of approximately 800 nm (Timpl et al., 1981). This network of type IV collagen dimers allows some degree of deformation as indicated by changes of the surface area of the BM measured at different lung volumes which shows two-dimensional strain (Tschumperlin and Margulies, 1999). At the same time, the BM has given proof of its resilience against stress failure in several studies. While injurious mechanical ventilation destroys the alveolar epithelial cells in rodent lungs (the AE1 much more than the AE2 cells!), the ultrastructure of the underlying BM remains preserved (Dreyfuss and Saumon, 1998; Albert et al., 2020). Notably, at low lung volumes, the blood-gas barrier including the epithelial BM creates pleats and these pleats are recruited with inspiration (see below) so that the BM together with the attached epithelial cells become planar. Hence, it seems reasonable that BM becomes stress bearing at larger lung volumes and contributes to lung mechanical properties measured at the organ scale similarly to the collagen fibrils within the interalveolar septa discussed above (Maina and West, 2005). An intact surfactant system and the elasticity of the scaffold of the interalveolar septa protect the cellular components of the blood-gas barrier, above all the AE1 cells, from injurious strain during tidal ventilation. These counterbalanced forces keep the cells from bearing substantial stress within the physiological range of breathing (Wilson and Bachofen, 1982). The observation that the mechanical properties of the lung hardly change during the process of de-cellularization supports this notion (Nonaka et al., 2014).

It is well known that there is some heterogeneity in ventilation, and therefore strain, within the human lung at macroscopic scale, a feature that has recently been observed in mice and rats as well (Arora et al., 2021). At the microscopic level such as within an acinus, however, heterogeneity, appears to be avoided. Because neighboring alveoli are divided by shared septa and the network of stress-transferring structures running throughout the interalveolar septa interconnects numerous alveoli, the mechanical properties of the alveoli are interdependent. Impaired mechanics, e.g. due to alveolar flooding of one alveolus, have an impact on the mechanics of adjacent alveoli and deformation/stretching of those bounding septa creates a stress concentration (Perlman et al., 2011). In a healthy lung, however, the pulmonary surfactant system not only reduces but also harmonizes surface tension in the alveoli, so that alveoli of different sizes can co-exist and stress concentration is avoided (Schürch, 1982; Schirrmann et al., 2010). Low volume mechanical ventilation or spontaneous breathing in presence of stress concentrations, such as microatelectases or flooded alveoli, results in injury of the blood-gas barrier and degradation of lung mechanics, despite no increase in strain at the organ level (Wu et al., 2014; Albert et al., 2020; Krischer et al., 2021; Bachmann et al., 2022). High tidal volume ventilation with low positive end-expiratory pressure produces progressive ventilation-induced lung injury with severe damage of the blood-gas barrier in mice (Hamlington et al., 2018). Analysis of the progression of this ventilation-induced injury reveals that cellular injury initially forms in quasi-random locations. Continued ventilation causes those initial points of injury to spread locally so that the number of damaged cells in an “injury cluster” grows with continued ventilation, with the initially injured lung regions acting as seeding point. As such, injury occurs predominantly at the interface between injured and healthy lung regions and this can be explained by stress concentration and alveolar interdependence (Cereda et al., 2017; Mattson et al., 2022).

In the healthy lung, the biomechanical properties of the interalveolar septa are relatively homogenous so that ventilation (strain) and parenchymal stress are also quite homogenous, preventing stress concentrations and subsequent stress failure of the delicate structures in the blood-gas barrier (Mead et al., 1970; Makiyama et al., 2014; Albert et al., 2019; Perlman, 2020). Given that lung parenchyma of an average human must withstand approximately 10^9 low- and 10^7 higher-volume (e.g. exercise, deep sighs) breathing cycles it becomes obvious that the avoidance of local stress concentration is of high importance (Fredberg and Kamm, 2006).

Generally, stresses in the acinus result in deformation of the acinar airways and interalveolar septa. The mechanisms of tissue deformation that accompany ductal and alveolar airspace volume changes are quite different due to the structural arrangement of the surrounding tissues. Volumetric strain within the alveolar duct is linked with deformation of the mesh-like network of alveolar entrance rings forming its boundary, while strain of alveoli requires adaptation of the interalveolar septa. Within the interalveolar septa, strains are imposed on both the lumen of alveolar capillary network and the blood-gas barrier. The cellular components of the blood-gas barrier are particularly vulnerable to injury caused by excessive deformation. A two-dimensional cyclic strain of 25% applied to alveolar epithelial cells has been shown to induce cellular injury and apoptosis in *in vitro* model systems, emphasizing the vulnerability of these cells and thus the need to protect them (Tschumperlin et al., 2000; Dolinay et al., 2017).

Recent advances in clinical imaging now allow visualization of some aspects of the spatial heterogeneity discussed above. For instance, dual energy computed tomography has been applied to investigate regional ventilation (volumetric strain) within the lung parenchyma in spontaneously breathing patients suffering from idiopathic pulmonary fibrosis (IPF), a progressive, scarring lung disease with limited prognosis. Scharm and co-workers used end-inspiratory and end-expiratory scans to quantify regional volume changes (Scharm et al., 2021). IPF is characterized by an increased heterogeneity of regional ventilation compared to healthy subjects. The ventilation heterogeneity is highly correlated with future decline in lung function, and the regions with increased strain are at the highest risk for fibrotic remodeling (Scharm et al., 2022). In other words, abnormalities in regional ventilation precede fibrotic remodeling so that it is tempting to hypothesize that excessive strain of fine lung parenchyma (i.e. abnormal acinar micromechanics) is a trigger for the formation of scars and degradation of lung function (Knudsen et al., 2017; Albert et al., 2019), a concept which has recently been supported in mice (Beike et al., 2019; Wu et al., 2020). Nevertheless, the exact abnormalities at the micromechanical level responsible for these clinical imaging-based observations remain unclear.

To investigate all aspects of acinar micromechanics during spontaneous breathing or invasive mechanical ventilation, real-time visualization of the affected structures in three dimensions is desirable. Intravital microscopy has been applied to study the dynamics of subpleural alveoli, providing valuable insights into to changes in alveolar dimensions, capillary network perfusion, and oxygenation during mechanical ventilation (Matuszak et al., 2020; Masterson et al., 2021). Under physiological conditions, changes in alveolar volume occurs in synchrony with the respirator (Tabuchi et al., 2016) and the alveolar volume changes are comparably small so that alveolar volumetric strains are low with physiological tidal volumes (Schiller et al., 2003). Linear strain of alveoli in the volume range of quiet spontaneous breathing has also been estimated using lungs fixed at different lung volumes and quantitative microscopy. These strains range from 4% (Mercer et al., 1987; Tschumperlin and Margulies, 1999; Roan and Waters, 2011) to 10% (Gil et al., 1979). Imaging the same alveoli at different airway pressures with confocal microscopy in an *ex vivo* model-system resulted in similar findings: increasing pressure from 5 to 10 or 15 cmH_2O was linked with an increase in alveolar perimeter of less than 5 or 10%, respectively. Moreover, alveoli expanded non-uniformly with septal surface covered by AE1 cells deforming more than that covered by AE2 cells (Perlman and Bhattacharya, 2007), an observation supported by design-based stereological investigations at the electron microscopic level during deflation from 10 to 2 cmH_2O (Ruhl et al., 2019).

However, the penetration depth of intravital microscopy is limited to subpleural alveoli. The relevance of this limitation is highlighted in a recent study that used confocal microscopic imaging of cleared lungs to show that the subpleural parenchymal architecture differs from other regions of the lung in diverse species (including humans) (Mitzner et al., 2020). The alveolar ducts run perpendicular to visceral pleural surface so that the region immediately beneath the pleura contains a single layer of alveoli with boundaries and numbers of neighboring alveoli that significantly differ from regions deeper in the lung. Hence, the micromechanics of subpleural alveoli are likely to differ from other regions.

Micro-computed tomography or synchrotron-based tomography have sufficient resolution to resolve interalveolar septa in more central regions of the lungs. Accordingly, Sera and co-workers imaged mouse lungs repetitively at different degrees of quasi-static inflation with synchrotron refraction enhanced computed tomography to describe a complex, accordion-like expansion of the acini. Moreover, at lower lung volumes up to an airway opening pressure of 8 cmH_2O, strain appeared to be larger in the alveolar ducts than in the alveoli. At higher lung volumes both of these compartments are subject to approximately equal deformations (Sera et al., 2013). Similar results have been reported based on three-dimensional reconstructions of alveoli using serial sections from lungs fixed at different lung volumes during expiration (Mercer et al., 1987). Those studies determined acinar micromechanical behavior under quasi-static conditions. However, due to the viscoelastic properties of the parenchyma it is likely that under physiological, dynamic breathing the micromechanical properties are different.

Advances in imaging methodology including tracking X-ray tomography (Chang et al., 2015) and synchrotron-based, phase-contrast micro computed tomography (Bayat et al., 2022) now allow study of dynamic processes within the acinus. Chang and co-workers tracked profiles of alveoli in different lung regions of mice during spontaneous breathing by X-ray tomography. Inflation was heterogeneous, resulting in a dynamic linear septal strain of 5.7% in apical and 8.7% in basal lung region. Overall, approximately 1/3rd of tidal volume was delivered to the alveolar compartment and 2/3rd to alveolar ducts (Chang et al., 2015). These estimations align with the findings under quasi-static conditions mentioned above (Sera et al., 2013). Cercos-Pita and colleagues used synchrotron-based dual energy micro computed tomography to image acinar airspaces of mechanically ventilated rats with a high temporal resolution of 78 three-dimensional datasets per breath. At a tidal volume of 8 ml/kg (PEEP = 6 cmH_2O, peak inspiratory pressure = 12 cmH_2O) the relationship between acinar volume (V_A) and surface area (S_A) given by the formula $S_A = k\ V_A{}^n$ suggests distension of alveoli as the predominant mechanism of the acini to accommodate to volume changes (Cercos-Pita et al., 2022). This discrepancy might be explained by differences in the protocols, e.g. investigating spontaneously breathing animals or mechanically ventilated animals with higher PEEP. Although synchrotron-based micro computed tomography is a very powerful imaging approach to investigate acinar micromechanics, access to the required equipment is limited.

Imaging techniques with a resolution at the light microscopic level are appropriate to investigate alterations in alveolar and ductal airspaces. However, the different compartments of the interalveolar septa are generally beyond the resolution of light microscopy or x-ray-based imaging modalities. During the respiratory cycle, those components of the interalveolar septa have to adapt to volume changes within the airspaces. Based on investigations including morphometry using light and transmission electron microscopy of lungs fixed at different lung volumes in the expiratory limb of a pressure-volume loop, investigators suggested several adaptive mechanisms of alveoli and subsequently of the interalveolar septa. These include 1) recruitment and derecruitment of complete alveoli, 2) recruitment and derecruitment of parts of alveoli by folding and unfolding of pleats of the interalveolar septa, 3) balloon-like change in alveolar size by stretching and de-stretching of the septal tissue (including the blood-gas barrier) and 4) alteration in the alveolar shape without stretching/de-stretching or recruitment/derecruitment of folds (Gil et al., 1979; Wilson and Bachofen, 1982; Bachofen et al., 1987; Knudsen and Ochs, 2018).

Aside from alveolar recruitment and derecruitment, which has been observed directly by investigators using *in vivo*/intravital microscopy, particularly in acutely injured lungs (Carney et al., 1999; Schiller et al., 2001; Halter et al., 2007; Pavone et al., 2007), it is difficult to visualize the other mechanisms using real-time imaging. Those mechanisms predominantly involving the blood-gas barrier, such as folding/unfolding or de-stretching/stretching, require electron microscopic resolution to identify the AE1 cells and the underlying BM (Bachofen et al., 1987; Tschumperlin and Margulies, 1999; Ruhl et al., 2019). In order to quantify the contribution of the different mechanisms to the adaptation of alveoli and their walls to changes in lung volumes, quantitative morphology based on design-based stereology and electron microscopy is the method of choice (Hsia et al., 2010; Ochs and Schipke, 2021). The stereological parameters useful for quantification of alveolar recruitment and derecruitment, recruitment and derecruitment of pleats, and stretching of the BM are summarized in the Table and will be introduced in more detail in the following sections.

3.1 The concept of design-based stereology

Design-based or unbiased stereology is founded on stochastic geometry. It derives three-dimensional data from two-dimensional sections and can be applied to any imaging modality (Knudsen et al., 2021). This section provides a brief introduction into the concepts of design-based stereology. Afterwards, we will summarize the available literature in which design-based stereology has been used to investigate acinar micromechanics with a focus on the septa.

In order to analyze the fine three-dimensional structure of biological samples, nearly two-dimensional sections are classically visualized using microscopy. This approach holds some problems because the structures are three-dimensional and one dimension is lost when the investigation is performed in two-dimensions. A second problem is the fact that the nearly two-dimensional sections represent only a small fraction of the entire organ. Hence, the observations might not be representative. A third problem is called the "reference trap." Consider the case where the lungs of two study groups are to be compared with each other. One study group suffers from high surface tension which results in an instability of alveolar airspaces so that microatelectases occur, there is less air inside the lungs, and lung volumes are 1/3 smaller. Light microscopic quantification reveals that 35% and 25% of lung volumes are comprised of interalveolar septa in the high surface tension and control groups, respectively. This might lead to the erroneous conclusion that there is more septal tissue in the group suffering from high surface tension, which is not the case since the lung volumes (the *reference space*) are different. Multiplication of the volume fraction of interalveolar septa (35% and 25%, respectively) with the associated lung volumes yields the absolute volumes of interalveolar septa per lung and reveals whether or not a difference exists. To avoid this reference trap, the reference volumes must be determined and quantitative structural data need to be related to the reference volume (Tschanz et al., 2014).

Design-based stereology, which is predicated on mathematical principles, is an efficient solution for the problems mentioned above. It does not make any assumptions considering the orientation, size, spatial distribution or shape of the structures under study. Hans Elias, who pioneered the development of stereology in biomedical research, expressed the following definition for stereology: "extrapolation from two to three-dimensional space, or three-dimensional interpretation of two-dimensional images, by methods of geometric probability" (Elias, 1971). Although two-dimensional images are used, stereology provides three-dimensional, representative and unbiased data of structures of interest. To get three-dimensional information from two-dimensional images, geometric test-systems are randomly superimposed on randomly sampled images and interact with the structures of interest (e.g., the surface area of the BM) in a stochastic way. The dimension of the structure of interest and the dimension of the test-system always sum up to 3. For example, the surface area of the epithelial BM (a two-dimensional parameter) is assessed with a test system comprised of one-dimensional lines. Here, the test-lines are projected onto randomly selected images and interact with the surface of the BM by creating intersections. On the two-dimensional sections, the surface area of any structure has lost one dimension so that a surface appears as a line. The number of counted intersections between the test-lines and surface boundary is a stochastic value and may have slightly different values each time the process is repeated due to the randomization of images and line placements. Nevertheless, the expected number of line-surface intersections is directly proportional to the length of the test-line (which is known) and the density of BM surface area per volume of the reference space (e.g., the volume of the lung). The same rules apply to determination of volumes (e.g., the volume of interalveolar septa), lengths (e.g., the length of blood vessels), and numbers (e.g., the number of AT2 cells) which require test-points, test-areas and test-volumes for counting, respectively (Figure 4). Practical "guidelines" how to use design-based stereology in lung research have been reviewed in several publications, e.g., (Mühlfeld et al., 2013; Tschanz et al., 2014; Mühlfeld et al., 2015).

To guarantee that stereological data are unbiased the tissue processing and sampling steps are critical. Every part of the organ must have the same chance of being investigated. For example, quantification of the number of alveoli per lung requires that each alveolus, independent of its features such as size or orientation, must have the same probability of being counted. An unbiased stereological design achieves this requirement by randomization at each step of the study, starting with study subject and ending with the projections of the test-systems on the randomized fields of view for counting. Several methods for randomization of tissue samples have been published (Ochs and Schipke, 2021). A further source of bias is changes in tissue dimensions during the processing steps for microscopy. In particular, paraffin embedding results in large, unpredictable, and heterogeneous shrinkage (up to 50%–60% by volume). Osmification and embedding in plastic (e.g. glycol methacrylate or epoxy resin) is preferred for quantification of lung structure because this approach prevents tissue shrinkage (Schneider and Ochs, 2014). When studying acinar micromechanics by comparing data from lungs fixed at different degrees of lung inflation heterogenous shrinkage in critical because the *in vivo* dimensions of the structures must be preserved. A limitation of quantitative morphology including design-based stereology is that there is no optimal fixation technique, e.g., a gold standard available to preserve the structure in a way that reflects all aspects of the *in vivo* architecture. If, for example, perfusion fixation is used to preserve the airspace morphometry then the dimensions of the vascular structures are dependent on the perfusion pressure.

Nevertheless, to obtain valid data from stereological investigation the fixation technique and the fixation solution can be optimized for the structures of interest. As pointed out earlier, surface tension and the elastic fiber system are important contributors to micromechanical behavior of the acini. Therefore, when studying the dimensions of the airspace and interalveolar septa the lungs need to be preserved in a way that reliably fixes the elastic fibers and preserves the shaping effect of surface tension on the acinar microarchitecture. Moreover, fixation needs to be performed at an airway opening pressure which is of relevance for the given research question, e.g., within the range of transpulmonary pressures used for mechanical ventilation. This goal can be achieved by vascular perfusion, which preserves the hypophase including the intra-alveolar surfactant. In their guidelines paper, Hsia and co-workers suggested fixing the lungs by vascular perfusion with glutaraldehyde, osmium tetroxide (OsO_4), and ethanol to maintain the surface liquid layer and lung volume (Bachofen et al., 1982; Hsia et al., 2010). The glutaraldehyde fixes tissue by crosslinking proteins whereby maintaining the ultrastructure for electron microscopic investigation. However, it does not entirely fix the elastic fibers. Thus the remaining elastic recoil might result in volume loss during lung preparation (Oldmixon et al., 1985). The additional perfusion of the pulmonary vasculature with OsO_4 and ethanol fixes the elastic

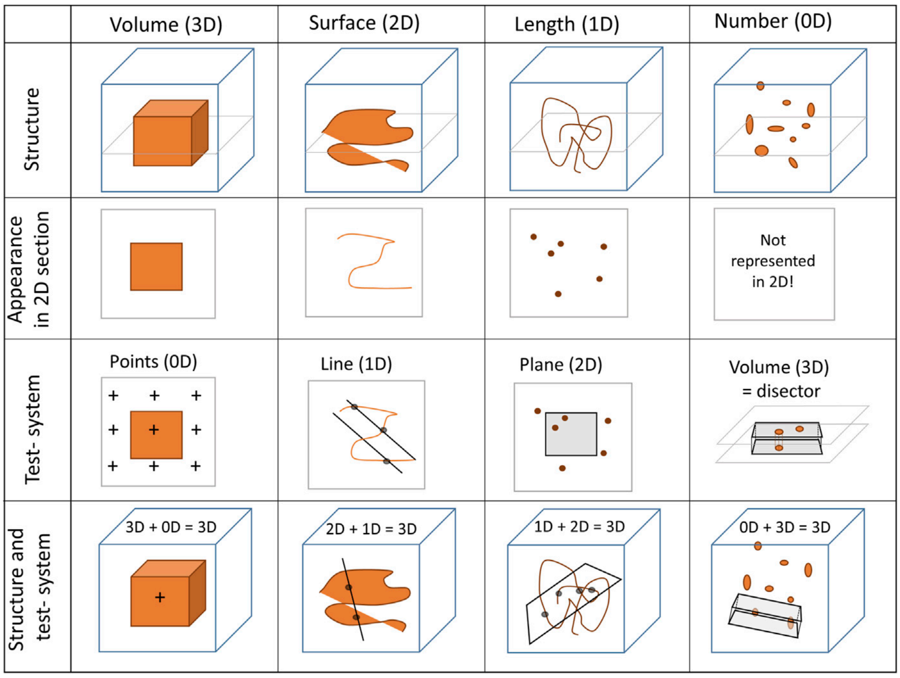

FIGURE 4
Stereological test-systems: On two-dimensional (2D) sections, three-dimensional structures (3D) lose one dimension. Accordingly, a volume appears as an area (2D), a surface area as a line (1D) and a length as a point (0D). The numerical quantity of a structure is a dimensionless (0D) parameter in three-dimensional space. Since a negative dimension is not possible this parameter is not represented on two-dimensional images. Hence, quantity of any structure cannot be determined from single sections based on the principles of stochastic geometry (or any other method)—an unbiased test-volume (3D) generated by a disector is required.

fibers more reliably and thereby stabilizes the lung volume. In most cases the perfusion with OsO_4 is omitted due to the high toxicity and rather small effects of the remaining elastic recoil on lung volume after glutaraldehyde fixation, which has been estimated ≈2% in linear dimensions in rat lungs (Tschumperlin and Margulies, 1999; Knudsen et al., 2018).

Design-based stereology has been employed in several studies to analyze acinar micromechanics using lungs fixed under quasi-static conditions representing different degrees of inflation up to TLC or deflation coming down from TLC (Gil et al., 1979; Bachofen et al., 1987; Knudsen et al., 2018; Smith et al., 2020). The total lung capacity corresponds to a lung volume at transpulmonary pressure of 25–30 cmH_2O. The range of physiological, quiet breathing corresponds to 40%–80% of TLC and is located in the linear portion of the pulmonary pressure-volume curve (Suki et al., 2011). Here, the transpulmonary pressures needed to reach a certain lung volume differ between the inspiratory and expiratory limb. On expiration, the range of transpulmonary pressures to reach 40%–80% TLC is roughly between 3–4 and 8–10 cmH_2O in rats, rabbits and mice (Bachofen et al., 1987; Tschumperlin and Margulies, 1999; Lai and Chou, 2000). Lungs may be fixed either *in vivo* or *ex vivo*, and in both cases careful control of the lung volume is critical. Under *ex vivo* conditions a drop of the lung volume below residual volume must be avoided since this introduces unphysiological conditions (e.g., complete or partial lung collapse) that reflect in lung structure. *Ex vivo*, the airway opening pressure equals the transpulmonary pressure. *In vivo*, however, the calculation of the transpulmonary pressure requires the knowledge of the pleural pressure or a thoracotomy. How the airway opening pressure translates to the transpulmonary pressure in anesthetized mice has been described by Lai and Chou (Lai and Chou, 2000).

3.2 The acinar airspaces: Alveolar and alveolar duct compartment

The acinar airspaces are subject to cyclic volume changes during respiration. In three-dimensional datasets from, e.g., micro computed tomography or synchrotron-based imaging, appropriate image processing protocols can segment acini and compute their surface area and air volume semi-automatically (Vasilescu et al., 2012; Haberthür et al., 2021). These data provide valuable information on deformation when determined at different levels of inflation or (preferably) dynamically during ventilation (Cercos-Pita et al., 2022). Using two-dimensional images, which are oftentimes more readily obtainable, an efficient and easy tool to investigate the dimensions of the acinar airspaces is the determination of chord lengths (= linear intercept length), which are randomized, linear measurements from one boundary of the acinar airspace to the next (Knudsen et al., 2010). Although it is an one-dimensional parameter describing a complex three-dimensional anatomical structure, it can easily be determined with the help of test-lines projected on the randomized fields of view (Figure 5). An advantage is that chord length measurements

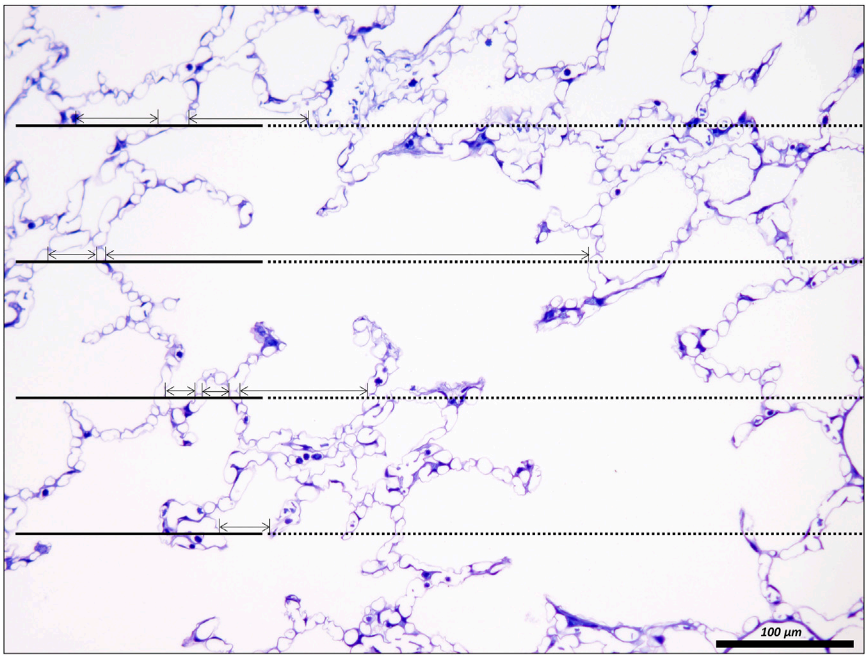

FIGURE 5
Unbiased test-system for measurements of chord length of acinar air spaces. A healthy rat lung was fixed *in vivo* by vascular perfusion *via* the vena cava caudalis at an airway opening pressure of 5 cmH_2O on expiration after two recruitment maneuvers (3 s pause at 30 cmH_2O) (Knudsen et al., 2018). The parameter "chord length" is also known as the linear intercept length. It is based on simple, linear measurements of the dimension of the acinar airspaces from one border to the next. The left side of the randomly sampled image contains four straight line-segments, extended to the right by a dashed line, the so-called guard line. The line segments on the left serve to sample the starting point of the measurements. Each time the line segment intersects an interalveolar septum a measurement is performed from the intersection to the next surface of an interalveolar septum. The direction of the measurement follows the run of the test line and if needed also the dashed guard line. In order to locate the points of measurements exactly the top border of the line segment is used. The arrows label the measurements in this example. Some measurements are performed within an alveolus, others, however, travers *via* the alveolar opening through the alveolar duct airspace to the other side so that these measurements encompass both alveolar and alveolar duct airspaces.

also provide information of lung function in terms of the free path of oxygen to the alveolar wall as well as airspace heterogeneity occurring with different lung volumes. The chord length of acinar airspaces correlates well with the apparent diffusion index of hyperpolarized helium determined with magnetic resonance tomography (MRI) (Woods et al., 2006), an *in vivo* measurement that also gives information on regional mechanics and microarchitecture (Choy et al., 2010). Chord length measurements can be performed with non-destructive imaging including micro computed tomography as well as MRI (Chan et al., 2021). In healthy lungs and early bleomycin-induced acute lung injury fixed *in vivo* at stable airway pressures of 10 or 1 cmH_2O on expiration (Lutz et al., 2015; Knudsen et al., 2018), the distribution plots of chord lengths are comparable at low lung volumes (Figure 6). With higher lung volume the heterogeneity of chord lengths increases, a pattern which is more pronounced in lung injury. The most frequently observed intercept length (peak of the histogram) is shifted to the right (larger lengths) in the injured compared to the healthy lungs. Also, a second peak is unmasked in the injured but not in the healthy lung in the range of 150 µm. Thus, the dimensions of the acinar airspaces become more heterogeneous in injured lungs at higher pressures although at that very early timepoint after bleomycin the injury is subtle. These observations in the distribution of chord lengths might indicate abnormalities in acinar micromechanics resulting in increased ventilatory heterogeneity, a mechanism which has been discussed to contribute to ventilation-induced lung injury (VILI) *via* mechanical stress (Albert et al., 2019; Nieman et al., 2020).

The chord length measurements, however, do not differentiate between alveolar and ductal airspaces. The strain is different in these two compartments and depends on the considered range of lung volumes (Mercer et al., 1987; Sera et al., 2013; Chang et al., 2015; Cercos-Pita et al., 2022). In healthy lungs, at lower lung volumes, volume changes manifest predominantly within the alveolar duct compartment. In contrast, at larger lung volumes with transpulmonary pressure above 8–10 cm investigations suggest that volume changes occur in alveolar and ductal airspaces alike, or even predominantly in the alveolar compartment. During acute lung injury due to VILI or intratracheal bleomycin several studies demonstrated that loss of volume primarily happens in the alveolar compartment while the alveolar duct compartment remains stable or even increases in size (Lutz et al., 2015; Smith et al., 2020). Thus, it makes sense to quantify these two compartments separately to provide a more nuanced description. Figure 7 shows micrographs of healthy lungs fixed *in vivo* by vascular perfusion at airway opening pressures of 1, 5 and 10 cmH_2O on expiration (Knudsen et al., 2018). In order to separate alveolar and ductal airspaces, straight lines are drawn

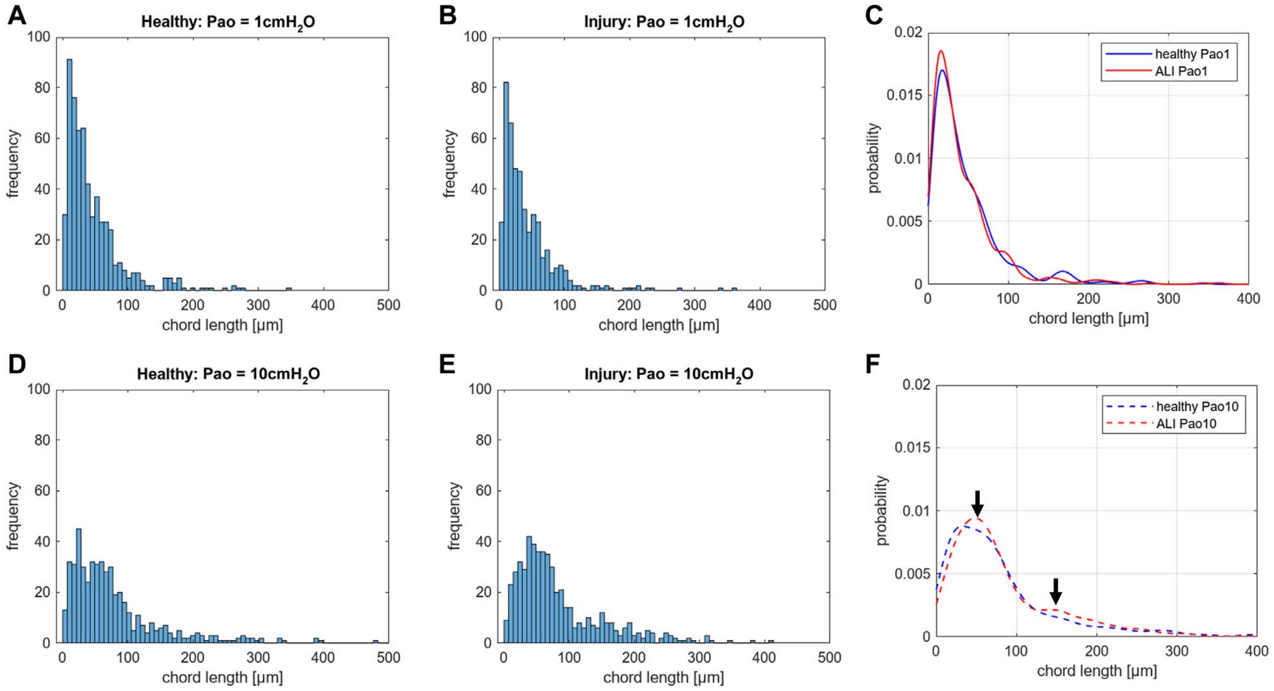

FIGURE 6
Distribution of chord lengths of acinar airspaces: Healthy and injured (ALI) rat lungs were fixed *in vivo* by vascular perfusion *via* the vena cava caudalis at an airway opening pressure (Pao) of either 1 cmH$_2$O on expiration or 10 cmH$_2$O on expiration after two recruitment maneuvers (3 s pause at 30 cmH$_2$O) (Knudsen et al., 2018). The distributions of chord lengths of acinar airspaces are illustrated as histograms and probability based on the Kernel probability distribution function. In both healthy and injured lungs fixation at higher Pao on expiration results in a right shift of the measurements. At Pao = 1 cmH$_2$O, hardly any differences can be identified in the histograms between healthy **(A)** and injured lungs **(B)**. Accordingly, the Kernel probability distribution function shows hardly any differences **(C)**. At Pao = 10 cmH$_2$O, the histograms suggest a right shift of the peak in the injured lung **(E)** compared to the healthy lung **(D)**. The Kernel probability distribution function supports this right shift and indicates a second peak at larger chord length in the range of 150 µm **(F)**. Note, the investigation was performed at a very early time point of bleomycin-induced acute lung injury development at which lung mechanical measurements were scarcely affected. In each group, 500 measurements were performed on randomized fields of view from two lungs.

between the free edges of the interalveolar septa, representing the alveolar entrance rings. The volume fraction of these two compartments in the lung parenchyma is then determined by applying a stereological test system of test points to randomized micrographs and counting points falling on alveolar or alveolar duct airspace. On expiration, the ratio of the volumes fractions of alveolar airspaces (V_A) to alveolar duct airspaces (V_D) is roughly stable in the range of 1.5–2 at airway opening pressures above 10 cmH$_2$0. This indicates that during deflation, and under quasi-static conditions, the absolute volume changes in the alveolar compartment is 1.5–2 times larger than that one found in the alveolar duct compartment keeping the V_A/V_D ratio stable. As pressures drop below 5 cmH$_2$O the V_A/V_D ratio increases up to 2.8–4, so that volume loss is higher in alveolar duct compartment (Mercer et al., 1987; Knudsen et al., 2018).

In lung injury models, the absolute volume of the alveolar duct compartment remains stable or increases so that the V_A/V_D ratio is in general smaller over a wide range of airway opening pressures (Knudsen et al., 2018; Beike et al., 2019; Smith et al., 2020; Rizzo et al., 2022). The expansion of the alveolar ducts can best be explained by the Wilson-Bachofen model: lung injury related high surface tension retracts the alveolar septa so that the duct volume increases (Bachofen et al., 1979; Wilson and Bachofen, 1982).

3.3 Interalveolar septa

Injury-induced alterations in the alveolar compartment often demonstrate strong correlations with abnormalities in lung mechanics. For example, the degree of alveolar collapse highly correlates with the pulmonary system elastance as shown in several studies (Lopez-Rodriguez et al., 2016; Steffen et al., 2017; Beike et al., 2019; Smith et al., 2020). In healthy lungs, the decline in mean alveolar size at low lung volumes correlates highly with an increase in pulmonary system elastance measured at corresponding pressures (Knudsen et al., 2018). The alterations in the alveolar compartment are accompanied by deformations of the interalveolar septa including the recruitment/derecruitment of septal pleats, stretching/un-stretching of the tissue, and shape changes without stretching. These biomechanical modifications of the interalveolar septa all appear to contribute to lung mechanical function in different ways.

3.3.1 Folding and unfolding of septal pleats

Pleats are where parts of the interalveolar septal epithelial surface is not exposed to air. Instead, sections of the blood-gas barrier that form pleats are folded upon themselves, with a thin intervening layer of fluid as shown schematically in Figure 13. The

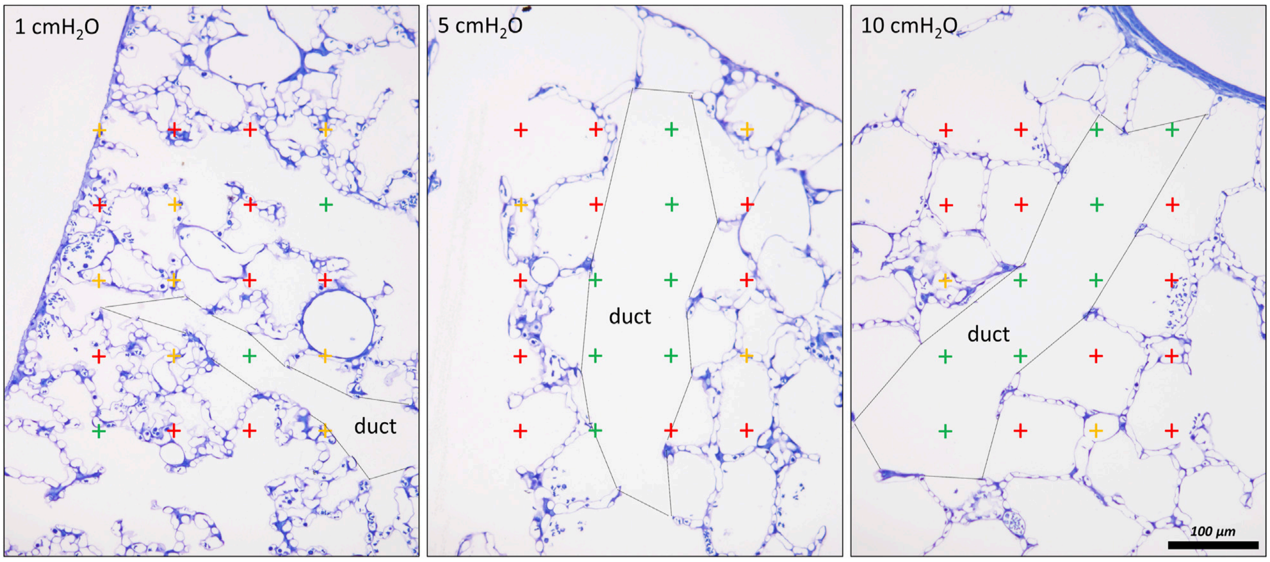

FIGURE 7
Differentiation of acinar airspaces by point counting: Healthy rat lungs were fixed *in vivo* by vascular perfusion *via* the vena cava caudalis at airway opening pressures of either 1, 5, and 10 cmH$_2$O on expiration after two recruitment maneuvers (3 s pause at 30 cmH$_2$O) (Knudsen et al., 2018). In order to determine the volume fractions of tissue, alveolar or alveolar duct airspaces within the lung, test points were superimposed on randomized fields of view. Lungs were treated by immersion in 4% OsO$_4$ before dehydration and embedded in glycol methacrylate to avoid shrinkage/tissue deformation after fixation. The probability of a test point hitting the profile of a structure of interest is directly proportional to the volume fraction of this structure of interest within the reference space. The ratio of test points hitting the structure of interest and the reference space provides the volume fraction of the structure of interest. In the examples, the probability of a test point placed on the randomly sampled fields of view depends on the volume fraction of tissue, alveolar airspace or alveolar duct airspace within the lung. The multiplication of the volume fractions with the lung volume will result in the absolute volumes of tissue, alveolar airspace or alveolar duct airspace per lung. With the goal to separate alveolar duct and alveolar airspace, the entrances into the alveoli were closed by drawing a straight line between the edges of the interalveolar septa. Points hitting alveolar duct airspace (green), alveolar airspace (red) and tissue (yellow) were labelled in the examples. At low Pao, the alveolar ducts were small and the inter-alveolar septa appeared to be at rest with a curvy or in part crumpled surface. At larger Pao, the alveolar ducts widened considerably, the inter-alveolar septa straightened (and appeared to be under tension) and the alveoli became larger. The number of test points hitting alveolar as well as alveolar duct airspaces increased on the expense of the tissue. If the images were representative for the whole organ, one would assume that the volume fractions of tissue deceases with inflation pressure. In order to be representative, however, it is advised to count 100—200 hits on a structure of interest from at least 60 randomized fields of view sampled from at least four randomized sections per organ.

detection of pleats requires electron microscopic resolution. Whether such pleats exist in healthy lungs *in vivo* during spontaneous breathing or mechanical ventilation is not entirely clear. Many studies performed under *ex vivo* as well as *in vivo* conditions describe the existence of pleats in lung tissue fixed by vascular perfusion (Gil and Weibel, 1972; Bachofen et al., 1987; Tschumperlin and Margulies, 1999; Knudsen et al., 2018). Oldmixon and Hoppin investigated lungs fixed *in vivo* at airway opening pressures between 0 and 45 cmH$_2$O with varying volume history. Based on light and electron microscopic imaging they concluded that the occurrence of pleats is governed by the volume history and that pleats were not present as long as the airway opening pressure remained above 2-3 cmH$_2$O (Oldmixon and Hoppin, 1991). Other investigators, however, noted that pleats were not rare events at the electron microscopic level even after recruiting the lungs and performing fixation at pressures from 1 to 25 cm H$_2$O on expiration from TLC (Tschumperlin and Margulies, 1999; Knudsen et al., 2018). Pleats can either involve the blood-gas barrier exclusively or result from folding of the complete interalveolar septum. Pleats exclusively formed by the blood-gas barrier can be found in healthy rat lungs, fixed *in vivo* by vascular perfusion at end-inspiration and end-expiration, and form sickle-shaped invaginations into the underlying capillaries (Figures 8, 9). Pleats involving more than just the blood-gas barrier can predominantly be observed at septal junctions or between the meshwork of the alveolar capillary network (Figures 2, 3, 10). The septum piles up so that a multilayer of the alveolar capillary network is present in a seemingly thickened interalveolar septum. In the depth of such a pleat AE2 cells can often be encountered (Figures 2, 3, 10). Due to the arrangement of the alveolar capillary network in layers, these pleats may also become visible at light microscopic level. The presence of high surface tension is accompanied by more pronounced formation of pleats and piling up of complete septa thereby forming conglomerations of collapsed alveoli, also referred to as microatelectases (Figure 11). In general, the formation of pleats leads to a loss of air-exposed alveolar epithelial surface area.

3.3.2 Recruitment and derecruitment of complete alveoli

In healthy lungs the mechanisms of recruitment and derecruitment of complete alveoli have been suggested from *ex vivo* experiments of isolated and perfused lungs where volumes were allowed to fall below the residual volume so that partial collapse was present before re-expansion and fixation (Gil and Weibel, 1972; Bachofen et al., 1987). Although this scenario is not generally physiologically relevant, it could describe the condition of a

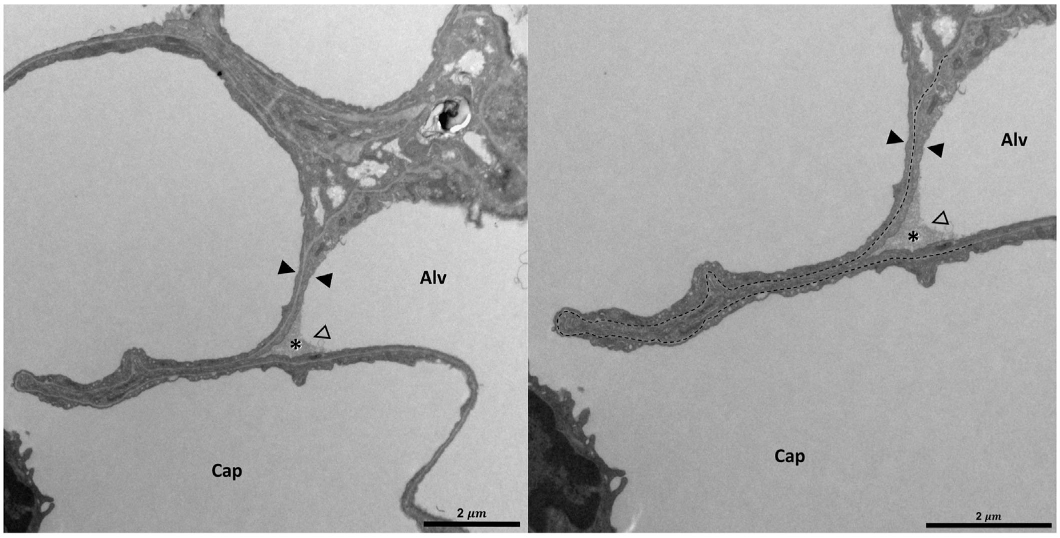

FIGURE 8
Pleating of the blood-gas barrier: A healthy rat lung was fixed *in vivo* by vascular perfusion *via* the vena cava caudalis at an airway opening pressure of 5 cmH_2O on expiration after two recruitment maneuvers (3 s pause at 30 cmH_2O) (Knudsen et al., 2018). The capillary network is open and nearly free of blood cells. The empty arrowhead points to the entrance of a pleat that is filled with a protein containing fluid (asterisk). Pleats are generally filled with a small quantity of proteinaceous fluid but occasionally locations of direct epithelial-epithelial contact are observed. The pleat is limited to the blood-gas barrier, which invaginates into a capillary (Cap). Two filled arrowheads locate the blood-gas barrier. The image on the right shows the run of the basement membrane (black dashed line), shared by the endothelial cell and the alveolar epithelial type 1 cell, within the pleat.

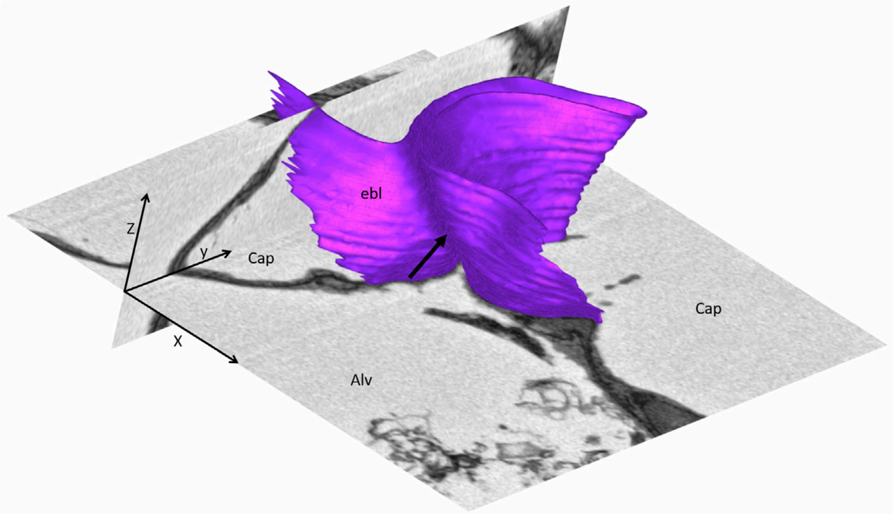

FIGURE 9
Three-dimensional model of a pleat: The mouse lung was fixed *in situ* by vascular perfusion *via* the right ventricle at an airway opening pressure of 2 cmH_2O on expiration after two recruitment maneuvers (3 s pause at 30 cmH_2O) (Ruhl et al., 2019) and processed for serial block-face scanning electron microscopy (SBF-SEM) (Buchacker et a. 2019). The EM image stack was used to segment the shared basement membrane of the endothelial and alveolar epithelial type I cell (ebl, magenta) within a pleat. The arrow points at the slit-like entrance to the pleat, which is created by the blood-gas barrier and invaginates sickle-shaped into the capillary (Cap). The model of the pleat is put into the context of the EM stack by two-dimensional images.

pneumothorax. *In vivo* microscopy of an initially partially collapsed lung provided evidence that alveolar recruitment (or the unfolding of septa forming the boundaries of a cluster of alveoli) is involved during the first respiratory cycles to adapt to lung volume changes. Computational simulations indicate that alveolar recruitment can explain the hysteresis of the first pressure-volume loops of a degassed lung (Bachofen et al., 1987; Carney et al., 1999; Bates and Irvin, 2002). Further imaging studies in healthy lungs using

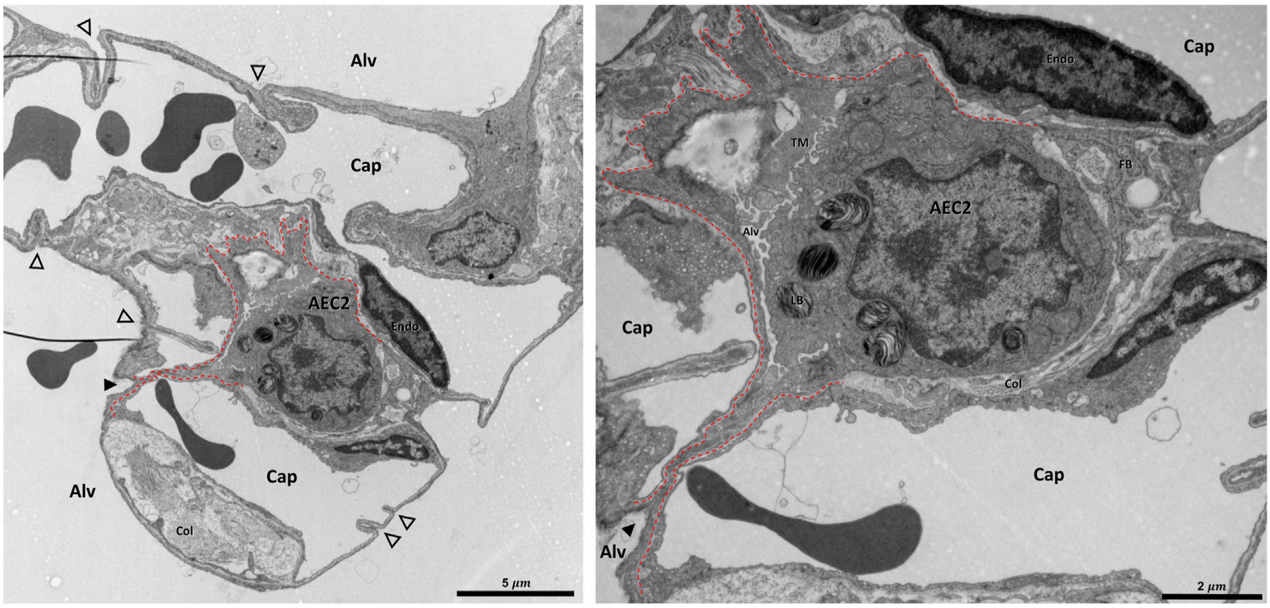

FIGURE 10
Pleat involving more components of the interalveolar septa: A healthy rat lung was fixed *in vivo* by vascular perfusion *via* the vena cava caudalis at an airway opening pressure of 5 cmH_2O on expiration after two recruitment maneuvers (3 s pause at 30 cmH_2O) (Knudsen et al., 2018). The alveolar airspaces (Alv) and the alveolar capillary network (Cap) is open but contains red blood cells. The capillaries are lined by endothelial cells (Endo). The filled arrowhead points at the entrance to a pleat, the black dashed line marks the run of the epithelial basement membrane into the pleat. The pleat is partly bordered by the apical plasma membrane of an alveolar epithelial type 2 cell (AEC2) with its characteristic organelle, the lamellar body (LB). Moreover, the pleat contains some fluid and intraalveolar surfactant, represented by tubular myelin (TM). Underneath the AEC2, interstitial tissue is located, e.g. collagen fibrils (Col) and fibrobasts (FB) are visible. Note that two dark lines at left of left image are an artifact due to folding of the ultrathin section, not part of the tissue structure. The empty arrowheads point at pleats formed exclusively by the blood-gas barrier.

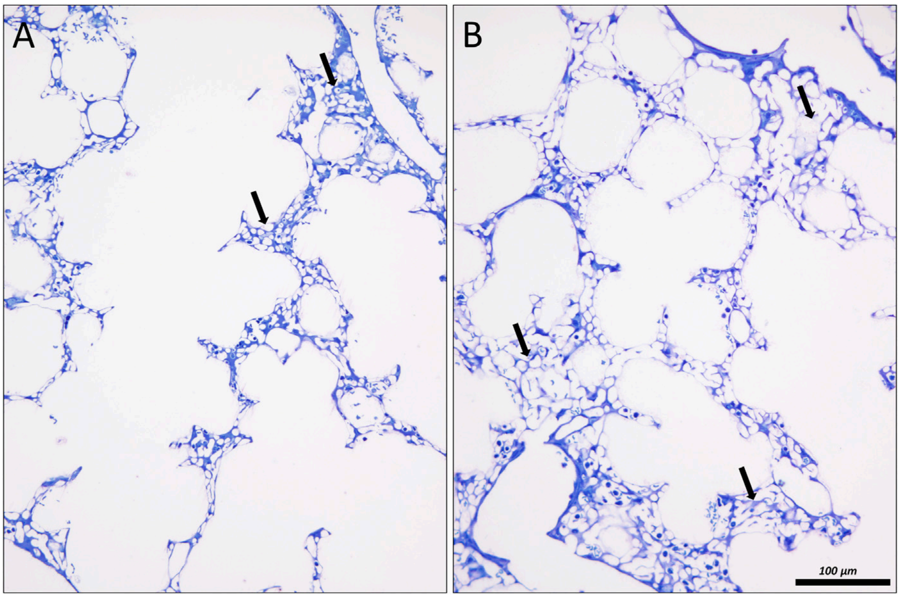

FIGURE 11
Lung injury and microatelectases: In **(A)** an image of the lung of a surfactant protein B knock out mouse is shown, fixed *in situ* by vascular perfusion *via* the right ventricle at an airway opening pressure of 10 cmH_2O on expiration two recruitment maneuvers (3 s pause at 30 cmH_2O) (Ruhl et al., 2019). The alveolar ducts are enlarged. Alveolar airspaces are rare and appear to be shallow. Instead, microatelectases (arrows) can be identified as seemingly thickened interalveolar septa characterized by a conglomeration of capillaries. In **(B)** similar findings can be observed in a rat lung 1 day after instillation of bleomycin to induce lung injury. The lung was fixed *in vivo* by vascular perfusion *via* the vena cava caudalis at an airway opening pressure of 10 cmH_2O on inspiration, coming from 1 cmH_2O after two recruitment maneuvers (3 s pause at 30 cmH_2O).

intravital microscopy, optical coherence tomography, and sections of fixed tissue where the lungs were kept above the residual volume do not provide evidence for alveolar recruitment or decruitment (Pavone et al., 2007; Perlman et al., 2011; Tabuchi et al., 2016; Knudsen et al., 2018; Ruhl et al., 2019; Smith et al., 2020). Hence, the healthy lung and the alveoli can be considered to be stable in presence of an intact surfactant system (Fung, 1975).

In contrast, severe abnormalities in alveolar dynamics including alveolar recruitment/derecruitment have been observed using intravital microscopy in lung injury induced, e.g., by lavage with detergents to remove surfactant or injurious mechanical ventilation (Schiller et al., 2001; Kollisch-Singule et al., 2020). However, other investigators did not find any evidence of intratidal recruitment/derecruitment during mechanical ventilation with physiological tidal volumes using similar imaging techniques (Mertens et al., 2009; Tabuchi et al., 2016; Nguyen and Perlman, 2018; Grune et al., 2019). Instead, these studies showed heterogeneous and asynchronous ventilation patterns in subpleural alveoli. These heterogeneous alveolar dynamics are characterized by subpopulations of alveoli showing decreased size changes while others are overdistended. Asynchronies include, e.g., inverse alveolar ventilation, alveolar stunning as well as the phenomenon of alveolar Pendelluft. The later results in a decrease in alveolar size during an inspiratory hold while other alveoli increase in size. Some of these abnormal patterns of alveolar dynamics can, at least in part, be explained by alveolar interdependence at the interface between injured and healthy lung regions. Alveolar injury can manifest as vascular leakage with alveolar edema accumulation or microatelectases with relatively minor alveolar fluid accumulation. Both of these alveolar-level injury manifestations exert tethering forces on the surrounding alveoli that affect their behavior during ventilation.

Derecruitment has been hypothesized to occur in the acutely injured lung when the transpulmonary pressure drops below a certain value termed alveolar closing pressure. Likewise, recruitment of alveoli during inspiration requires the transgression of an alveolar opening pressure that is greater than the closing pressure (Bates and Irvin, 2002). Using design-based stereology and injured lungs fixed at different airway opening pressures during expiration from TLC, several studies have explored how the distribution of alveolar closing pressures is related to the degree of injury using stereology (Knudsen et al., 2018; Ruhl et al., 2019; Smith et al., 2020). In healthy lungs, the number of alveoli per lung remained stable with airway opening pressures ranging from 20 down to 1 cmH_2*O. Minor* injury shortly after bleomycin challenge induced alveolar instability in a cohort of alveoli at airway opening pressures below 5 cmH_2O. With injury progression the pressure needed to prevent the collapse of unstable alveoli was increased to 10 cmH_2O and an additional cohort of alveoli was identified that could not be recruited with pressures up to 30 cmH_2O. Furthermore, the alveolar opening pressures were much higher than the alveolar closing pressures so that during ventilation with physiological tidal volumes and PEEP <5 cmH_2O hardly any intratidal alveolar recruitment/derecruitment could be detected (Knudsen et al., 2018). A VILI induced by high tidal volumes suggests three alveolar phenotypes after vascular perfusion fixation at different airway pressures: apparently healthy alveoli that were stable at low lung volumes, unstable but recruitable alveoli that collapsed at airway opening pressures below 5 cmH_2O, and a third cohort that was flooded with edema and not recruitable (Smith et al., 2020). These findings transfer at least in part to clinical ARDS (Caironi et al., 2010; Cressoni et al., 2017).

Alveolar instability might also be of relevance in the pathophysiology of fibrosing lung diseases (Knudsen et al., 2017). In lungs of patients suffering from IPF, dysfunctional AE2 cells have been identified by many investigators (Parimon et al., 2020). In a recent study, fibrosis-induced increased proliferation of and Notch signaling in AE2 cells were linked with defective processing of hydrophobic SP-B and SP-C both being of high importance for biophysical properties of surfactant (Wasnick et al., 2023). These observations explain the reduced surface tension lowering properties of alveolar surfactant from IPF patients (Günther et al., 1999). Accordingly, evidence of alveolar instability could be derived from end-expiratory high-resolution CT in subpleural regions of the IPF lung and also from studies investigating the origin of inspiratory Velcro crackles in IPF (Vyshedskiy et al., 2009; Petroulia et al., 2018). Velcro crackles are likely to result from to explosive and energy-rich re-opening of alveolar airspaces. With disease progression, it has been suggested that alveoli remained collapsed throughout the entire respiratory cycle and trigger lung injury in the surrounding tissue *via* mechanical stress (Albert et al., 2019). Remnants of collapsed alveoli with their former entrances overgrown by epithelial cells have been found in fibrotic tissue in IPF. This phenomenon has been termed collapse induration and is a feature of IPF, idiopathic interstitial pneumonia, and COVID-19 (Katzenstein, 1985; Myers and Katzenstein, 1988; Ochs et al., 2021). Since alveolar surface area is considerably decreased in IPF it is plausible that alveolar collapse and collapse induration play important roles in the pathophysiology of IPF (Coxson et al., 1997).

The stereological parameters used to quantify the degree of alveolar derecruitment at different airway opening pressures included the alveolar number, the alveolar surface area, and the volume of the alveolar airspaces (Table 1). All these parameters can be determined both by light microscopy and with microcomputed tomography image stacks (Vasilescu et al., 2020). All parameters are calculated as absolute data per organ to avoid the reference trap. Of these three parameters, the alveolar number is the most technically challenging because it requires the use of a stereological test-volume. This can be generated by two microscopic sections from the same region separated by a known distance (= physical disector). Counting frames with a defined area are randomly superimposed on the microscopic sections (Ochs et al., 2004) so that the test volume is the product of the section separation distance and the area of the counting frame. Alveoli, that are open to the alveolar duct on the one section but not on the other, are counted if the counting event is within the counting frame (Figure 12). Scrolling through a microcomputed tomography image stack is a very efficient alternative to light microscopy when counting alveolar openings to determine alveolar number (McDonough et al., 2015; Knudsen et al., 2021). Another very efficient way to quantify microatelectases is the determination of the volume of collapsed and recruited septa by means of point-counting. Here, collapsed septa in adult lungs are defined by the existence of more than one layer of the alveolar capillary network, provided that the capillaries are open and can be identified accurately (Rizzo et al., 2022) (Figure 11).

TABLE 1 Design-based stereological parameters to study the micromechanics of interalveolar septa. Note, a forth mechanism is shape change due to mechanisms other than stretching/de-stretching or recruitment/de-recruitment (e.g. Reimelt et al., 2023). An example is the straightening of the curvy run of the blood-gas barrier which can occur independently from stretching or recruitment of the blood-gas barrier. As a result, the alveolar volume increases but the surface area of the air-exposed alveolar epithelium remains stable. * Did not determine surface area using stereological test-systems.

Mechanism	Imaging modalities	Stereological parameter	Comments	References
Alveolar recruitment/ derecruitment (R/D)	Light microscopy, Micro computed tomography and synchrotron-based micro computed tomography	**First choices:**	High correlation with lung mechanical impairment	e.g. Ochs et al. (2004), Knudsen et al. (2018), Beike et al. (2019), Smith et al. (2020)
		Number of open alveoli per lung (Figure 12)		
		Volume of microatelectases/ collapsed septa per lung (Figure 11)		e.g. Lutz et al. (2015), Ruwisch et al. (2020), Rizzo et al. (2022)
		Second choices:		e.g. Knudsen et al. (2018), Beike et al. (2019), Smith et al. (2020)
		Alveolar surface area per lung		
		Volume of alveolar airspaces per lung (Figure 7)	No proof of alveolar R/D	e.g. Lutz et al. (2015), Knudsen et al. (2018), Beike et al. (2019), Smith et al. (2020)
		Volume of interalveolar septa per lung and mean thickness of interalveolar septa (calculated from surface to volume ratio)	Mean thickness of interalveolar septa correlates inversely with number of open alveoli	e.g. Lutz et al. (2015)
Recruitment and derecruitment of pleats	Electron microscopy	Total surface area of alveolar epithelium hidden in pleats	In an air-filled lung the surface area of the alveoli does not equal the surface area of the alveolar epithelium	Bachofen et al. (1987), Ruhl et al. (2019), Engelmann et al. (2021)
		Total surface area of alveolar epithelium exposed to air		
		Total surface area of epithelial basement membrane (Figure 14)		
Stretching of the blood-gas barrier	Electron microscopy	Total surface area of epithelial basement membrane (Figure 14)	Changes in the surface area are directly linked with stretching/ strain of epithelium and endothelium	Bachofen et al. (1987), Tschumperlin and Margulies (1999)*, Ruhl et al. (2019), Engelmann et al. (2021)

3.3.3 Folding and unfolding of pleats without recruitment and derecruitment of complete alveoli

Septal pleats invaginating the blood-gas barrier or the entire interalveolar septa, without the derecruitment of complete alveoli, have been described based on electron microscopy in healthy lungs from mice and rats (Tschumperlin and Margulies, 1999; Knudsen et al., 2018; Ruhl et al., 2019). These pleats hide alveolar epithelial surface area and are typically filled with a thin layer of protein-containing liquid. Intraalveolar surfactant, e.g. tubular myelin can often be seen at the entrance to the pleats. These pleats, and the associated liquid layer, have been investigated using design-based stereology at the electron microscopic level at different airway pressures (Ruhl et al., 2019). Decreasing the airway opening pressure to 2 cmH_2O on the expiratory limb of the pressure volume loop increased the frequency of observed pleats in healthy mice and rats, a finding that correlates with an increase in tissue elastance (Knudsen et al., 2018). The surface area of alveolar epithelial cells covered by the intra-pleat fluid increased while the aerated surface area decreased. At higher lung volumes, the majority of protein containing fluid was located in the corners of alveoli. With decreasing lung volume, liquid was integrated into the increasing number of pleats and formed a very thin layer so that the mean thickness of the liquid layer determined via stereology decreased. From these observations it is likely that there is recruitment and derecruitment of pleats accompanied by a reorganization of the alveolar lining fluid, at least under quasi-static conditions at lung volumes within the range of physiological breathing. From a physiological point of view this is an appealing mechanism since it allows the alveolar volume and surface area to change without strain of the blood-gas barrier. In other words, with inflation the aerated alveolar surface area increases while the thickness of the blood-gas barrier and surface area of the epithelial BM remain stable. Septal stretching would result in an increase of the surface area of the epithelial BM combined with thinning of the blood-gas barrier (Bachofen et al., 1987; Leuenberger et al., 2012). Lung physiological studies in humans provide indirect evidence of the existence of this micromechanical mechanism under *in vivo* conditions. A modeling-based approach indicates that the measured diffusion capacity with increasing lung volume of up to 80% TLC could best be explained by an increase in air-exposed alveolar surface area without a decrease in the diffusion membrane thickness, suggesting that recruitment of pleats occurs up to 80% of TLC (Miserocchi et al., 2008).

In an *ex vivo* lung study, Bachofen and co-workers used design-based stereology to quantify the alveolar surface area (S_A) and the surface area of the alveolar epithelial BM (S_{ebl}) at quasi-static conditions during pressure volumes loops starting with a pressure near zero (Bachofen et al., 1987). The S_A-to-S_{ebl} ratio as well as the S_{ebl} increased during inflation, indicating that the increase in surface area is a result of both stretching of the blood-gas barrier and recruitment of surface area hidden in pleats. However, these findings may not be directly applicable to the *in vivo* situation since inflation started below residual volume. Furthermore, Bachofen et al. did not differentiate between recruitment of whole alveoli and recruitment of pleats of the interalveolar septa

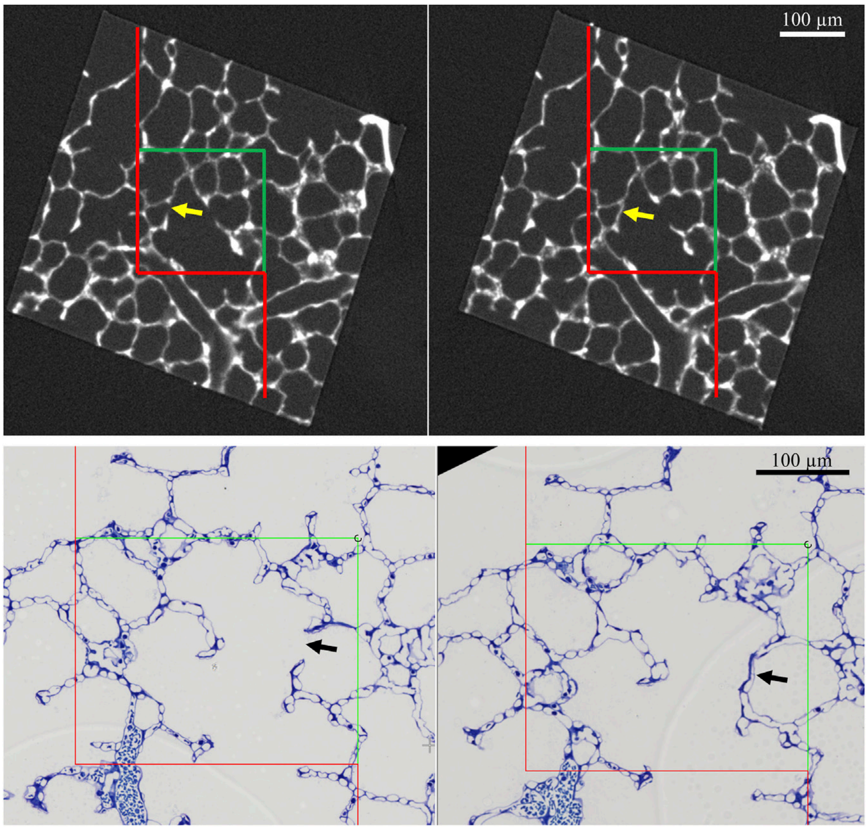

FIGURE 12
Counting open alveoli. Top: A mouse lung was fixed *in situ* by vascular perfusion *via* the right ventricle at an airway opening pressure of 10 cmH_2O on expiration after two recruitment maneuvers (3 s pause at 30 cmH_2O). Tissue was sampled, treated with OsO_4 and embedded in epoxy resin (Ruhl et al., 2019). A tissue block was imaged by micro computed tomography (Nanotom M, Waygate Technology, Wunsdorf, Germany) at a voxel size 1 µm. A pair of images from the stack showing the same region is given. The distance from the top of the left image to the top of the right image is 4 µm. An unbiased counting frame of the area A_{Frame} is superimposed on the images. The counting frame area and the distance between the counting frames generates a test volume. In this test volume, the number of alveolar openings are determined as follows: alveoli open to the alveolar duct on one image but not on the other (arrow) are counted, provided that the opening to the duct is located within the counting frame and does not touch the red line (= forbidden line). Bottom: A healthy rat lung was fixed *in vivo* by vascular perfusion *via* the vena cava caudalis at an airway opening pressure of 10 cmH_2O after two recruitment maneuvers (3 s pause at 30 cmH_2O) (Knudsen et al., 2018). After randomized sampling and embedding, serial sections of a thickness of 1.5 µm were cut. The 1st and the 4th section of a consecutive row of sections was collected and randomized pairs of fields of view showing corresponding regions from these 2 sections were images. An example is given here. The arrow points at a counting event which is defined above.

of those alveoli which are already open. In a later study, lungs were fixed *in situ* at either 10 or 2 cmH_2O following deflation from 30 cmH_2O, thus maintaining a volume history above the residual volume (Ruhl et al., 2019). There was no significant difference in alveolar number, indicating that whole-alveolar derecruitment did not occur. The S_A-to-S_{ebl} ratio decreased from 0.75 to 0.52 during expiration, supporting the conclusion that the loss of aerated alveolar epithelial surface area during deflation is due to both de-recruitment of pleats and de-stretching of the blood-gas barrier because derecruitment without de-stretching would have resulted in a decline of the ratio from 0.75 to 0.42. Estimation of the differential contribution of these two mechanisms to the decline in aerated alveolar surface assigns approximately 40% to the formation of pleats and derecruitment and 60% to de-stretching (Ruhl et al., 2019). However, these studies do not reveal the precise range of lung pressures and volumes during inflation and deflation where these processes occur, and whether they occur during dynamic breathing.

As mentioned earlier, the recruitment of pleats is a way to adapt to volume changes without stretch of the blood-gas barrier but it is also associated with a reorganization of the liquid lining layer and associated pulmonary surfactant. The opposing blood-gas barriers of the pleats are peeled off each other during inflation and the fluid oscillates on the surface of the epithelial cells (Figure 13). Based on *in vitro* experiments and computational modeling this opening process can be linked with potentially harmful forces acting on the epithelial lining if surface tension is elevated due to surfactant dysfunction, a typical feature of lung injury (Bilek et al., 2003; Kay et al., 2004; Naire and Jensen, 2005; Ravasio et al., 2011; Hobi et al., 2012). Hence, the recruitment process of pleats might be detrimental in conditions of high surface tension by causing additional injury of the blood-gas barrier and dysfunction of the AE2 cells, a mechanism referred to as microatelectrauma.

3.3.4 Stretching of the blood-gas barrier

A few studies have quantified the S_{ebl} under quasi-static conditions, using design-based stereology or comparable unbiased

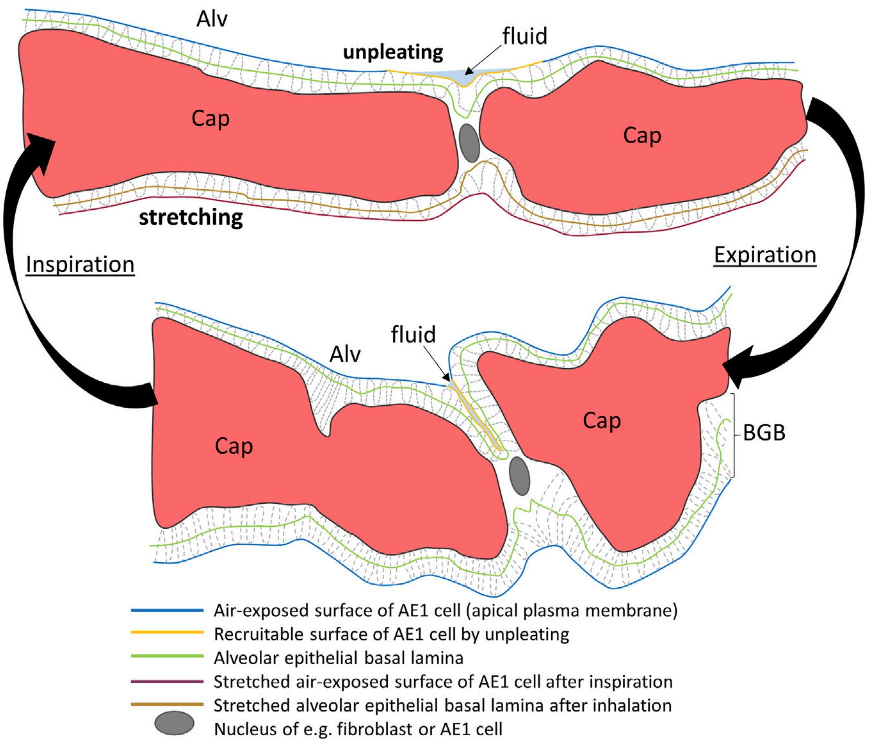

FIGURE 13
Micromechanics of the blood-gas barrier. Schematic of an interalveolar septum at end-expiration (bottom) and end-inspiration (top). The end-expiratory drawing is based on an electron microscopic image and shows in the upper blood-gas barrier (BGB) a pleat filled with fluid (light blue). The surface area of the involved alveolar epithelial cell is hidden in the pleat (yellow) and not exposed to air. After inspiration, the pleat has been opened and its surface area, although still covered by fluid is now exposed to the alveolar lumen. As a result, there is an increase in surface area and adaptation to changing alveolar size without stretching of the alveolar epithelial cell or the epithelial basement membrane (green). The BGB at the bottom of the septum however, does not have a pleat. The BGB is therefore stretched during inspiration which results in an increase in the surface area of both air-exposed apical membranes of alveolar epithelial cells and epithelial basement membrane. The BGB is thinned due to stretching. Capillaries (Cap) and the BGB are also subject to shape changes to adapt to an increase in alveolar volume during inspiration which do not result in an increase in the surface area of the basement membrane or apical plasma membrane of epithelial cells. This schematic is based on classical transmission electron microscopic images which are not able to visualize the complete liquid lining layer. Please note, that the fixation process with glutaraldehyde is based on cross-linking of proteins. Hence, only those parts of the liquid lining layer which contain proteins can be visualized and are given in this schematic.

methods, to reveal the degree of stretching/de-stretching and pleating/unpleating of the blood-gas barrier as lung volume changes (Figure 14). These studies intended to define the range of lung volumes in which stretching/de-stretching occurs (Bachofen et al., 1987; Tschumperlin and Margulies, 1999). The investigated species and volume histories differed between studies; thus, direct comparison is difficult. As mentioned earlier, Bachofen et al. started inflation of isolated and perfused rabbit lungs with transpulmonary pressures close to zero and fixed the lungs during the first and second respiratory cycle. The fixed lungs covered the range of lung volumes between 40% (≈ functional residual capacity) and 100% of TLC during both inspiration and expiration. In the second respiratory cycle S_{ebl} increases by 26% at a lung volume of 80% TLC compared to 40% TLC. Tschumperlin and Margulies ventilated explanted rat lungs for several respiratory cycles with transpulmonary pressures well above the residual volume to avoid any lung collapse. Lungs were fixed at 100% TLC and during expiration at lung volumes corresponding to 82%, 60%, 42% and finally 24% of TLC which occurred at transpulmonary pressures from 25 to 2 cmH_2O. At TLC S_{ebl} was 40% larger compared to a lung volume of 24% TLC. However, the majority (approximately 70%) of the changes in S_{ebl} could be documented between 100% and 80% TLC. Hence, the authors concluded that stretching/de-stretching of the blood-gas barrier predominantly takes place at lung volumes above 80% TLC and thus above the range of lung volume in which quiet spontaneous breathing takes place. Computational modeling using measurements of pulmonary diffusion capacity at 80% and 100% TLC in humans supports these findings. The observed increase in diffusion capacity could best be explained by a thinning of the blood-gas barrier and thus stretching instead of increase in surface area by unfolding processes (Miserocchi et al., 2008). Rühl et al. also quantified the S_{ebl} during expiration in mouse lungs. Because the lung fixation was carried out at set transpulmonary pressures of 2 and 10 cm H_2O, instead of lung volume, a direct comparison to the other publications is difficult. The two-dimensional strain of the blood-gas barrier occurring between those pressures (calculated from S_{ebl}) was 23%, a value a bit larger than that one calculated by Tschumperlin and Margulies between 24% TLC (transpulmonary pressure = 2 cmH_20) and 82% TLC (transpulmonary pressure = 8.8 cmH_2O) which was in the range of 12%–16%. The current available data suggest that within the range of physiological lung volumes both unfolding/folding and stretching/de-stretching occur in parallel as illustrated in Figure 13.

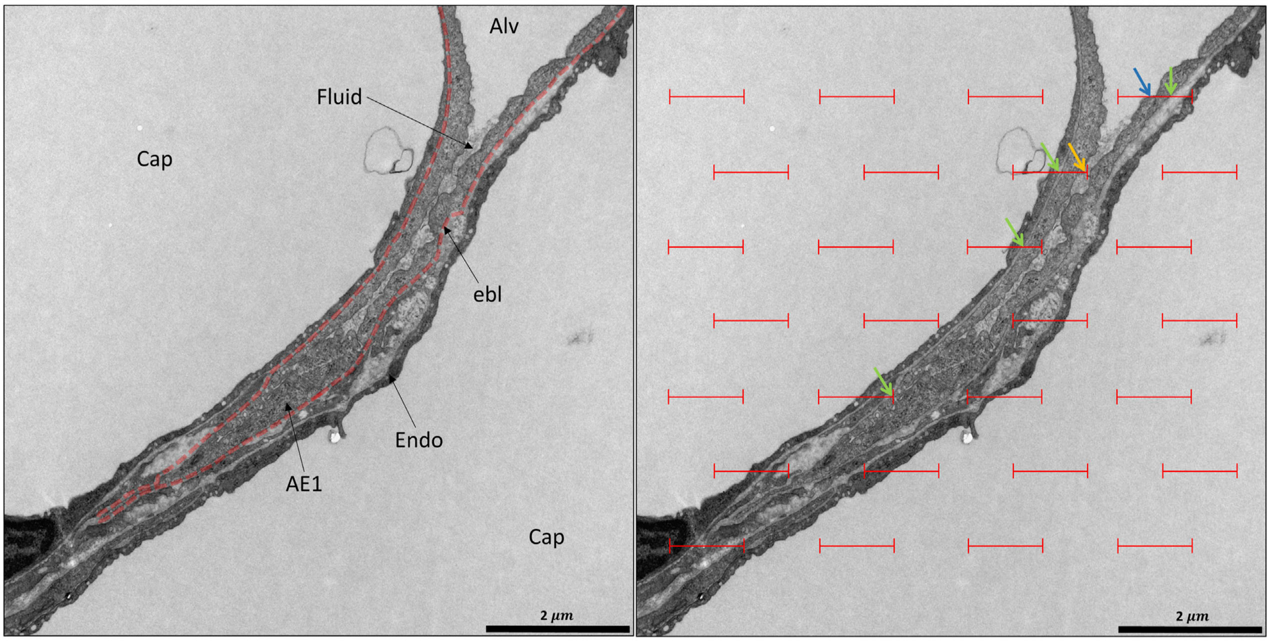

FIGURE 14
Design-based stereology of the blood-gas barrier: A healthy rat lung was fixed *in vivo* by vascular perfusion *via* the vena cava caudalis at an airway opening pressure of 10 cmH_2O after two recruitment maneuvers (3 s pause at 30 cmH_2O) (Knudsen et al., 2018). In the center, a pleat filled with protein-containing fluid and bordered by the blood-gas barriers can be seen. On the left, the epithelial basement membrane (ebl) is delineated (dashed red line). While at the top right corner, the alveolar epithelium is exposed to air (Alv), the pleat hides epithelial surface area which might be recruitable on inspiration. The pleat is filled by a grayish material representing preserved parts of the liquid-lining layer. In order to quantify the surface area covered by air or hidden within pleats, test lines can be projected on randomized electron microscopic images for intersection counting as shown on the right. Line segments of a certain length are superimposed on the image. The probability of these line segments to intersect air covered or hidden alveolar epithelium is proportional to the collective length (L) of the line segments but also to the surface density of, e.g. air-covered or hidden alveolar epithelium. Hence, intersection (I) counting can be applied to determine the surface density (Sv) of the desired structures, given by the equation Sv = 2*I/L. Intersections are indicated as follows: blue arrow: air-covered alveolar epithelial surface area; yellow arrow: hidden alveolar epithelial surface area. The same line segments can be used to determine the surface area of the epithelial basement membrane, a parameter eligible to quantify stretch of the blood-gas barrier. The green arrows point at intersections of the line segments with the epithelial basement membrane.

The strain of the blood-gas barrier is not homogenous, and the regional deformation changes with lung volume. This strain heterogeneity was investigated using design-based stereology and electron microscopy to estimate the surface area of the epithelial BM covered by AE1 and AE2 cells in mice at 10 and 2 cmH_2O on expiration. While the surface area of the BM covered by AE2 cells remained rather stable, the area covered by AE1 cells differed between those two pressures (Ruhl et al., 2019). These observations are supported by confocal microscopy of lungs inflated to different lung volumes (Perlman and Bhattacharya, 2007). Thus, in the range of lung volumes of physiological breathing the strain of AE1 cells is larger than that one of AE2 cells. This may occur because at lower lung volumes the AE2 cells are preferentially located within pleats and those pleats must be unfolded before the AE2 cells are subjects to strain. Based on these considerations it appears to be reasonable that AE2 cells are only stretched at higher lung volumes, e.g., above 80% of TLC.

3 Conclusion

Recent innovations in three and four-dimensional imaging techniques have expanded our knowledge of the micromechanics of acini and alveoli. At the largest scale, these dynamics are manifest as volumetric strain which can be quantified using imaging techniques with light microscopic resolution. However, the micromechanical mechanisms by which the interalveolar septa adapt to alveolar volume changes during breathing or mechanical ventilation, including tissue strain and recruitment of septal pleats, require inclusion of electron microscopic resolution. Pleats can involve either the blood-gas barrier alone, creating invaginations into the alveolar capillaries, or small folds of the entire interalveolar septum. In the latter case, the folding predominantly occurs between the piles of the alveolar capillary network located at the junctions of inter-alveolar septa (the corners of the alveoli). Pleating is a consequence of a complex interplay of tissue tension (fiber system) and surface forces at the air-liquid interface and result in a loss of alveolar surface area. In the context of lung injury, surface tension can increase considerably so that complete alveoli collapse and form microatelectases. These induce potentially harmful stresses on adjoining interalveolar septa, a mechanism discussed to be involved in ventilation-induced lung injury but also the progression of fibrosis lung diseases. The micromechanical mechanisms of alveolar septal deformation can be quantified using design-based stereology and transmission electron microscopy. Data suggest that in healthy lungs, with a volume history above the residual volume, recruitment of entire alveoli is infrequent. Instead, volume changes up to 80% of TLC are accommodated by recruitment of septal pleats and septal stretching which, in combination, yield increased gas exchanging surface area (Figure 13). However, above 80% TLC, stretching might dominate recruitment.

Author contributions

LK: Reviewing of literature, drafting of the manuscript, preparation of figures, interpretation of images, approving the final version of this manuscript. BH: Reviewing of literature, preparation of figures, interpretation of images, editing of the manuscript, approving the final version of the manuscript. CW: Reviewing of literature, preparation of figures, interpretation of images, editing of the manuscript, approving the final version of the manuscript. RZ: Reviewing of literature, preparation of figures, interpretation of images, editing of the manuscript, approving the final version of the manuscript. CEP: Reviewing of literature, preparation of figures, interpretation of images, editing of the manuscript, approving the final version of the manuscript. BS: reviewing of literature, drafting of the manuscript, preparation of figures, interpretation of images, approving the final version of this manuscript.

Funding

LK received funding from the German Research Foundation (DFG, funding ID: 471334884) and the Ministry for Education and Research (BMBF) *via* the German Center for Lung research (DZL). BS is supported by National Institutes of Health (NIH) R01 HL151630 and R01 HD107700 as well as National Science Foundation (NSF) 2225554. CEP is supported by NIH R01 113577.

Conflict of interest

The authors declare that the research was conducted in the absence of any commercial or financial relationships that could be construed as a potential conflict of interest.

Publisher's note

References

Albert, K., Krischer, J. M., Pfaffenroth, A., Wilde, S., Lopez-Rodriguez, E., Braun, A., et al. (2020). Hidden microatelectases increase vulnerability to ventilation-induced lung injury. *Front. Physiol.* 11, 530485. doi:10.3389/fphys.2020.530485

Albert, R. K., Smith, B., Perlman, C. E., and Schwartz, D. A. (2019). Is progression of pulmonary fibrosis due to ventilation-induced lung injury? *Am. J. Respir. Crit. Care Med.* 200, 140–151. doi:10.1164/rccm.201903-0497PP

Angelidis, I., Simon, L. M., Fernandez, I. E., Strunz, M., Mayr, C. H., Greiffo, F. R., et al. (2019). An atlas of the aging lung mapped by single cell transcriptomics and deep tissue proteomics. *Nat. Commun.* 10, 963. doi:10.1038/s41467-019-08831-9

Arora, H., Mitchell, R. L., Johnston, R., Manolesos, M., Howells, D., Sherwood, J. M., et al. (2021). Correlating local volumetric tissue strains with global lung mechanics measurements. *Mater. (Basel)* 14 (6), 439. doi:10.3390/ma14020439

Bachmann, M. C., Cruces, P., Díaz, F., Oviedo, V., Goich, M., Fuenzalida, J., et al. (2022). Spontaneous breathing promotes lung injury in an experimental model of alveolar collapse. *Sci. Rep.* 12, 12648. doi:10.1038/s41598-022-16446-2

Bachofen, H., Ammann, A., Wangensteen, D., and Weibel, E. (1982). Perfusion fixation of lungs for structure-function analysis: Credits and limitations. *J. Appl. Physiol.* 53, 528–533. doi:10.1152/jappl.1982.53.2.528

Bachofen, H., Gehr, P., and Weibel, E. R. (1979). Alterations of mechanical properties and morphology in excised rabbit lungs rinsed with a detergent. *J. Appl. Physiol.* 47, 1002–1010. doi:10.1152/jappl.1979.47.5.1002

Bachofen, H., Gerber, U., Gehr, P., Amrein, M., Schürch, S., et al. (2005). Structures of pulmonary surfactant films adsorbed to an air-liquid interface in vitro. *Biochim Biophys Acta* 1720, 59–72. doi:10.1016/j.bbamem.2005.11.007

Bachofen, H., and Schürch, S. (2001). Alveolar surface forces and lung architecture. *Comp. Biochem. Physiol. A Mol. Integr. Physiol.* 129, 183–193. doi:10.1016/s1095-6433(01)00315-4

Bachofen, H., Schürch, S., Urbinelli, M., and Weibel, E. (1987). Relations among alveolar surface tension, surface area, volume, and recoil pressure. *J. Appl. Physiol.* 62, 1878–1887. doi:10.1152/jappl.1987.62.5.1878

Barkauskas, C. E., Cronce, M. J., Rackley, C. R., Bowie, E. J., Keene, D. R., Stripp, B. R., et al. (2013). Type 2 alveolar cells are stem cells in adult lung. *J. Clin. Invest* 123, 3025–3036. doi:10.1172/JCI68782

Barré, S. F., Haberthür, D., Cremona, T. P., Stampanoni, M., and Schittny, J. C. (2016). The total number of acini remains constant throughout postnatal rat lung development. *Am. J. Physiol. Lung Cell Mol. Physiol.* 311, L1082–L1089. doi:10.1152/ajplung.00325.2016

Barré, S. F., Haberthür, D., Stampanoni, M., and Schittny, J. C. (2014). Efficient estimation of the total number of acini in adult rat lung. *Physiol. Rep.* 2 (7), e12063. doi:10.14814/phy2.12063

Bastacky, J., Lee, C. Y., Goerke, J., Koushafar, H., Yager, D., Kenaga, L., et al. (1995). Alveolar lining layer is thin and continuous: Low-temperature scanning electron microscopy of rat lung. *J. Appl. Physiol.* 79:1615–1628. doi:10.1152/jappl.1995.79.5.1615

Bates, J. H., and Irvin, C. G. (2002). Time dependence of recruitment and derecruitment in the lung: A theoretical model. *J. Appl. Physiol.* 93, 705–713. doi:10.1152/japplphysiol.01274.2001

Bayat, S., Fardin, L., Cercos-Pita, J. L., Perchiazzi, G., and Bravin, A. (2022). Imaging regional lung structure and function in small animals using synchrotron radiation phase-contrast and K-edge subtraction computed tomography. *Front. Physiol.* 13, 825433. doi:10.3389/fphys.2022.825433

Beike, L., Wrede, C., Hegermann, J., Lopez-Rodriguez, E., Kloth, C., Gauldie, J., et al. (2019). Surfactant dysfunction and alveolar collapse are linked with fibrotic septal wall remodeling in the TGF-β1-induced mouse model of pulmonary fibrosis. *Lab. Invest* 99, 830–852. doi:10.1038/s41374-019-0189-x

Beretta, E., Romanò, F., Sancini, G., Grotberg, J. B., Nieman, G. F., and Miserocchi, G. (2021). Pulmonary interstitial matrix and lung fluid balance from normal to the acutely injured lung. *Front. Physiol.* 12, 781874. doi:10.3389/fphys.2021.781874

Bilek, A. M., Dee, K. C., and Gaver, D. P. (2003). Mechanisms of surface-tension-induced epithelial cell damage in a model of pulmonary airway reopening. *J. Appl. Physiol.* 94:770–783. doi:10.1152/japplphysiol.00764.2002

Bou Jawde, S., Takahashi, A., Bates, J. H. T., and Suki, B. (2020). An analytical model for estimating alveolar wall elastic moduli from lung tissue uniaxial stress-strain curves. *Front. Physiol.* 11, 121. doi:10.3389/fphys.2020.00121

Buchacker, T., Mühlfeld, C., Wrede, C., Wagner, W. L., Beare, R., McCormick, M., et al. (2019). Assessment of the alveolar capillary network in the postnatal mouse lung in 3D using serial block-face scanning electron microscopy. *Front. Physiol.* 10, 1357. doi:10.3389/fphys.2019.01357

Caironi, P., Cressoni, M., Chiumello, D., Ranieri, M., Quintel, M., Russo, S. G., et al. (2010). Lung opening and closing during ventilation of acute respiratory distress syndrome. *Am. J. Respir. Crit. Care Med.* 181, 578–586. doi:10.1164/rccm.200905-0787OC

Carney, D. E., Bredenberg, C. E., Schiller, H. J., Picone, A. L., McCann, U. G., Gatto, L. A., et al. (1999). The mechanism of lung volume change during mechanical ventilation. *Am. J. Respir. Crit. Care Med.* 160, 1697–1702. doi:10.1164/ajrccm.160.5.9812031

Cercos-Pita, J. L., Fardin, L., Leclerc, H., Maury, B., Perchiazzi, G., Bravin, A., et al. (2022). Lung tissue biomechanics imaged with synchrotron phase contrast microtomography in live rats. *Sci. Rep.* 12, 5056. doi:10.1038/s41598-022-09052-9

Cereda, M., Xin, Y., Hamedani, H., Bellani, G., Kadlecek, S., Clapp, J., et al. (2017). Tidal changes on CT and progression of ARDS. *Thorax* 72, 981–989. doi:10.1136/thoraxjnl-2016-209833

Chan, H. F., Collier, G. J., Parra-Robles, J., and Wild, J. M. (2021). Finite element simulations of hyperpolarized gas DWI in micro-CT meshes of acinar airways: Validating the cylinder and stretched exponential models of lung microstructural length scales. *Magn. Reson Med.* 86, 514–525. doi:10.1002/mrm.28703

Chang, S., Kwon, N., Kim, J., Kohmura, Y., Ishikawa, T., Rhee, C. K., et al. (2015). Synchrotron X-ray imaging of pulmonary alveoli in respiration in live intact mice. *Sci. Rep.* 5, 8760. doi:10.1038/srep08760

Choy, S., Wheatley, A., McCormack, D. G., and Parraga, G. (2010). Hyperpolarized (3)He magnetic resonance imaging-derived pulmonary pressure-volume curves. *J. Appl. Physiol.* 109:574–585. doi:10.1152/japplphysiol.01085.2009

Coxson, H. O., Hogg, J. C., Mayo, J. R., Behzad, H., Whittall, K. P., Schwartz, D. A., et al. (1997). Quantification of idiopathic pulmonary fibrosis using computed tomography and histology. *Am. J. Respir. Crit. Care Med.* 155, 1649–1656. doi:10.1164/ajrccm.155.5.9154871

Crapo, J., Barry, B., Gehr, P., Bachofen, M., and Weibel, E. (1982). Cell number and cell characteristics of the normal human lung. *Am. Rev. Respir. Dis.* 125, 740–745. doi:10.1164/arrd.1982.125.6.740

Cressoni, M., Chiumello, D., Algieri, I., Brioni, M., Chiurazzi, C., Colombo, A., et al. (2017). Opening pressures and atelectrauma in acute respiratory distress syndrome. *Intensive Care Med.* 43, 603–611. doi:10.1007/s00134-017-4754-8

Dietl, P., and Haller, T. (2005). Exocytosis of lung surfactant: from the secretory vesicle to the air-liquid interface. *Annu Rev Physiol* 67, 595–621. doi:10.1146/annurev.physiol.67.040403.102553

Dolinay, T., Himes, B. E., Shumyatcher, M., Lawrence, G. G., and Margulies, S. S. (2017). Integrated stress response mediates epithelial injury in mechanical ventilation. *Am. J. Respir. Cell Mol. Biol.* 57, 193–203. doi:10.1165/rcmb.2016-0404OC

Dreyfuss, D., and Saumon, G. (1998). Ventilator-induced lung injury: Lessons from experimental studies. *Am. J. Respir. Crit. Care Med.* 157, 294–323. doi:10.1164/ajrccm.157.1.9604014

Elias, H. (1971). Three-dimensional structure identified from single sections. *Science* 174, 993–1000. doi:10.1126/science.174.4013.993

Engelmann, T. A., Knudsen, L., Leitz, D. H. W., Duerr, J., Beers, M. F., Mall, M. A., et al. (2021). Linking fibrotic remodeling and ultrastructural alterations of alveolar epithelial cells after deletion of *nedd4-2. Int. J. Mol. Sci.* 22 (14), 7607. doi:10.3390/ijms22147607

Fredberg, J. J., and Kamm, R. D. (2006). Stress transmission in the lung: Pathways from organ to molecule. *Annu. Rev. Physiol.* 68, 507–541. doi:10.1146/annurev.physiol.68.072304.114110

Fung, Y. C. (1975). Does the surface tension make the lung inherently unstable? *Circ. Res.* 37, 497–502. doi:10.1161/01.res.37.4.497

Fung, Y. C., and Sobin, S. S. (1969). Theory of sheet flow in lung alveoli. *J. Appl. Physiol.* 26, 472–488. doi:10.1152/jappl.1969.26.4.472

Gehr, P., Bachofen, M., and Weibel, E. R. (1978). The normal human lung: Ultrastructure and morphometric estimation of diffusion capacity. *Respir. Physiol.* 32, 121–140. doi:10.1016/0034-5687(78)90104-4

Gil, J., Bachofen, H., Gehr, P., and Weibel, E. (1979). Alveolar volume-surface area relation in air- and saline-filled lungs fixed by vascular perfusion. *J. Appl. Physiol.* 47, 990–1001. doi:10.1152/jappl.1979.47.5.990

Gil, J., and Weibel, E. R. (1972). Morphological study of pressure-volume hysteresis in rat lungs fixed by vascular perfusion. *Respir. Physiol.* 15, 190–213. doi:10.1016/0034-5687(72)90098-9

Grothausmann, R., Knudsen, L., Ochs, M., and Mühlfeld, C. (2017). Digital 3D reconstructions using histological serial sections of lung tissue including the alveolar capillary network. *Am. J. Physiol. Lung Cell Mol. Physiol.* 312, L243–L257. doi:10.1152/ajplung.00326.2016

Grune, J., Tabuchi, A., and Kuebler, W. M. (2019). Alveolar dynamics during mechanical ventilation in the healthy and injured lung. *Intensive Care Med. Exp.* 7, 34. doi:10.1186/s40635-019-0226-5

Günther, A., Schmidt, R., Nix, F., Yabut-Perez, M., Guth, C., Rosseau, S., et al. (1999). Surfactant abnormalities in idiopathic pulmonary fibrosis, hypersensitivity pneumonitis and sarcoidosis. *Eur. Respir. J.* 14, 565–573. doi:10.1034/j.1399-3003.1999.14c14.x

Haberthür, D., Yao, E., Barré, S. F., Cremona, T. P., Tschanz, S. A., and Schittny, J. C. (2021). Pulmonary acini exhibit complex changes during postnatal rat lung development. *PLoS One* 16, e0257349. doi:10.1371/journal.pone.0257349

Haefeli-Bleuer, B., and Weibel, E. (1988). Morphometry of the human pulmonary acinus. *Anat. Rec.* 220, 401–414. doi:10.1002/ar.1092200410

Halter, J. M., Steinberg, J. M., Gatto, L. A., DiRocco, J. D., Pavone, L. A., Schiller, H. J., et al. (2007). Effect of positive end-expiratory pressure and tidal volume on lung injury induced by alveolar instability. *Crit. Care* 11 (1), R20. doi:10.1186/cc5695

Hamlington, K. L., Smith, B. J., Dunn, C. M., Charlebois, C. M., Roy, G. S., and Bates, J. H. T. (2018). Linking lung function to structural damage of alveolar epithelium in ventilator-induced lung injury. *Respir. Physiol. Neurobiol.* 255, 22–29. doi:10.1016/j.resp.2018.05.004

Hobi, N., Ravasio, A., and Haller, T. (2012). Interfacial stress affects rat alveolar type II cell signaling and gene expression. *Am. J. Physiol. Lung Cell Mol. Physiol.* 303, L117–L129. doi:10.1152/ajplung.00340.2011

Hogg, J. C., Paré, P. D., and Hackett, T. L. (2017). The contribution of small airway obstruction to the pathogenesis of chronic obstructive pulmonary disease. *Physiol. Rev.* 97, 529–552. doi:10.1152/physrev.00025.2015

Holm, B. A., Enhorning, G., and Notter, R. H. (1988). A biophysical mechanism by which plasma proteins inhibit lung surfactant activity. *Chem. Phys. Lipids* 49, 49–55. doi:10.1016/0009-3084(88)90063-1

Holm, B. A., Wang, Z., and Notter, R. H. (1999). Multiple mechanisms of lung surfactant inhibition. *Pediatr. Res.* 46, 85–93. doi:10.1203/00006450-199907000-00015

Hsia, C. C., Hyde, D. M., Ochs, M., and Weibel, E. R.ATS/ERS Joint Task Force on Quantitative Assessment of Lung Structure (2010). An official research policy statement of the American thoracic society/European respiratory society: Standards for quantitative assessment of lung structure. *Am. J. Respir. Crit. Care Med.* 181, 394–418. doi:10.1164/rccm.200809-1522ST

Ingber, D. E. (2003). Tensegrity I. Cell structure and hierarchical systems biology. *J. Cell Sci.* 116, 1157–1173. doi:10.1242/jcs.00359

Jansing, N. L., McClendon, J., Henson, P. M., Tuder, R. M., Hyde, D. M., and Zemans, R. L. (2017). Unbiased quantitation of alveolar type II to alveolar type I cell transdifferentiation during repair after lung injury in mice. *Am. J. Respir. Cell Mol. Biol.* 57, 519–526. doi:10.1165/rcmb.2017-0037MA

Jiang, D., Liang, J., Fan, J., Yu, S., Chen, S., Luo, Y., et al. (2005). Regulation of lung injury and repair by Toll-like receptors and hyaluronan. *Nat. Med.* 11, 1173–1179. doi:10.1038/nm1315

Kadur Lakshminarasimha Murthy, P., Sontake, V., Tata, A., Kobayashi, Y., Macadlo, L., Okuda, K., et al. (2022). Human distal lung maps and lineage hierarchies reveal a bipotent progenitor. *Nature* 604, 111–119. doi:10.1038/s41586-022-04541-3

Katzenstein, A. (1985). Pathogenesis of "fibrosis" in interstitial pneumonia: An electron microscopic study. *Hum. Pathol.* 16, 1015–1024. doi:10.1016/s0046-8177(85)80279-3

Kay, S. S., Bilek, A. M., Dee, K. C., and Gaver, D. P. (2004). Pressure gradient, not exposure duration, determines the extent of epithelial cell damage in a model of pulmonary airway reopening. *J. Appl. Physiol.* 97:269–276. doi:10.1152/japplphysiol.01288.2003

Kharge, A. B., Wu, Y., and Perlman, C. E. (2014). Surface tension *in situ* in flooded alveolus unaltered by albumin. *J. Appl. Physiol.* 117, 440–451. doi:10.1152/japplphysiol.00084.2014

Knudsen, L., Boxler, L., Muhlfeld, C., Schaefer, I. M., Becker, L., Bussinger, C., et al. (2012). Lung preservation in experimental ischemia/reperfusion injury and lung transplantation: A comparison of natural and synthetic surfactants. *J. Heart Lung Transplant.* 31, 85–93. doi:10.1016/j.healun.2011.10.002

Knudsen, L., Brandenberger, C., and Ochs, M. (2021). Stereology as the 3D tool to quantitate lung architecture. *Histochem Cell Biol.* 155, 163–181. doi:10.1007/s00418-020-01927-0

Knudsen, L., Lopez-Rodriguez, E., Berndt, L., Steffen, L., Ruppert, C., Bates, J. H. T., et al. (2018). Alveolar micromechanics in bleomycin-induced lung injury. *Am. J. Respir. Cell Mol. Biol.* 59, 757–769. doi:10.1165/rcmb.2018-0044OC

Knudsen, L., and Ochs, M. (2018). The micromechanics of lung alveoli: Structure and function of surfactant and tissue components. *Histochem Cell Biol.* 150, 661–676. doi:10.1007/s00418-018-1747-9

Knudsen, L., Ruppert, C., and Ochs, M. (2017). Tissue remodelling in pulmonary fibrosis. *Cell Tissue Res.* 367, 607–626. doi:10.1007/s00441-016-2543-2

Knudsen, L., Weibel, E. R., Gundersen, H. J. G., Weinstein, F. V., and Ochs, M. (2010). Assessment of air space size characteristics by intercept (chord) measurement: An accurate and efficient stereological approach. *J. Appl. Physiol.* 108, 412–421. doi:10.1152/japplphysiol.01100.2009

Kollisch-Singule, M., Satalin, J., Blair, S. J., Andrews, P. L., Gatto, L. A., Nieman, G. F., et al. (2020). Mechanical ventilation lessons learned from alveolar micromechanics. *Front. Physiol.* 11, 233. doi:10.3389/fphys.2020.00233

König, M. F., Lucocq, J. M., and Weibel, E. R. (1993). Demonstration of pulmonary vascular perfusion by electron and light microscopy. *J. Appl. Physiol.* 75, 1877–1883. doi:10.1152/jappl.1993.75.4.1877

Konkimalla, A., Konishi, S., Kobayashi, Y., Kadur Lakshminarasimha Murthy, P., Macadlo, L., Mukherjee, A., et al. (2022). Multi-apical polarity of alveolar stem cells and their dynamics during lung development and regeneration. *iScience* 25, 105114. doi:10.1016/j.isci.2022.105114

Krischer, J. M., Albert, K., Pfaffenroth, A., Lopez-Rodriguez, E., Ruppert, C., Smith, B. J., et al. (2021). Mechanical ventilation-induced alterations of intracellular surfactant pool and blood-gas barrier in healthy and pre-injured lungs. *Histochem Cell Biol.* 155, 183–202. doi:10.1007/s00418-020-01938-x

Lai, Y. L., and Chou, H. (2000). Respiratory mechanics and maximal expiratory flow in the anesthetized mouse. *J. Appl. Physiol.* 88, 939–943. doi:10.1152/jappl.2000.88.3.939

Lettau, M., Timm, S., Dittmayer, C., Lopez-Rodriguez, E., Ochs, M., et al. (2022). The ultrastructural heterogeneity of lung surfactant revealed by serial section electron tomography: insights into the 3-D architecture of human tubular myelin. *Am J Physiol Lung Cell Mol Physiol* 322, L873–L881. doi:10.1152/ajplung.00020.2022

Leuenberger, A., Gazdhar, A., Herrmann, G., Ochs, M., Geiser, T., and Knudsen, L. (2012). Cell-specific expression of human HGF by alveolar type II cells induces remodeling of septal wall tissue in the lung: A morphometric study. *J. Appl. Physiol.* 113, 799–807. doi:10.1152/japplphysiol.00411.2012

Liang, J., Zhang, Y., Xie, T., Liu, N., Chen, H., Geng, Y., et al. (2016). Hyaluronan and TLR4 promote surfactant-protein-C-positive alveolar progenitor cell renewal and prevent severe pulmonary fibrosis in mice. *Nat. Med.* 22 (11), 1285–1293. doi:10.1038/nm.4192

Lopez-Rodriguez, E., Boden, C., Echaide, M., Perez-Gil, J., Kolb, M., Gauldie, J., et al. (2016). Surfactant dysfunction during overexpression of TGF-beta 1 precedes profibrotic lung remodeling *in vivo*. *Am. J. Physiology-Lung Cell. Mol. Physiology* 310, L1260–L1271. doi:10.1152/ajplung.00065.2016

Loring, S. H., Topulos, G. P., and Hubmayr, R. D. (2016). Transpulmonary pressure: The importance of precise definitions and limiting assumptions. *Am. J. Respir. Crit. Care Med.* 194, 1452–1457. doi:10.1164/rccm.201512-2448CP

Lutz, D., Gazdhar, A., Lopez-Rodriguez, E., Ruppert, C., Mahavadi, P., Gunther, A., et al. (2015). Alveolar derecruitment and collapse induration as crucial mechanisms in lung injury and fibrosis. *Am. J. Respir. Cell Mol. Biol.* 52, 232–243. doi:10.1165/rcmb.2014-0078OC

Maina, J. N., and West, J. B. (2005). Thin and strong! The bioengineering dilemma in the structural and functional design of the blood-gas barrier. *Physiol. Rev.* 85, 811–844. doi:10.1152/physrev.00022.2004

Makiyama, A. M., Gibson, L. J., Harris, R. S., and Venegas, J. G. (2014). Stress concentration around an atelectatic region: A finite element model. *Respir. Physiol. Neurobiol.* 201, 101–110. doi:10.1016/j.resp.2014.06.017

Masterson, C. H., Tabuchi, A., Hogan, G., Fitzpatrick, G., Kerrigan, S. W., Jerkic, M., et al. (2021). Intra-vital imaging of mesenchymal stromal cell kinetics in the pulmonary vasculature during infection. *Sci. Rep.* 11, 5265. doi:10.1038/s41598-021-83894-7

Mattson, C. L., Okamura, K., Hume, P. S., and Smith, B. J. (2022). Spatiotemporal distribution of cellular injury and leukocytes during the progression of ventilator-induced lung injury. *Am. J. Physiol. Lung Cell Mol. Physiol.* 323, L281–L296. doi:10.1152/ajplung.00207.2021

Matuszak, J., Tabuchi, A., and Kuebler, W. M. (2020). Ventilation and perfusion at the alveolar level: Insights from lung intravital microscopy. *Front. Physiol.* 11, 291. doi:10.3389/fphys.2020.00291

McDonough, J. E., Knudsen, L., Wright, A. C., Elliott, W. M., Ochs, M., and Hogg, J. C. (2015). Regional differences in alveolar density in the human lung are related to lung height. *J. Appl. Physiology* 118, 1429–1434. doi:10.1152/japplphysiol.01017.2014

Mead, J., Takishima, T., and Leith, D. (1970). Stress distribution in lungs: A model of pulmonary elasticity. *J. Appl. Physiol.* 28, 596–608. doi:10.1152/jappl.1970.28.5.596

Mead, J. (1961). Mechanical properties of lungs. *Physiol. Rev.* 41, 281–330. doi:10.1152/physrev.1961.41.2.281

Mercer, R. R., Laco, J. M., and Crapo, J. D. (1987). Three-dimensional reconstruction of alveoli in the rat lung for pressure-volume relationships. *J. Appl. Physiol.* 62, 1480–1487. doi:10.1152/jappl.1987.62.4.1480

Mertens, M., Tabuchi, A., Meissner, S., Krueger, A., Schirrmann, K., Kertzscher, U., et al. (2009). Alveolar dynamics in acute lung injury: Heterogeneous distension rather than cyclic opening and collapse. *Crit. Care Med.* 37, 2604–2611. doi:10.1097/CCM.0b013e3181a5544d

Miserocchi, G., Messinesi, G., Tana, F., Passoni, E., Adamo, S., Romano, R., et al. (2008). Mechanisms behind inter-individual differences in lung diffusing capacity. *Eur. J. Appl. Physiol.* 102, 561–568. doi:10.1007/s00421-007-0625-2

Mitzner, W., Loube, J., Venezia, J., and Scott, A. (2020). Self-organizing pattern of subpleural alveolar ducts. *Sci. Rep.* 10, 3185. doi:10.1038/s41598-020-59752-3

Mizuuchi, T., Kida, K., and Fujino, Y. (1994). Morphological studies of growth and aging in the lungs of Fischer 344 male rats. *Exp. Gerontol.* 29, 553–567. doi:10.1016/0531-5565(94)90038-8

Mostaco-Guidolin, L. B., Loube, J., Barlow, A., Osei, E. T., Vasilescu, D. M., Hsieh, A., et al. (2021). Second harmonic generation imaging of collagen scaffolds within the alveolar ducts of healthy and emphysematous mouse lungs. *Histochem Cell Biol.* 155, 279–289. doi:10.1007/s00418-020-01959-6

Mühlfeld, C., Hegermann, J., Wrede, C., and Ochs, M. (2015). A review of recent developments and applications of morphometry/stereology in lung research. *Am. J. Physiol. Lung Cell Mol. Physiol.* 309, L526–L536. doi:10.1152/ajplung.00047.2015

Mühlfeld, C., Knudsen, L., and Ochs, M. (2013). Stereology and morphometry of lung tissue. *Methods Mol. Biol.* 931, 367–390. doi:10.1007/978-1-62703-056-4_18

Mühlfeld, C., Weibel, E. R., Hahn, U., Kummer, W., Nyengaard, J. R., and Ochs, M. (2010). Is length an appropriate estimator to characterize pulmonary alveolar capillaries? A critical evaluation in the human lung. *Anat. Rec. Hob.* 293, 1270–1275. doi:10.1002/ar.21158

Myers, J., and Katzenstein, A. (1988). Epithelial necrosis and alveolar collapse in the pathogenesis of usual interstitial pneumonia. *Chest* 94, 1309–1311. doi:10.1378/chest.94.6.1309

Nag, K., Perez-Gil, J., Ruano, M. L., Worthman, L. A., Stewart, J., Casals, C., et al. (1998). Phase transitions in films of lung surfactant at the air-water interface. *Biophys. J.* 74, 2983–2995. doi:10.1016/S0006-3495(98)78005-1

Naire, S., and Jensen, O. E. (2005). Epithelial cell deformation during surfactant-mediated airway reopening: A theoretical model. *J. Appl. Physiol.* 99, 458–471. doi:10.1152/japplphysiol.00796.2004

Nguyen, T. L., and Perlman, C. E. (2020). Sulforhodamine B and exogenous surfactant effects on alveolar surface tension under acute respiratory distress syndrome conditions. *J. Appl. Physiol.* 129, 1505–1513. doi:10.1152/japplphysiol.00422.2020

Nguyen, T. L., and Perlman, C. E. (2018). Tracheal acid or surfactant instillation raises alveolar surface tension. *J. Appl. Physiol.* 125, 1357–1367. doi:10.1152/japplphysiol.00397.2017

Nieman, G. F., Al-Khalisy, H., Kollisch-Singule, M., Satalin, J., Blair, S., Trikha, G., et al. (2020). A physiologically informed strategy to effectively open, stabilize, and protect the acutely injured lung. *Front. Physiol.* 11, 227. doi:10.3389/fphys.2020.00227

Nieman, G. F., Bredenberg, C. E., Clark, W. R., and West, N. R. (1981). Alveolar function following surfactant deactivation. *J. Appl. Physiol. Respir. Environ. Exerc Physiol.* 51, 895–904. doi:10.1152/jappl.1981.51.4.895

Nonaka, P. N., Uriarte, J. J., Campillo, N., Melo, E., Navajas, D., Farré, R., et al. (2014). Mechanical properties of mouse lungs along organ decellularization by sodium dodecyl sulfate. *Respir. Physiol. Neurobiol.* 200, 1–5. doi:10.1016/j.resp.2014.04.008

Notter, R. H., Wang, Z., Egan, E. A., and Holm, B. A. (2002). Component-specific surface and physiological activity in bovine-derived lung surfactants. *Chem. Phys. Lipids* 114, 21–34. doi:10.1016/s0009-3084(01)00197-9

Ochs, M. (2010). The closer we look the more we see? Quantitative microscopic analysis of the pulmonary surfactant system. *Cell Physiol Biochem.* 25, 27–40. doi:10.1159/000272061

Ochs, M., Hegermann, J., Lopez-Rodriguez, E., Timm, S., Nouailles, G., Matuszak, J., et al. (2020). On top of the alveolar epithelium: Surfactant and the glycocalyx. *Int. J. Mol. Sci.* 21 (9), 3075. doi:10.3390/ijms21093075

Ochs, M., Nyengaard, L. R., Lung, A., Knudsen, L., Voigt, M., Wahlers, T., et al. (2004). The number of alveoli in the human lung. *Am. J. Respir. Crit. Care Med.* 169, 120–124. doi:10.1164/rccm.200308-1107OC

Ochs, M., and Schipke, J. (2021). A short primer on lung stereology. *Respir. Res.* 22, 305. doi:10.1186/s12931-021-01899-2

Ochs, M., Timm, S., Elezkurtaj, S., Horst, D., Meinhardt, J., Heppner, F. L., et al. (2021). Collapse induration of alveoli is an ultrastructural finding in a COVID-19 patient. *Eur. Respir. J.* 57 (5), 2004165. doi:10.1183/13993003.04165-2020

Oldmixon, E. H., and Hoppin, F. G. (1991). Alveolar septal folding and lung inflation history. *J. Appl. Physiol.* 71, 2369–2379. doi:10.1152/jappl.1991.71.6.2369

Oldmixon, E. H., Suzuki, S., Butler, J. P., and Hoppin, F. G. (1985). Perfusion dehydration fixes elastin and preserves lung air-space dimensions. *J. Appl. Physiol.* 58, 105–113. doi:10.1152/jappl.1985.58.1.105

Osmanagic, E., Sukstanskii, A. L., Quirk, J. D., Woods, J. C., Pierce, R. A., Conradi, M. S., et al. (2010). Quantitative assessment of lung microstructure in healthy mice using an MR-based 3He lung morphometry technique. *J. Appl. Physiol.* 109, 1592–1599. doi:10.1152/japplphysiol.00736.2010

Parimon, T., Yao, C., Stripp, B. R., Noble, P. W., and Chen, P. (2020). Alveolar epithelial type II cells as drivers of lung fibrosis in idiopathic pulmonary fibrosis. *Int. J. Mol. Sci.* 21 (7), 2269. doi:10.3390/ijms21072269

Pavone, L. A., Albert, S., Carney, D., Gatto, L. A., Halter, J. M., and Nieman, G. F. (2007). Injurious mechanical ventilation in the normal lung causes a progressive pathologic change in dynamic alveolar mechanics. *Crit. Care* 11, R64. doi:10.1186/cc5940

Perlman, C. E., and Bhattacharya, J. (2007). Alveolar expansion imaged by optical sectioning microscopy. *J. Appl. Physiol.* 103, 1037–1044. doi:10.1152/japplphysiol.00160.2007

Perlman, C. E., Lederer, D. J., and Bhattacharya, J. (2011). Micromechanics of alveolar edema. *Am. J. Respir. Cell Mol. Biol.* 44, 34–39. doi:10.1165/rcmb.2009-0005OC

Perlman, C. E. (2020). The contribution of surface tension-dependent alveolar septal stress concentrations to ventilation-induced lung injury in the acute respiratory distress syndrome. *Front. Physiol.* 11, 388. doi:10.3389/fphys.2020.00388

Petroulia, V., Funke, M., Zumstein, P., Berezowska, S., Ebner, L., Geiser, T., et al. (2018). Increased expiratory computed tomography density reveals possible abnormalities in radiologically preserved lung parenchyma in idiopathic pulmonary fibrosis. *Invest Radiol.* 53, 45–51. doi:10.1097/RLI.0000000000000405

Quirk, J. D., Sukstanskii, A. L., Woods, J. C., Lutey, B. A., Conradi, M. S., Gierada, D. S., et al. (2016). Experimental evidence of age-related adaptive changes in human acinar airways. *J. Appl. Physiol.* 120, 159–165. doi:10.1152/japplphysiol.00541.2015

Ravasio, A., Hobi, N., Bertocchi, C., Jesacher, A., Dietl, P., and Haller, T. (2011). Interfacial sensing by alveolar type II cells: A new concept in lung physiology? *Am. J. Physiol. Cell Physiol.* 300, C1456–C1465. doi:10.1152/ajpcell.00427.2010

Reifenrath, R. (1975). The significance of alveolar geometry and surface tension in the respiratory mechanics of the lung. *Respir. Physiol.* 24, 115–137. doi:10.1016/0034-5687(75)90107-3

Reifenrath, R., and Zimmermann, I. (1973). Surface tension properties of lung alveolar surfactant obtained by alveolar micropuncture. *Respir. Physiol.* 19, 369–393. doi:10.1016/0034-5687(73)90040-6

Reimelt, A., Vasilescu, D. M., Beare, R., Labode, J., Knudsen, L., and Grothausmann, R. (2023). Analysis of the alveolar shape in 3D. *Am. J. Physiol. Lung Cell Mol. Physiol.* (in press). doi:10.1152/ajplung.00069.2022

Rizzo, A. N., Haeger, S. M., Oshima, K., Yang, Y., Wallbank, A. M., Jin, Y., et al. (2022). Alveolar epithelial glycocalyx degradation mediates surfactant dysfunction and contributes to acute respiratory distress syndrome. *JCI Insight* 7 (2), e154573. doi:10.1172/jci.insight.154573

Roan, E., and Waters, C. M. (2011). What do we know about mechanical strain in lung alveoli? *Am. J. Physiol. Lung Cell Mol. Physiol.* 301, L625–L635. doi:10.1152/ajplung.00105.2011

Ruhl, N., Lopez-Rodriguez, E., Albert, K., Smith, B. J., Weaver, T. E., Ochs, M., et al. (2019). Surfactant protein B deficiency induced high surface tension: Relationship between alveolar micromechanics, alveolar fluid properties and alveolar epithelial cell injury. *Int. J. Mol. Sci.* 20 (17), 4243. doi:10.3390/ijms20174243

Ruwisch, J., Sehlmeyer, K., Roldan, N., Garcia-Alvarez, B., Perez-Gil, J., Weaver, T. E., et al. (2020). Air space distension precedes spontaneous fibrotic remodeling and impaired cholesterol metabolism in the absence of surfactant protein C. *Am. J. Respir. Cell Mol. Biol.* 62, 466–478. doi:10.1165/rcmb.2019-0358OC

Sapoval, B., Filoche, M., and Weibel, E. (2002). Smaller is better--but not too small: A physical scale for the design of the mammalian pulmonary acinus. *Proc. Natl. Acad. Sci. U. S. A.* 99, 10411–10416. doi:10.1073/pnas.122352499

Scharm, S. C., Schaefer-Prokop, C., Willmann, M., Vogel-Claussen, J., Knudsen, L., Jonigk, D., et al. (2022). Increased regional ventilation as early imaging marker for future disease progression of interstitial lung disease: A feasibility study. *Eur. Radiol.* 32, 6046–6057. doi:10.1007/s00330-022-08702-w

Scharm, S. C., Vogel-Claussen, J., Schaefer-Prokop, C., Dettmer, S., Knudsen, L., Jonigk, D., et al. (2021). Quantification of dual-energy CT-derived functional parameters as potential imaging markers for progression of idiopathic pulmonary fibrosis. *Eur. Radiol.* 31, 6640–6651. doi:10.1007/s00330-021-07798-w

Schiller, H. B., Montoro, D. T., Simon, L. M., Rawlins, E. L., Meyer, K. B., Strunz, M., et al. (2019). The Human Lung Cell Atlas - a high-resolution reference map of the human lung in health and disease. *Am. J. Respir. Cell Mol. Biol.* 61 (1), 31–41. doi:10.1165/rcmb.2018-0416TR

Schiller, H. J., McCann, U. G., Carney, D. E., Gatto, L. A., Steinberg, J. M., and Nieman, G. F. (2001). Altered alveolar mechanics in the acutely injured lung. *Crit. Care Med.* 29, 1049–1055. doi:10.1097/00003246-200105000-00036

Schiller, H. J., Steinberg, J., Halter, J., McCann, U., DaSilva, M., Gatto, L. A., et al. (2003). Alveolar inflation during generation of a quasi-static pressure/volume curve in the acutely injured lung. *Crit. Care Med.* 31, 1126–1133. doi:10.1097/01.CCM.0000059997.90832.29

Schirrmann, K., Mertens, M., Kertzscher, U., Kuebler, W. M., and Affeld, K. (2010). Theoretical modeling of the interaction between alveoli during inflation and deflation in normal and diseased lungs. *J. Biomech.* 43, 1202–1207. doi:10.1016/j.jbiomech.2009.11.025

Schmiedl, A., Ochs, M., Mühlfeld, C., Johnen, G., Brasch, F., et al. (2005). Distribution of surfactant proteins in type II pneumocytes of newborn, 14-day old, and adult rats: an immunoelectron microscopic and stereological study. *Histochem Cell Biol.* 124, 465–476. doi:10.1007/s00418-005-0066-0

Schneider, J. P., and Ochs, M. (2014). Alterations of mouse lung tissue dimensions during processing for morphometry: A comparison of methods. *Am. J. Physiol. Lung Cell Mol. Physiol.* 306, L341–L350. doi:10.1152/ajplung.00329.2013

Schneider, J. P., Wrede, C., Hegermann, J., Weibel, E. R., Mühlfeld, C., and Ochs, M. (2019). On the topological complexity of human alveolar epithelial type 1 cells. *Am. J. Respir. Crit. Care Med.* 199, 1153–1156. doi:10.1164/rccm.201810-1866LE

Schulte, H., Mühlfeld, C., and Brandenberger, C. (2019). Age-related structural and functional changes in the mouse lung. *Front. Physiol.* 10, 1466. doi:10.3389/fphys.2019.01466

Schürch, D., Ospina, O. L., Cruz, A., and Pérez-Gil, J. (2010). Combined and independent action of proteins SP-B and SP-C in the surface behavior and mechanical stability of pulmonary surfactant films. *Biophys. J.* 99, 3290–3299. doi:10.1016/j.bpj.2010.09.039

Schürch, S., Bachofen, H., and Possmayer, F. (2001). Surface activity in situ, in vivo, and in the captive bubble surfactometer. *Comp Biochem Physiol A Mol Integr Physiol* 129, 195–207. doi:10.1016/s1095-6433(01)00316-6

Schürch, S., Goerke, J., and Clements, J. A. (1976). Direct determination of surface tension in the lung. *Proc. Natl. Acad. Sci. U. S. A.* 73, 4698–4702. doi:10.1073/pnas.73.12.4698

Schürch, S. (1982). Surface tension at low lung volumes: Dependence on time and alveolar size. *Respir. Physiol.* 48, 339–355. doi:10.1016/0034-5687(82)90038-x

Sera, T., Yokota, H., Tanaka, G., Uesugi, K., Yagi, N., and Schroter, R. C. (2013). Murine pulmonary acinar mechanics during quasi-static inflation using synchrotron refraction-enhanced computed tomography. *J. Appl. Physiol.* 115, 219–228. doi:10.1152/japplphysiol.01105.2012

Smith, B. J., Roy, G. S., Cleveland, A., Mattson, C., Okamura, K., Charlebois, C. M., et al. (2020). Three alveolar phenotypes govern lung function in murine ventilator-induced lung injury. *Front. Physiol.* 11, 660. doi:10.3389/fphys.2020.00660

Sobin, S. S., Fung, Y. C., and Tremer, H. M. (1988). Collagen and elastin fibers in human pulmonary alveolar walls. *J. Appl. Physiol.* 64, 1659–1675. doi:10.1152/jappl.1988.64.4.1659

Stamenović, D. (1990). Micromechanical foundations of pulmonary elasticity. *Physiol. Rev.* 70, 1117–1134. doi:10.1152/physrev.1990.70.4.1117

Steffen, L., Ruppert, C., Hoymann, H. G., Funke, M., Ebener, S., Kloth, C., et al. (2017). Surfactant replacement therapy reduces acute lung injury and collapse induration-related lung remodeling in the bleomycin model. *Am. J. Physiol. Lung Cell Mol. Physiol.* 313, L313–L327. doi:10.1152/ajplung.00033.2017

Subramaniam, K., Kumar, H., and Tawhai, M. H. (2017). Evidence for age-dependent air-space enlargement contributing to loss of lung tissue elastic recoil pressure and increased shear modulus in older age. *J. Appl. Physiol.* 123, 79–87. doi:10.1152/japplphysiol.00208.2016

Suki, B., Ito, S., Stamenovic, D., Lutchen, K. R., and Ingenito, E. P. (2005). Biomechanics of the lung parenchyma: Critical roles of collagen and mechanical forces. *J. Appl. Physiol.* 98, 1892–1899. doi:10.1152/japplphysiol.01087.2004

Suki, B., Stamenović, D., and Hubmayr, R. (2011). Lung parenchymal mechanics. *Compr. Physiol.* 1, 1317–1351. doi:10.1002/cphy.c100033

Tabuchi, A., Nickles, H. T., Kim, M., Semple, J. W., Koch, E., Brochard, L., et al. (2016). Acute lung injury causes asynchronous alveolar ventilation that can Be corrected by individual sighs. *Am. J. Respir. Crit. Care Med.* 193, 396–406. doi:10.1164/rccm.201505-0901OC

Timpl, R., Wiedemann, H., van Delden, V., Furthmayr, H., and Kühn, K. (1981). A network model for the organization of type IV collagen molecules in basement membranes. *Eur. J. Biochem.* 120, 203–211. doi:10.1111/j.1432-1033.1981.tb05690.x

Tschanz, S., Schneider, J. P., and Knudsen, L. (2014). Design-based stereology: Planning, volumetry and sampling are crucial steps for a successful study. *Ann. Anat.* 196, 3–11. doi:10.1016/j.aanat.2013.04.011

Tschumperlin, D. J., and Margulies, S. S. (1999). Alveolar epithelial surface area-volume relationship in isolated rat lungs. *J. Appl. Physiol.* 86, 2026–2033. doi:10.1152/jappl.1999.86.6.2026

Tschumperlin, D. J., Oswari, J., and Margulies, A. S. (2000). Deformation-induced injury of alveolar epithelial cells. Effect of frequency, duration, and amplitude. *Am. J. Respir. Crit. Care Med.* 162, 357–362. doi:10.1164/ajrccm.162.2.9807003

Untersee, P., Gil, J., and Weibel, E. R. (1971). Visualization of extracellular lining layer of lung alveoli by freeze-etching. *Respir. Physiol.* 13, 171–185. doi:10.1016/0034-5687(71)90088-0

Vasilescu, D. M., Gao, Z., Saha, P. K., Yin, L., Wang, G., Haefeli-Bleuer, B., et al. (2012). Assessment of morphometry of pulmonary acini in mouse lungs by nondestructive imaging using multiscale microcomputed tomography. *Proc. Natl. Acad. Sci. U. S. A.* 109, 17105–17110. doi:10.1073/pnas.1215112109

Vasilescu, D. M., Phillion, A. B., Kinose, D., Verleden, S. E., Vanaudenaerde, B. M., Verleden, G. M., et al. (2020). Comprehensive stereological assessment of the human lung using multiresolution computed tomography. *J. Appl. Physiol.* 128, 1604–1616. doi:10.1152/japplphysiol.00803.2019

Vlahakis, N. E., and Hubmayr, R. D. (2005). Cellular stress failure in ventilator-injured lungs. *Am. J. Respir. Crit. Care Med.* 171, 1328–1342. doi:10.1164/rccm.200408-1036SO

Vyshedskiy, A., Alhashem, R. M., Paciej, R., Ebril, M., Rudman, I., Fredberg, J. J., et al. (2009). Mechanism of inspiratory and expiratory crackles. *Chest* 135, 156–164. doi:10.1378/chest.07-1562

Wagner, W., Bennett, R. D., Ackermann, M., Ysasi, A. B., Belle, J., Valenzuela, C. D., et al. (2015). Elastin cables define the axial connective tissue system in the murine lung. *Anat. Rec. Hob.* 298, 1960–1968. doi:10.1002/ar.23259

Wasnick, R., Korfei, M., Piskulak, K., Henneke, I., Wilhelm, J., Mahavadi, P., et al. (2023). Notch1 induces defective epithelial surfactant processing and pulmonary fibrosis. *Am. J. Respir. Crit. Care Med.* 207, 283–299. doi:10.1164/rccm.202105-1284OC

Webb, W. R. (2006). Thin-section CT of the secondary pulmonary lobule: Anatomy and the image--the 2004 fleischner lecture. *Radiology* 239, 322–338. doi:10.1148/radiol.2392041968

Weibel, E. R., Federspiel, W., Fryder-Doffey, F., Hsia, C., König, M., Stalder-Navarro, V., et al. (1993). Morphometric model for pulmonary diffusing capacity. I. Membrane diffusing capacity. *Respir. Physiol.* 93, 125–149. doi:10.1016/0034-5687(93)90001-q

Weibel, E. R., and Gil, J. (1968). Electron microscopic demonstration of an extracellular duplex lining layer of alveoli. *Respir. Physiol.* 4, 42–57. doi:10.1016/0034-5687(68)90006-6

Weibel, E. R., and Gomez, D. (1962). Architecture of the human lung. Use of quantitative methods establishes fundamental relations between size and number of lung structures. *Science* 137, 577–585. doi:10.1126/science.137.3530.577

Weibel, E. R., and Knight, B. (1964). A morphometric study on the thickness of the pulmonary air-blood barrier. *J. Cell Biol.* 21, 367–396. doi:10.1083/jcb.21.3.367

Weibel, E. R. (2017). Lung morphometry: The link between structure and function. *Cell Tissue Res.* 367, 413–426. doi:10.1007/s00441-016-2541-4

Weibel, E. R. (2009). What makes a good lung? *Swiss Med. Wkly.* 139, 375–386. doi:10.4414/smw.2009.12270

Wilson, T. A., and Bachofen, H. (1982). A model for mechanical structure of the alveolar duct. *J. Appl. Physiol.* 52, 1064–1070. doi:10.1152/jappl.1982.52.4.1064

Wirtz, H. R., and Dobbs, L. G. (1990). Calcium mobilization and exocytosis after one mechanical stretch of lung epithelial cells. *Science* 250, 1266–1269. doi:10.1126/science.2173861

Woods, J. C., Choong, C. K., Yablonskiy, D. A., Bentley, J., Wong, J., Pierce, J. A., et al. (2006). Hyperpolarized 3He diffusion MRI and histology in pulmonary emphysema. *Magn. Reson Med.* 56, 1293–1300. doi:10.1002/mrm.21076

Wu, H., Yu, Y., Huang, H., Hu, Y., Fu, S., Wang, Z., et al. (2020). Progressive pulmonary fibrosis is caused by elevated mechanical tension on alveolar stem cells. *Cell* 180, 107–121. doi:10.1016/j.cell.2019.11.027

Wu, Y., Kharge, A. B., and Perlman, C. E. (2014). Lung ventilation injures areas with discrete alveolar flooding, in a surface tension-dependent fashion. *J. Appl. Physiol.* 117, 788–796. doi:10.1152/japplphysiol.00569.2014

Yazicioglu, T., Mühlfeld, C., Autilio, C., Huang, C. K., Bär, C., Dittrich-Breiholz, O., et al. (2020). Aging impairs alveolar epithelial type II cell function in acute lung injury. *Am. J. Physiol. Lung Cell Mol. Physiol.* 319, L755–L769. doi:10.1152/ajplung.00093.2020

Frontiers in Physiology

TYPE Review
PUBLISHED 22 March 2023
DOI 10.3389/fphys.2023.1130096

OPEN ACCESS

EDITED BY
Sam Bayat,
Université Grenoble Alpes, France

REVIEWED BY
Tilo Winkler,
Massachusetts General Hospital and Harvard Medical School, United States
Gergely H. Fodor,
University of Szeged, Hungary
François Marchal,
Université de Lorraine, France

*CORRESPONDENCE
Greetje Vande Velde,
✉ greetje.vandevelde@kuleuven.be

SPECIALTY SECTION
This article was submitted to Respiratory Physiology and Pathophysiology, a section of the journal Frontiers in Physiology

RECEIVED 22 December 2022
ACCEPTED 10 March 2023
PUBLISHED 22 March 2023

CITATION
Ahookhosh K, Vanoirbeek J and Vande Velde G (2023), Lung function measurements in preclinical research: What has been done and where is it headed?
Front. Physiol. 14:1130096.
doi: 10.3389/fphys.2023.1130096

Lung function measurements in preclinical research: What has been done and where is it headed?

Kaveh Ahookhosh[1], Jeroen Vanoirbeek[2] and Greetje Vande Velde[1]*

[1]Biomedical MRI, Department of Imaging and Pathology, KU Leuven, Leuven, Belgium, [2]Centre of Environment and Health, Department of Public Health and Primary Care, KU Leuven, Leuven, Belgium

Due to the close interaction of lung morphology and functions, repeatable measurements of pulmonary function during longitudinal studies on lung pathophysiology and treatment efficacy have been a great area of interest for lung researchers. Spirometry, as a simple and quick procedure that depends on the maximal inspiration of the patient, is the most common lung function test in clinics that measures lung volumes against time. Similarly, in the preclinical area, plethysmography techniques offer lung functional parameters related to lung volumes. In the past few decades, many innovative techniques have been introduced for *in vivo* lung function measurements, while each one of these techniques has their own advantages and disadvantages. Before each experiment, depending on the sensitivity of the required pulmonary functional parameters, it should be decided whether an invasive or non-invasive approach is desired. On one hand, invasive techniques offer sensitive and specific readouts related to lung mechanics in anesthetized and tracheotomized animals at endpoints. On the other hand, non-invasive techniques allow repeatable lung function measurements in conscious, free-breathing animals with readouts related to the lung volumes. The biggest disadvantage of these standard techniques for lung function measurements is considering the lung as a single unit and providing only global readouts. However, recent advances in lung imaging modalities such as x-ray computed tomography and magnetic resonance imaging opened new doors toward obtaining both anatomical and functional information from the same scan session, without the requirement for any extra pulmonary functional measurements, in more regional and non-invasive manners. Consequently, a new field of study called pulmonary functional imaging was born which focuses on introducing new techniques for regional quantification of lung function non-invasively using imaging-based techniques. This narrative review provides first an overview of both invasive and non-invasive conventional methods for lung function measurements, mostly focused on small animals for preclinical research, including discussions about their advantages and disadvantages. Then, we focus on those newly developed, non-invasive, imaging-based techniques that can provide either global or regional lung functional readouts at multiple time-points.

KEYWORDS

pulmonary function tests, non-invasive tests, invasive tests, pulmonary functional imaging, imaging-based techniques

1 Introduction

Lungs play the most important role in the gas exchange process by transferring oxygen from the inhaled air to blood. Any chronic pulmonary abnormality eventually causes morphological destructions in the lung, which consequently reflect as pulmonary functional changes (Hoymann, 2007). Due to this close relationship between lung morphology and function, accurate measurement of lung function at multiple time-points is of great interest for diagnostic and prognostic purposes. Since the primary function of the lung is gas exchange, the pulmonary function can be characterized by ventilation, the distribution of the inhaled air into and out of the alveoli, and perfusion, the flow of blood to alveolar capillaries (Powers and Dhamoon, 2019).

Pulmonary function tests (PFTs) are not only valuable in the clinical context, but also in an experimental context which they are of utmost importance. Animal models are extremely crucial for gaining deeper insight into the cellular and molecular mechanisms involved in the pathogenesis of pulmonary diseases, simply because they allow experiments that are not authorized with humans (Nemery et al., 1987; Bates and Irvin, 2003). The principles controlling ventilation, airflow, lung volume, and gas exchange are almost the same among most of the mammals (Costa and Tepper, 1988; Hoymann, 2007; Hoymann, 2012). During the past decades, the growing interest in longitudinal lung functional studies on rodents led to an exploration for finding novel, more sensitive, non-invasive methods for repeated pulmonary function measurements (Glaab et al., 2007; Hoymann, 2007; Bates, 2017). This search resulted in introducing many invasive and non-invasive techniques for obtaining lung functional data during longitudinal animal studies in different lung research areas, such as pharmacological efficacy studies, safety pharmacological studies, and toxicological investigations (Bates and Irvin, 2003; Glaab et al., 2005; Hoymann, 2007; Hoymann, 2012; Bates, 2017). Each of these methods has their own advantages and disadvantages, which makes them suitable only for certain kinds of experiments (Glaab et al., 2007; de Andrade Castro and Russo, 2019). On one hand, invasive methods use anesthetized, paralyzed, tracheotomized animals, which are far from their natural conditions, however, they offer precise and specific readouts closely related to lung mechanics (De Vleeschauwer et al., 2011). On the other hand, non-invasive methods conveniently allow repeated pulmonary functional measurements in conscious animals with readouts related to the lung volumes, but with less sensitivity to pulmonary mechanics compared to the invasive methods (Hoymann, 2007). Therefore, based on the goal of the experiment, it should be decided whether functional readouts related to natural breathing patterns of conscious animals are required (non-invasive methods), or sensitive, accurate, and specific parameters related to lung mechanics (invasive methods).

These conventional methods of lung function measurements, invasive and non-invasive, only deliver global readouts. While, a wide range of lung diseases start locally by deteriorating lung parenchyma as well as small airways, and their functional effects are usually masked by lung compensatory mechanisms until significant sections of the lung structure are lost (Hsia, 2004; Burgel et al., 2013; Hsia, 2017; Stockley et al., 2017). Since small airways contribute minimally to airflow resistance, standard PFTs in clinics, such as spirometry and plethysmography which measure pulmonary functional parameters related to lung volumes cannot detect their loss at early stages. In the case of small airway diseases, such as COPD, fibrosis, emphysema, etc., these PFTs detect the lung function loss only after obstruction/destruction of 75% of the small airways (Cosio et al., 1978; Burgel et al., 2013). Therefore, the site of these small airways, approximately from the 8th generation to terminal bronchioles and respiratory bronchioles, is called the "silent zone" (Burgel et al., 2013; Stockley et al., 2017). The biggest disadvantage of standard PFTs is that they consider the lung as a single unit, providing only global averages of functional parameters for the whole lung, which are not sensitive enough for early detection of most of the lung abnormalities (Ohno et al., 2022). This major limitation of the conventional PFTs prompted a search for techniques to acquire regional lung function data instead of global readouts. These techniques can be performed at experimental end-point, but are preferably non-invasive in the sense that the animals can fully recover from repeated functional measurements without any long-term injuries interfering with the experimental research question. Due to the recent advances of lung imaging modalities such as computed tomography (CT), magnetic resonance imaging (MRI), and nuclear medicine techniques, a new concept has emerged called "pulmonary functional imaging", which utilizes imaging-based techniques to regionally measure lung functions (Gefter et al., 2021; Ohno et al., 2021). Pulmonary functional imaging with ability to provide regional lung functional data significantly improves our ability to detect and longitudinally evaluate many chronic pulmonary diseases at early stages. In the past few decades, several non-invasive techniques have been proposed for pulmonary functional imaging using CT, MRI, and nuclear medicine for clinical applications (Gefter et al., 2021; Ohno et al., 2021; Kooner et al., 2022; Ohno et al., 2022). Due to the importance of animal models in the understanding of pathogenesis of pulmonary diseases, these non-invasive, imaging-based techniques for regional lung function measurements are equally important for preclinical lung research.

In this narrative review, we describe and discuss both conventional and state-of-the-art experimental methods for lung function measurements focusing on small animals for preclinical and basic lung research. These methods fall roughly into two major categories, namely invasive, *i.e.* end-point measurements and non-invasive methods that can be applied repeatedly in the same animal, with or without a short anesthesia period. We further divide the non-invasive methods into imaging-based and non-imaging-based techniques. Then, we focus on those newly developed, non-invasive, imaging-based techniques that can provide either global or regional lung functional readouts at multiple time-points. We conclude with a discussion about future perspective of PFTs for longitudinal animal studies in biomedical research.

2 The role of pulmonary function tests in preclinical lung research

Murphy DG (2002) described the function of the respiratory system as a pumping apparatus, which includes nervous and muscular components, and a gas exchange unit (Murphy, 2002). While defects in the pumping apparatus can disrupt the breathing pattern, structural changes in airways, alveoli, and interstitial tissues including blood and lymph vessels that form the gas exchange unit lead to obstructive or restrictive diseases. Therefore, any change in pulmonary function detected by the standard PFTs stems from either disruption in pulmonary ventilation, or alteration in the mechanical properties of lungs (Murphy, 2002; Hoymann, 2012). For capturing these pulmonary function changes during progression of respiratory disorders, various invasive and non-invasive methods have been introduced throughout the past decades. These PFTs offer different lung functional parameters with different levels of sensitivities, with each one of these methods fitting to certain research questions. In the following subsections, we provide a detailed overview of both invasive and non-invasive PFTs for lung function measurements mostly in rodents, as well as discussions about their advantages and disadvantages that make them suitable for certain kinds of *in vivo* experiments.

2.1 Invasive methods for lung function measurements

Under invasive techniques for lung function measurements, we consider those methods that require the animals to be either orotracheally intubated (Likens and Mauderly, 1982; Brown et al., 1999; Glaab et al., 2004) or intubated *via* tracheostomy (Palecek et al., 1967), while breathing spontaneously or being mechanically ventilated during the procedure (Jackson and Watson, 1982; Schuessler and Bates, 1995). As this will lead to long-term injury, in practice, these methods are mostly considered as end-point measurements, carried out under terminal anesthesia compared to non-invasive methods, the value of invasive PFTs and pulmonary maneuvers lies in that they are far more sensitive for detecting those obstructive/restrictive lung disorders that change the mechanical properties of the gas exchange units.

2.1.1 Dynamic compliance and lung resistance with plethysmography

Measurement of parameters such as dynamic compliance (C_{dyn}) and lung resistance (R_L) using invasive lung function measurements is a classical approach to determine pulmonary mechanics and airway responsiveness (Glaab et al., 2007). For the first time, in 1988, Martin et al. showed the viability of measuring these two parameters, C_{dyn} and R_L, in anesthetized, tracheotomized, and ventilated mice using body plethysmography (Martin et al., 1988). In this study, for evaluation of the bronchoconstrictor responses of normal C57BL/6 mice to bronchoconstrictor agonists, the authors connected the tracheotomized mice placed in a plethysmograph chamber to a pressure transducer and ventilator, where the device was set to provide 150 breathes/min with tidal volumes of 5–6 ml/kg. Lung volume changes of the mice were recorded by the plethysmograph using the pressure changes inside the chamber, which alongside the transducer signal and flow information were used to calculate the pulmonary compliance and resistance by the method of Amdur and Mead. (1958), that relates the tidal volume and the flow rate to intrapleural pressure at specific points during the respiratory cycle information to acquire the mechanical properties of the lungs. Followed by this pioneering technique, many more methods have been reported for measurement of C_{dyn} and R_L in anesthetized, tracheotomized mice using body plethysmography (Takeda et al., 1997; Taube et al., 2002; Irvin and Bates, 2003). In an attempt for repetitive measurements of C_{dyn} and R_L in mice, Brown et al. proposed a rapid, repeated intubation technique for anesthetized mice instead of tracheotomy (Brown et al., 1999). In this technique, the animal should be suspended at a 45° angle using a plexiglass support, while a light source illuminated the trachea below the vocal cord for better visualization. For a better view of the tracheal opening, a metal laryngoscope was used to keep the mouth open and hold the tongue out of the way to intubate the animal with a catheter attached to the hub of a needle. In this investigation, the authors have studied neither the maximum number of repeated intubations nor the timing between them which left doubts about the feasibility of the proposed method for repetitive measurements of C_{dyn} and R_L in anesthetized, instrumented mice (Brown et al., 1999).

In general, pulmonary compliance (C) can be defined as a parameter for measurement of lung expansion per each unit increase in the transpulmonary pressure, which can be divided into static and dynamic compliances (Marshall, 1957; Desai and Moustarah, 2020). While static compliance (C_{stat}) represents pulmonary compliance when there is a fixed volume and no airflow, dynamic compliance describes the compliance during breathing and it monitors both elastic and airway resistance (Desai and Moustarah, 2020). Since certain respiratory disorders such as pulmonary fibrosis, emphysema, COPD, atelectasis, and newborn respiratory distress syndrome directly change the elastic properties of lung parenchyma, monitoring the compliance curve can be helpful to determine their progression (Lu and Rouby, 2000). In general, important factors such as elasticity of lung parenchyma, surface tension, surfactant, lung volume, smooth muscle contraction, and peripheral airway inhomogeneity can be considered as direct determinants of pulmonary compliance (Glaab et al., 2007; Desai and Moustarah, 2020). R_L, which represents both airway and tissue resistance, is a dynamic force against the tracheobronchial tree and to some extend parenchyma deformation, which reflects both narrowing of the conducting airways and parenchymal viscosity (Glaab et al., 2007). Airway resistance (R_{aw}), which can be described as the ratio between the pressure drop across the airway tree and the resulting airflow, highly depends on the geometry of the airway tree and the viscosity of the resident gas (Czovek, 2019). As the other contributor to lung resistance, tissue resistance (R_{ti}), is a fundamental characteristic that is highly related to the elastic property of the tissue (Czovek, 2019). Asthma, COPD, cystic fibrosis, emphysema, and airway tumors are common pathological conditions that increase lung resistance (Özdilek, 2022).

Airway resistance and dynamic compliance are widely considered gold-standard parameters for diagnosis and quantification of bronchoconstriction and obstruction (Glaab et al., 2005; Hoymann, 2007; Ewart et al., 2010). The sensitivity and specificity of these parameters make them ideal choices for follow-up studies of testing safety of pharmacological compounds; however, despite many advantages, most of the approaches that measure pulmonary compliance and resistance require anesthetized and intubated/tracheotomized animals, which is far from the natural condition and mostly an endpoint for them (Bates and Irvin, 2003).

2.1.2 Forced oscillation technique

The forced oscillation technique (FOT), for the first time introduced by DuBois et al. (1956), is a technique based on sinusoidal sound waves of a single frequency that pass through the lungs to provide information about pulmonary mechanics with parameters such as respiratory impedance (Zrs). Zrs is defined as the mechanical load of the respiratory system to ventilation (Navajas et al., 1991), and can be divided into resistance, which describes the resistance of conducting airways and tissue, and reactance (X), which reflects respiratory compliance and characterizes lung parenchyma (Glaab et al., 2007). For more insights into the basic concepts of FOT, we refer to (Pride, 1992; MacLeod and Birch, 2001; Oostveen et al., 2003; Tepper and Costa, 2015; Lundblad et al., 2021). To investigate the effects of drugs and diseases on pulmonary mechanics, FOT has been employed for measuring respiratory impedance both in rats (Jackson and Watson, 1982; Preuss et al., 1999) and mice (Schuessler and Bates, 1995; Vanoirbeek et al., 2010; Devos et al., 2017; Mori et al., 2017). Compared to the classical FOT approach for measuring pulmonary resistance and compliance, low-frequency forced oscillation technique (LFOT) provides even more details about pulmonary mechanics (Irvin and Bates, 2003; Peslin and Fredberg, 2011). In the case of LFOT, because a lower frequency sound wave travels further in the conducting airways and reaches smaller airways and lung parenchyma, it can provide more detailed information about lung mechanics (Brashier and Salvi, 2015). The biggest advantage of LFOT is the capability of showing differentiation between airway and tissue mechanics (Glaab et al., 2007).

The impulse oscillometry system (IOS), introduced by Michaelson et al., in 1975 using a computer-driven loudspeaker, is a FOT technique that utilizes multiple sound frequencies at the same time instead of a single frequency (Michaelson et al., 1975). The main advantage of employing multiple oscillation frequencies is that IOS calculates airway resistance in a way that allows differentiation between the behavior of large and small airways. Nowadays, almost all of the commercialized devices for lung function measurements such as FlexiVent [SCIREQ© (Inc, 2022)] employ multiple oscillation frequencies for pulmonary functional and mechanical assessments. In the case of any airway obstruction, either in the central or peripheral airways, the total airway resistance increases above the normal value (Brashier and Salvi, 2015). Therefore, LFOT and IOS are accurate and powerful techniques to measure parameters such as resistance, reactance, and consequently respiratory impedance over a range of frequencies. However, similar to invasive plethysmography techniques, implementing these techniques still requires anesthesia, intubation, and even a higher level of expertise in handling.

Similar to preclinical lung research, FOT measurements also play an important role in clinical practice for early detection of the effects of smoking and COPD (Goldman, 2001; Oostveen et al., 2003; Ribeiro et al., 2018; Bhattarai et al., 2020). FOT as a non-invasive technique for measuring respiratory mechanics is already approved after comparative studies with classical spirometry readouts (Dellacà et al., 2004; Faria et al., 2010; Amaral et al., 2013; Su et al., 2018). The modern clinical devices for FOT measurements are able to cover a wide range of frequencies, lower than 5 Hz to assess peripheral airways and higher than 20 Hz to measure proximal airway resistance, which allows independent evaluation of proximal and peripheral airways (Shinke et al., 2013; Contoli et al., 2016; Berger, 2018). For low frequency measurements, i.e. less than 5 Hz, loudspeakers, a piston-type mechanical device (Kaczka et al., 1997), or pneumatic proportional solenoid valves (Kaczka and Lutchen, 2004) are used. Despite the advantages of FOT measurements, more clinical studies are required for correct interpretation of parameters such as elastance and reactance that highly depend on frequency (King et al., 2020).

2.1.3 Forced pulmonary maneuvers

The two most commonly used commercially available devices for invasive lung function measurements in small animals are FlexiVent [SCIREQ© (Inc, 2022)] and Buxco-forced pulmonary maneuvers [DSI© (Buxco, 2022)] (Figure 1). These devices are widely considered the gold-standard for *in vivo* lung function measurements, since both of them are capable of performing forced oscillation technique, negative pressure-driven forced expiratory maneuvers (NPFE), and measuring standard pressure-volume (PV) curves. These techniques offer relevant parameters such as resistance, compliance, and elastance in anesthetized animals with high sensitivity and specificity. To delineate the existing potential of the invasive and non-invasive methods for lung function measurements, Vanoirbeek et al. (2010) employed FlexiVent and Buxco systems, as well as unrestrained plethysmography to assess two well-established models lung disease: a model of elastase-induced pulmonary emphysema, and a model of bleomycin-induced pulmonary fibrosis. The invasive techniques, unlike unrestrained plethysmography, using lung functional parameters such as functional residual capacity, total lung capacity, vital capacity, and compliance of the respiratory system could effectively distinguish the pulmonary emphysema from fibrosis. They concluded that both invasive systems for lung function measurements are sensitive enough for monitoring lung pathologies, however, FlexiVent has the advantage of an in-line nebulizer for testing hyperreactivity with methacholine. However, these commercialized devices for lung function measurements share the same disadvantages as the previous invasive techniques, including the requirement for terminal anesthesia, intubation/tracheostomy, high level of expertise in handling, and ventilatory maneuvers instead of spontaneous breathing, which does not always reflect the physiological situation (de Andrade Castro and Russo, 2019). Furthermore, one animal at a time can be handled during each lung function measurement which makes the technique time-consuming in *vivo* animal studies. Among these, the most important drawback is that these are endpoint lung function measurements due to tracheostomy, however, attempts have been made to address this issue by replacing tracheostomy with intubation for repeated invasive lung function measurements (Glaab et al., 2004; Glaab et al., 2005; De Vleeschauwer et al., 2011; Bonnardel et al., 2019). In a recent attempt, Bonnardel et al. used the FlexiVent system to prove the feasibility of repeated lung function measurements by intubation of healthy BALB/cJ mice and C57BL/6J mice to obtain parameters such as forced vital capacity (FVC), compliance of respiratory system (Crs), and forced expiratory volume in the first 0.1 s (FEV0.1) (Bonnardel et al., 2019). The authors reported an accurate evaluation of FVC, Crs, and FEV0.1 for intubated BALB/cJ mice, and FVC, FEV0.1, and inspiratory capacity (A)

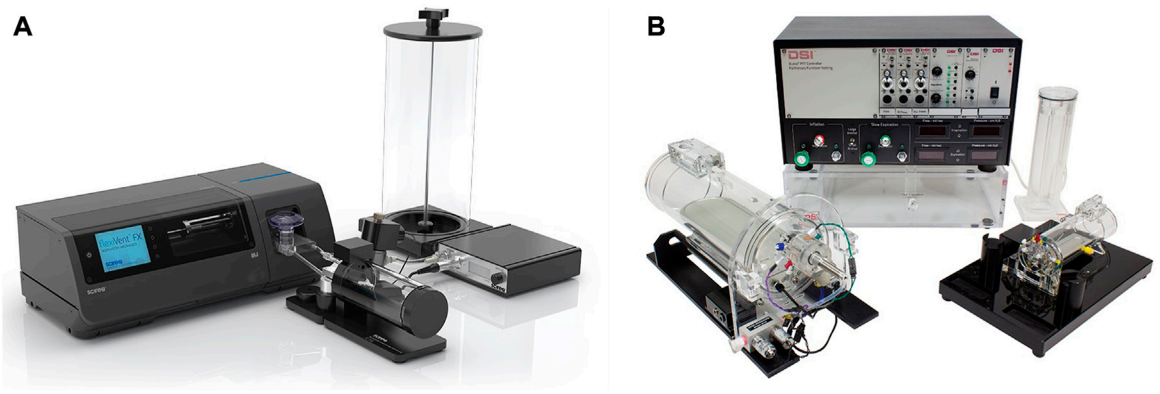

FIGURE 1
Commercially available experimental setups for *in vivo* lung function measurements in small animals **(A)** FlexiVent [reprinted from www.scireq.com (Inc, 2022)]; **(B)** Buxco [reprinted from www.datasci.com (Buxco, 2022)].

for intubated C57BL/6J mice. Despite the efforts for showing the feasibility of performing repetitive invasive lung function measurements in small animals, they are not suitable for reproducibly repeated measurements, resulting in that commercially available devices are still routinely used for endpoint measurements only. The lack of an alternative, truly non-invasive method for reproducible, repetitive detailed lung function measurements warrants further investigations for finding a reliable method with the least invasiveness for obtaining detailed lung functional data with direct readouts related to lung mechanics.

2.2 Non-invasive methods for lung function measurements in rodents

For *in vivo* longitudinal investigations of pulmonary function as well as screening large numbers of conscious small animals, non-invasive approaches are a prerequisite. In the following sections, we divide the non-invasive conventional methods and state-of-the-art techniques for lung function measurements into imaging-based and non-imaging-based methods and discussed them in detail.

2.2.1 Non-imaging-based techniques

2.2.1.1 Unrestrained whole-body plethysmography

Non-invasive plethysmography techniques offer lung function readouts of conscious animals longitudinally. Unrestrained whole-body plethysmography (UWBP), as an extreme of non-invasiveness, provides lung function data of several awake mice/rats at the same time and at several time points. Basically, the animals are placed each into a separate closed chamber to record breathing-induced oscillations of pressure inside the chamber by employing a barometric analysis technique. This technique provides parameters such as tidal volume and respiratory frequency (Glaab et al., 2007; Vanoirbeek et al., 2010; Bates, 2017). UWBP has been employed by many researchers for longitudinal measurement of lung functions in spontaneously breathing animals, especially by reporting a parameter called enhanced pause (Penh) (Hamelmann et al., 1997; Chong et al., 1998; Finotto et al., 2001; Donaldson et al., 2002). Penh is a dimensionless parameter used for the evaluation of changes in the shape of the airflow entering and leaving a whole-body plethysmograph (Bates, 2017). In 1997, for the first time using UWBP, a study on airway hyperresponsiveness (AHR) using aerosolized methacholine challenge in conscious, spontaneously breathing mice, revealed a good correlation between Penh and readouts such as lung resistance obtained from an invasive method (Hamelmann et al., 1997). Following this pioneering study, a few more investigations confirmed good correlations between Penh and gold-standard functional parameters obtained from invasive lung function measurements (Chong et al., 1998; Berry et al., 1999; Finotto et al., 2001; Donaldson et al., 2002; Kumar et al., 2004). However, further experiments have raised serious uncertainties and questions such as: what Penh as a dimensionless index really measures and to what extent it can be related to lung mechanics (Lundblad et al., 2002; Mitzner and Tankersley, 2003; Adler et al., 2004; Bates et al., 2004; Sly et al., 2005). Using unrestrained plethysmography investigating the relationship between Penh and lung resistance, it has been shown that UWBP can determine lung resistance only when tidal volume and functional lung capacity are measured independently. Also, humidity and temperature of the gas inside the chamber should be preconditioned to the animal's body (Lundblad et al., 2002). Since fulfilling these conditions with conscious, unrestrained animals are not possible, the authors suggested that Penh should not be used for bronchial responsiveness assessments and sent a clear warning to the community that Penh cannot represent airway or pulmonary resistance. Followed by this enlightening study, more researchers (Adler et al., 2004; Bates et al., 2004) shared their serious concerns about replacing invasive mechanical indexes such as lung resistance with Penh, since this dimensionless parameter lacks the necessary physical principles. Despite intense criticism against the application of Penh to measure airway reactivity and AHR, for further exploration of Penh, Lomask discussed the mathematics of unrestrained plethysmography for two types of whole-body plethysmographs, pressure (PWBP) and flow (FWBP) plethysmographs (Lomask, 2006). The author confirmed that PWBP that utilizes a sealed chamber poorly correlates with airway resistance at room temperature. However, the Penh values obtained by FWBP that uses a chamber with a pneumotachograph correlate with resistance. Similarly, the relationships between Penh and thoracic airflow patterns have shown that Penh of plethysmography airflow is a sensitive indicator of an increase in specific airway resistance (Frazer et al., 2011). Nevertheless, UWBP as a convenient, quick, and non-invasive method can be employed for gross screening of overall ventilatory function in rodents. However, considering the cautionary warnings toward the misusage of Penh, especially in lung studies on airway responsiveness, ventilatory function obtained from UWBP should be corroborated with independent direct measurements of pulmonary mechanics (Vanoirbeek et al., 2004; Vanoirbeek et al., 2006; Hoymann, 2007; Tarkowski et al., 2007).

2.2.1.2 Unrestrained video-assisted plethysmography

Since lung function data obtained from unrestrained plethysmography have no direct link to the mechanical properties of the lung, Bates et al. (2008) introduced unrestrained video-assisted plethysmography (UVAP) to non-invasively determine lung mechanical function in small animals. Reliable measurement of lung mechanical function requires a precise assessment of lung volume changes during the animal's breathing, which is beyond the capability of UWBP (Lundblad et al., 2002; Adler et al., 2004; Bates et al., 2004). However UVAP, as an extension of UWBP, was an attempt to more precisely estimate lung volume using orthogonal video imaging (Bates et al., 2008). In UWBP, the measurements are based on the chamber pressure fluctuations due to the animal's breathing, which results from the fact that the change in lung volume is not equal to the volume of inspired air from the chamber. Two physical processes can be introduced as the reason for this difference (Mitzner and Tankersley, 2003; Adler et al., 2004; Bates et al., 2008): (Hoymann, 2007) During inspiration, the respiratory musculature produces a necessary pressure gradient that drives the inspired air through the resistive airways, which also leads to thoracic gas compression; (Powers and Dhamoon, 2019); Due to the different temperature and humidity inside the thorax compared to the chamber, the inspired air expands inside the lungs. It has been shown that the pressure change due to the gas conditioning inside the lungs can be eliminated by heating and humidifying the air inside the plethysmography chamber to match the condition inside the lungs (Lundblad et al., 2002). Therefore, by preconditioning the air inside the chamber, the pressure fluctuations during the animal's breathing can be related directly to the thoracic gas compression, which is also influenced by tidal volume (Bates et al., 2008). The constructed plethysmograph was a cuboidal chamber with two clear orthogonal sides for monitoring the animal, and a water jacket on the remaining sides for controlling the temperature inside the chamber. The humidity of the chamber was also controlled continuously by introducing a stream of air to the chamber after passing over a flask of hot water, except for those brief moments when lung function measurements were acquired, and the chamber was completely sealed. A pressure transducer was utilized for assessment of the pressure inside the chamber relative to the atmospheric pressure and two video cameras were fixed close to the plethysmography chamber to monitor the two orthogonal sides. Using this setup, the authors tried to simultaneously measure the pressure inside the chamber, as well as the changes in lung volume by assuming the animal's body as an elliptical cross section in the acquired orthogonal silhouettes (Bates et al., 2008).

As the biggest advantage of this system, UVAP is able to directly and more precisely measure specific airway resistance in unrestrained and spontaneously breathing mice compared to UWBP. However, there are still downsides to this system (Reynolds and Frazer, 2011): (Hoymann, 2007) movements of the animals are problematic due to the slow sampling resolution (25 Hz, camera speed) of the cameras; (Powers and Dhamoon, 2019); controlling the conditions inside the chamber including temperature and humidity makes the system more complicated and even may induce stress to the animal. Due to the mentioned limitations, despite the solid theory related to lung mechanics behind the UVAP, this extension of unrestrained plethysmography was unable to replace the invasive methods for lung function measurements and never became a widely used method for lung mechanical function measurements in small animals.

2.2.1.3 Acoustic whole-body plethysmography

Acoustic whole-body plethysmography (AWBP), similar to UVAP, attempts to measure tidal volume more accurately compared to UWBP. The acoustic plethysmograph proposed by Reynolds and Frazer included a main chamber, nozzle, speaker, microphone, and end stop assembly to change the volume, which represents a resonant cavity that operates at a frequency that depended on the volume of the cavity and also the dimensions of the nozzle (Reynolds and Frazer, 2006). During the breathing of the animal in the plethysmography chamber, the volume around the animal changes due to the thorax movements which influences the amplitude of the acoustic pressure inside the chamber. In this system, the acoustic pressure of the chamber is almost independent of the animal's lung volume, due to the fact that the acoustic input impedance of the system is very large because of the large change in area from the chamber to the nasal opening (Reynolds and Frazer, 2006). Since the sound pressure level (SPL) of the plethysmograph has a direct relationship with the signal-to-noise ratio of volume measurements, the sensitivity of the AWBP can be increased with higher values of SPLs, which is tolerable for mice (Fay, 1988). The acquired acoustic pressure signal inside the chamber was related to tidal volume using a signal processing technique. Similar to UVAP, VWBP can directly measure specific airway resistance in unrestrained, spontaneously breathing animals. However, this system is susceptible to ambient noise frequencies near the excitation frequency (Reynolds and Frazer, 2011), making it impractical to use for precise assessment of lung volume changes during the animal's breathing in a laboratory setting without acoustic insulation.

2.2.1.4 Head-out body plethysmography

In head-out body plethysmography (Glaab et al., 2007), the head and body of the animal are separated by a seal in the plethysmograph, wherein the animal's head is exposed to a continuous airflow in the head chamber, and the rest of the body

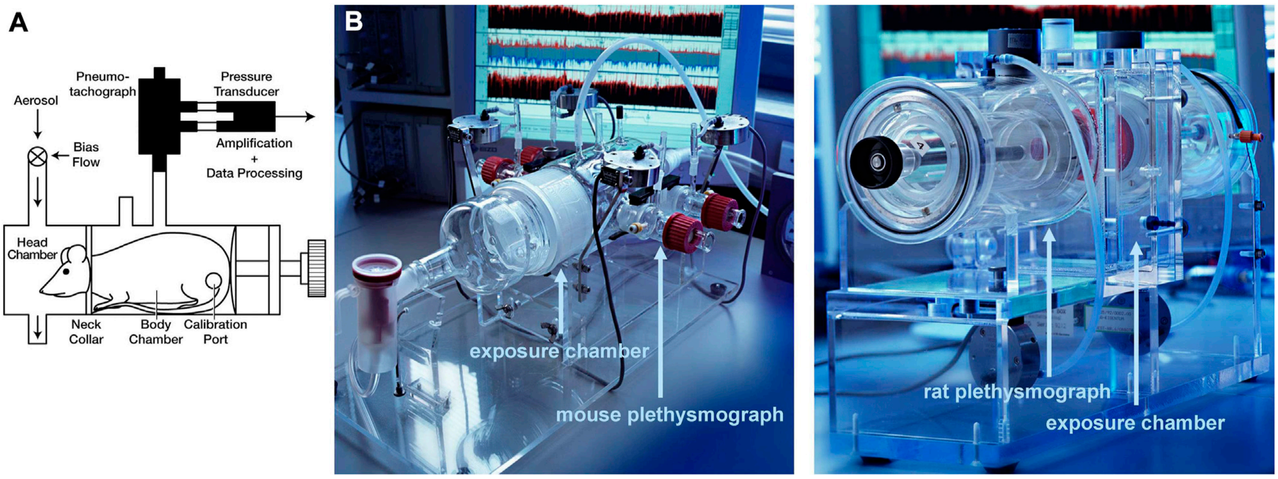

FIGURE 2
Head-out plethysmography **(A)** Schematic and **(B)** Photos of head-out plethysmography systems for mice and rats [reprinted from Hoymann. (2012)].

is placed in the body chamber which is attached to a pressure transducer by a pneumotachograph tube (Figure 2). In the body chamber, the thoracic movements of the animal drive the flow to the pneumotachograph tube which finally reaches the differential pressure transducer, where the respiratory flow is measured and parameters such as respiratory rate and tidal volume are obtained (Hoymann, 2007). Commonly for employing this approach, the animals should be trained a few days before the lung function measurements to get used to the head-out plethysmograph (Hoymann, 2012). The introduction of head-out body plethysmography dates back to 1994, when Vijayaraghavan et al. non-invasively measured mid-expiratory flow (EF_{50}) for the assessment of airway responsiveness in conscious mice (Vijayaraghavan et al., 1994). EF_{50} is the midpoint of expiratory tidal volume, which can perfectly describe the main changes in tidal volume due to an airflow limitation caused by bronchoconstriction, edema, or accumulation of mucus (Glaab et al., 2007; Hoymann, 2012). Since then, many other research groups employed head-out plethysmography for examination of drug effects and proposed EF_{50} as a meaningful, non-invasive parameter for determination of bronchoconstriction in mice and rats (Neuhaus-Steinmetz et al., 2000; Glaab et al., 2001; Glaab et al., 2002; Baelder et al., 2005; Glaab et al., 2005). In addition, validation studies by employing invasive and non-invasive PFTs showed good correlations between EF_{50} and gold-standard functional parameters (Glaab et al., 2001; Glaab et al., 2002; Glaab et al., 2005). In 2005, Glaab et al. utilized head-out body plethysmography to non-invasively measure EF_{50} in conscious mice which were exposed to inhalable *Aspergillus fumigatus* antigens, paralleled by invasive measurement of pulmonary conductance and dynamic compliance in anesthetized, orotracheally intubated mice (Glaab et al., 2005). The decrease in EF_{50} and pulmonary conductance and dynamic compliance correlated well and despite the higher sensitivity of gold-standard parameters, EF_{50} was sensitive enough to detect airway responsiveness in intact spontaneously breathing mice.

In conclusion, head-out body plethysmography is a non-invasive, simple, and repeatable method for lung function measurements that allows handling several conscious animals at the same time by attaching several chambers to a central system. Head-out body plethysmography offers valuable outputs such as EF_{50} with physical meaning [ml/s] that directly relates to gold-standard pulmonary functional parameters such as airway resistance (Glaab et al., 2007). Despite its advantages, there is a risk of inducing the influence of stress to the results due to retainment of the animal during the measurements. However, this issue can be mitigated to some extent by training the animals beforehand and starting lung function measurements only after the animals settled down to a stable level (Glaab et al., 2007).

2.2.1.5 Double-chamber plethysmography

Double-chamber plethysmograph, as the name explains, consists of two rigid chambers that separate the animal's body from the neck to isolate the animal's head and nose as hermetically as possible in the front chamber, from the rest of the body in the rear chamber (Figure 2). In the front chamber, where the restrained animal is consciously and spontaneously breathing, the produced flow from the nostrils is measured, while in the rear chamber the produced airflow by volume change due to the thorax movements is measured. Either using pressure transducers or pneumotachographs, waveform signals as a function of time from each chamber are recorded, which can finally produce respiratory parameters such as tidal volume and frequency (Reynolds and Frazer, 2011; Mailhot-Larouche et al., 2018). In addition to respiratory parameters, acquiring parameters such as EF_{50} and specific airway resistance (sRaw), which are sensitive to airflow obstruction, is also possible with double-chamber plethysmography (Pennock et al., 1979; Neuhaus-Steinmetz et al., 2000; Glaab et al., 2001; DeLorme and Moss, 2002; Glaab et al., 2002; Flandre et al., 2003). While measurement of airway resistance requires both waveform signals obtained from head- and body-chambers, for calculating EF_{50}, just like head-out body plethysmography, only the signal from body-chamber is needed. Therefore, depending on the application, double-chamber plethysmography can be employed with or without the head-chamber (Mailhot-Larouche et al., 2018). Regardless of the advantages, double-chamber plethysmography shares the same disadvantages as head-out plethysmography, which is the requirement of restraining the animal and facing the risk of inducing the effects of stress to the obtained results. Furthermore, the reproducibility of obtained parameters such as sRaw from double-chamber plethysmography for airway responsiveness has been challenged (Duguet et al., 2000; DeLorme and Moss, 2002). However, still many researchers suggest double-chamber plethysmography as a non-invasive, easy, rapid, and reproducible technique for longitudinal assessment of respiratory function in conscious animals after challenges with aerosolized substances (Lofgren et al., 2006; Mailhot-Larouche et al., 2018).

2.2.2 Imaging-based techniques

All the lung function measurement techniques outlined so far more or less provide lung function readouts on diagnosis of lung diseases and severity in animal studies of lung diseases. The Flexivent and Buxco systems, applied as end-point measurements, provide the most detailed set of lung functional and mechanical readouts including parameters related to lung volumes, quasi static pressure-volume curves, as well as the capability to distinguish lung tissue properties from airway characteristics using the low-frequency forced oscillation technique (Shalaby et al., 2010; Vanoirbeek et al., 2010; De Vleeschauwer et al., 2011; Bates, 2017; de Andrade Castro and Russo, 2019). As such, they can differentiate between obstructive and restrictive lung diseases and can be considered as the gold standard tools for lung function assessments. Nevertheless, as these lung function measurements provide global readouts of lung and airway performance, they may underestimate the extent of lung pathology in cases where unaffected lung regions compensate for affected regions, such as in chronic respiratory diseases (CRDs), lung transplantation, and pneumonectomy (Wu et al., 2000; Dane et al., 2013; Ravikumar et al., 2013; Vos et al., 2014; Dekoster et al., 2020; Li et al., 2020). Therefore, the early diagnosis and longitudinal assessments of lung performance in different cases is currently stalled due to the inability to capture the complete spatial distribution of lung function. We would ideally need a tool that can provide regional readouts on lung function.

Imaging modalities such as CT and MRI as efficient visual tools can be employed not only to monitor lung structural changes, but also to obtain lung functional data. While non-imaging-based methods for lung function measurements only provide global readouts for lung function assessment, some of the imaging-based methods can longitudinally provide detailed regional data of lung performance, which may allow researchers to detect pulmonary diseases in early stages and test the therapeutics more effectively. On one hand, micro-CT with high spatial and temporal resolution offers a great potential to obtain detailed regional information about lung structure and function in alive animals, which can enable us to quantify the severity of pulmonary diseases at earliest

Stages in a non-invasive manner. While, the ability of micro-CT in longitudinal assessments of lung structural changes is already well-established in *vivo* lung disease studies (De Langhe et al., 2012; Poelmans et al., 2016; Dekoster et al., 2020), its great potential in providing regional pulmonary functional data still needs to be revealed. On the other hand, MRI without ionizing radiation and with employing hyperpolaraized gases can provide regional ventilation and perfusion maps. This section investigates the abilities of current lung imaging modalities for the regional/global assessment of lung function and biomechanics non-invasively in the presence of lung pathologies.

2.2.2.1 X-ray computed tomography

In clinics, X-ray CT as the gold-standard modality for lung medical imaging, plays an important role in the diagnostic and therapeutic workup of many lung diseases, due to its extensive availability, speed, high-resolution, and high signal-to-noise ratio for lung tissue (Simon, 2000; Tielemans et al., 2020). High-resolution computed tomography (HRCT) is the most updated optimized technique to acquire the most detailed lung images with a multidetector CT scanner (Verschakelen, 2010) (Figure 3). In addition to its traditional role in the diagnostic of diffuse parenchymal and interstitial lung diseases (DPILDs), CT techniques have been developed and utilized as non-invasive methods to measure regional ventilation in the lung for many years (Gur et al., 1979; Gur et al., 1981; Herbert et al., 1982; Snyder et al., 1984; Simon et al., 1998). Therefore, the significant potential of CT for developing new techniques has provided a magnificent opportunity to obtain not only detailed anatomical information on lung structure and pulmonary pathological patterns, but also quantitative functional characterization of the lung during the progression of pulmonary diseases (Young et al., 2019).

In preclinical research, μCT has proven to be a very powerful tool for longitudinal assessments of lung structural changes in chronic lung disease models, however, its routine implementation lags behind. Although, there are great opportunities to extract imaging-derived biomarkers not only on lung disease burdens, but also on lung function based on its ability to provide four dimensional (4D) data from different phases of the breathing cycle. Dynamic imaging of the lung using μCT to obtain 4D datasets is possible either with prospective synchronization (signal-based gating), triggering the image acquisition at certain phases of the respiratory cycle during scanning, or retrospective synchronization (image-based gating), sorting the acquired images according to their respiratory phases as a post-processing step (Liu et al., 2017). 4D-μCT of the lung using synchronization thereby not only reduces motion artifacts induced by cardiac and respiratory cycles, but also provides opportunities to extract end-inspiratory and end-expiratory images of the lungs, that can then be used to calculate (regional) tidal expansion (Ding et al., 2010; Vinogradskiy et al., 2012; Brennan et al., 2015). Using density measurements, several μCT-derived biomarkers such as mean lung density, total lung volume, areated and non-areated lung volumes have been introduced to longitudinally investigate the onset and progression of pulmonary diseases such as lung fibrosis, invasive pulmonary aspergillosis, and pulmonary cryptococcosis (De Langhe et al., 2012; Vande Velde et al., 2016; Dekoster et al., 2020). Furthermore, the distribution of air volume inside the lung can be obtained at several positive end-expiratory pressures (PEEPs) to plot a pressure-volume

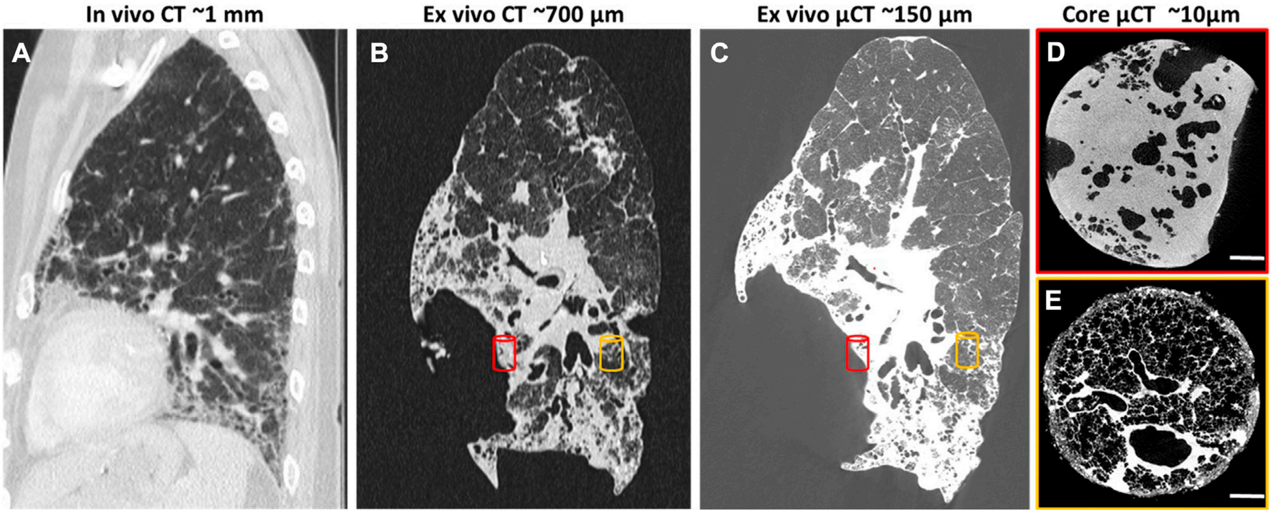

FIGURE 3
HRCT scans of human lung with usual interstitial pneumonia (UIP)[reprinted with permission from Tielemans et al. (2020)] **(A)** *In vivo* HRCT scan of the lung with resolution of 1 mm 6 months before lung transplantation; **(B)** *Ex vivo* CT scan of the lung after transplantation with resolution of 700 µm; **(C)** *Ex vivo* µCT scan of the same lung with higher resolution, 150 µm; **(D, E)** Core *ex vivo* µCT scan with resolution of 10 µm, showing severe fibrosis (red cylinder) and more healthy area (orange cylinder).

(P-V) curve, which can describe the static mechanical P-V relationship of the respiratory system with the assumption that the alveolar pressures are equilibrated (Marcucci et al., 2001). Calculating the distribution of regional air content and lung volume using density-based techniques has been employed by several researchers in a variety of applications to study topics such as post-pneumonectomy lung growth, special species adaptations, and respiratory distress syndrome (Hoffman and Ritman, 1985; Gattinoni et al., 1993; Olson and Hoffman, 1994; Gattinoni et al., 1995). The following sections investigate the x-ray-based techniques developed for lung function measurements in the recent years for preclinical lung research in more detail.

2.2.2.2 Xenon-CT regional ventilation imaging

Application of Xenon (Xe) gas as a contrast agent for CT-based regional ventilation measurements as a non-invasive procedure for evaluation of pulmonary function dates back to 1979, when Gur et al. used ventilation rate constants to discuss the pulmonary function of normal and impaired lungs (Gur et al., 1979). Since the density of Xe is higher than air, in the presence of this gas in the airways, the density of those areas in the CT images linearly increases with the Xe concentration; therefore, by serial scanning of the same ROI in the lung during wash-in and wash-out of Xe, regional ventilation can be mapped by density measurement techniques (Simon et al., 1998; Simon, 2005). Xe-CT ventilation imaging has been employed in many lung studies to non-invasively measure regional distributions of ventilation, perfusion, and ventilation/perfusion (V/Q) ratio (Figure 4) (Hoffman et al., 1995; Simon et al., 1998; Tajik et al., 1998; Marcucci et al., 2001; Jones et al., 2003; Sauter et al., 2019). However, despite many advantages such as providing high-resolution, regional ventilation maps non-invasively, Xe-CT method includes also several limitations. As an anesthetic gas, the concentartion of Xe cannot exceed 30%–35% for ventilation measurements in humans due to the side effects, which consequently limits the maximum CT density enhancement that can be acquired (Simon, 2000). Furthermore, since Xe is soluble in blood, the maximum alveolar concentration of this gas reduces during washing; while, most of the employed models for Xe-CT ventilation measurements consider no uptake and recirculation of Xe. In addition, due to the higher density and viscosity of Xe compared to air, the regional distribution of ventilation can be different from normal respiratory gases, especially at higher inspiratory flow rates (Simon, 2005).

2.2.2.3 X-ray body plethysmography

X-ray body plethysmography was another attempt to cover the limitations of UWBP for accurate measurements of tidal and end-expiratory volumes using single projection x-ray imaging, with the purpose of assessing airway resistance in conscious, spontaneously breathing mice (Lai-Fook et al., 2008). The proposed plethysmograph by Lai-Fook et al. included a transparent plastic tube with a cone-shaped end which was connected to a thin-walled copper cylinder. The x-ray source and sensor were located in the plastic tube to acquire single projection images of the animal's thorax using a single x-ray pulse of 10 ms exposure time to minimize image blur due to respiratory and cardiac cycles. The plethysmograph also included a heat lamp in the transparent plastic tube and a pressure transducer, thermistor, and humidity gauge in the thin-wall copper cylinder for controlling the air condition inside the chamber and measuring the pressure. Since evaluation airway resistance requires both tidal and end-expiratory volumes, single projection x-ray images and pressure oscillations inside the chamber were used to estimate these lung volumes in spontaneously breathing mice. Pressure oscillations inside the plethysmography chamber were assumed as sinusoidal variations. The biggest advantage of x-ray body plethysmography was the capability of

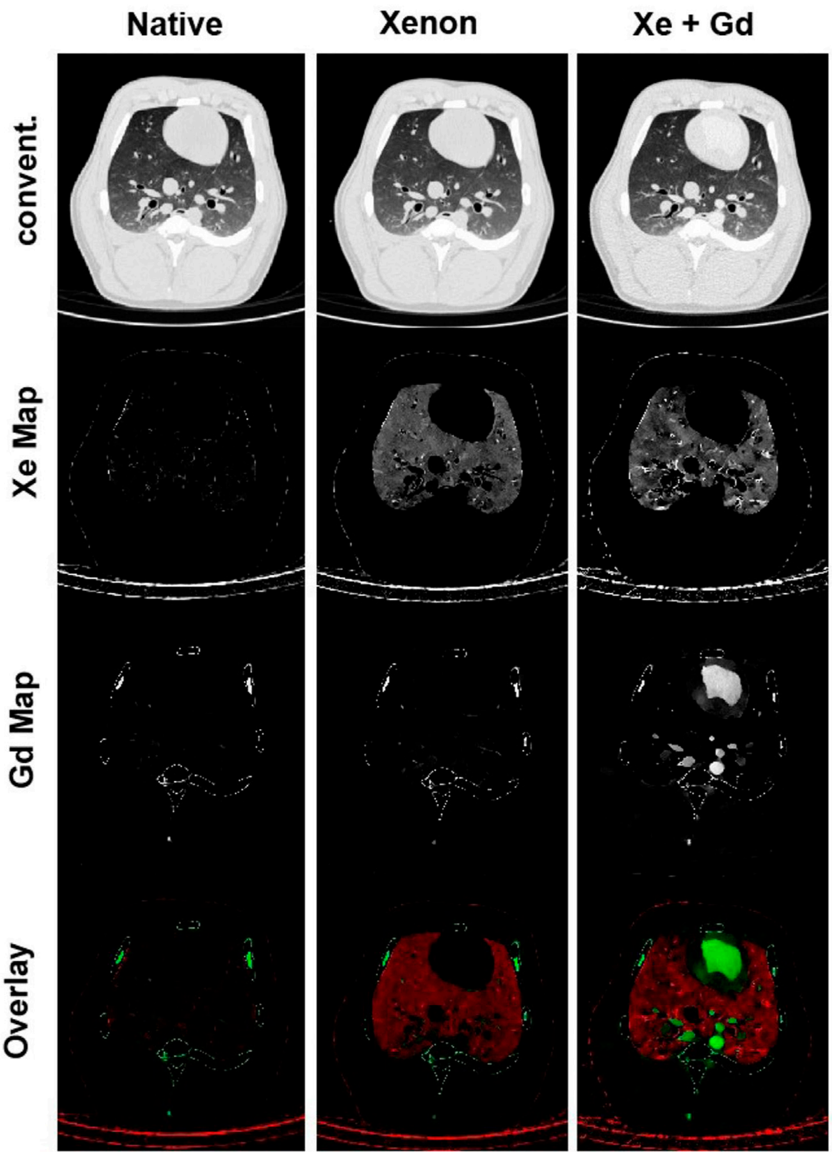

FIGURE 4
Xenon ventilation and gadolinium perfusion maps of a landrace pig acquired using dual-energy CT [reprinted from Sauter et al. (2019)]. Last row shows the overlay of the xenon and gadolinium density maps as a combined ventilation/perfusion maps.

measuring lung volumes in a way that allows separate estimations of airway resistance and compliance; however, the high cost of the x-ray system, slow collection of x-ray images throughout a breathing cycle, and the manual segmentation of the images, halted the way of seeing this system as an efficient screening tool (Bates et al., 2008; Reynolds and Frazer, 2011).

2.2.2.4 X-ray lung function

In further exploration for finding a non-invasive method for lung function measurements and address drawbacks of plethysmography techniques, Dullin et al. (2016) introduced an imaging-based technique called x-ray lung function (XLF) method. XLF is a non-invasive technique for lung function measurements that employs low-dose planar cinematic x-ray imaging to monitor the animal's breathing during the measurements. In this *in vivo* approach for lung function measurements, a video of 2D radiographs of the chest movements during spontaneously breathing of the unrestrained, anesthetized animal was captured to measure the average x-ray transmission of the lungs in each frame of the recorded video. The intensity fluctuations of the animal's chest movements normalized by the average background signal in the acquired 2D movie were described using an x-ray transmission function (XTF) over time. After filtering, the breathing cycles of the XTF for each animal were parameterized using a third-order polynomial and the average of each parameter (b_1- b_5) over all of the breathing cycles were used to characterize the lung function by the ratio between inhalation and exhalation times as well as the maximum air content in the lung. Applying the XLF technique to an ovalbumin-induced experimental allergic airway disease mouse model mimicking severe acute asthma (SAA), Dullin et al.

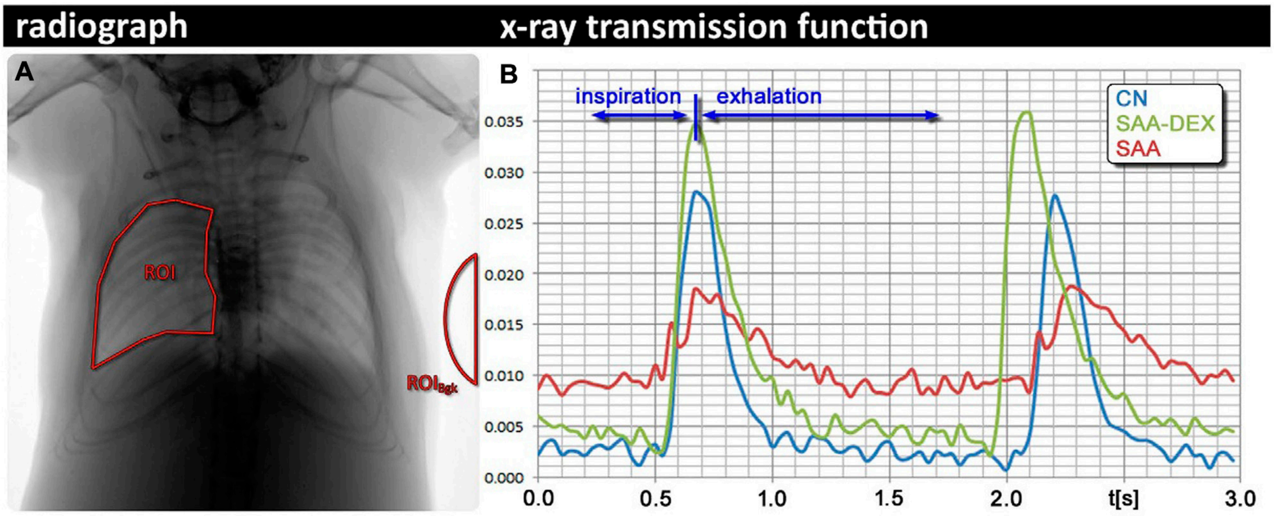

FIGURE 5
X-ray lung function (XLF) technique **(A)** Region of the interest of the lung in an exemplified radiograph. **(B)** Comparison between breathing cycles of a healthy control mouse (CN), a mouse with severe accute airway inflammation (SAA) 2 days after the last challenge, and a mouse from the same model, treated with dexamethasone before each challenge [reprinted from Dullin et al. (2016)].

showed a significantly higher sensitivity for XLF in detecting the elasticity reduction of the lungs in comparison to UWBP (Dullin et al., 2016). XLF using the XTF parameters (b_1- b_5), showed shorter relative inspiration periods and reduced air flows in the lungs, which both pointed to a reduction in elasticity related to the inflammation in SAA. UWBP using parameters such as MaxSlope and MinSlope showed the same trend in air flow reduction for SAA mice compared to the controls. Furthermore, the authors also assessed the efficacy of dexamethasone as the common treatment of SAA (Figure 5), and correlated the results with UWBP, and further with post-mortem histology, broncho-alveolar lavage (BAL), and synchrotron phase contrast CT. Similarly, in comparison to UWBP, XLF with higher accuracy showed the improvement of lung function parameters in the treated mice with dexamethasone.

For further evaluation on reliability and sensitivity of XLF technique, the same research group used XLF and propagation synchrotron phase-contrast computed tomography (pSRμCT) for quantification of lung remodeling in an allergic airway inflammation (AAI) mouse model (Markus et al., 2017). In the lung function measurements using XLF, the breathing frequency during acquisition was adjusted to one breathing cycle in 1,400 msec using the level of anesthesia and overall for each mouse 21 breathing cycles were recorded. Using the same parameterization technique explained above, XTF parameters (b_1- b_5) were used to characterize the lung function of each animal. After each lung function measurement, the mice were euthanized for *in situ* lung imaging by synchrotron pSRμCT, to assess whether the XLF findings in the recovered mice are associated with subtle structural changes. Based on the pSRμCT results, the authors showed the persistence of airway remodeling after the resolution of the inflammatory response. In addition, they found a high degree of correlation between the pSRμCT volume ratio and XLF results, which showed a significant air trapping in AAI mice in comparison to controls, most probably due to the reduction of elasticity in the lungs induced by allergic exposure. The authors concluded that the persistent loss of lung elasticity in AAI mice even after a few months' recovery can be related to the loss of elastic fibers. The results of this study once again confirmed the reliability and sensitivity of XLF as a non-invasive, *in vivo* technique for longitudinal lung function measurements in AAI mouse models.

Since none of the functional parameters (b_1- b_5) of XLF described pulmonary air volume, Dullin's research group developed a unique experimental setup to simultaneously perform either XLF or μCT with WBP (Khan et al., 2021). They replaced the animal's bed inside the gantry of the μCT scanner with a custom-made plethysmography chamber, which included a differential pressure sensor and isoflurane inlet-outlet for anesthesia (Figure 6). The original approach in XLF for calibration of x-ray transmission over time included a background selection for normalization, which required a large field of view (FOV) that led to low image resolution (Dullin et al., 2016). In this study, the XTF function was modified by applying a new approach for background correction, an adaptive moving filter, which provided the possibility of using a smaller FOV during the XLF measurements and consequently a better image resolution at the lung region (Khan et al., 2021). The relative x-ray transmission function (rXTF) was used for analysis of the breathing cycles and quantitative functional parameters such as end-inspiration lung volume (EIV), the relative x-ray transmission at end-expiration, as well as the decay rate of the expiration phase. The results showed a strong correlation between the acquired lung volume by rXTF function in XLF technique and those extracted from the μCT data; however, the XLF data were obtained by only 7% of the x-ray dose and 13% of the acquisition time used in μCT, which shows the capability of XLF as a reliable technique for *in vivo,* non-invasive lung volume measurements in longitudinal studies on lung diseases.

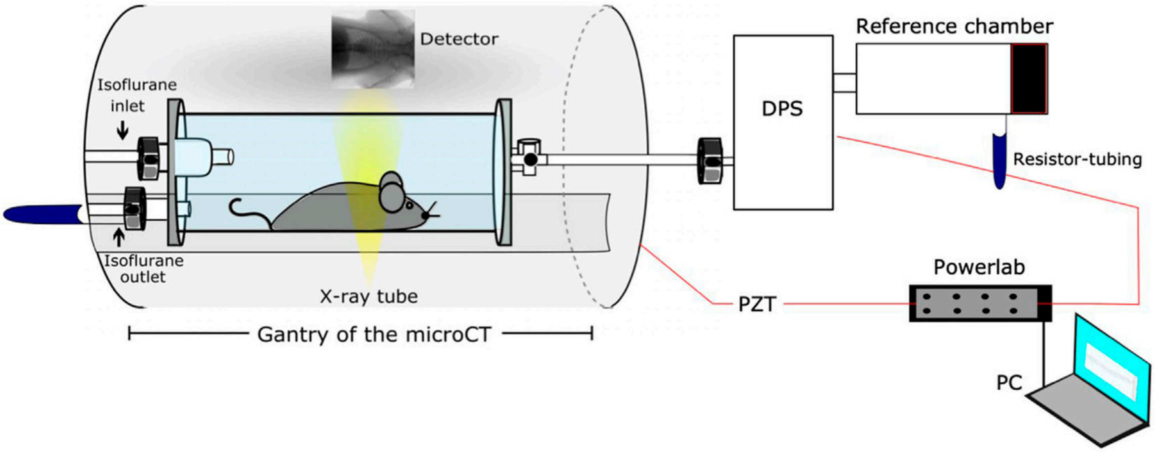

FIGURE 6
Schematic of the developed setup by Khan et al. for correlative XLF, WBP, and μCT measurements [reprinted from Khan et al. (Khan et al., 2021)].

Since 2D radiographs of the chest movements are used by XLF protocol, the acquired imaging data could only be used for monitoring the animal's breathing during the measurements and no anatomical information could be obtained. To address this issue, Dullin et al. proposed a new technique based on XLF to quantify lung function in the raw data of retrospectively gated lung μCT scans, which is called retrospective gating-based x-ray lung function measurement (rgXLF) (Dullin et al., 2022). For assessment of the newly developed technique, they applied the rgXLF protocol on mdx mice, the most commonly used mouse model for studying Duchenne muscular dystrophy (DMD). The authors employed the same strategy for parameterization of the breathing pattern that Khan et al. (Khan et al., 2021) used in their study. The comparison of functional parameters between XLF and rgXLF revealed a strong correlation, with almost the same k-values of the expiration phase and similar heart rates. In a comparison between control and mdx mice, both cross sections and 3D lung reconstruction showed the differences in the shape diaphragm between the mice (Figure 7). Therefore, rgXLF with a low x-ray dose, short acquisition time, and minimum voxel size of 40 μm showed the ability for longitudinal lung function measurements and also providing anatomical information without the requirement for additional scanning.

2.2.2.5 Phase contrast X-ray lung function

The continuous search for finding new imaging-based techniques to obtain regional lung function and biomechanics data led to employing synchrotron radiation sources to produce highly coherent, high flux x-rays that are required for phase contrast x-ray imaging (PCXI) [see (Bayat et al., 2001), (Bayat et al., 2009), (Porra et al., 2004), (Monfraix et al., 2004), (Bayat et al., 2022a), (Cercos-Pita et al., 2022), (Bayat et al., 2022b)]. PCXI is a high-resolution imaging technique, capable of differentiating between soft tissues by enhancing the contrast of biological interfaces and also providing dynamic motions of lung tissue. Recently, Bayat et al. throughly reviewed the present methods for synchrotron radiation-based imaging that have been used for regional lung function measurements [see (Bayat et al., 2020)]. The synchrotron radiation-based imaging methods included free propagation-based phase-contrast lung imaging (PBI), speckle-based lung imaging, 4D lung imaging, and K-edge subtraction (KES) imaging as well as their applications in preclinical animal models.

Four-dimensional x-ray velocimetry (4DxV) is a PCXI-based technique that can capture the expansion/contraction of lung tissue throughout a breathing process and also measure the airflow inside the airways. Therefore, any regional structural change of lung parenchyma and alteration of airflow inside the airways due to obstructive/restrictive lung diseases can be detected using this technique (Dubsky et al., 2010; Dubsky et al., 2012; Fouras et al., 2012). Since most of the 4DxV techniques were developed and validated in synchrotron radiation facilities, a more compact and accessible experimental setup was required to make 4DxV mapping more commonly-used in lung research laboratories (Tuohimaa et al., 2007; Bravin et al., 2012; Krenkel et al., 2016). In 2020, Murrie et al. introduced a dynamic *in vivo* 4DxV imaging system using a liquid-metal-jet microfocus X-ray source for regional lung function measurements in β-ENaC mice, a mouse model of cystic fibrosis (CF) (Figure 8) (Murrie et al., 2020). Mice were anesthetized, intubated, and ventilated during scanning. The results of 4DxV analysis, the expiratory time constant, showed a dramatic decrease in regional lung expansion of the left lung for β-ENaC mice in comparison to healthy controls, which correlated directly to the reduction of aeration due to the patchy CF-like airway obstructions in this region. This reduction of aeration directly indicates the regional reduction of lung function for the β-ENaC mouse, which can be considered as a biomarker for early detection of an obstructive airway disease (Figure 9). The proposed 4DxV imaging system is capable of regional imaging of lungs and airways with 60 μm resolution d 30 frames per second for pulmonary functional imaging and obtaining 3D ventilation maps. However, ionizing radiation measurements showed 1.47–1.74 *Gy* radiation dose delivered to each animal during image acquisition, which was below the lethal radiation dose to damage lung tissue (7.5 *Gy* for

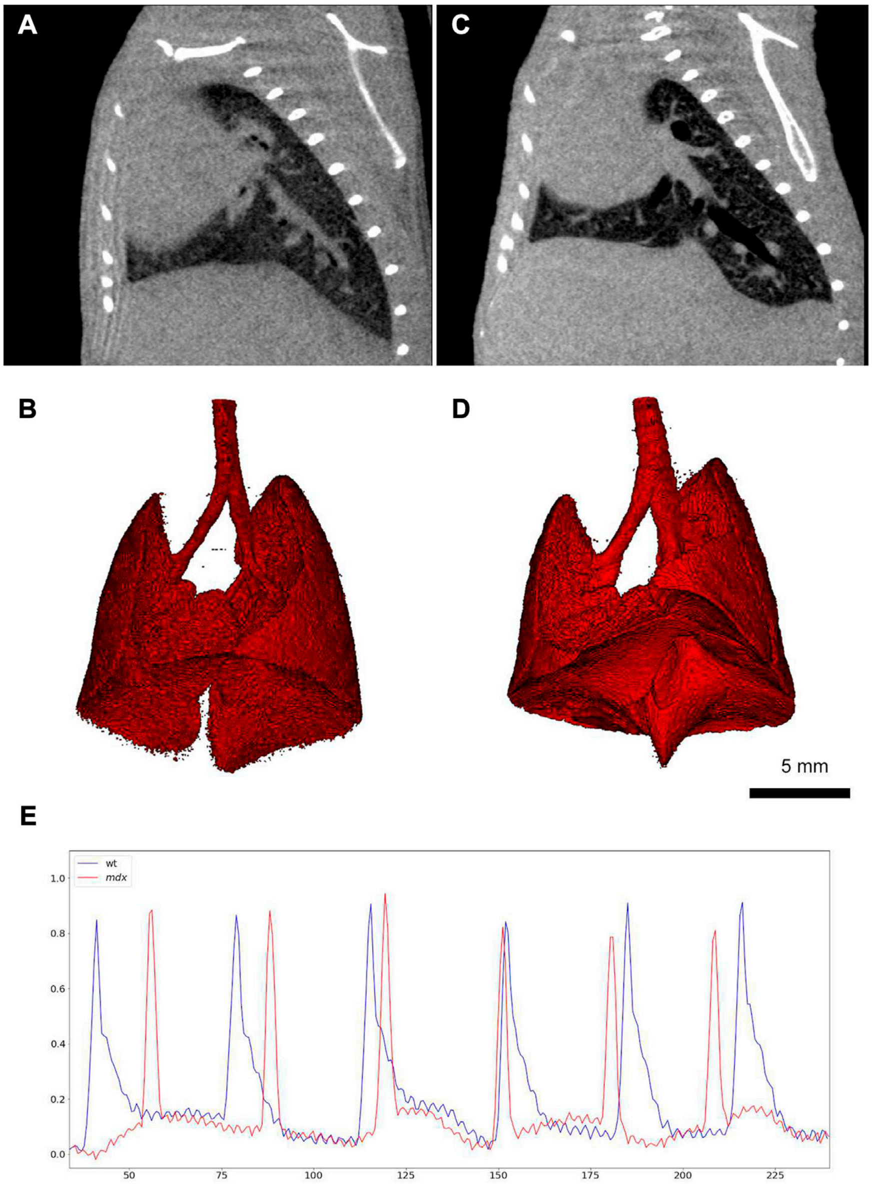

FIGURE 7
Retrospective gating-based x-ray lung function measurement (rgXLF) **(A, C)** µCT images of a healthy control mouse and a mdx mouse respectively, showing the difference in the shape of the diaphragms; **(B, D)** 3D renderings of the healthy and mdx mice; **(E)** Comparison of the breathing patterns of the healthy and mdx mice (healthy = blue and mdx = blue), showing a more rapid decay in the expiration phase of the mdx mouse [reprinted from Dullin et al. (2022)].

BALB/C mice and 8.3 *Gy* for C57BL/6 mice (Okunieff et al., 1996)), but still high enough to be considered as the endpoint for the animal.

2.2.2.6 Optical respiratory dynamics tracking

Search for finding a simpler way than WBP and XLF to monitor respiratory dynamics, resulted in introduction of an optical technique by Svetlove et al. called optical respiratory dynamics tracking (ORDT) (Svetlove et al., 2022). This technique is especially useful for tracking diaphragm function of mice with neuromuscular diseases such as Duchenne muscular dystrophy (DMD). ORDT is a simple method for monitoring respiratory dynamics of anesthetized mice using camera tracing of chest surface markers. For developing this optical technique, the authors utilized a camera with the ability to produce images with 600 × 400 pixels resolution for 10 s at 100 frames/sec. They placed four paper markers with black cross-hair pattern on the thoracic-abdominal region of the mice with double-sided tape and tracked the movements of these markers in the acquired video with Linear Assignment Problem algorithms. The expiration constant was computed in XLF software. To assess the performance of ORDT technique, the authors used mdx mouse model to investigate the irregularities in the breathing pattern of the mice due to respiratory muscle weakness, which is one of the common characteristics of DMD. In comparison with the data acquired by XLF, the results

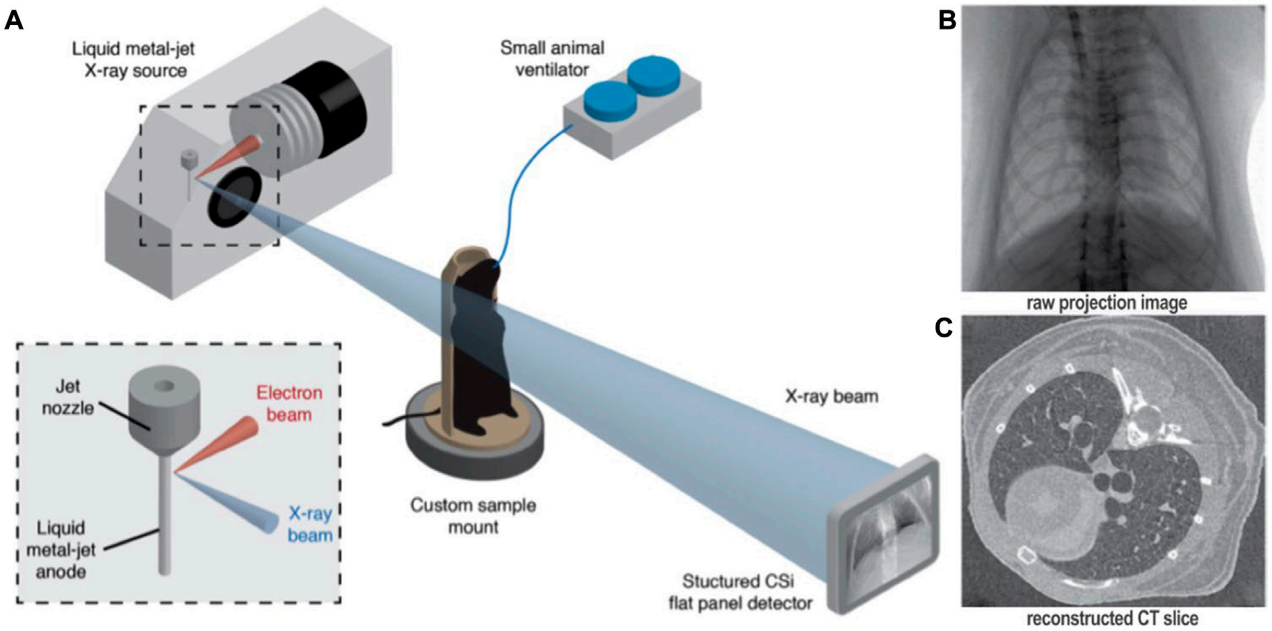

FIGURE 8
Four-dimensional x-ray velocimetry (4DxV) technique for regional lung function assessments [reprinted from Murrie et al. (2020)]: **(A)** Experimental image acquisition setup using a liquid-metal-jet microfocus X-ray source, introduced by Murrie et al. (2020) for *in vivo* regional lung function measurements; **(B)** Raw 2D projections acquired over 360° using the proposed image acquisition setup; **(C)** Reconstructed CT images from the binned projections to produce 4D CT dataset.

obtained by ORDT showed significantly steeper expiration for mdx mice compared to the controls by calculating the expiration constant (k), which most probably shows the higher sensitivity of ORDT compared to XLF in capturing the change of respiratory dynamics in dmx mice. Furthermore, unlike XLF technique, ORDT was also able to show the differences between fast and slow expiratory phases in mdx mice, while healthy controls had almost the same fast and slow phases. Compared to the alternative methods for longitudinal assessment of diaphragm function in mice, e. i. WBP and XLF, ORTD is easier to perform, completely non-invasive (no ionizing radiation), cheaper, and can be performed by commonly available tools and equipment (Svetlove et al., 2022). Furthermore, since this optical technique directly assess the dynamics of the body surface, it has a greater potential in detecting abnormal breathing patterns.

2.2.2.7 Pulmonary functional magnetic resonance imaging

In the past decades, alongside CT and nuclear medicine, magnetic resonance imaging (MRI) has been employed to evaluate chronic lung diseases in terms of gas exchange (Ohno et al., 2022). Pulmonary functional imaging with MRI includes measurements of ventilation, perfusion, as well as respiratory motion and mechanics (Wielpütz and Kauczor, 2012), which dates back to 1990s when hyperpolarized (HP) noble gas MR imaging and oxygen-enhanced MRI were introduced for the first time (Albert et al., 1994; Edelman et al., 1996; Kauczor et al., 1998).

Due to the abundance of hydrogen atoms in soft tissues (water and fat protons ^{1}H) which contain polar nuclei, MRI of lung tissues results in high-quality images. However, in an inflated lung that approximately 80% filled with air, MRI is challenging due to low proton density and abundant air-tissue interfaces, which reduce signal-to-noise ratio and increase magnetic susceptibility effects, resulting in very low inherent signal that is available for lung imaging (Velde et al., 2014; Dubsky and Fouras, 2015; Kumar et al., 2016). Inhalation of HP noble gases by improving the MRI signal overcomes this issue (Dubsky and Fouras, 2015). Contrast agents such as helium-3 (^{3}He) and xenon-129 (^{129}Xe) are the most commonly-used non-radioactive noble gases for HP MRI (Ohno et al., 2022), which have been studied extensively for evaluation of diseases burden and efficacy assessment of therapeutics (Ruppert et al., 2000; Altes et al., 2001; Fain et al., 2006; Fain et al., 2007; Kirby et al., 2012; Chang, 2013). Physical methods of polarization such as spin-exchange optical pumping (SEOP) and metastability exchange (ME) can increase the polarization up to 4-5 order of magnitude above the thermal equilibrium which compensates for the low density of the inhaled noble gas inside the lung (Fain et al., 2010; Adamson et al., 2017). SEOP can be used for polarization of both ^{3}He and ^{129}Xe; however, ME can be employed only for ^{3}He applications (Adamson et al., 2017).

The biggest advantage of HP ^{3}He MRI is the visualization of areas in the lung which are actively involved in ventilation such as terminal respiratory bronchioles and adjacent alveoli (Santyr et al., 2009; Fain et al., 2010). ^{3}He, with low solubility and a high diffusion coefficient, is the most commonly-used HP noble gas for pulmonary functional imaging due to its large gyromagnetic ratio which offers the strongest signal (Santyr et al., 2009). Due to this unique ability, HP ^{3}He MRI has been used to study many animal models of lung diseases such as asthma, pulmonary fibrosis and emphysema (Holmes et al., 2005; Mata et al., 2007; Thomas et al., 2009;

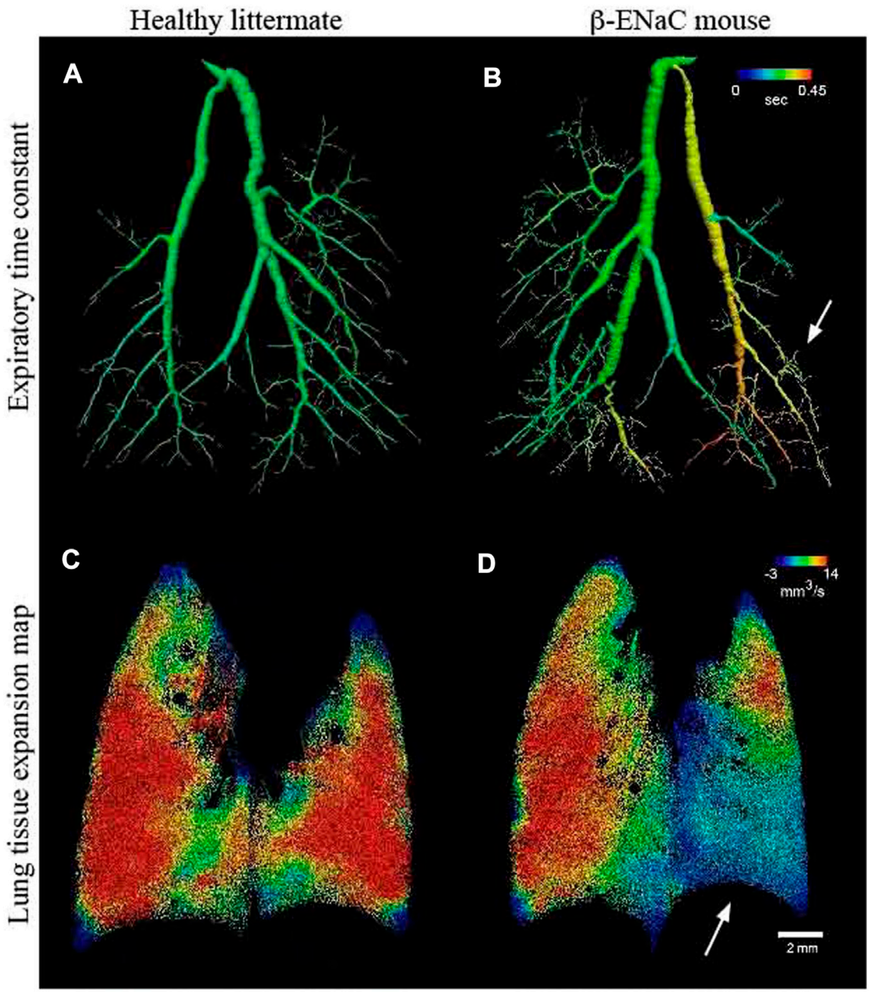

FIGURE 9
Lung function assessments using 4DxV technique [reprinted from Murrie et al. (Murrie et al., 2020)] **(A, B)** Airway 3D models of a healthy and β-ENaC mice, respectively, colored by local expiratory time constant from 4DxV analysis showing an increased expiratory time constant (arrow) for the β-ENaC mouse compared to the healthy littermate; **(C, D)** Comparison of the lung tissue expantion maps of the healthy and β-ENaC mice, respectively, revealing a reduction in regional tissue expansion (arrow) for the β-ENaC mouse compared to the healthy littermate.

Stephen et al., 2010). For early detection of bleomycin-induced pulmonary fibrosis progression in Sprague-Dawley rats, Stephen et al. employed HP ^3He MR imaging and pulmonary function testing by a plethysmography chamber for validation purposes (Stephen et al., 2010). To evaluate lung function and structure of the animals, they used apparent diffusion coefficient (ADC) and fractional ventilation as the most commonly-used metrics. While PFTs showed no significant differences between the treatment groups, fractional ventilation and the ADC value in small airways and alveoli declined for the fibrotic rats, suggesting that the metrics of ^3He MRI are more sensitive measures to monitor the progression of pulmonary fibrosis in animal models compared to the parameters of lung function tests. Despite showing the feasibility of measuring the ventilation changes in fibrotic rats, this method had limited success most probably due to the fact that ventilation is an indirect measure of the severity of pulmonary fibrosis (Adamson et al., 2017). In the case of emphysema, it has been shown that ^3He ADC is sensitive to alveolar damage due to emphysema in both humans (Salerno et al., 2002; Swift et al., 2005) and animal models (Woods et al., 2004; Jacob et al., 2008; Rodríguez et al., 2009). Also, Xu et al. hypothesized and proved that the transverse diffusion coefficient (D_T) of ^3He apparent diffusion, measured at sub-milli-second diffusion times, is a more sensitive metric for detecting the alveolar damage in the elastase-instillation model of emphysema in rats compared to the longitudinal diffusion coefficient (D_L) (Xu et al., 2012). Nevertheless, despite many advantages, due to the extremely limited quantity of ^3He available worldwide, the cost of using this contrast agent for pulmonary functional imaging is very high which currently limited its application (Fain et al., 2010).

On the other hand, ^{129}Xe as a by-product of the liquid air industry can be found in abundance which consequently leads to a relatively cheaper price compared to ^3He (Santyr et al., 2009; Fain et al., 2010). In addition, compared to ^3He, ^{129}Xe has higher solubility in tissues and blood which results in a higher ability for quantitative modeling of gas exchange (Kaushik et al., 2013; Qing et al., 2014a; Qing et al., 2014b). To address this issue, due to a lower gyromagnetic ratio and more challenging polarization protocols compared to ^{3}He, the application of HP ^{129}Xe MRI lagged behind (Fain et al., 2010). However, recent protocols for HP ^{129}Xe MRI employs a mixture of Xe with ^{129}Xe isotope enriched up to 85%, which improves the MR signal and solves the problem of low gyromagnetic ratio (Kirby and Parraga, 2013; Mugler and Altes, 2013). In recent years, HP ^{129}Xe MR imaging has been employed in many lung disease studies with different animal models such as radiation-induced lung injury (RILI), allergic inflammation models of asthma, bleomycin models of pulmonary fibrosis, etc. (Cleveland et al., 2014; Doganay et al., 2016; Li et al., 2016; Lilburn et al., 2016; Sharma et al., 2017).

Despite the potential of pulmonary functional MRI (PfMRI) using inhaled hyperpolarized gases (^{3}He; ^{129}Xe), the development and application of PfMRI have been hampered due to technological challenges such as limited access to MRI and the requirement for multinuclear capabilities which consist of a dedicated ^{129}Xe coil and the polarizer (Kooner et al., 2022). By addressing these technological challenges, further validation, and standardization of imaging protocols and analysis, PfMRI can play an important role in clinical care of many chronic lung diseases such as asthma and interstitial lung diseases to detect symptoms, guide therapy interventions and investigate treatment response (Kooner et al., 2022).

3 Toward clinical applications: Translational problems and future perspective of lung function tests

Both invasive and non-invasive conventional methods for lung function measurements, such as plethysmography techniques, have their own advantages and disadvantages (Sections 2.1 and Section 2.2.1). Furthermore, imaging-based techniques for lung function measurements offer non-invasive methods to acquire relevant readouts related to ventilation, perfusion, gas exchange, and lung mechanics (Section 2.2.2). However, almost all of these methods for lung function measurements evaluate the whole lung as a single unit and only offer global readouts. These global lung functional parameters are not sensitive enough to detect the onset and progression of many lung diseases, simply because these pulmonary abnormalities start regionally and their functional effects are masked by lung compensatory mechanisms (Hsia, 2004; Vande Velde et al., 2016; Hsia, 2017; Dekoster et al., 2020). The destructive effects of these lung diseases reflect on global lung functional readouts only after depletion of significant portions of the lung parenchyma. In addition, many of these traditional methods lack the necessary spatial and temporal resolution for the evaluation of lung physiology (Gefter et al., 2021; Ohno et al., 2021). Pulmonary functional imaging is capable of regional quantification of lung physiology as well as pulmonary mechanics with reference to spatial and temporal information derived from time-resolved anatomical imaging (Ohno et al., 2022). Longitudinal evaluation of pulmonary abnormalities on a regional basis in a non-invasive manner is the biggest advantage of pulmonary functional imaging over plethysmography techniques as well as most of the imaging-based techniques for lung function measurements. Pulmonary functional imaging with the capability of capturing regional subtle changes in ventilation even overcomes classical gold-standard techniques, such as FOT, for functional and mechanical assessments of lung. Nowadays, X-ray-CT and MRI by providing high spatial and temporal resolution are the primary imaging modalities for pulmonary functional imaging.

In the past few decades, as pulmonary functional imaging, many non-invasive, novel µCT- and MR-based techniques have been introduced for ventilation and perfusion imaging as well as biomechanics evaluation. On one hand, CT-based methods such as XLF techniques (Section 2.2.2.4), non-invasively offer pulmonary functional readouts related to lung volumes and elasticity in longitudinal *in vivo* animal studies [see (Dullin et al., 2016; Markus et al., 2017; Khan et al., 2021; Dullin et al., 2022)]. In addition, Xe-enhanced ventilation µCT can provide ventilation maps for regional ventilation assessments during the progression of pulmonary diseases with higher spatial resolution than any other imaging modality (Ohno et al., 2021). With further optimization for radiation dose reduction, validation, and standardization of imaging protocols, it is expected that Xe-enhanced ventilation µCT play a more important role in pulmonary functional imaging in near future. Furthermore, PCXI, (Section 2.2.2.5), as a sensitive, high-resolution imaging technique with the capability of providing regional information about airflow and ventilation, as well as structural changes of lung parenchyma showed a promising potential for pulmonary functional imaging (Murrie et al., 2020). With more developments in technology and the availability of *in vivo* 4DxV imaging systems, in near future, PCXI technique can be an inevitable part of every *in vivo* longitudinal animal study for assessment of lung disease models. On the other hand, MR-based techniques such as hyperpolarized noble gas MR imaging using ^{3}He and ^{129}Xe have been widely used for ventilation imaging to evaluate the severity of many chronic pulmonary diseases such as cystic fibrosis, asthma, COPD, etc. [see (Altes et al., 2001; Fain et al., 2006; Thomas et al., 2009; Stephen et al., 2010; Kirby et al., 2012; Cleveland et al., 2014; Doganay et al., 2016; Lilburn et al., 2016)]. Furthermore, oxygen-enhanced MR imaging offers not only valuable information related to regional oxygen enhancement based on oxygen diffusion, but also demonstrates oxygen uptake based on respiration itself. Still, some technical challenges and drawbacks such as dependence on the polarizer and multinuclear technology remain to be overcome to reach the point that these MR-based techniques become fully functional in preclinical and clinical areas (Kooner et al., 2022; Ohno et al., 2022). Considering the future perspective of pulmonary functional imaging using MR, Fluorine-19 (^{19}F) MRI looks like a more promising approach as an economical alternative for hyperpolarized noble gas MRI (17). This technique uses inert fluorinated gases which are non-toxic, inexpensive, and can be found in abundance. In addition, in contrast to hyperpolarized noble gas MRI, ^{19}F MRI can be performed by any MRI scanner with broadband multinuclear imaging capabilities (Couch et al., 2014; Ohno et al., 2022). As the physiological concentrations of detectable mobile fluorine are negligible, it can be a challenge to reach a sufficiently high density of ^{19}F nuclei to label the lung tissue that is required to produce high-quality images (Ruiz-Cabello et al., 2011; Chapelin et al., 2018). If this technical challenge can be overcome, ^{19}F MRI has great potential to become a feasible and reliable technique for pulmonary functional imaging both in preclinical and clinical areas, but still further validation and optimizations are required.

Since almost all of the pulmonary abnormalities are heterogeneously distributed in the lungs, e.g. interstitial lung diseases, pulmonary functional imaging with the ability to quantify lung functional parameters regionally seems to hold the key for early diagnosis of many lung disorders in the future. Despite the great potential of pulmonary functional imaging for regional lung function assessments, still global conventional spirometric measurements are used in clinics to measure lung volumes, which are not sensitive enough to detect restrictive lung diseases at earliest stages. Several methods of pulmonary functional imaging including ^{129}Xe and ^{19}F MR imaging and Xe-enhanced lung ventilation CT imaging have already shown promising results in the early detection of interstitial lung diseases in humans (Couch et al., 2014; Kong et al., 2014; Ohno et al., 2022). Yet, due to the lack of optimization and standardization of imaging protocols as well as validations in truly clinical trials, these pulmonary functional imaging methods are not translated into the clinics as quantitative tools for monitoring the onset and progression of interstitial lung diseases. Both in clinical and preclinical areas, state-of-the-art lung physiology assessments are gradually, but steadily, shifting toward pulmonary functional imaging using X-ray CT and MRI due to the high temporal and spatial resolution. To accelerate this clinical translation process, interdisiplinary research groups including researchers with different expertise such as pulmonary medicine, imaging, physiology, etc. should be formed to clinically validate the techniques and increase the clinical adoptation of these pulmonary functional methods.

Author contributions

The authors confirm contribution to the submitted review paper as follows: Study conception and design: GV and KA. Literature review and manuscript preparation: KA. Supervision, feedback, and proofreading: GV. Feedback and proofreading: JV. All authors reviewed and approved the final version of the manuscript.

Funding

The authors acknowledge research support by KU Leuven Internal Funds (C24/17/061) and the Flemish Research Foundation (FWO, G0G4820N, G057721N).

Conflict of interest

The authors declare that the research was conducted in the absence of any commercial or financial relationships that could be construed as a potential conflict of interest.

Publisher's note

References

Adamson, E. B., Ludwig, K. D., Mummy, D. G., and Fain, S. B. (2017). Magnetic resonance imaging with hyperpolarized agents: Methods and applications. *Phys. Med. Biol.* 62 (13), R81–R123. doi:10.1088/1361-6560/aa6be8

Adler, A., Cieslewicz, G., and Irvin, C. G. (2004). Unrestrained plethysmography is an unreliable measure of airway responsiveness in BALB/c and C57BL/6 mice. *J. Appl. physiology* 97 (1), 286–292. doi:10.1152/japplphysiol.00821.2003

Albert, M. S., Cates, G. D., Driehuys, B., Happer, W., Saam, B., Springer, C. S., et al. (1994). Biological magnetic resonance imaging using laser-polarized 129Xe. *Nature* 370 (6486), 199–201. doi:10.1038/370199a0

Altes, T. A., Powers, P. L., Knight-Scott, J., Rakes, G., Platts-Mills, T. A. E., de Lange, E. E., et al. (2001). Hyperpolarized 3He MR lung ventilation imaging in asthmatics: Preliminary findings. *J. Magnetic Reson. Imaging An Official J. Int. Soc. Magnetic Reson. Med.* 13 (3), 378–384. doi:10.1002/jmri.1054

Amaral, J. L. M., Lopes, A. J., Jansen, J. M., Faria, A. C. D., and Melo, P. L. (2013). An improved method of early diagnosis of smoking-induced respiratory changes using machine learning algorithms. *Comput. methods programs Biomed.* 112 (3), 441–454. doi:10.1016/j.cmpb.2013.08.004

Amdur, M. O., and Mead, J. (1958). Mechanics of respiration in unanesthetized Guinea pigs. *Am. J. Physiology-Legacy Content* 192 (2), 364–368. doi:10.1152/ajplegacy.1958.192.2.364

Baelder, R., Fuchs, B., Bautsch, W., Zwirner, J., Köhl, J., Hoymann, H. G., et al. (2005). Pharmacological targeting of anaphylatoxin receptors during the effector phase of allergic asthma suppresses airway hyperresponsiveness and airway inflammation. *J. Immunol.* 174 (2), 783–789. doi:10.4049/jimmunol.174.2.783

Bates, J., Irvin, C., Brusasco, V., Drazen, J., Fredberg, J., Loring, S., et al. (2004). The use and misuse of Penh in animal models of lung disease. *Am. J. Respir. Cell Mol. Biol.* 31 (3), 373–374. doi:10.1165/ajrcmb.31.3.1

Bates, J. H. T. (2017). Corp: Measurement of lung function in small animals. *J. Appl. Physiology* 123 (5), 1039–1046. doi:10.1152/japplphysiol.00243.2017

Bates, J. H. T., and Irvin, C. G. (2003). Measuring lung function in mice: The phenotyping uncertainty principle. *J. Appl. physiology* 94 (4), 1297–1306. doi:10.1152/japplphysiol.00706.2002

Bates, J. H. T., Thompson-Figueroa, J., Lundblad, L. K. A., and Irvin, C. G. (2008). Unrestrained video-assisted plethysmography: A noninvasive method for assessment of lung mechanical function in small animals. *J. Appl. physiology* 104 (1), 253–261. doi:10.1152/japplphysiol.00737.2007

Bayat, S., Cercos, J., Fardin, L., Perchiazzi, G., and Bravin, A. (2022). *Pulmonary vascular biomechanics imaged with synchrotron phase contrast microtomography in live rats.* Switzerland: Eur Respiratory Soc.

Bayat, S., Fardin, L., Cercos-Pita, J. L., Perchiazzi, G., and Bravin, A. (2022). Imaging regional lung structure and function in small animals using synchrotron radiation phase-contrast and K-edge subtraction computed tomography. *Front. Physiology* 13, 385. doi:10.3389/fphys.2022.825433

Bayat, S., Le Duc, G., Porra, L., Berruyer, G., Nemoz, C., Monfraix, S., et al. (2001). Quantitative functional lung imaging with synchrotron radiation using inhaled xenon as contrast agent. *Phys. Med. Biol.* 46 (12), 3287–3299. doi:10.1088/0031-9155/46/12/315

Bayat, S., Porra, L., Suortti, P., and Thomlinson, W. (2020). Functional lung imaging with synchrotron radiation: Methods and preclinical applications. *Phys. Medica* 79, 22–35. doi:10.1016/j.ejmp.2020.10.001

Bayat, S., Strengell, S., Porra, L., Janosi, T. Z., Petak, F., Suhonen, H., et al. (2009). Methacholine and ovalbumin challenges assessed by forced oscillations and synchrotron lung imaging. *Am. J. Respir. Crit. care Med.* 180 (4), 296–303. doi:10.1164/rccm.200808-1211OC

Berger, K. I. (2018). Small airway disease syndromes. Piercing the quiet zone. *Ann. Am. Thorac. Soc.* 15, S26–S29. doi:10.1513/AnnalsATS.201710-767KV

Berry, G., DeKruyff, R. H., Umetsu, D. T., and Hansen, G. (1999). Allergen-specific Th1 cells fail to counterbalance Th2 cell-induced airway hyperreactivity but cause severe airway inflammation. *J. Clin. Invest.* 103, 175–183. doi:10.1172/JCI5155

Bhattarai, P., Myers, S., Chia, C., Weber, H. C., Young, S., Williams, A. D., et al. (2020). Clinical application of forced oscillation technique (FOT) in early detection of airway changes in smokers. *J. Clin. Med.* 9 (9), 2778. doi:10.3390/jcm9092778

Bonnardel, E., Prevel, R., Campagnac, M., Dubreuil, M., Marthan, R., Berger, P., et al. (2019). Determination of reliable lung function parameters in intubated mice. *Respir. Res.* 20 (1), 211–214. doi:10.1186/s12931-019-1177-9

Brashier, B., and Salvi, S. (2015). Measuring lung function using sound waves: Role of the forced oscillation technique and impulse oscillometry system. *Breathe* 11 (1), 57–65. doi:10.1183/20734735.020514

Bravin, A., Coan, P., and Suortti, P. (2012). X-Ray phase-contrast imaging: From pre-clinical applications towards clinics. *Phys. Med. Biol.* 58 (1), R1–R35. doi:10.1088/0031-9155/58/1/R1

Brennan, D., Schubert, L., Diot, Q., Castillo, R., Castillo, E., Guerrero, T., et al. (2015). Clinical validation of 4-dimensional computed tomography ventilation with pulmonary function test data. *Int. J. Radiat. Oncology* Biology* Phys.* 92 (2), 423–429. doi:10.1016/j.ijrobp.2015.01.019

Brown, R. H., Walters, D. M., Greenberg, R. S., and Mitzner, W. (1999). A method of endotracheal intubation and pulmonary functional assessment for repeated studies in mice. *J. Appl. Physiology* 87 (6), 2362–2365. doi:10.1152/jappl.1999.87.6.2362

Burgel, P-R., Bergeron, A., De Blic, J., Bonniaud, P., Bourdin, A., Chanez, P., et al. (2013). Small airways diseases, excluding asthma and COPD: An overview. *Eur. Respir. Rev.* 22 (128), 131–147. doi:10.1183/09059180.00001313

Buxco, D. S. I. (2022). *Pulmonary function test*. Germany: Springer.

Cercos-Pita, J-L., Fardin, L., Leclerc, H., Maury, B., Perchiazzi, G., Bravin, A., et al. (2022). Lung tissue biomechanics imaged with synchrotron phase contrast microtomography in live rats. *Sci. Rep.* 12 (1), 5056–5066. doi:10.1038/s41598-022-09052-9

Chang, Y. V. (2013). Moxe: A model of gas exchange for hyperpolarized 129Xe magnetic resonance of the lung. *Magnetic Reson. Med.* 69 (3), 884–890. doi:10.1002/mrm.24304

Chapelin, F., Capitini, C. M., and Ahrens, E. T. (2018). Fluorine-19 MRI for detection and quantification of immune cell therapy for cancer. *J. Immunother. cancer* 6, 105–111. doi:10.1186/s40425-018-0416-9

Chong, B. T. Y., Agrawal, D. K., Romero, F. A., and Townley, R. G. (1998). Measurement of bronchoconstriction using whole-body plethysmograph: Comparison of freely moving versus restrained Guinea pigs. *J. Pharmacol. Toxicol. methods* 39 (3), 163–168. doi:10.1016/s1056-8719(98)00021-5

Cleveland, Z. I., Virgincar, R. S., Qi, Y., Robertson, S. H., Degan, S., and Driehuys, B. (2014). 3D MRI of impaired hyperpolarized 129Xe uptake in a rat model of pulmonary fibrosis. *NMR Biomed.* 27 (12), 1502–1514. doi:10.1002/nbm.3127

Contoli, M., Bellini, F., Morandi, L., Forini, G., Bianchi, S., Gnesini, G., et al. (2016). Assessing small airway impairment in mild-to-moderate smoking asthmatic patients. *Eur. Respir. J.* 47 (4), 1264–1267. doi:10.1183/13993003.01708-2015

Cosio, M., Ghezzo, H., Hogg, J. C., Corbin, R., Loveland, M., Dosman, J., et al. (1978). The relations between structural changes in small airways and pulmonary-function tests. *N. Engl. J. Med.* 298 (23), 1277–1281. doi:10.1056/NEJM197806082982303

Costa, D. L., and Tepper, J. S. (1988). *Approaches to lung function assessment in small mammals*. New York: Toxicology of the Lung Raven Press.

Couch, M. J., Ball, I. K., Li, T., Fox, M. S., Ouriadov, A. V., Biman, B., et al. (2014). Inert fluorinated gas MRI: A new pulmonary imaging modality. *NMR Biomed.* 27 (12), 1525–1534. doi:10.1002/nbm.3165

Czovek, D. (2019). "Pulmonary function tests in infants and children," in *Kendig's disorders of the respiratory tract in children* (Netherlands: Elsevier).

Dane, D. M., Yilmaz, C., Estrera, A. S., and Hsia, C. C. W. (2013). Separating *in vivo* mechanical stimuli for postpneumonectomy compensation: Physiological assessment. *J. Appl. physiology* 114 (1), 99–106. doi:10.1152/japplphysiol.01213.2012

de Andrade Castro, J. M., and Russo, M. (2019). Use and limitations of noninvasive and invasive methods for studying pulmonary function. *Drug Discov. Today Dis. Models* 29, 3–9. doi:10.1016/j.ddmod.2019.07.001

De Langhe, E., Vande Velde, G., Hostens, J., Himmelreich, U., Nemery, B., Luyten, F. P., et al. (2012). Quantification of lung fibrosis and emphysema in mice using automated micro-computed tomography. *PLoS One* 7, e43123. doi:10.1371/journal.pone.0043123

De Vleeschauwer, S. I., Rinaldi, M., De Vooght, V., Vanoirbeek, J. A., Vanaudenaerde, B. M., Verbeken, E. K., et al. (2011). Repeated invasive lung function measurements in intubated mice: An approach for longitudinal lung research. *Lab. Anim.* 45 (2), 81–89. doi:10.1258/la.2010.010111

Dekoster, K., Decaesteker, T., Berghen, N., Van den Broucke, S., Jonckheere, A-C., Wouters, J., et al. (2020). Longitudinal micro-Computed Tomography-derived biomarkers quantify non-resolving lung fibrosis in a silicosis mouse model. *Sci. Rep.* 10 (1), 16181–16190. doi:10.1038/s41598-020-73056-6

Dellacà, R. L., Santus, P., Aliverti, A., Stevenson, N., Centanni, S., Macklem, P. T., et al. (2004). Detection of expiratory flow limitation in COPD using the forced oscillation technique. *Eur. Respir. J.* 23 (2), 232–240. doi:10.1183/09031936.04.00046804

DeLorme, M. P., and Moss, O. R. (2002). Pulmonary function assessment by whole-body plethysmography in restrained versus unrestrained mice. *J. Pharmacol. Toxicol. methods* 47 (1), 1–10. doi:10.1016/s1056-8719(02)00191-0

Desai, J. P., and Moustarah, F. (2020). *Pulmonary compliance*. Florida: StatPearls.

Devos, F. C., Maaske, A., Robichaud, A., Pollaris, L., Seys, S., Lopez, C. A., et al. (2017). Forced expiration measurements in mouse models of obstructive and restrictive lung diseases. *Respir. Res.* 18 (1), 123–136. doi:10.1186/s12931-017-0610-1

Ding, K., Bayouth, J. E., Buatti, J. M., Christensen, G. E., and Reinhardt, J. M. (2010). 4DCT-based measurement of changes in pulmonary function following a course of radiation therapy. *Med. Phys.* 37 (3), 1261–1272. doi:10.1118/1.3312210

Doganay, O., Stirrat, E., McKenzie, C., Schulte, R. F., and Santyr, G. E. (2016). Quantification of regional early stage gas exchange changes using hyperpolarized 129Xe MRI in a rat model of radiation-induced lung injury. *Med. Phys.* 43 (5), 2410–2420. doi:10.1118/1.4946818

Donaldson, D. D., Dakhama, A., Takeda, E. W., Rha, Y-H., Park, J-W., Balhorn, A., et al. (2002). The role of IL-13 in established allergic airway disease. *J. Immunol.* 169, 6482–6489. doi:10.4049/jimmunol.169.11.6482

DuBois, A. B., Brody, A. W., Lewis, D. H., and Burgess, B. F., Jr (1956). Oscillation mechanics of lungs and chest in man. *J. Appl. physiology* 8 (6), 587–594. doi:10.1152/jappl.1956.8.6.587

Dubsky, S., and Fouras, A. (2015). Imaging regional lung function: A critical tool for developing inhaled antimicrobial therapies. *Adv. drug Deliv. Rev.* 85, 100–109. doi:10.1016/j.addr.2015.03.010

Dubsky, S., Hooper, S. B., Siu, K. K. W., and Fouras, A. (2012). Synchrotron-based dynamic computed tomography of tissue motion for regional lung function measurement. *J. R. Soc. Interface* 9 (74), 2213–2224. doi:10.1098/rsif.2012.0116

Dubsky, S., Jamison, R. A., Irvine, S. C., Siu, K. K. W., Hourigan, K., and Fouras, A. (2010). Computed tomographic x-ray velocimetry. *Appl. Phys. Lett.* 96 (2), 023702. doi:10.1063/1.3285173

Duguet, A., Biyah, K., Minshall, E., Gomes, R., Wang, C-G., Taoudi-Benchekroun, M., et al. (2000). Bronchial responsiveness among inbred mouse strains: Role of airway smooth-muscle shortening velocity. *Am. J. Respir. Crit. care Med.* 161 (3), 839–848. doi:10.1164/ajrccm.161.3.9906054

Dullin, C., Markus, M. A., Larsson, E., Tromba, G., Hülsmann, S., and Alves, F. (2016). X-Ray based Lung Function measurement-a sensitive technique to quantify lung function in allergic airway inflammation mouse models. *Sci. Rep.* 6, 36297. doi:10.1038/srep36297

Dullin, C., Svetlove, A., Zschüntzsch, J., and Alves, F. (2022). "Improved retrospectively gated *in-vivo* microCT for simultaneous assessment of lung function and anatomy in mice,". CC BY 4.0.

Edelman, R. R., Hatabu, H., Tadamura, E., Li, W., and Prasad, P. V. (1996). Noninvasive assessment of regional ventilation in the human lung using oxygen–enhanced magnetic resonance imaging. *Nat. Med.* 2 (11), 1236–1239. doi:10.1038/nm1196-1236

Ewart, L. C., Haley, M., Bickerton, S., Bright, J., Elliott, K., McCarthy, A., et al. (2010). Pharmacological validation of a telemetric model for the measurement of bronchoconstriction in conscious rats. *J. Pharmacol. Toxicol. methods* 61 (2), 219–229. doi:10.1016/j.vascn.2010.02.008

Fain, S., Schiebler, M. L., McCormack, D. G., and Parraga, G. (2010). Imaging of lung function using hyperpolarized helium-3 magnetic resonance imaging: Review of current and emerging translational methods and applications. *J. magnetic Reson. imaging* 32 (6), 1398–1408. doi:10.1002/jmri.22375

Fain, S. B., Korosec, F. R., Holmes, J. H., O'Halloran, R., Sorkness, R. L., and Grist, T. M. (2007). Functional lung imaging using hyperpolarized gas MRI. *J. Magnetic Reson. Imaging An Official J. Int. Soc. Magnetic Reson. Med.* 25 (5), 910–923. doi:10.1002/jmri.20876

Fain, S. B., Panth, S. R., Evans, M. D., Wentland, A. L., Holmes, J. H., Korosec, F. R., et al. (2006). Early emphysematous changes in asymptomatic smokers: Detection with 3He MR imaging. *Radiology* 239 (3), 875–883. doi:10.1148/radiol.2393050111

Faria, A. C. D., da Costa, A. A., Lopes, A. J., Jansen, J. M., and de Melo, P. L. (2010). Forced oscillation technique in the detection of smoking-induced respiratory alterations: Diagnostic accuracy and comparison with spirometry. *Clinics* 65 (12), 1295–1304. doi:10.1590/s1807-59322010001200012

Fay, R. R. (1988). Comparative psychoacoustics. *Hear. Res.* 34 (3), 295–305. doi:10.1016/0378-5955(88)90009-3

Finotto, S., De Sanctis, G. T., Lehr, H. A., Herz, U., Buerke, M., Schipp, M., et al. (2001). Treatment of allergic airway inflammation and hyperresponsiveness by antisense-induced local blockade of GATA-3 expression. *J. Exp. Med.* 193 (11), 1247–1260. doi:10.1084/jem.193.11.1247

Flandre, T. D., Leroy, P. L., and Desmecht, D. J. M. (2003). Effect of somatic growth, strain, and sex on double-chamber plethysmographic respiratory function values in healthy mice. *J. Appl. Physiology* 94 (3), 1129–1136. doi:10.1152/japplphysiol.00561.2002

Fouras, A., Allison, B. J., Kitchen, M. J., Dubsky, S., Nguyen, J., Hourigan, K., et al. (2012). Altered lung motion is a sensitive indicator of regional lung disease. *Ann. Biomed. Eng.* 40 (5), 1160–1169. doi:10.1007/s10439-011-0493-0

Frazer, D. G., Reynolds, J. S., and Jackson, M. C. (2011). Determining when enhanced pause (Penh) is sensitive to changes in specific airway resistance. *J. Toxicol. Environ. Health, Part A.* 74 (5), 287–295. doi:10.1080/15287394.2010.514235

Gattinoni, L., D'Andrea, L., Pelosi, P., Vitale, G., Pesenti, A., and Fumagalli, R. (1993). Regional effects and mechanism of positive end-expiratory pressure in early adult respiratory distress syndrome. *Jama* 269 (16), 2122–2127. doi:10.1001/jama.1993.03500160092039

Gattinoni, L., Pelosi, P., Crotti, S., and Valenza, F. (1995). Effects of positive end-expiratory pressure on regional distribution of tidal volume and recruitment in adult respiratory distress syndrome. *Am. J. Respir. Crit. care Med.* 151 (6), 1807–1814. doi:10.1164/ajrccm.151.6.7767524

Gefter, W. B., Lee, K. S., Schiebler, M. L., Parraga, G., Seo, J. B., Ohno, Y., et al. (2021). Pulmonary functional imaging: Part 2—state-of-the-Art clinical applications and opportunities for improved patient care. *Radiology* 299 (3), 524–538. doi:10.1148/radiol.2021204033

Glaab, T., Daser, A., Braun, A., Neuhaus-Steinmetz, U., Fabel, H., Alarie, Y., et al. (2001). Tidal midexpiratory flow as a measure of airway hyperresponsiveness in allergic mice. *Am. J. Physiology-Lung Cell. Mol. Physiology* 280 (3), L565–L573. doi:10.1152/ajplung.2001.280.3.L565

Glaab, T., Hoymann, H. G., Hohlfeld, J. M., Korolewitz, R., Hecht, M., Alarie, Y., et al. (2002). Noninvasive measurement of midexpiratory flow indicates bronchoconstriction in allergic rats. *J. Appl. Physiology* 93 (4), 1208–1214. doi:10.1152/japplphysiol.01121.2001

Glaab, T., Mitzner, W., Braun, A., Ernst, H., Korolewitz, R., Hohlfeld, J. M., et al. (2004). Repetitive measurements of pulmonary mechanics to inhaled cholinergic challenge in spontaneously breathing mice. *J. Appl. physiology* 97 (3), 1104–1111. doi:10.1152/japplphysiol.01182.2003

Glaab, T., Taube, C., Braun, A., and Mitzner, W. (2007). Invasive and noninvasive methods for studying pulmonary function in mice. *Respir. Res.* 8 (1), 63–10. doi:10.1186/1465-9921-8-63

Glaab, T., Ziegert, M., Baelder, R., Korolewitz, R., Braun, A., Hohlfeld, J. M., et al. (2005). Invasive versus noninvasive measurement of allergic and cholinergic airway responsiveness in mice. *Respir. Res.* 6 (1), 139–148. doi:10.1186/1465-9921-6-139

Goldman, M. D. (2001). Clinical application of forced oscillation. *Pulm. Pharmacol. Ther.* 14 (5), 341–350. doi:10.1006/pupt.2001.0310

Gur, D., Drayer, B. P., Borovetz, H. S., Griffith, B. P., Hardesty, R. L., and Wolfson, S. K. (1979). Dynamic computed tomography of the lung: Regional ventilation measurements. *J. Comput. assisted Tomogr.* 3 (6), 749–753. doi:10.1097/00004728-197903060-00007

Gur, D., Shabason, L., Borovetz, H. S., Herbert, D. L., Reece, G. J., Kennedy, W. H., et al. (1981). Regional pulmonary ventilation measurements by xenon enhanced dynamic computed tomography: An update. *J. Comput. assisted Tomogr.* 5 (5), 678–683. doi:10.1097/00004728-198110000-00015

Hamelmann, E., Schwarze, J., Takeda, K., Oshiba, A., Larsen, G. L., Irvin, C. G., et al. (1997). Noninvasive measurement of airway responsiveness in allergic mice using barometric plethysmography. *Am. J. Respir. Crit. care Med.* 156 (3), 766–775. doi:10.1164/ajrccm.156.3.9606031

Herbert, D. L., Gur, D., Shabason, L., Good, W. F., Rinaldo, J. E., Snyder, J. V., et al. (1982). Mapping of human local pulmonary ventilation by xenon enhanced computed tomography. *J. Comput. assisted Tomogr.* 6 (6), 1088–1093. doi:10.1097/00004728-198212000-00006

Hoffman, E. A., and Ritman, E. L. (1985). Effect of body orientation on regional lung expansion in dog and sloth. *J. Appl. Physiology* 59 (2), 481–491. doi:10.1152/jappl.1985.59.2.481

Hoffman, E. A., Tajik, J. K., and Kugelmass, S. D. (1995). Matching pulmonary structure and perfusion via combined dynamic multislice CT and thin-slice high-resolution CT. *Comput. Med. Imaging Graph.* 19 (1), 101–112. doi:10.1016/0895-6111(94)00035-2

Holmes, J. H., Sorkness, R. L., Meibom, S. K., Sundaram, S. K., Perlman, S. B., Converse, A. K., et al. (2005). Noninvasive mapping of regional response to segmental allergen challenge using magnetic resonance imaging and [F-18] fluorodeoxyglucose positron emission tomography. *Magnetic Reson. Med. An Official J. Int. Soc. Magnetic Reson. Med.* 53 (6), 1243–1250. doi:10.1002/mrm.20504

Hoymann, H. G. (2007). Invasive and noninvasive lung function measurements in rodents. *J. Pharmacol. Toxicol. Methods* 55 (1), 16–26. doi:10.1016/j.vascn.2006.04.006

Hoymann, H. G. (2012). Lung function measurements in rodents in safety pharmacology studies. *Front. Pharmacol.* 3, 156. doi:10.3389/fphar.2012.00156

Hsia, C. C. W. (2017). Comparative analysis of the mechanical signals in lung development and compensatory growth. *Cell tissue Res.* 367 (3), 687–705. doi:10.1007/s00441-016-2558-8

Hsia, C. C. W. (2004). Signals and mechanisms of compensatory lung growth. *J. Appl. physiology* 97 (5), 1992–1998. doi:10.1152/japplphysiol.00530.2004

Inc, S. S. R. E. (2022). *FlexiVent for* in vivo *lung function measurements*. Canada: SCIREQ.

Irvin, C. G., and Bates, J. H. T. (2003). Measuring the lung function in the mouse: The challenge of size. *Respir. Res.* 4 (1), 4–9. doi:10.1186/rr199

Jackson, A. C., and Watson, J. W. (1982). Oscillatory mechanics of the respiratory system in normal rats. *Respir. Physiol.* 48 (3), 309–322. doi:10.1016/0034-5687(82)90036-6

Jacob, R. E., Minard, K. R., Laicher, G., and Timchalk, C. (2008). 3D 3He diffusion MRI as a local *in vivo* morphometric tool to evaluate emphysematous rat lungs. *J. Appl. Physiology* 105 (4), 1291–1300. doi:10.1152/japplphysiol.90375.2008

Jones, A. T., Hansell, D. M., and Evans, T. W. (2003). Pulmonary perfusion quantified by electron-beam computed tomography: Effects of hypoxia and inhaled NO. *Eur. Respir. J.* 21 (5), 855–861. doi:10.1183/09031936.03.00085002

Kaczka, D. W., Ingenito, E. P., Suki, B., and Lutchen, K. R. (1997). Partitioning airway and lung tissue resistances in humans: Effects of bronchoconstriction. *J. Appl. Physiology* 82 (5), 1531–1541. doi:10.1152/jappl.1997.82.5.1531

Kaczka, D. W., and Lutchen, K. R. (2004). Servo-controlled pneumatic pressure oscillator for respiratory impedance measurements and high-frequency ventilation. *Ann. Biomed. Eng.* 32, 596–608. doi:10.1023/b:abme.0000019179.87974.7d

Kauczor, H. U., Surkau, R., and Roberts, T. (1998). MRI using hyperpolarized noble gases. *Eur. Radiol.* 8 (5), 820–827. doi:10.1007/s003300050479

Kaushik, S. S., Freeman, M. S., Cleveland, Z. I., Davies, J., Stiles, J., Virgincar, R. S., et al. (2013). Probing the regional distribution of pulmonary gas exchange through single-breath gas-and dissolved-phase 129Xe MR imaging. *J. Appl. physiology* 115 (6), 850–860. doi:10.1152/japplphysiol.00092.2013

Khan, A., Markus, A., Rittmann, T., Albers, J., Alves, F., Hülsmann, S., et al. (2021). Simple low dose radiography allows precise lung volume assessment in mice. *Sci. Rep.* 11 (1), 4163–4173. doi:10.1038/s41598-021-83319-5

King, G. G., Bates, J., Berger, K. I., Calverley, P., de Melo, P. L., Dellacà, R. L., et al. (2020). Technical standards for respiratory oscillometry. *Eur. Respir. J.* 55 (2), 1900753. doi:10.1183/13993003.00753-2019

Kirby, M., and Parraga, G. (2013). Pulmonary functional imaging using hyperpolarized noble gas MRI: Six years of start-up experience at a single site. *Acad. Radiol.* 20 (11), 1344–1356. doi:10.1016/j.acra.2013.02.020

Kirby, M., Svenningsen, S., Owrangi, A., Wheatley, A., Farag, A., Ouriadov, A., et al. (2012). Hyperpolarized 3He and 129Xe MR imaging in healthy volunteers and patients with chronic obstructive pulmonary disease. *Radiology* 265 (2), 600–610. doi:10.1148/radiol.12120485

Kong, X., Sheng, H. X., Lu, G. M., Meinel, F. G., Dyer, K. T., Schoepf, U. J., et al. (2014). Xenon-enhanced dual-energy CT lung ventilation imaging: Techniques and clinical applications. *Am. J. Roentgenol.* 202 (2), 309–317. doi:10.2214/AJR.13.11191

Kooner, H. K., McIntosh, M. J., Desaigoudar, V., Rayment, J. H., Eddy, R. L., Driehuys, B., et al. (2022). Pulmonary functional MRI: Detecting the structure–function pathologies that drive asthma symptoms and quality of life. *Respirology* 27 (2), 114–133. doi:10.1111/resp.14197

Krenkel, M., Töpperwien, M., Dullin, C., Alves, F., and Salditt, T. (2016). Propagation-based phase-contrast tomography for high-resolution lung imaging with laboratory sources. *AIP Adv.* 6 (3), 035007. doi:10.1063/1.4943898

Kumar, R. K., Herbert, C., Webb, D. C., Li, L., and Foster, P. S. (2004). Effects of anticytokine therapy in a mouse model of chronic asthma. *Am. J. Respir. Crit. Care Med.* 170, 1043–1048. doi:10.1164/rccm.200405-681OC

Kumar, S., Liney, G., Rai, R., Holloway, L., Moses, D., and Vinod, S. K. (2016). Magnetic resonance imaging in lung: A review of its potential for radiotherapy. *Br. J. radiology* 89 (1060), 20150431. doi:10.1259/bjr.20150431

Lai-Fook, S. J., Houtz, P. K., and Lai, Y-L. (2008). End-expiratory and tidal volumes measured in conscious mice using single projection x-ray images. *J. Appl. Physiology* 104 (2), 521–533. doi:10.1152/japplphysiol.00729.2007

Li, H., Zhang, Z., Zhao, X., Sun, X., Ye, C., and Zhou, X. (2016). Quantitative evaluation of radiation-induced lung injury with hyperpolarized xenon magnetic resonance. *Magnetic Reson. Med.* 76 (2), 408–416. doi:10.1002/mrm.25894

Li, N., Li, Q., Bai, J., Chen, K., Yang, H., Wang, W., et al. (2020). The multiple organs insult and compensation mechanism in mice exposed to hypobaric hypoxia. *Cell Stress Chaperones* 25 (5), 779–791. doi:10.1007/s12192-020-01117-w

Likens, S. A., and Mauderly, J. L. (1982). Effect of elastase or histamine on single-breath N2 washouts in the rat. *J. Appl. Physiology* 52 (1), 141–146. doi:10.1152/jappl.1982.52.1.141

Lilburn, D. M. L., Tatler, A. L., Six, J. S., Lesbats, C., Habgood, A., Porte, J., et al. (2016). Investigating lung responses with functional hyperpolarized xenon-129 MRI in an *ex vivo* rat model of asthma. *Magnetic Reson. Med.* 76 (4), 1224–1235. doi:10.1002/mrm.26003

Liu, X., Salmon, P. L., Laperre, K., and Sasov, A. (2017). *A comparison study: Image-based vs signal-based retrospective gating on microCT2017*. Bellingham: SPIE.

Lofgren, J. L. S., Mazan, M. R., Ingenito, E. P., Lascola, K., Seavey, M., Walsh, A., et al. (2006). Restrained whole body plethysmography for measure of strain-specific and allergen-induced airway responsiveness in conscious mice. *J. Appl. Physiology* 101 (5), 1495–1505. doi:10.1152/japplphysiol.00464.2006

Lomask, M. (2006). Further exploration of the Penh parameter. *Exp. Toxicol. Pathology* 57, 13–20. doi:10.1016/j.etp.2006.02.014

Lu, Q., and Rouby, J-J. (2000). Measurement of pressure-volume curves in patients on mechanical ventilation: Methods and significance. *Crit. Care* 4 (2), 91–100. doi:10.1186/cc662

Lundblad, L. K. A., Irvin, C. G., Adler, A., and Bates, J. H. T. (2002). A reevaluation of the validity of unrestrained plethysmography in mice. *J. Appl. physiology* 93 (4), 1198–1207. doi:10.1152/japplphysiol.00080.2002

Lundblad, L. K. A., Siddiqui, S., Bossé, Y., and Dandurand, R. J. (2021). Applications of oscillometry in clinical research and practice. *Can. J. Respir. Crit. Care, Sleep Med.* 5 (1), 54–68. doi:10.1080/24745332.2019.1649607

MacLeod, D., and Birch, M. (2001). Respiratory input impedance measurement: Forced oscillation methods. *Med. Biol. Eng. Comput.* 39, 505–516. doi:10.1007/BF02345140

Mailhot-Larouche, S., Deschênes, L., Lortie, K., Gazzola, M., Marsolais, D., Brunet, D., et al. (2018). Assessment of respiratory function in conscious mice by double-chamber plethysmography. *JoVE J. Vis. Exp.* 137 (137), e57778. doi:10.3791/57778

Marcucci, C., Nyhan, D., and Simon, B. A. (2001). Distribution of pulmonary ventilation using Xe-enhanced computed tomography in prone and supine dogs. *J. Appl. physiology* 90 (2), 421–430. doi:10.1152/jappl.2001.90.2.421

Markus, M. A., Borowik, S., Reichardt, M., Tromba, G., Alves, F., and Dullin, C. (2017). X-ray-based lung function measurement reveals persistent loss of lung tissue elasticity in mice recovered from allergic airway inflammation. *Am. J. Physiol. Lung Cell Mol. Physiol.* 313 (5), L763–L771. doi:10.1152/ajplung.00136.2017

Marshall, R. (1957). The physical properties of the lungs in relation to the subdivisions of lung volume. *Clin. Sci.* 16 (3), 507–515.

Martin, T. R., Gerard, N. P., Galli, S. J., and Drazen, J. M. (1988). Pulmonary responses to bronchoconstrictor agonists in the mouse. *J. Appl. Physiology* 64 (6), 2318–2323. doi:10.1152/jappl.1988.64.6.2318

Mata, J. F., Altes, T. A., Cai, J., Ruppert, K., Mitzner, W., Hagspiel, K. D., et al. (2007). Evaluation of emphysema severity and progression in a rabbit model: Comparison of hyperpolarized 3He and 129Xe diffusion MRI with lung morphometry. *J. Appl. physiology* 102 (3), 1273–1280. doi:10.1152/japplphysiol.00418.2006

Michaelson, E. D., Grassman, E. D., and Peters, W. R. (1975). Pulmonary mechanics by spectral analysis of forced random noise. *J. Clin. investigation* 56 (5), 1210–1230. doi:10.1172/JCI108198

Mitzner, W., and Tankersley, C. (2003). Interpreting Penh in mice. *J. Appl. physiology* 94 (2), 828–831. doi:10.1152/japplphysiol.00815.2002

Monfraix, S., Bayat, S., Porra, L., Berruyer, G., Nemoz, C., Thomlinson, W., et al. (2004). Quantitative measurement of regional lung gas volume by synchrotron radiation computed tomography. *Phys. Med. Biol.* 50 (1), 1–11. doi:10.1088/0031-9155/50/1/001

Mori, V., Oliveira, M. A., Vargas, M. H. M., da Cunha, A. A., de Souza, R. G., Pitrez, P. M., et al. (2017). Input respiratory impedance in mice: Comparison between the flow-based and the wavetube method to perform the forced oscillation technique. *Physiol. Meas.* 38 (6), 992–1005. doi:10.1088/1361-6579/aa6b75

Mugler, J. P., Iii, and Altes, T. A. (2013). Hyperpolarized 129Xe MRI of the human lung. *J. Magnetic Reson. Imaging* 37 (2), 313–331. doi:10.1002/jmri.23844

Murphy, D. J. (2002). Assessment of respiratory function in safety pharmacology. *Fundam. Clin. Pharmacol.* 16 (3), 183–196. doi:10.1046/j.1472-8206.2002.00060.x

Murrie, R. P., Werdiger, F., Donnelley, M., Lin, Y., Carnibella, R. P., Samarage, C. R., et al. (2020). Real-time *in vivo* imaging of regional lung function in a mouse model of cystic fibrosis on a laboratory X-ray source. *Sci. Rep.* 10 (1), 447–448. doi:10.1038/s41598-019-57376-w

Navajas, D., Farre, R., and Rotger, M. (1991). "Respiratory impedance," in *Pulmonary function in mechanically ventilated patients*. Editors S. Benito and A. Net (Berlin, Heidelberg: Springer Berlin Heidelberg).

Nemery, B., Dinsdale, D., and Verschoyle, R. D. (1987). Detecting and evaluating chemical-induced lung damage in experimental animals. *Clin. Respir. Physiol.* 23 (5), 501–528.

Neuhaus-Steinmetz, U., Glaab, T., Daser, A., Braun, A., Lommatzsch, M., Herz, U., et al. (2000). Sequential development of airway hyperresponsiveness and acute airway obstruction in a mouse model of allergic inflammation. *Int. archives allergy Immunol.* 121 (1), 57–67. doi:10.1159/000024298

Ohno, Y., Hanamatsu, S., Obama, Y., Ueda, T., Ikeda, H., Hattori, H., et al. (2022). Overview of MRI for pulmonary functional imaging. *Br. J. Radiology* 95 (1132), 20201053. doi:10.1259/bjr.20201053

Ohno, Y., Seo, J. B., Parraga, G., Lee, K. S., Gefter, W. B., Fain, S. B., et al. (2021). Pulmonary functional imaging: Part 1—state-of-the-art technical and physiologic underpinnings. *Radiology* 299 (3), 508–523. doi:10.1148/radiol.2021203711

Okunieff, P., Wu, T., Huang, K., and Ding, I. (1996). Differential radioprotection of three mouse strains by basic or acidic fibroblast growth factor. *Br. J. cancer Suppl.* 27, S105–S108.

Olson, L. E., and Hoffman, E. A. (1994). Lung volumes and distribution of regional air content determined by cine X-ray CT of pneumonectomized rabbits. *J. Appl. Physiology* 76 (4), 1774–1785. doi:10.1152/jappl.1994.76.4.1774

Oostveen, E., MacLeod, D., Lorino, H., Farre, R., Hantos, Z., Desager, K., et al. (2003). The forced oscillation technique in clinical practice: Methodology, recommendations and future developments. *Eur. Respir. J.* 22 (6), 1026–1041. doi:10.1183/09031936.03.00089403

Özdilek, A. (2022). "Lung mechanics-compliance and resistance-extrapulmonary response," in *Teaching pearls in noninvasive mechanical ventilation* (Germany: Springer).

Palecek, F., Palecekova, M., and Aviado, D. M. (1967). Emphysema in immature rats: Condition produced by tracheal constriction and papain. *Archives Environ. Health An Int. J.* 15 (3), 332–342. doi:10.1080/00039896.1967.10664929

Pennock, B. E., Cox, C. P., Rogers, R. M., Cain, W. A., and Wells, J. H. (1979). A noninvasive technique for measurement of changes in specific airway resistance. *J. Appl. Physiology* 46 (2), 399–406. doi:10.1152/jappl.1979.46.2.399

Peslin, R., and Fredberg, J. J. (2011). Oscillation mechanics of the respiratory system. *Compr. Physiol.*, 145–177. doi:10.1002/cphy.cp030311

Poelmans, J., Hillen, A., Vanherp, L., Govaerts, K., Maertens, J., Dresselaers, T., et al. (2016). Longitudinal, *in vivo* assessment of invasive pulmonary aspergillosis in mice by computed tomography and magnetic resonance imaging. *Lab. Investig.* 96 (6), 692–704. doi:10.1038/labinvest.2016.45

Porra, L., Monfraix, S., Berruyer, G., Le Duc, G., Nemoz, C., Thomlinson, W., et al. (2004). Effect of tidal volume on distribution of ventilation assessed by synchrotron radiation CT in rabbit. *J. Appl. Physiology* 96 (5), 1899–1908. doi:10.1152/japplphysiol.00866.2003

Powers, K. A., and Dhamoon, A. S. (2019). *Physiology, pulmonary ventilation and perfusion*. Florida: StatPearls Publishing.

Preuss, J. M. H., Hall, G. L., and Sly, P. D. (1999). Repeat measurement of respiratory mechanics using the forced oscillation technique in non-paralysed rats. *Pulm. Pharmacol. Ther.* 12 (3), 173–183. doi:10.1006/pupt.1999.0198

Pride, N. B. (1992). Forced oscillation techniques for measuring mechanical properties of the respiratory system. *Thorax* 47 (4), 317–320. doi:10.1136/thx.47.4.317

Qing, K., Mugler, J. P., Iii, Altes, T. A., Jiang, Y., Mata, J. F., Miller, G. W., et al. (2014). Assessment of lung function in asthma and COPD using hyperpolarized 129Xe chemical shift saturation recovery spectroscopy and dissolved-phase MRI. *NMR Biomed.* 27 (12), 1490–1501. doi:10.1002/nbm.3179

Qing, K., Ruppert, K., Jiang, Y., Mata, J. F., Miller, G. W., Shim, Y. M., et al. (2014). Regional mapping of gas uptake by blood and tissue in the human lung using hyperpolarized xenon-129 MRI. *J. magnetic Reson. imaging* 39 (2), 346–359. doi:10.1002/jmri.24181

Ravikumar, P., Yilmaz, C., Bellotto, D. J., Dane, D. M., Estrera, A. S., and Hsia, C. C. W. (2013). Separating *in vivo* mechanical stimuli for postpneumonectomy compensation: Imaging and ultrastructural assessment. *J. Appl. Physiology* 114 (8), 961–970. doi:10.1152/japplphysiol.01394.2012

Reynolds, J. S., and Frazer, D. G. (2011). Noninvasive pulmonary function screening in spontaneously breathing rodents: An engineering systems perspective. *Pharmacol. Ther.* 131 (3), 359–368. doi:10.1016/j.pharmthera.2011.05.003

Reynolds, J. S., and Frazer, D. G. (2006). Unrestrained acoustic plethysmograph for measuring tidal volume in mice. *Ann. Biomed. Eng.* 34 (9), 1494–1499. doi:10.1007/s10439-006-9159-8

Ribeiro, C. O., Faria, A. C. D., Lopes, A. J., and de Melo, P. L. (2018). Forced oscillation technique for early detection of the effects of smoking and COPD: Contribution of fractional-order modeling. *Int. J. Chronic Obstr. Pulm. Dis.* 13, 3281–3295. doi:10.2147/COPD.S173686

Rodríguez, I., Pérez-Sánchez, J. M., Peces-Barba, G., Kaulisch, T., Stiller, D., and Ruiz-Cabello, J. (2009). Long-range diffusion of hyperpolarized 3He in rats. *Magnetic Reson. Med. An Official J. Int. Soc. Magnetic Reson. Med.* 61 (1), 54–58. doi:10.1002/mrm.21826

Ruiz-Cabello, J., Barnett, B. P., Bottomley, P. A., and Bulte, J. W. M. (2011). Fluorine (19F) MRS and MRI in biomedicine. *NMR Biomed.* 24 (2), 114–129. doi:10.1002/nbm.1570

Ruppert, K., Brookeman, J. R., Hagspiel, K. D., and Mugler, J. P., Iii (2000). Probing lung physiology with xenon polarization transfer contrast (XTC). *Magnetic Reson. Med. An Official J. Int. Soc. Magnetic Reson. Med.* 44 (3), 349–357. doi:10.1002/1522-2594(200009)44:3<349:aid-mrm2>3.0.co;2-j

Salerno, M., de Lange, E. E., Altes, T. A., Truwit, J. D., Brookeman, J. R., and Mugler, J. P. (2002). Emphysema: Hyperpolarized helium 3 diffusion MR imaging of the lungs compared with spirometric indexes—initial experience. *Radiology* 222 (1), 252–260. doi:10.1148/radiol.2221001834

Santyr, G. E., Lam, W. W., Parra-Robles, J. M., Taves, T. M., and Ouriadov, A. V. (2009). Hyperpolarized noble gas magnetic resonance imaging of the animal lung: Approaches and applications. *J. Appl. Phys.* 105 (10), 102004. doi:10.1063/1.3112143

Sauter, A. P., Hammel, J., Ehn, S., Achterhold, K., Kopp, F. K., Kimm, M. A., et al. (2019). Perfusion-ventilation CT via three-material differentiation in dual-layer CT: A feasibility study. *Sci. Rep.* 9 (1), 5837–5838. doi:10.1038/s41598-019-42330-7

Schuessler, T. F., and Bates, J. H. T. (1995). A computer-controlled research ventilator for small animals: Design and evaluation. *IEEE Trans. Biomed. Eng.* 42 (9), 860–866. doi:10.1109/10.412653

Shalaby, K. H., Gold, L. G., Schuessler, T. F., Martin, J. G., and Robichaud, A. (2010). Combined forced oscillation and forced expiration measurements in mice for the assessment of airway hyperresponsiveness. *Respir. Res.* 11, 82–13. doi:10.1186/1465-9921-11-82

Sharma, S., Narayanasamy, G., Przybyla, B., Webber, J., Boerma, M., Clarkson, R., et al. (2017). Advanced small animal conformal radiation therapy device. *Technol. Cancer Res. Treat.* 16 (1), 45–56. doi:10.1177/1533034615626011

Shinke, H., Yamamoto, M., Hazeki, N., Kotani, Y., Kobayashi, K., and Nishimura, Y. (2013). Visualized changes in respiratory resistance and reactance along a time axis in smokers: A cross-sectional study. *Respir. Investig.* 51 (3), 166–174. doi:10.1016/j.resinv.2013.02.006

Simon, B. A., Marcucci, C., Fung, M., and Lele, S. R. (1998). Parameter estimation and confidence intervals for Xe-CT ventilation studies: A Monte Carlo approach. *J. Appl. physiology* 84 (2), 709–716. doi:10.1152/jappl.1998.84.2.709

Simon, B. A. (2000). Non-invasive imaging of regional lung function using x-ray computed tomography. *J. Clin. Monit. Comput.* 16 (5), 433–442. doi:10.1023/a:1011444826908

Simon, B. A. (2005). Regional ventilation and lung mechanics using X-Ray CT. *Acad. Radiol.* 12 (11), 1414–1422. doi:10.1016/j.acra.2005.07.009

Sly, P. D., Turner, D. J., Collins, R. A., and Hantos, Z. (2005). Penh is not a validated technique for measuring airway function in mice. *Am. J. Respir. Crit. care Med.* 172 (2), 256. doi:10.1164/ajrccm.172.2.954

Snyder, J. V., Pennock, B., Herbert, D., Rinaldo, J. E., Culpepper, J., Good, W. F., et al. (1984). Local lung ventilation in critically ill patients using nonradioactive xenon-enhanced transmission computed tomography. *Crit. care Med.* 12 (1), 46–51. doi:10.1097/00003246-198401000-00013

Stephen, M. J., Emami, K., Woodburn, J. M., Chia, E., Kadlecek, S., Zhu, J., et al. (2010). Quantitative assessment of lung ventilation and microstructure in an animal model of idiopathic pulmonary fibrosis using hyperpolarized gas MRI. *Acad. Radiol.* 17 (11), 1433–1443. doi:10.1016/j.acra.2010.06.019

Stockley, J. A., Cooper, B. G., Stockley, R. A., and Sapey, E. (2017). Small airways disease: Time for a revisit? *Int. J. chronic Obstr. Pulm. Dis.* 12, 2343–2353. doi:10.2147/COPD.S138540

Su, Z-Q., Guan, W-J., Li, S-Y., Ding, M., Chen, Y., Jiang, M., et al. (2018). Significances of spirometry and impulse oscillometry for detecting small airway disorders assessed with endobronchial optical coherence tomography in COPD. *Int. J. chronic Obstr. Pulm. Dis.* 13, 3031–3044. doi:10.2147/COPD.S172639

Svetlove, A., Albers, J., Hülsmann, S., Markus, M. A., Zschüntzsch, J., Alves, F., et al. (2022). Non-invasive optical motion tracking allows monitoring of respiratory dynamics in dystrophin-deficient mice. *Cells* 11 (5), 918. doi:10.3390/cells11050918

Swift, A. J., Wild, J. M., Fichele, S., Woodhouse, N., Fleming, S., Waterhouse, J., et al. (2005). Emphysematous changes and normal variation in smokers and COPD patients using diffusion 3He MRI. *Eur. J. radiology* 54 (3), 352–358. doi:10.1016/j.ejrad.2004.08.002

Tajik, J. K., Tran, B. Q., and Hoffman, E. A. (1998). *New technique to quantitate regional pulmonary microvascular transit times from dynamic X-ray CT images1998.* Bellingham: International Society for Optics and Photonics.

Takeda, K., Hamelmann, E., Joetham, A., Shultz, L. D., Larsen, G. L., Irvin, C. G., et al. (1997). Development of eosinophilic airway inflammation and airway hyperresponsiveness in mast cell–deficient mice. *J. Exp. Med.* 186 (3), 449–454. doi:10.1084/jem.186.3.449

Tarkowski, M., Vanoirbeek, J. A. J., Vanhooren, H. M., Vooght, V. D., Mercier, C. M., Ceuppens, J., et al. (2007). Immunological determinants of ventilatory changes induced in mice by dermal sensitization and respiratory challenge with toluene diisocyanate. *Am. J. Physiology-Lung Cell. Mol. Physiology* 292 (1), L207–L214. doi:10.1152/ajplung.00157.2005

Taube, C., Duez, C., Cui, Z-H., Takeda, K., Rha, Y-H., Park, J-W., et al. (2002). The role of IL-13 in established allergic airway disease. *J. Immunol.* 169 (11), 6482–6489. doi:10.4049/jimmunol.169.11.6482

Tepper, J. S., and Costa, D. L. (2015). *Methods, measurements, and interpretation of animal lung function in health and disease. Comparative biology of the normal lung.* Germany: Elsevier.

Thomas, A. C., Potts, E. N., Chen, B. T., Slipetz, D. M., Foster, W. M., and Driehuys, B. (2009). A robust protocol for regional evaluation of methacholine challenge in mouse models of allergic asthma using hyperpolarized 3He MRI. *NMR Biomed. An Int. J. Devoted Dev. Appl. Magnetic Reson. vivo* 22 (5), 502–515. doi:10.1002/nbm.1362

Tielemans, B., Dekoster, K., Verleden, S. E., Sawall, S., Leszczyński, B., Laperre, K., et al. (2020). From mouse to man and back: Closing the correlation gap between imaging and histopathology for lung diseases. *Diagnostics* 10 (9), 636. doi:10.3390/diagnostics10090636

Tuohimaa, T., Otendal, M., and Hertz, H. M. (2007). Phase-contrast x-ray imaging with a liquid-metal-jet-anode microfocus source. *Appl. Phys. Lett.* 91 (7), 074104. doi:10.1063/1.2769760

Vande Velde, G., Poelmans, J., De Langhe, E., Hillen, A., Vanoirbeek, J., Himmelreich, U., et al. (2016). Longitudinal micro-CT provides biomarkers of lung disease that can be used to assess the effect of therapy in preclinical mouse models, and reveal compensatory changes in lung volume. *Dis. Models Mech.* 9 (1), 91–98. doi:10.1242/dmm.020321

Vanoirbeek, J. A. J., Rinaldi, M., De Vooght, V., Haenen, S., Bobic, S., Gayan-Ramirez, G., et al. (2010). Noninvasive and invasive pulmonary function in mouse models of obstructive and restrictive respiratory diseases. *Am. J. Respir. Cell Mol. Biol.* 42 (1), 96–104. doi:10.1165/rcmb.2008-0487OC

Vanoirbeek, J. A. J., Tarkowski, M., Ceuppens, J. L., Verbeken, E. K., Nemery, B., and Hoet, P. H. M. (2004). Respiratory response to toluene diisocyanate depends on prior frequency and concentration of dermal sensitization in mice. *Toxicol. Sci.* 80 (2), 310–321. doi:10.1093/toxsci/kfh155

Vanoirbeek, J. A. J., Tarkowski, M., Vanhooren, H. M., De Vooght, V., Nemery, B., and Hoet, P. H. M. (2006). Validation of a mouse model of chemical-induced asthma using trimellitic anhydride, a respiratory sensitizer, and dinitrochlorobenzene, a dermal sensitizer. *J. Allergy Clin. Immunol.* 117 (5), 1090–1097. doi:10.1016/j.jaci.2006.01.027

Velde, G. V., De Langhe, E., Poelmans, J., Dresselaers, T., Lories, R. J., and Himmelreich, U. (2014). Magnetic resonance imaging for noninvasive assessment of lung fibrosis onset and progression: Cross-validation and comparison of different magnetic resonance imaging protocols with micro–computed tomography and histology in the bleomycin-induced mouse model. *Investig. Radiol.* 49 (11), 691–698. doi:10.1097/RLI.0000000000000071

Verschakelen, J. A. (2010). The role of high-resolution computed tomography in the work-up of interstitial lung disease. *Curr. Opin. Pulm. Med.* 16 (5), 503–510. doi:10.1097/MCP.0b013e32833cc997

Vijayaraghavan, R., Schaper, M., Thompson, R., Stock, M. F., Boylstein, L. A., Luo, J. E., et al. (1994). Computer assisted recognition and quantitation of the effects of airborne chemicals acting at different areas of the respiratory tract in mice. *Archives Toxicol.* 68 (8), 490–499. doi:10.1007/s002040050101

Vinogradskiy, Y. Y., Castillo, R., Castillo, E., Chandler, A., Martel, M. K., and Guerrero, T. (2012). Use of weekly 4DCT-based ventilation maps to quantify changes in lung function for patients undergoing radiation therapy. *Med. Phys.* 39 (1), 289–298. doi:10.1118/1.3668056

Vos, R., Ruttens, D., Verleden, S. E., Vandermeulen, E., Bellon, H., Vanaudenaerde, B. M., et al. (2014). Pregnancy after heart and lung transplantation. *Best Pract. Res. Clin. Obstetrics Gynaecol.* 28 (8), 1146–1162. doi:10.1016/j.bpobgyn.2014.07.019

Wielpütz, M., and Kauczor, H-U. (2012). MRI of the lung: State of the art. *Diagnostic interventional radiology* 18 (4), 344–353. doi:10.4261/1305-3825.DIR.5365-11.0

Woods, J. C., Yablonskiy, D. A., Chino, K., Tanoli, T. S. K., Cooper, J. D., and Conradi, M. S. (2004). Magnetization tagging decay to measure long-range 3He diffusion in healthy and emphysematous canine lungs. *Magnetic Reson. Med. An Official J. Int. Soc. Magnetic Reson. Med.* 51 (5), 1002–1008. doi:10.1002/mrm.20070

Wu, E. Y., Hsia, C. C. W., Estrera, A. S., Epstein, R. H., Ramanathan, M., and Johnson, R. L., Jr (2000). Preventing mediastinal shift after pneumonectomy does not abolish physiological compensation. *J. Appl. Physiology* 89 (1), 182–191. doi:10.1152/jappl.2000.89.1.182

Xu, X., Boudreau, M., Ouriadov, A., and Santyr, G. E. (2012). Mapping of 3He apparent diffusion coefficient anisotropy at sub-millisecond diffusion times in an elastase-instilled rat model of emphysema. *Magnetic Reson. Med.* 67 (4), 1146–1153. doi:10.1002/mrm.23098

Young, H. M., Eddy, R. L., and Parraga, G. (2019). MRI and CT lung biomarkers: Towards an *in vivo* understanding of lung biomechanics. *Clin. Biomech.* 66, 107–122. doi:10.1016/j.clinbiomech.2017.09.016

Frontiers in Physiology

TYPE Original Research
PUBLISHED 21 April 2023
DOI 10.3389/fphys.2023.1144192

Machine learning for screening of at-risk, mild and moderate COPD patients at risk of FEV_1 decline: results from COPDGene and SPIROMICS

Jennifer M. Wang[1]*, Wassim W. Labaki[1], Susan Murray[2], Fernando J. Martinez[3], Jeffrey L. Curtis[1,4], Eric A. Hoffman[5], Sundaresh Ram[6,7], Alexander J. Bell[6], Craig J. Galban[6], MeiLan K. Han[1] and Charles Hatt[6,8]

[1]Division of Pulmonary and Critical Care Medicine, University of Michigan, Ann Arbor, MI, United States, [2]Department of Biostatistics, School of Public Health, University of Michigan, Ann Arbor, MI, United States, [3]Weill Cornell Medical College, New York, NY, United States, [4]Medical Service, VA Ann Arbor Healthcare System, Ann Arbor, MI, United States, [5]Department of Radiology, University of Iowa, Iowa City, IA, United States, [6]Department of Radiology, University of Michigan, Ann Arbor, MI, United States, [7]Department of Biomedical Engineering, University of Michigan, Ann Arbor, MI, United States, [8]Imbio Inc., Minneapolis, MN, United States

Purpose: The purpose of this study was to train and validate machine learning models for predicting rapid decline of forced expiratory volume in 1 s (FEV_1) in individuals with a smoking history at-risk-for chronic obstructive pulmonary disease (COPD), Global Initiative for Chronic Obstructive Lung Disease (GOLD 0), or with mild-to-moderate (GOLD 1–2) COPD. We trained multiple models to predict rapid FEV_1 decline using demographic, clinical and radiologic biomarker data. Training and internal validation data were obtained from the COPDGene study and prediction models were validated against the SPIROMICS cohort.

Methods: We used GOLD 0–2 participants (n = 3,821) from COPDGene (60.0 ± 8.8 years, 49.9% male) for variable selection and model training. Accelerated lung function decline was defined as a mean drop in FEV_1% predicted of > 1.5%/year at 5-year follow-up. We built logistic regression models predicting accelerated decline based on 22 chest CT imaging biomarker, pulmonary function, symptom, and demographic features. Models were validated using n = 885 SPIROMICS subjects (63.6 ± 8.6 years, 47.8% male).

Results: The most important variables for predicting FEV_1 decline in GOLD 0 participants were bronchodilator responsiveness (BDR), post bronchodilator FEV_1% predicted (FEV_1.pp.post), and CT-derived expiratory lung volume; among GOLD 1 and 2 subjects, they were BDR, age, and $PRM_{\text{lower lobes fSAD}}$. In the validation cohort, GOLD 0 and GOLD 1–2 full variable models had significant predictive performance with AUCs of 0.620 ± 0.081 (p = 0.041) and 0.640 ± 0.059 (p < 0.001). Subjects with higher model-derived risk scores had significantly greater odds of FEV_1 decline than those with lower scores.

Conclusion: Predicting FEV_1 decline in at-risk patients remains challenging but a combination of clinical, physiologic and imaging variables provided the best performance across two COPD cohorts.

OPEN ACCESS

EDITED BY
Sam Bayat,
Université Grenoble Alpes, France

REVIEWED BY
Sandeep Bodduluri,
University of Alabama at Birmingham, United States
Mustafa Ghaderzadeh,
Shahid Beheshti University of Medical Sciences, Iran

*CORRESPONDENCE
Jennifer M. Wang,
wangjenn@med.umich.edu

RECEIVED 13 January 2023
ACCEPTED 03 April 2023
PUBLISHED 21 April 2023

CITATION
Wang JM, Labaki WW, Murray S, Martinez FJ, Curtis JL, Hoffman EA, Ram S, Bell AJ, Galban CJ, Han MK and Hatt C (2023), Machine learning for screening of at-risk, mild and moderate COPD patients at risk of FEV_1 decline: results from COPDGene and SPIROMICS.
Front. Physiol. 14:1144192.
doi: 10.3389/fphys.2023.1144192

KEYWORDS

chronic obstructive pulmonary disease, machine learning, computed tomography, lung function decline, quantitative imaging

Introduction

Chronic obstructive pulmonary disease (COPD) is characterized by a variety of clinical phenotypes and disease courses that are often difficult to predict (Miravitlles et al., 2013; Mathioudakis et al., 2020). There is a pressing need to create actionable tools to assist clinicians and researchers in identifying patients who are at higher risk for accelerated lung function decline so that early, directed therapies can be appropriately initiated. In addition to conventional markers of lung function decline using pulmonary function testing (PFT) metrics, novel advanced chest imaging analytic techniques are currently being explored to identify high risk patients. Among these techniques are Parametric Response Mapping (PRM), which co-registers inspiratory and expiratory images to distinguish between normal lung, emphysema, and non-emphysematous air trapping (functional small airways disease, fSAD). Prior studies using PRM have demonstrated the association between fSAD and 5-year forced expiratory volume in 1 s (FEV_1) decline, progression of emphysema and exacerbation risk (Bhatt et al., 2016; Han et al., 2017; Labaki et al., 2019).

Vascular remodeling is also prevalent among COPD patients and believed to be part of the pathogenesis of this disease. CT scans have been used to visualize changes in distal pruning of blood vessels (Rahaghi et al., 2019). The ratio of blood volume in vessels with a cross-sectional area $< 5\ mm^2$ to total blood vessel volume (TBV) has been proposed as an imaging biomarker and, consistent with this theory, has been shown to decrease as COPD progresses (Estepar et al., 2013). Increased airway wall thickness (AWT) has also been associated with more frequent COPD exacerbations (Han et al., 2011) and with greater FEV_1 decline and development of airflow limitation in smokers (Mohamed et al., 2015). AWT is often measured using Pi10, the square root of an airway wall area with a 10 mm lumen perimeter (Nakano et al., 2005).

Predictive models have been widely used for prediction of clinically meaningful outcomes in subjects with COPD. These models have been used to identify factors that place patients at-risk-for exacerbations and hospital admissions and readmissions and to demonstrate the effect of smoking reduction on FEV_1 decline (Simmons et al., 2005; Bahadori et al., 2009; Bertens et al., 2013). Predictive models have also been combined with deep learning methods to assist in staging COPD severity and predict disease progression using automated CT staging to quantify the degree of emphysema and air trapping visualized on images (Hasenstab et al., 2021). Predicting risk of mortality, both in patients admitted to the ICU with exacerbations (Jain et al., 2018) and those in the outpatient primary care setting using a variety of predictive modeling methods (Kiddle et al., 2020) has been extensively studied. However, prediction of FEV_1 decline has remained challenging with currently available risk models.

The purpose of this study was to train and evaluate logistic regression prediction models for rapid FEV_1 decline over a 5-year time span in ever-smoking participants of the Genetic Epidemiology of Chronic Obstructive Pulmonary Disease (COPDGene) study who were either at-risk-for COPD (smoking history but normal spirometry, GOLD 0) or with mild-moderate COPD (GOLD 1–2). We used a variable importance methodology to select and rank a subset of variables that were important for prediction of rapid FEV_1 decline (defined as a drop in $FEV_1\%$ predicted of $> 1.5\%$/year). Models using only imaging biomarkers and data readily available from the Digital Imaging and Communications in Medicine (DICOM) header (i.e., age, sex) were also trained and compared to full data models to determine if data captured only in a CT scan has adequate predictive value. Finally, we externally validated these prediction models in the large Subpopulations and Intermediate Outcome Measures in COPD (SPIROMICS) cohort.

Materials and methods

This study is a retrospective analysis of prospectively acquired data obtained from two large North American cohorts. Both studies were IRB-approved at all clinical centers, elicited written informed consent from all participants, and were compliant with the Health Insurance Portability and Accountability Act (HIPAA).

COPDGene (ClinicalTrials.gov Identifier: NCT 00608764) is an ongoing NIH-sponsored, prospective, multicenter ($n = 21$), observational cohort study starting in November 2007 and consisting of more than 10,000 individuals who were current or former smokers at the time of enrollment. COPDGene aims to understand the etiology, progression, and heterogeneity of COPD (Regan et al., 2010). Inclusion criteria were age 45–80 years old at baseline visit, > 10 pack-years cigarette smoking history, and non-Hispanic white or African American race. Exclusion criteria were other lung diseases, pregnancy, cancer other than skin cancer in the 5 years prior to study entry, receiving antibiotics for a COPD exacerbation in the month prior to study enrollment, and relative of a previously enrolled participant.

SPIROMICS (ClinicalTrials.gov Identifier: NCT 01969344) is an ongoing NIH-sponsored prospective, multicenter ($n = 12$), observational cohort study starting in November 2010 and consisting of 2,981 current, former, and never-smokers at the time of enrollment (Couper et al., 2014). Inclusion criteria were age 40–80 years old at baseline visit, >20 pack-year cigarette smoking history for current or former smokers, and meeting lung function criteria based on spirometry without bronchodilators. An extensive list of exclusion criteria can be found on the ClinicalTrials.gov website (https://clinicaltrials.gov/ct2/show/NCT01969344).

Analysis utilized inspiratory and expiratory chest CT scans from both COPDGene (Regan et al., 2010; Han et al., 2011) and SPIROMICS cohorts (Sieren et al., 2016). In COPDGene, CT scanning occurred at three phases between 2007 and 2022. The intervals between phases were Phase 1–2 5.68 ± 0.89 (mean ± standard deviation, SD) years, Phase 2-3 4.60 ± 0.63 years, and Phase 1–3 10.09 ± 0.40 years. In SPIROMICS, CT scanning occurred at five timepoints between 2010 and 2022, with the baseline and fifth timepoint used in this analysis occurring 6.13 ± 1.05 years apart.

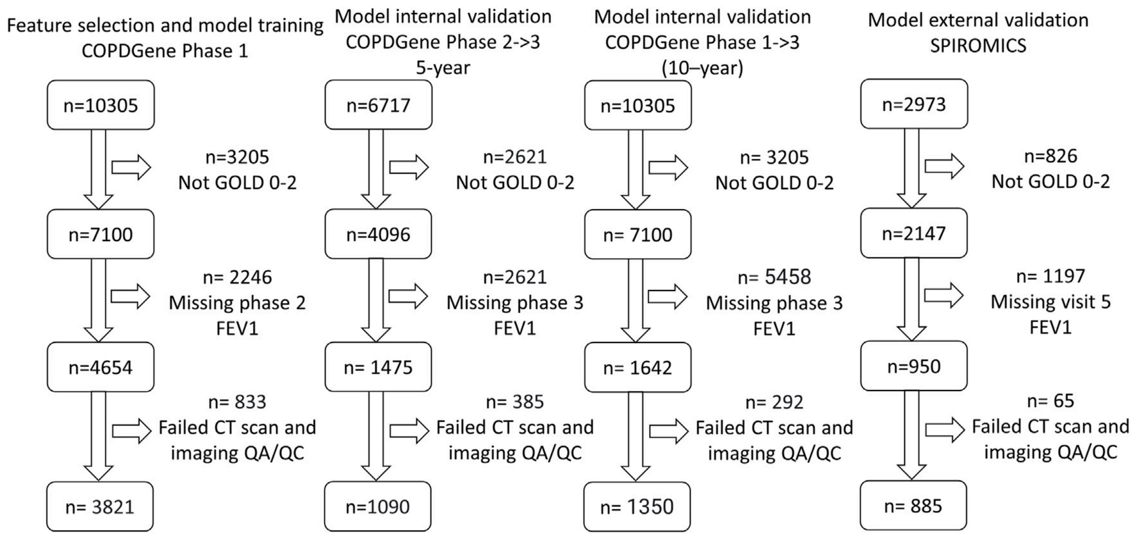

FIGURE 1
Consolidated Standards of Reporting Trials (CONSORT) diagram for model training. (COPDGene Phase 1), 5-year internal validation (COPDGene Phase 2–3), 10-year internal validation (COPDGene Phase 1–3), and external validation (SPIROMICS) datasets.

For both studies, COPD was defined by a post-bronchodilator FEV_1/FVC (forced vital capacity) < 0.7 at the baseline visit, as specified in the GOLD guidelines at the time of study inclusion (Rabe et al., 2007). GOLD grades 1–4, based on post-bronchodilator spirometry, were used to define disease severity (GOLD 1, $FEV_1 \geq$ 80% predicted; GOLD 2, FEV_1 50%–79% predicted; GOLD 3, FEV_1 30%–49% predicted; and GOLD 4, FEV_1 < 30% predicted), with GOLD 0 classification defined by a post-bronchodilator $FEV_1/FVC \geq 0.7$ and FEV_1% predicted ≥ 80%. We performed risk modeling based on GOLD category on the following numbers of participants: in COPDGene, GOLD 0 (n = 2,298) and GOLD 1–2 (n = 1,523), and in SPIROMICS, GOLD 0 (n = 385) and GOLD 1–2 (n = 500) (Figure 1; Tables 1, 2).

Image processing

For all scans, Imbio Inc. Lung Density Analysis version 3.1 (Minneapolis, MN, United States) was used to perform PRM, lung volume measurements, TBV, and tBV5 (the ratio of vascular tree length in vessels with a cross-sectional area less than 5 mm^2 to total vascular tree volume). $PRM_{emphysema}$ is defined as the percentage of lung voxels less than −950 Hounsfield units (HU) on the inspiratory CT scan and less than −856 HU on the expiratory CT scan following deformable registration; PRM_{fSAD} is defined as the percentage of lung voxels greater than or equal to −950 HU on the inspiratory CT scan but less than −856 HU on the expiratory CT. PRM metrics were binarized into clinically significant ($PRM_{emphysema} > 2.0\%$, $PRM_{fSAD} > 10.0\%$) and non-clinically significant categories. The 2% and 10% thresholds were chosen by finding the thresholds that had the highest combination of sensitivity and specificity for univariate prediction of rapid decline in GOLD 0–2 subjects. Bone Mineral Density Analysis v.0.1 (Imbio Inc.) was used to compute the average HU value within the trabecular region of the T12 vertebral body (BMD_{T12}). Airway analysis metrics such as mean segmental AWT and AWT for all airways with an internal perimeter of 10 mm (Pi10) were computed and analyzed in the feature selection step, but could not be used because different software vendors processed data for COPDGene (Thirona) and SPIROMICS (Vida Diagnostics), and thus, the high inter-software variability associated with airway measurements precluded comparisons of models using this data.

At the time this study was conducted, co-author CH, who performed the following statistical analysis and developed the machine learning models, was employed by Imbio Inc. Neither Imbio nor CH had influence over participant inclusion.

Definition of accelerated FEV_1 decline

There is no universally accepted definition of accelerated FEV_1 decline. Martinez et al. defined it as 60 mL/year, roughly double the normal rate of decline in non-smokers (Martinez et al., 2018). However, in the COPDGene cohort, significantly more men than women fit this categorization. To develop sex-agnostic models, we instead categorized rapid progression as a drop of more than 1.5% FEV_1 percent predicted per year (Δ FEV_1%pred), which roughly corresponds to the top quartile of decline. Because a competing risk for accelerated decline is mortality, models were trained to classify participants at-risk-for rapid FEV_1 decline given survival.

Feature selection

We initially considered a set of K = 29 features consisting of symptoms, spirometry, demographic, and CT imaging biomarker data (Figure 2). To simplify the models and to increase reliability of the inputs, we chose to not use self-reported data. A 29 × 29 table of

TABLE 1 Summary statistics for COPDGene Phase 1, COPDGene Phase 2, and SPIROMICS cohorts for GOLD 0 subjects.

	COPDGene P1	COPDGene P2	*p*-value COPDGene P2 vs. COPDGene P1	COPDGene P3	*p*-value COPDGene P3 vs. COPDGene P1	SPIROMICS	*p*-value SPIROMICS vs. COPDGene P1
GOLD 0 totals	2,298	665		839		385	
Rapid decline (>1.5% Δ FEV$_1$% pred)	26.5%	27.4%	*$p = 0.62$	12.8%	*$p = 0.94$	14.0%	*$p = 0.71$
Male	51.8%	55.0%	*$p = 0.47$	52.7%	*$p = 0.58$	55.8%	*$p = 0.27$
White	31.0%	25.6%	*$p = 0.68$	30.9%	*$p = 0.68$	49.3%	*$p = 0.22$
Current smokers	48.9%	33.5%	*$p = 0.69$	48.5%	*$p = 0.61$	42.9%	*$p = 0.38$
Lower lobe PRM$_{fSAD}$ > 10%	10.6%	7.4	*$p = 0.85$	10.5%	*$p = 0.81$	6.2%	*$p = 0.79$
Upper lobe PRM$_{emphysema}$ > 2%	14.4%	11.9	*$p = 0.78$	15.7%	*$p = 0.75$	10.1%	*$p = 0.7$
Age (years)	58.0 ± 8.5	**63.6 ± 8.3**	**$p < 0.001$**	57.6 ± 8.3	$p = 0.26$	**61.9 ± 9.3**	**$p < 0.001$**
Height (cm)	169.9 ± 9.4	**168.4 ± 9.2**	**$p < 0.001$**	169.7 ± 9.2	$p = 0.73$	169.1 ± 9.4	$p = 0.13$
Weight (kg)	84.4 ± 18.4	83.4 ± 19.0	$p = 0.25$	83.8 ± 17.7	$p = 0.39$	84.0 ± 17.6	$p = 0.68$
FVC% predicted	97.5 ± 11.5	98.2 ± 11.7	$p = 0.2$	98.0 ± 11.5	$p = 0.25$	97.0 ± 12.4	$p = 0.25$
Post-bronchodilator FEV$_1$/FVC	0.8 ± 0.1	0.8 ± 0.5	$p = 0.16$	0.8 ± 0.1	$p = 0.58$	**1.0 ± 0.1**	**$p < 0.001$**
SGRQ score	14.8 ± 16.7	**12.8 ± 15.3**	**$p = 0.01$**	14.2 ± 16.3	$p = 0.36$	**22.9 ± 17.1**	**$p < 0.001$**
6MWD (m)	469.6 ± 106.5	**448.9+-120.7**	**$p < 0.001$**	474.8 ± 110.2	$p = 0.23$	**438.3 ± 90.2**	**$p < 0.001$**
Smoking pack-years	37.1 ± 20.3	38.1 ± 20.3	$p = 0.25$	36.5 ± 19.4	$p = 0.51$	**44.0 ± 27.8**	**$p < 0.001$**
Inspiratory CT volume (mL)	5318.8 ± 1237.7	5273.9 ± 1261.7	$p = 0.41$	5325.2 ± 1251.6	$p = 0.90$	5226.4 ± 1253.5	$p = 0.18$
Expiratory CT volume (mL)	2639.3 ± 649.8	2600.3 ± 621.2	$p = 0.17$	2597.6 ± 652.4	$p = 0.11$	2685.6 ± 684.1	$p = 0.2$
TBV (mL)	172.9 ± 38.9	**169.3 ± 35.8**	**$p = 0.03$**	175.7 ± 40.6	$p = 0.08$	171.0 ± 35.7	$p = 0.35$
tBV5 (%)	77.8 ± 4.0	**79.9 ± 4.1**	**$p < 0.001$**	77.8 ± 4.1	$p = 0.74$	**79.4 ± 3.3**	**$p < 0.001$**
trabecular.T12 (HU)	162.7 ± 50.5	**143.9 ± 41.8**	**$p < 0.001$**	162.9 ± 48.7	$p = 0.95$	**151.4 ± 49.8**	**$p < 0.001$**
cortical.T12 (HU)	332.7 ± 57.2	**316.4 ± 55.8**	**$p < 0.001$**	333.6 ± 54.2	$p = 0.69$	**320.1 ± 54.8**	**$p < 0.001$**

*The z-proportions test was used to compute *p*-values for binary variables. The unpaired *t*-test was used to compute *p*-values for continuous data. Bolded text indicates a *p*-value < 0.05. Abbreviations: SGRQ, St. George's Respiratory Questionnaire; 6MWD, 6-min walk distance; TBV, total blood vessel volume; tBV5, ratio of vascular tree length in vessels with a cross-sectional area less than 5 mm^2 to total vascular tree volume; trabecular.T12, average Hounsfield unit (HU) value within the trabecular region of the T12 vertebral body; cortical.T12, average Hounsfield unit (HU) value within the cortical region of the T12 vertebral body.

Spearman correlations between each feature was generated to assess feature redundancy (Parr et al., 2020) using data from GOLD 0–2 subjects. Features that had a Spearman correlation > 0.80 with any other variables were considered for removal due to information redundancy. For example, we retained weight and height but removed body mass index (BMI) because weight and height were independent from each other, but weight was highly correlated to BMI. Forced mid-expiratory flow (FEF$_{25.75}$) was removed because it correlated strongly with FEV$_1$/FVC. Finally, of the PRM imaging biomarker variables, PRM$_{upper\ lobes\ emphysema}$ and PRM$_{lower\ lobes\ fSAD}$ had the lowest correlation and thus were retained.

Following manual feature pruning, we conducted a "drop-column" feature-importance ranking and data-driven pruning procedure for the remaining 22 parameters. Classification models were trained using COPDGene Phase 1 data, with the outcome Δ FEV$_1$%pred variable measured between Phase 1 and Phase 2. We generated an initial model using all K = 22 features to arrive at a baseline model performance based on the receiver operating characteristic area under the curve (ROC-AUC). To arrive at AUC distribution, model performance was assessed using repeat cross-validation (M = 5,000 cross-validations with a train/test ratio of 80%/20%). The same procedure was repeated K = 22 times, each

TABLE 2 Summary statistics for COPDGene Phase 1, COPDGene Phase 2, and SPIROMICS cohorts for GOLD 1–2 subjects.

	COPDGene P1	COPDGene P2	p-value COPDGene P2 vs. COPDGene P1	COPDGene P3	p-value COPDGene P3 vs. COPDGene P1	SPIROMICS	p-value SPIROMICS vs. COPDGene P1
GOLD 1–2 totals	1,523	425		511		500	
Rapid decline (>1.5% Δ FEV$_1$% pred)	29.8%	38.4%	*$p = 0.49$	25.2%	*$p = 0.72$	24.8%	*$p = 0.72$
Male	46.9%	43.8%	*$p = 0.54$	45.2%	*$p = 0.6$	41.6%	*$p = 0.63$
White	81.0%	80.9%	*$p = 0.68$	81.2%	*$p = 0.73$	70.0%	*$p = 0.56$
Current smokers	44.5%	34.4%	*$p = 0.64$	41.5%	*$p = 0.62$	36.6%	*$p = 0.67$
Lower lobe PRM$_{fSAD}$ > 10%	59.8%	60.5%	*$p = 0.45$	55.6%	*$p = 0.57$	52.6%	*$p = 0.59$
Upper lobe PRM$_{emphysema}$ > 2%	55.7%	55.8%	*$p = 0.47$	57.5%	*$p = 0.53$	52.8%	*$p = 0.57$
Age (years)	63.0 ± 8.5	**67.8 ± 8.1**	**$p < 0.001$**	62.5 ± 8.1	$p = 0.23$	**65.6 ± 7.6**	**$p < 0.001$**
Height (cm)	170.1 ± 9.7	170.3 ± 9.8	$p = 0.68$	170.6 ± 9.5	$p = 0.31$	170.8 ± 9.3	$p = 0.15$
Weight (kg)	82.3 ± 18.2	81.6 ± 18.3	$p = 0.45$	81.6 ± 17.8	$p = 0.41$	82.0 ± 17.7	$p = 0.70$
FVC% predicted	72.8 ± 14.3	**74.4 ± 15.8**	**$p = 0.05$**	**75.0 ± 15.4**	**$p < 0.001$**	**75.2 ± 14.8**	**$p < 0.001$**
Post-bronchodilator FEV$_1$/FVC	0.6 ± 0.1	0.6 ± 0.1	$p = 0.79$	0.6 ± 0.08	$p = 0.84$	**0.8 ± 0.1**	**$p < 0.001$**
SGRQ score	26.1 ± 20.7	**23.0 ± 19.0**	**$p = 0.01$**	**23.4 ± 19.9**	**$p = 0.01$**	**29.9 ± 16.5**	**$p < 0.001$**
6MWD (m)	431.2 ± 109.4	424.1 ± 115.2	$p = 0.24$	**449.4 ± 105.5**	**$p < 0.001$**	421.9 ± 98.3	$p = 0.09$
Smoking pack-years	49.1 ± 25.1	49.5 ± 23.7	$p = 0.75$	47.7 ± 23.0	$p = 0.27$	51.4 ± 25.3	$p = 0.08$
Inspiratory CT volume (mL)	5788.4 ± 1384.2	5878.2 ± 1438.3	$p = 0.24$	5890.9 ± 1432.1	$p = 0.15$	5896.5 ± 1418.4	$p = 0.13$
Expiratory CT volume (mL)	3312.9 ± 860.5	3311.7 ± 842.0	$p = 0.98$	3278.6 ± 856.8	$p = 0.44$	**3425.1 ± 886.1**	**$p = 0.01$**
TBV (mL)	179.0 ± 39.5	176.3 ± 37.8	$p = 0.21$	180.4 ± 38.8	$p = 0.50$	182.6 ± 38.0	$p = 0.08$
tBV5 (%)	78.2 ± 4.2	**79.9 ± 3.9**	**$p < 0.001$**	78.1 ± 4.3	$p = 0.49$	**78.0 ± 3.4**	**$p < 0.001$**
trabecular.T12 (HU)	141.4 ± 71.0	**133.3 ± 44.6**	**$p = 0.03$**	143.2 ± 47.6	$p = 0.59$	**133.6 ± 42.1**	**$p = 0.02$**
cortical.T12 (HU)	319.5 ± 62.4	**312.5 ± 59.3**	**$p = 0.04$**	320.3 ± 57.1	$p = 0.8$	**313.5 ± 59.8**	$p = 0.06$

*The z-proportions test was used to compute p-values for binary variables. The unpaired t-test was used to compute p-values for continuous data. Bolded text indicates a p-value < 0.05. Abbreviations: SGRQ, St. George's Respiratory Questionnaire; 6MWD, 6-min walk distance; TBV, total blood vessel volume; tBV5, ratio of vascular tree length in vessels with a cross-sectional area less than 5 mm^2 to total vascular tree volume; trabecular.T12, average Hounsfield unit (HU) value within the trabecular region of the T12 vertebral body; cortical.T12, average Hounsfield unit (HU) value within the cortical region of the T12 vertebral body.

time removing a single feature, which produced a distribution of AUC reductions for each instance of feature removal. Features that resulted in a decrease in model AUC performance when "dropped" were retained for use in the final model; all others were removed (Figure 2). The drop-column procedure was performed separately for GOLD 0 and GOLD 1–2 subjects, resulting in two distinct variables sets for the final models.

In addition to a full variable model considering all variables that survived feature selection, we also created limited models using only imaging biomarkers (i.e., lung volumes, PRM, vascular, and bone density measurements) and data readily available from the DICOM header (i.e., age, sex), referred to hereafter as "CT-limited model." The purpose of this analysis was to determine the predictive value of data that could only be obtained from a CT scan file within the electronic medical record.

Machine learning methods and parameters

A wide variety of machine-learning techniques can be used to predict biological outcomes from multiple sources of data (Garavand et al., 2022). In this study, models were developed

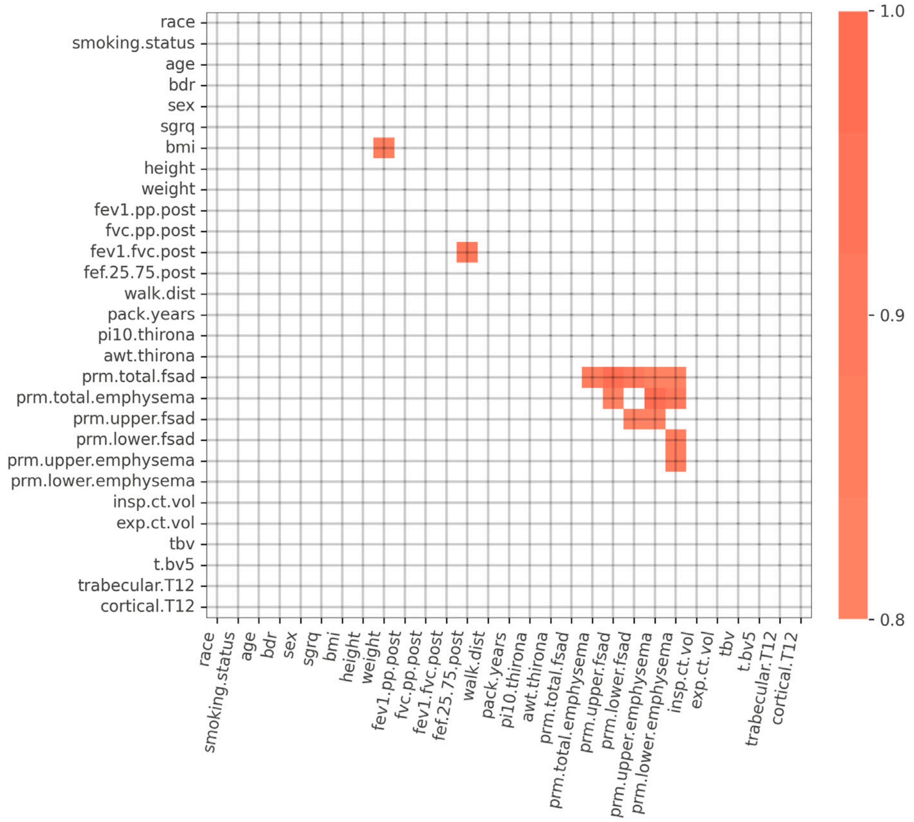

FIGURE 2
Spearman correlation matrix for the initial 29 variables. Spearman correlations > 0.80 are highlighted in orange. Strong correlations exist between PRM imaging biomarker variables, FEV_1/FVC and FEF_{25-75}, and BMI and weight. Abbreviations: bdr, bronchodilator responsiveness; sgrq, St. George's Respiratory Questionnaire; BMI, body mass index; FEV1.pp.post, post bronchodilator FEV_1% predicted; FVC.pp.post, post bronchodilator FVC % predicted; FEV1.FVC.post, post bronchodilator FEV_1/FVC; FEF.25.75.post, post bronchodilator forced mid-expiratory flow; walk.dist, 6-min walk distance; pi10.thirona, square root of an airway wall area with a 10 mm lumen perimeter, measured by Thirona software; awt.thirona, segmental airway wall thickness, measured by Thirona software; prm.total.fsad, PRM total fSAD > 10%; prm.total.emphysema, PRM total emphysema > 2%; prm.upper.fsad, PRM upper lobes fSAD > 10%; prm.lower.fsad, PRM lower lobes fSAD > 10%; prm.upper.emphysema, PRM upper lobes emphysema > 2%; prm.lower.emphysema, PRM lower lobes emphysema > 2%; insp.ct.vol, CT-derived inspiratory lung volume; exp.ct.vol, CT-derived expiratory lung volume; tbv, total blood vessel volume; t.bv5, ratio of vascular tree length in vessels with a cross-sectional area less than 5 mm^2 to total vascular tree volume; trabecular.T12, average Hounsfield unit (HU) value within the trabecular region of the T12 vertebral body; cortical.T12, average Hounsfield unit (HU) value within the cortical region of the T12 vertebral body.

and validated using logistic regression with an L1 regularization penalty (a.k.a. LASSO) due to simplicity of implementation (i.e., few hyper-parameters) compared to other popular machine learning frameworks such as Random Forests or XGBoost. The L1 regularization penalty was employed to learn models that have a sparse set of significant predictor variables. We used the scikit-learn software package v1.0.2 within Python version 3.8.10 for all model development and validation. Model hyper-parameters were optimized using a Randomized Cross Validation search algorithm (sklearn.model_selection.RandomizedSearchCV). The cross validation hyper-parameter search resulted in an optimal inverse regularization penalty weight of C = 0.3.

Internal and external validation

Internal validation was performed in two ways. First, we applied the models developed on the COPDGene Phase 1 training data to the COPDGene Phase 2 data, where the output variable was the Δ FEV_1% pred between the Phase 2 and Phase 3 visits. Second, we validated the model developed on the COPDGene Phase 1 data against the Δ FEV_1% pred between the Phase 1 and Phase 3 data, which were roughly 10 years apart. External validation was performed on data from the SPIROMICS study. Differences in the distribution between data in the training, internal validation, and external validation cohorts are shown in Table 1. Confidence intervals were computed by computing 1.96 × SD of the AUC using bootstrapping with 5,000 resamples. Permutation testing was used to generate AUC *p*-values.

Relative risk based on model output probabilities

Following model generation, we recorded the logistic regression output probabilities associated with the lower 25th (p_{25}) and upper 75th (p_{75}) percentiles of the training data. We computed the relative risk between participants with FEV_1%pred decline risk > p_{75} and those with risk < p_{25} for the training dataset (COPDGene Phase 1-Phase 2), the

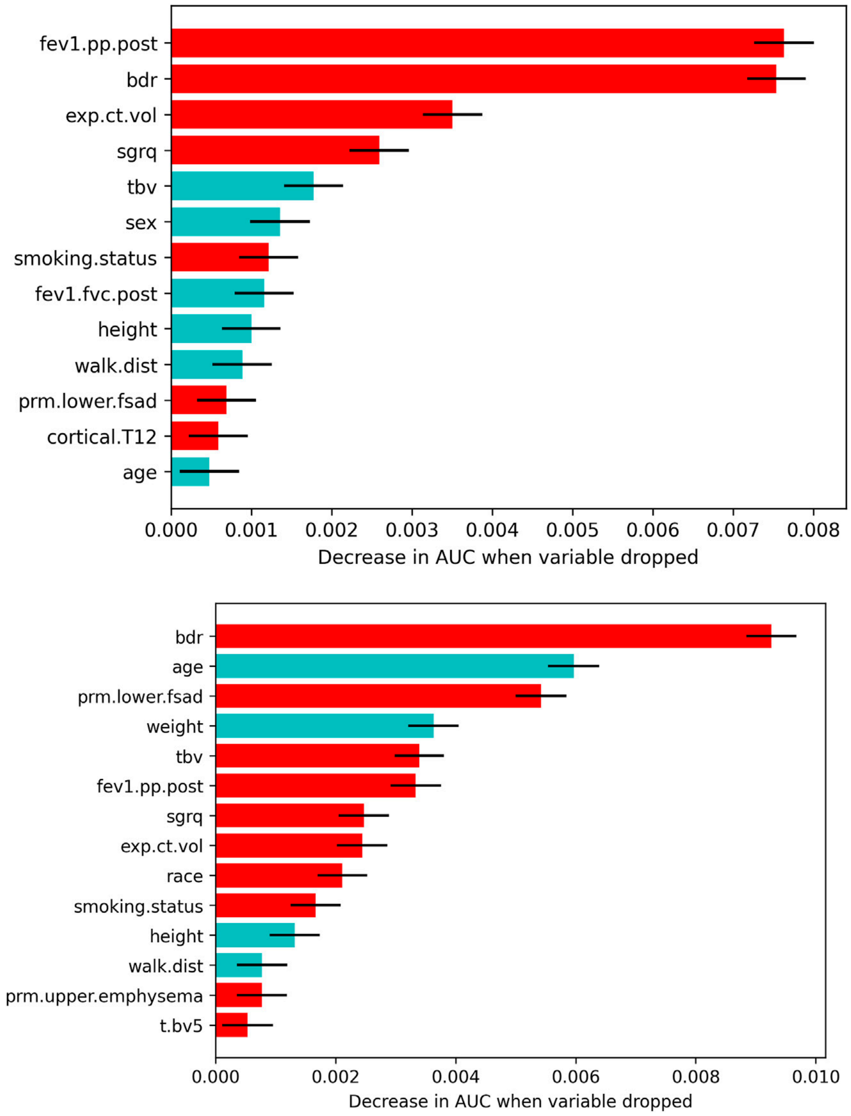

FIGURE 3
Features that survived the drop-column variable selection procedure for each GOLD group and model type (top: GOLD 0; bottom: GOLD 1–2). The mean ±1.96 × SD decrease in AUC related to dropping each feature is plotted only for features that significantly affected the model. Red bars indicate a higher risk of rapid FEV_1 decline with increasing value, having bronchodilator reversibility, African American race, and/or being a current smoker. Blue bars indicate a higher risk of rapid FEV_1 decline with decreasing value and male sex. Abbreviations: fev1.pp.post, post bronchodilator FEV_1% predicted; bdr, bronchodilator responsiveness; exp.ct.vol, CT-derived expiratory lung volume; sgrq, St. George's Respiratory Questionnaire; tbv, total blood vessel volume; fev1.fvc.post, post bronchodilator FEV_1/FVC; walk.dist, 6-min walk distance; prm.lower.fsad, PRM lower lobes fSAD > 10%; cortical.T12, average HU value in the cortical region of the T12 vertebra; prm.upper.emphysema, PRM upper lobes emphysema > 2%; t.bv5, ratio of vascular tree length in vessels with a cross-sectional area less than 5 mm^2 to total vascular tree volume.

internal validation dataset (COPDGene Phase 2-Phase 3), and the external validation dataset. Additionally, we looked at the relative risk of rapid decline over 10 years by examining subjects that had Δ FEV_1% pred data between COPDGene Phase 1 and Phase 3. Relative risk was computed using the scipy.stats.contingency.relative_risk software package v1.8.1.

Results

Results are separated into 3 broad sections: 1) feature selection to create the training model, 2) within the COPDGene cohort cross validation and 3) external SPIROMICS cohort validation, followed by a section on relative risk.

Within cohort analysis

Figure 3 depicts all features that survived the variable selection procedure during model training in models developed on COPDGene Phase 1-Phase 2 data. In the full-variable model for the GOLD 0 cohort, higher post bronchodilator FEV_1% predicted (FEV_1pp.post), bronchodilator responsiveness (BDR), greater expiratory CT volume, and a higher St. George's Respiratory

TABLE 3 Cross-validation AUCs, listed as mean ± 1.96 standard deviation (SD).

	Full model*	CT-limited model**
5-year COPDGene P1–P2 (training)		
GOLD 0	0.653 ± 0.025 ($p < 0.001$)	0.592 ± 0.027 ($p < 0.001$)
GOLD 1–2	0.713 ± 0.028 ($p < 0.001$)	0.650 ± 0.030 ($p < 0.001$)
5-year COPDGene P2–P3 (Internal validation)		
GOLD 0	0.622 ± 0.048 ($p < 0.001$)	0.562 ± 0.048 ($p = 0.028$)
GOLD 1–2	0.644 ± 0.054 ($p < 0.001$)	0.591 ± 0.059 ($p = 0.008$)
10-year COPDGene P1–P3 (Internal validation)		
GOLD 0	0.680 ± 0.053 ($p < 0.001$)	0.603 ± 0.057 ($p = 0.005$)
GOLD 1–2	0.753 ± 0.047 ($p < 0.001$)	0.679 ± 0.028 ($p < 0.001$)
SPIROMICS (external validation)		
GOLD 0	0.622 ± 0.081 ($p = 0.021$)	0.571 ± 0.089 ($p = 0.120$)
GOLD 1–2	0.640 ± 0.059 ($p < 0.001$)	0.568 ± 0.059 ($p = 0.056$)

*GOLD 0 full model variables: post bronchodilator FEV_1% predicted, BDR, CT-derived expiratory lung volume, SGRQ score, TBV, sex, smoking status, post bronchodilator FEV1/FVC, height, 6MWD, PRMlower lobes fSAD > 10%, cortical.T12, age.

*GOLD 1–2 full model variables: BDR, age, $PRM_{\text{lower lobes fSAD}}$ > 10%, weight, TBV, post bronchodilator FEV_1% predicted, SGRQ score, CT-derived expiratory lung volume, race, smoking status, height, 6MWD, $PRM_{\text{upper lobes emphysema}}$ > 2%, tBV5.

**GOLD 0 CT-limited model variables: CT-derived expiratory lung volume, TBV, sex, $PRM_{\text{lower lobes fSAD}}$ > 10%, cortical.T12, age.

**GOLD 1–2 CT-limited model variables: age, $PRM_{\text{lower lobes fSAD}}$ > 10%, TBV, CT-derived expiratory lung volume, $PRM_{\text{upper lobes emphysema}}$ > 2%, tBV5.

Questionnaire (SGRQ) score were the most important variables for predicting rapid FEV_1 decline. Less significant variables included a lower TBV, male sex, and current smoking status.

In the full-variable model for the GOLD 1–2 cohort, BDR, younger age, $PRM_{\text{lower lobes fSAD}}$ > 10%, and higher blood vessel volume were the most important variables predicting rapid FEV_1 decline. Less significant variables included higher SGRQ score, lower weight, higher FEV_1pp.post, current smoking status, higher expiratory CT volume, shorter height and 6-min walk distance (6MWD), African American race, and PRMupper lobes emphysema > 2%.

Within cohort validation

Following model training, we validated the CT-limited COPDGene models using the same training variables within the COPDGene cohort. This process used data from both the 5-year (P2–P3) and 10-year (P1–P3) follow-up periods. For the GOLD 0 models, AUCs were similar to those from the training dataset, whereas the GOLD 1–2 models were still significant but had much lower AUCs during the 5-year follow up (P2–P3) than during training (Table 3).

Surprisingly, AUCs increased for all models in the 10-year validation (P1–P3). This result is atypical in machine learning, as model AUCs tend to be highest in training data. A possible explanation is that we employed the same pool of independent variables used for training to predict the same signal, but over a longer period of time. This process might decrease the noise inherent in serial FEV_1 measurements, and thus increase the prediction accuracy.

External cohort validation

External validation on SPIROMICS data resulted in trends similar to COPDGene P2–P3 data, showing slight predictive drops in performance. The full variable models were significant ($p < 0.05$) for both the GOLD 0 and GOLD 1–2 groups; however, the performance of the CT-limited models declined and were no longer significant for GOLD 0 participants. A possible explanation is that there were only roughly half as many SPIROMICS participants as in the COPDGene P2–P3 analysis.

In general, GOLD 1–2 models consistently performed better than GOLD 0 models. This finding suggests that accelerated lung function decline can be predicted with greater accuracy in those who already have spirometric evidence of airflow obstruction. Additionally, the prediction accuracy of the CT-limited models was much lower than the full variable models across all training and validation groups.

Relative risk

We next computed relative risk between two groups: those with rapid decline risk greater than the upper 75th (p_{75}) versus those with decline less than the lower 25th (p_{25}) (Table 4). For this purpose, we used the logistic regression output probabilities of the training data for all four datasets. The highest relative risk was consistently seen in the 10-year internal validation group (COPDGene P1–P3), suggesting that over longer follow-up, these predictive models can effectively discriminate those at highest risk of accelerated lung function decline.

Focusing only on GOLD 1–2 participants in the COPDGene P1–P3 group, the full model can predict an over 8-fold increased risk

TABLE 4 Relative risk of rapid FEV_1 decline associated with risk score greater than the upper 75th percentile (p_{75}) versus risk less than the lower 25th (p_{25}).

	Full model*		CT-limited model**	
	GOLD 0	GOLD 1, 2	GOLD 0	GOLD 1, 2
Training data COPDGene P1–P2	2.6 (2.1, 3.3)	3.7 (2.8, 4.9)	1.9 (1.5, 2.3)	2.7 (2.1, 3.5)
Internal validation COPDGene P2–P3 (5 year)	2.0 (1.4, 2.9)	2.5 (1.8, 3.5)	1.5 (1.1, 2.2)	1.3 (1.0, 1.6)
Internal validation COPDGene P1–P3 (10-year)	5.8 (2.8, 12.0)	8.1 (3.8, 16.9)	2.4 (1.5, 3.6)	3.5 (2.0, 5.6)
External validation SPIROMICS	2.5 (0.99, 6.3)	1.8 (1.16, 2.8)	2.14 (1.1, 4.1)	1.6 (1.0, 2.4)

95% confidence intervals are in parentheses.

*GOLD 0 full model variables: post bronchodilator FEV_1% predicted, BDR, CT-derived expiratory lung volume, SGRQ score, TBV, sex, smoking status, post bronchodilator FEV_1/FVC, height, 6MWD, $PRM_{lower\ lobes\ fSAD}$ > 10%, cortical.T12, age.

*GOLD 1–2 full model variables: BDR, age, $PRM_{lower\ lobes\ fSAD}$ > 10%, weight, TBV, post bronchodilator FEV_1% predicted, SGRQ score, CT-derived expiratory lung volume, race, smoking status, height, 6MWD, $PRM_{upper\ lobes\ emphysema}$ > 2%, tBV5.

**GOLD 0 CT-limited model variables: CT-derived expiratory lung volume, TBV, sex, $PRM_{lower\ lobes\ fSAD}$ > 10%, cortical.T12, age.

**GOLD 1–2 CT-limited model variables: age, $PRM_{lower\ lobes\ fSAD}$ > 10%, TBV, CT-derived expiratory lung volume, $PRM_{upper\ lobes\ emphysema}$ > 2%, tBV5.

of accelerated FEV_1 decline among p_{75} versus p_{25} participants. Relative risk was lower in all the tested cohorts when using the CT-limited model, consistent with prior results in this analysis.

Overall, these relative risk profiles suggest that the full variable models could effectively identify those at highest risk of lung function decline with sufficient accuracy to provide clinical relevancy and utility in decision making. By contrast, the CT-limited models lack significantly increased relative risk in the SPIROMICS data, despite promising results in the COPDGene 10-year analysis. This finding highlights the need for further external validation using 10-year follow-up data to determine more conclusively whether screening for rapid FEV_1 decline will be practically feasible using only data from DICOM files.

Discussion

We studied the important clinical question of whether machine learning techniques can predict which ever-smokers, either at-risk-for COPD or with mild-moderate disease, are at highest risk for accelerated FEV_1 decline. In an ideal world, one may imagine that identifying individuals at-risk-for disease progression only from data available in a chest CT would allow for increased availability of data to clinicians in a potentially automated fashion. Using logistic regression models built based on a combination of radiographic and clinical features, we show that this approach is feasible.

We were able to identify the most relevant imaging biomarker features predicting accelerated lung function decline, which importantly differed between those with established disease and those at-risk. Key variables in GOLD 1–2 participants included $PRM_{lower\ lobes\ fSAD}$ and demographic information such as age, expiratory lung volume in GOLD 0 participants, and pulmonary function results, particularly BDR, in both groups. Our models showed only modest decreases in predictive strength, as indicated by AUC analysis, in the external validation cohort, and improved at longer intervals in the training set (COPDGene), for which longer follow-up data were available. In the latter group, the full variable models were able to predict an 8-fold difference in relative risk between those in the highest versus lowest quartile of lung function decline. These findings support the use of combined radiographic and clinical data models to select participants for therapeutic trials of potentially disease-modifying agents in COPD.

A strength of this analysis is that the input variables in the full models are objective, and most are readily available, due to the use of spirometry rather than more complex pulmonary function testing and to the fact that many individuals also have recent CT scans. In the CT-limited model, additional variables, including TBV, were also found to be significant contributors to prediction of accelerated FEV_1 decline, though with interesting differences based on COPD status. Thus, FEV_1 decline was associated with lower TBV in GOLD 0, but with higher TBV in GOLD 1–2. One possible explanation for this disparity is the known association of distal pruning of pulmonary vessels with early COPD progression (Estepar et al., 2013; Synn et al., 2019; Weatherald et al., 2019). However, further studies are needed to understand why this relationship is reversed in later disease stages, where there may be additional anatomic changes associated with development of pulmonary hypertension (Elwing and Panos, 2008).

Our finding of the strong predictive impact of BDR is also noteworthy, as BDR has recently been associated with thicker airway walls in COPD subjects and decline in lung function (Donaldson et al., 2005; Kim et al., 2014). This may be due to active inflammatory disease at the level of the distal, smaller airways, leading to loss of lung function over time (Barjaktarevic et al., 2019).

Our results agree with a recent study that used similar machine learning techniques to predict progression of FEV_1 in COPDGene (Boueiz et al., 2022) and that also utilized P1–P2 and P1–P3 data for internal validation. Their machine learning models, both logistic regression and random forest, were able to predict an absolute cross-sectional FEV_1 at follow-up visits with excellent results (ROC-AUCs > 0.9). However, similar to our work, they had greater difficulty predicting change in FEV_1 over time, with ROC-AUCs around 0.7 for both types of their models. This may be due to the fact that the relative changes in FEV_1 over a few years are small and result in low signal-to-noise ratios. We extend those findings via use of novel PRM and vascular biomarkers in our prediction models, as well as by external validation in a separate cohort to improve their performance despite these inherent limitations.

The overall modest AUCs across our models, ranging roughly between 0.5–0.7, imply that FEV_1 is an imprecise (i.e., noisy) dependent variable. Models trained on noisy binary classification outcomes can still converge upon an optimal solution, as long as noise is symmetric, i.e., the same odds of false positive and false negative measurements, and there are sufficient observations (Lugosi, 1992). That AUCs were highest for GOLD 1-2 participants was expected, and in agreement with the analysis of Boueiz et al. (2022), as FEV_1 decline in COPD is most rapid in this group, making the signal-to-noise ratio highest (D'Amato et al., 2016). Also as expected, we found that pulmonary function, symptoms, and more extensive demographic data improved prediction accuracy over using imaging variables alone. In particular, BDR was consistently the most important non-imaging variable, with SGRQ score also providing significant information.

That some of our findings were no longer statistically significant in the CT-limited model for GOLD 0 indicates that screening this group using imaging data alone is inadequate. These findings further emphasize the challenge of predicting FEV_1 decline in ever-smokers without airflow obstruction. While currently available clinical parameters alone do not adequately predict risk in this group, it is promising that when combined with radiographic variables, these novel machine learning techniques can be harnessed to assist in clinical decision making in a relatively short period of time. There remains great potential to harness these techniques for a variety of clinical applications to fill patient care gaps. For example, the ability to better phenotype patients will allow researchers to identify suitable subjects for clinical trials, target subjects at greatest risk for accelerated lung function decline, and more rapidly assess response to new therapies.

We also acknowledge several limitations to our work and have identified key goals moving forward. We only tested logistic regression models using machine learning techniques for feature selection. Although we did not test other algorithms, notably decision tree models, we replicated findings of a recent study that did. Prior studies have attempted to phenotype subjects at risk of lung function decline using machine learning methods such as decision tree models in other cohorts, but did not adjust for decline associated with sex, which was the greatest predictor of decline (Nikolaou et al., 2021). As stated above, prediction of FEV_1 remains challenging, and continued refinement and optimization of our models will be required before these techniques can be applied clinically to account for lung function decline that may be fairly subtle over a few years. A wealth of biomarker data correlates to risk of COPD progression, exacerbations, and mortality (Leitao Filho et al., 2020; Tanimura et al., 2020; Pratte et al., 2021; Serban et al., 2021; Singh et al., 2021) that was not included in our current models, but in future iterations would be important to consider. Survivorship bias is another limitation in longitudinal observational cohort studies, especially in subjects with advanced COPD and increased short term mortality risk, that may influence our results. Finally, most of the longitudinal follow-up in this study occurred over a 5-year period, with some additional analysis based on 10-year follow-up data. However, a longer follow-up period may further enhance our model's performance and predictive ability.

In summary, we determined that a combination of radiographic and clinical variables can help predict which individuals are at highest risk for rapid FEV_1 decline. While logistic regression models trained on a limited but more easily obtainable dataset captured from CT scans also had significant predictive value, these models were not as accurate. Predicting FEV_1 decline continues to be challenging and there remains a strong unmet clinical need for further refinement of these models.

Data availability statement

The data analyzed in this study is subject to the following licenses/restrictions: The datasets presented in this study are not readily available because they are part of NIH sponsored clinical trials and require a data-use agreement to be signed. For access to COPDGene data visit https://www.copdgene.org/phase-1-study-documents.htm for instructions. For access to SPIROMICS data, visit https://www.spiromics.org/spiromics/obtaining-data for instructions. Requests to access these datasets should be directed to COPDGene: https://www.copdgene.org/phase-1-study-documents.htm; SPIROMICS: https://www.spiromics.org/spiromics/obtaining-data.

Author contributions

CH processed the imaging data with quantitative CT (QCT) biomarker software from Imbio. CH designed the analysis and CH and JW analyzed the data. JW drafted the manuscript with editing from CH, WL, and MH. All authors reviewed and approved the final version of the manuscript for publication.

Funding

This work was supported by NHLBI Grant R01 HL150023 and by NHLBI Grants U01 HL089897 and U01 HL089856, which support the COPDGene study. The COPDGene study (NCT00608764) is also supported by the COPD Foundation through contributions made to an Industry Advisory Committee comprised of AstraZeneca, Bayer Pharmaceuticals, Boehringer-Ingelheim, Genentech, GlaxoSmithKline, Novartis, Pfizer and Sunovion. SPIROMICS was supported by contracts from the NIH/NHLBI (HHSN 268200900013C, HHSN 268200900014C, HHSN 268200900015C, HHSN 268200900016C, HHSN 268200900017C, HHSN 268200900018C, HHSN 268200900019C, HHSN 268200900020C), grants from the NIH/NHLBI (U01 HL137880 and U24 HL141762), and supplemented by contributions made through the Foundation for the NIH and the COPD Foundation from AstraZeneca/MedImmune; Bayer; Bellerophon Therapeutics; Boehringer-Ingelheim Pharmaceuticals, Inc.; Chiesi Farmaceutici S.p.A.; Forest Research Institute, Inc.; GlaxoSmithKline; Grifols Therapeutics, Inc.; Ikaria, Inc.; Novartis Pharmaceuticals Corporation; Nycomed GmbH; ProterixBio; Regeneron Pharmaceuticals, Inc.; Sanofi; Sunovion; Takeda Pharmaceutical Company; and Theravance Biopharma and Mylan. The authors declare that support for the COPDGene and SPIROMICS studies include commercial funding, as described above. These commercial funders were not involved in the design, collection, analysis, or interpretation of data for the present study, the writing of this article, or the decision to submit it for publication.

Acknowledgments

The authors wish to thank Lee Olsen for assisting with manuscript preparation and editing. The authors thank the SPIROMICS participants and participating physicians, investigators and staff for making this research possible. More information about the study and how to access SPIROMICS data is available at www.spiromics.org. The authors would like to acknowledge the University of North Carolina at Chapel Hill BioSpecimen Processing Facility for sample processing, storage, and sample disbursements (http://bsp.web.unc.edu/). We would like to acknowledge the following current and former investigators of the SPIROMICS sites and reading centers: Neil E Alexis, MD; Wayne H Anderson, PhD; Mehrdad Arjomandi, MD; Igor Barjaktarevic, MD, PhD; R Graham Barr, MD, DrPH; Patricia Basta, PhD; Lori A Bateman, MSc; Surya P Bhatt, MD; Eugene R Bleecker, MD; Richard C Boucher, MD; Russell P Bowler, MD, PhD; Stephanie A Christenson, MD; Alejandro P Comellas, MD; Christopher B Cooper, MD, PhD; David J Couper, PhD; Gerard J Criner, MD; Ronald G Crystal, MD; JC; Claire M Doerschuk, MD; Mark T Dransfield, MD; Brad Drummond, MD; Christine M Freeman, PhD; CG, PhD; MH; Nadia N Hansel, MD, MPH; Annette T Hastie, PhD; Eric A EH, PhD; Yvonne Huang, MD; Robert J Kaner, MD; Richard E Kanner, MD; Eric C Kleerup, MD; Jerry A Krishnan, MD, PhD; Lisa M LaVange, PhD; Stephen C Lazarus, MD; FM; Deborah A Meyers, PhD; Wendy C Moore, MD; John D Newell Jr, MD; Robert Paine, III, MD; Laura Paulin, MD, MHS; Stephen P Peters, MD, PhD; Cheryl Pirozzi, MD; Nirupama Putcha, MD, MHS; Elizabeth C Oelsner, MD, MPH; Wanda K O'Neal, PhD; Victor E Ortega, MD, PhD; Sanjeev Raman, MBBS, MD; Stephen I. Rennard, MD; Donald P Tashkin, MD; J Michael Wells, MD; Robert A Wise, MD; and Prescott G Woodruff, MD, MPH. The project officers from the Lung Division of the National Heart, Lung, and Blood Institute were Lisa Postow, PhD, and Lisa Viviano, BSN.

Conflict of interest

WL reports personal fees from Konica Minolta and Continuing Education Alliance. JC reports grants from NHLBI and the COPD Foundation, during performance of this study; grants from NHLBI, NIAID, the Department of Veterans Affairs, and the Department of Defense, outside this study; consulting fees (paid to his institution) from AstraZeneca PLC and CLS Behring, LLC, outside this study; and personal fees from AstraZeneca Global, outside this study. CG is co-inventor of Parametric Response Mapping, which the University of Michigan has licensed to Imbio, LLC., and has a financial interest in Imbio, LLC. MH reports personal fees from GlaxoSmithKline, AstraZeneca, Boehringer Ingelheim, Cipla, Chiesi, Novartis, Pulmonx, Teva, Verona, Merck, Mylan, Sanofi, DevPro, Aerogen, Polarian, Regeneron, Amgen, UpToDate, Altesa Biopharma, Medscape, NACE, MDBriefcase and Integrity. She has received either in kind research support or funds paid to the institution from the NIH, Novartis, Sunovion, Nuvaira, Sanofi, AstraZeneca, Boehringer Ingelheim, Gala Therapeutics, Biodesix, the COPD Foundation and the American Lung Association. She has participated in Data Safety Monitoring Boards for Novartis and Medtronic with funds paid to the institution. She has received stock options from Meissa Vaccines and Altesa Biopharma. CH is employed by and has stock options in Imbio, Inc.

The remaining authors declare that the research was conducted in the absence of any commercial or financial relationships that could be construed as a potential conflict of interest.

Publisher's note

References

Bahadori, K., Fitzgerald, J. M., Levy, R. D., Fera, T., and Swiston, J. (2009). Risk factors and outcomes associated with chronic obstructive pulmonary disease exacerbations requiring hospitalization. *Can. Respir. J.* 16, e43–e49. doi:10.1155/2009/179263

Barjaktarevic, I. Z., Buhr, R. G., Wang, X., Hu, S., Couper, D., Anderson, W., et al. (2019). Clinical significance of bronchodilator responsiveness evaluated by forced vital capacity in COPD: SPIROMICS cohort analysis. *Int. J. Chron. Obstruct Pulmon Dis.* 14, 2927–2938. doi:10.2147/COPD.S220164

Bertens, L. C., Reitsma, J. B., Moons, K. G., van Mourik, Y., Lammers, J. W., Broekhuizen, B. D., et al. (2013). Development and validation of a model to predict the risk of exacerbations in chronic obstructive pulmonary disease. *Int. J. Chron. Obstruct Pulmon Dis.* 8, 493–499. doi:10.2147/COPD.S49609

Bhatt, S. P., Soler, X., Wang, X., Murray, S., Anzueto, A. R., Beaty, T. H., et al. (2016). Association between functional small airway disease and FEV1 decline in chronic obstructive pulmonary disease. *Am. J. Respir. Crit. Care Med.* 194, 178–184. doi:10.1164/rccm.201511-2219OC

Boueiz, A., Xu, Z., Chang, Y., Masoomi, A., Gregory, A., Lutz, S. M., et al. (2022). Machine learning prediction of progression in forced expiratory volume in 1 second in the COPDGene® study. *Chronic Obstr. Pulm. Dis.* 9, 349–365. doi:10.15326/jcopdf.2021.0275

Couper, D., Lavange, L. M., Han, M., Barr, R. G., Bleecker, E., Hoffman, E. A., et al. (2014). Design of the Subpopulations and intermediate outcomes in COPD study (SPIROMICS). *Thorax* 69, 491–494. doi:10.1136/thoraxjnl-2013-203897

D'Amato, R., Figueira Gonçalves, J. M., and García Talavera, I. (2016). Predictors of lung function deterioration in COPD. *Eur. Respir. J.* 48, PA4170.

Donaldson, G. C., Seemungal, T. A., Patel, I. S., Bhowmik, A., Wilkinson, T. M., Hurst, J. R., et al. (2005). Airway and systemic inflammation and decline in lung function in patients with COPD. *Chest* 128, 1995–2004. doi:10.1378/chest.128.4.1995

Elwing, J., and Panos, R. J. (2008). Pulmonary hypertension associated with COPD. *Int. J. Chron. Obstruct Pulmon Dis.* 3, 55–70. doi:10.2147/copd.s1170

Estepar, R. S., Kinney, G. L., Black-Shinn, J. L., Bowler, R. P., Kindlmann, G. L., Ross, J. C., et al. (2013). Computed tomographic measures of pulmonary vascular morphology in smokers and their clinical implications. *Am. J. Respir. Crit. Care Med.* 188, 231–239. doi:10.1164/rccm.201301-0162OC

Garavand, A., Salehnasab, C., Behmanesh, A., Aslani, N., Zadeh, A. H., and Ghaderzadeh, M. (2022). Efficient model for coronary artery disease diagnosis: A comparative study of several machine learning algorithms. *J. Healthc. Eng.* 2022, 5359540. doi:10.1155/2022/5359540

Han, M. K., Kazerooni, E. A., Lynch, D. A., Liu, L. X., Murray, S., Curtis, J. L., et al. (2011). Chronic obstructive pulmonary disease exacerbations in the COPDGene study: Associated radiologic phenotypes. *Radiology* 261, 274–282. doi:10.1148/radiol.11110173

Han, M. K., Quibrera, P. M., Carretta, E. E., Barr, R. G., Bleecker, E. R., Bowler, R. P., et al. (2017). Frequency of exacerbations in patients with chronic obstructive pulmonary disease: An analysis of the SPIROMICS cohort. *Lancet Respir. Med.* 5, 619–626. doi:10.1016/S2213-2600(17)30207-2

Hasenstab, K. A., Yuan, N., Retson, T., Conrad, D. J., Kligerman, S., Lynch, D. A., et al. (2021). Automated CT staging of chronic obstructive pulmonary disease severity for predicting disease progression and mortality with a deep learning convolutional neural network. *Radiol. Cardiothorac. Imaging* 3, e200477. doi:10.1148/ryct.2021200477

Jain, S. S., Sarkar, I. N., Stey, P. C., Anand, R. S., Biron, D. R., and Chen, E. S. (2018). Using demographic factors and comorbidities to develop a predictive model for ICU mortality in patients with acute exacerbation COPD. *AMIA Annu. Symp. Proc.* 2018, 1319–1328.

Kiddle, S. J., Whittaker, H. R., Seaman, S. R., and Quint, J. K. (2020). Prediction of five-year mortality after COPD diagnosis using primary care records. *PLoS One* 15, e0236011. doi:10.1371/journal.pone.0236011

Kim, V., Desai, P., Newell, J. D., Make, B. J., Washko, G. R., Silverman, E. K., et al. (2014). Airway wall thickness is increased in COPD patients with bronchodilator responsiveness. *Respir. Res.* 15, 84. doi:10.1186/s12931-014-0084-3

Labaki, W. W., Gu, T., Murray, S., Hatt, C. R., Galban, C. J., Ross, B. D., et al. (2019). Voxel-wise longitudinal parametric response mapping analysis of chest computed tomography in smokers. *Acad. Radiol.* 26, 217–223. doi:10.1016/j.acra.2018.05.024

Leitao Filho, F. S., Mattman, A., Schellenberg, R., Criner, G. J., Woodruff, P., Lazarus, S. C., et al. (2020). Serum IgG levels and risk of COPD hospitalization: A pooled meta-analysis. *Chest* 158, 1420–1430. doi:10.1016/j.chest.2020.04.058

Lugosi, G. (1992). Learning with an unreliable teacher. *Pattern Recognit.* 25, 79–87. doi:10.1016/0031-3203(92)90008-7

Martinez, F. J., Han, M. K., Allinson, J. P., Barr, R. G., Boucher, R. C., Calverley, P. M. A., et al. (2018). At the root: Defining and halting progression of early chronic obstructive pulmonary disease. *Am. J. Respir. Crit. Care Med.* 197, 1540–1551. doi:10.1164/rccm.201710-2028PP

Mathioudakis, A. G., Janssens, W., Sivapalan, P., Singanayagam, A., Dransfield, M. T., Jensen, J. S., et al. (2020). Acute exacerbations of chronic obstructive pulmonary disease: In search of diagnostic biomarkers and treatable traits. *Thorax* 75, 520–527. doi:10.1136/thoraxjnl-2019-214484

Miravitlles, M., Soler-Cataluña, J. J., Calle, M., and Soriano, J. B. (2013). Treatment of COPD by clinical phenotypes: Putting old evidence into clinical practice. *Eur. Respir. J.* 41, 1252–1256. doi:10.1183/09031936.00118912

Mohamed, H., de Jong, P. A., Lammers, J. W., Mali, W. P., Schmidt, M., de Koning, H. J., et al. (2015). Airway wall thickness associated with forced expiratory volume in 1 second decline and development of airflow limitation. *Eur. Respir. J.* 45, 644–651. doi:10.1183/09031936.00020714

Nakano, Y., Wong, J. C., de Jong, P. A., Buzatu, L., Nagao, T., Coxson, H. O., et al. (2005). The prediction of small airway dimensions using computed tomography. *Am. J. Respir. Crit. Care Med.* 171, 142–146. doi:10.1164/rccm.200407-874OC

Nikolaou, V., Massaro, S., Garn, W., Fakhimi, M., Stergioulas, L., and Price, D. B. (2021). Fast decliner phenotype of chronic obstructive pulmonary disease (COPD): Applying machine learning for predicting lung function loss. *BMJ Open Respir. Res.* 8, e000980. doi:10.1136/bmjresp-2021-000980

Parr, T., Wilson, J. D., and Hamrick, J. (2020). *Nonparametric feature impact and importance*. arXiv preprint arXiv:2006.04750.

Pratte, K. A., Curtis, J. L., Kechris, K., Couper, D., Cho, M. H., Silverman, E. K., et al. (2021). Soluble receptor for advanced glycation end products (sRAGE) as a biomarker of COPD. *Respir. Res.* 22, 127. doi:10.1186/s12931-021-01686-z

Rabe, K. F., Hurd, S., Anzueto, A., Barnes, P. J., Buist, S. A., Calverley, P., et al. (2007). Global strategy for the diagnosis, management, and prevention of chronic obstructive pulmonary disease: GOLD executive summary. *Am. J. Respir. Crit. Care Med.* 176, 532–555. doi:10.1164/rccm.200703-456SO

Rahaghi, F. N., Argemi, G., Nardelli, P., Dominguez-Fandos, D., Arguis, P., Peinado, V. I., et al. (2019). Pulmonary vascular density: Comparison of findings on computed tomography imaging with histology. *Eur. Respir. J.* 54, 1900370. doi:10.1183/13993003.00370-2019

Regan, E. A., Hokanson, J. E., Murphy, J. R., Make, B., Lynch, D. A., Beaty, T. H., et al. (2010). Genetic epidemiology of COPD (COPDGene) study design. *COPD* 7, 32–43. doi:10.3109/15412550903499522

Serban, K. A., Pratte, K. A., and Bowler, R. P. (2021). Protein biomarkers for COPD outcomes. *Chest* 159, 2244–2253. doi:10.1016/j.chest.2021.01.004

Sieren, J. P., Newell, J. D., JR., Barr, R. G., Bleecker, E. R., Burnette, N., Carretta, E. E., et al. (2016). SPIROMICS protocol for multicenter quantitative computed tomography to phenotype the lungs. *Am. J. Respir. Crit. Care Med.* 194, 794–806. doi:10.1164/rccm.201506-1208PP

Simmons, M. S., Connett, J. E., Nides, M. A., Lindgren, P. G., Kleerup, E. C., Murray, R. P., et al. (2005). Smoking reduction and the rate of decline in FEV(1): Results from the lung Health study. *Eur. Respir. J.* 25, 1011–1017. doi:10.1183/09031936.05.00086804

Singh, D., Criner, G. J., Dransfield, M. T., Halpin, D. M. G., Han, M. K., Lange, P., et al. (2021). InforMing the PAthway of COPD treatment (IMPACT) trial: Fibrinogen levels predict risk of moderate or severe exacerbations. *Respir. Res.* 22, 130. doi:10.1186/s12931-021-01706-y

Synn, A. J., Li, W., San Jose Estepar, R., Zhang, C., Washko, G. R., O'Connor, G. T., et al. (2019). Radiographic pulmonary vessel volume, lung function and airways disease in the Framingham Heart Study. *Eur. Respir. J.* 54, 1900408. doi:10.1183/13993003.00408-2019

Tanimura, K., Sato, S., Sato, A., Tanabe, N., Hasegawa, K., Uemasu, K., et al. (2020). Low serum free light chain is associated with risk of COPD exacerbation. *ERJ Open Res.* 6, 00288–02019. doi:10.1183/23120541.00288-2019

Weatherald, J., Montani, D., and Humbert, M. (2019). Seeing the forest for the (arterial) tree: Vascular pruning and the chronic obstructive pulmonary disease pulmonary vascular phenotype. *Am. J. Respir. Crit. Care Med.* 200, 406–408. doi:10.1164/rccm.201901-0248ED

Glossary

6MWD	6-min walk distance
AUC	area under the curve
AWT	airway wall thickness
awt.Thirona	segmental airway wall thickness, measured by Thirona software
BDR	bronchodilator responsiveness
BMI	body mass index
CONSORT	Consolidated Standards of Reporting Trials
COPD	chronic obstructive pulmonary disease
COPDGene	Genetic Epidemiology of Chronic Obstructive Pulmonary Disease
cortical.T12	average Hounsfield unit value within the cortical region of the T12 vertebral body
CT	computed tomography
DICOM	Digital Imaging and Communications in Medicine
exp.ct.vol	CT-derived expiratory lung volume
FEF$_{25.75}$	forced mid-expiratory flow
FEF.25.75.post	post bronchodilator forced mid-expiratory flow
FEV$_1$	forced expiratory volume in 1 s
FEV$_1$.FVC.post	post bronchodilator FEV$_1$/FVC
FEV$_1$.pp.post	post bronchodilator FEV$_1$% predicted
Δ FEV$_1$%pred	FEV$_1$ percent predicted per year
fSAD	functional small airways disease
FVC	forced vital capacity
FVC.pp.post	post bronchodilator FVC % predicted
GOLD	Global Initiative for Chronic Obstructive Lung Disease
HIPAA	Health Insurance Portability and Accountability Act
HU	Hounsfield unit
insp.ct.vol	CT-derived inspiratory lung volume
IRB	institutional review board
PFT	pulmonary function testing
Pi10	square root of an airway wall area with a 10 mm lumen perimeter
Pi10.thirona	square root of an airway wall area with a 10 mm lumen perimeter, measured by Thirona software
PRM	Parametric Response Mapping
prm.lower.emphysema	PRM lower lobes emphysema > 2%
prm.lower.fsad	PRM lower lobes fSAD > 10%
prm.total.emphysema	PRM total emphysema > 2%
prm.total.fsad	PRM total fSAD >10%
prm.upper.emphysema	PRM upper lobes emphysema > 2%
prm.upper.fsad	PRM upper lobes fSAD > 10%
ROC-AUC	receiver operating characteristic area under the curve
SD	standard deviation
SGRQ	St. George's Respiratory Questionnaire
SPIROMICS	Subpopulations and Intermediate Outcome Measures in COPD
TBV	total blood vessel volume
tBV5/t.bv5	ratio of vascular tree length in vessels with a cross-sectional area less than 5 mm^2 to total vascular tree volume
trabecular.T12	average Hounsfield unit value within the trabecular region of the T12 vertebral body
walk.dist	6-min walk distance

frontiers | Frontiers in Physiology

TYPE Original Research
PUBLISHED 26 April 2023
DOI 10.3389/fphys.2023.1085158

OPEN ACCESS

EDITED BY
Sam Bayat,
Université Grenoble Alpes, France

REVIEWED BY
Yi Xin,
University of Pennsylvania, United States
Maciej Orkisz,
Université Claude Bernard Lyon 1, France

*CORRESPONDENCE
Ge Ren,
✉ gary-ge.ren@polyu.edu.hk
Jing Cai,
✉ jing.cai@polyu.edu.hk

RECEIVED 31 October 2022
ACCEPTED 06 April 2023
PUBLISHED 26 April 2023

CITATION
Chen Z, Huang Y-H, Kong F-M, Ho WY, Ren G and Cai J (2023), A super-voxel-based method for generating surrogate lung ventilation images from CT.
Front. Physiol. 14:1085158.
doi: 10.3389/fphys.2023.1085158

A super-voxel-based method for generating surrogate lung ventilation images from CT

Zhi Chen[1], Yu-Hua Huang[1], Feng-Ming Kong[2,3], Wai Yin Ho[4], Ge Ren[1]* and Jing Cai[1]*

[1]Department of Health Technology and Informatics, The Hong Kong Polytechnic University, Hong Kong, China, [2]Department of Clinical Oncology, Queen Mary Hospital, Hong Kong, China, [3]Department of Clinical Oncology, The University of Hong Kong, Hong Kong, China, [4]Department of Nuclear Medicine, Queen Mary Hospital, Hong Kong, China

Purpose: This study aimed to develop and evaluate CTVI_{SVD}**,** a super-voxel-based method for surrogate computed tomography ventilation imaging (CTVI).

Methods and Materials: The study used four-dimensional CT (4DCT) and single-photon emission computed tomography (SPECT) images and corresponding lung masks from 21 patients with lung cancer obtained from the Ventilation And Medical Pulmonary Image Registration Evaluation dataset. The lung volume of the exhale CT for each patient was segmented into hundreds of super-voxels using the Simple Linear Iterative Clustering (SLIC) method. These super-voxel segments were applied to the CT and SPECT images to calculate the mean density values (D_{mean}) and mean ventilation values ($Vent_{mean}$), respectively. The final CT-derived ventilation images were generated by interpolation from the D_{mean} values to yield CTVI_{SVD}. For the performance evaluation, the voxel- and region-wise differences between CTVI_{SVD} and SPECT were compared using Spearman's correlation and the Dice similarity coefficient index. Additionally, images were generated using two deformable image registration (DIR)-based methods, CTVI_{HU} and CTVI_{Jac}, and compared with the SPECT images.

Results: The correlation between the D_{mean} and $Vent_{mean}$ of the super-voxel was 0.59 ± 0.09, representing a moderate-to-high correlation at the super-voxel level. In the voxel-wise evaluation, the CTVI_{SVD} method achieved a stronger average correlation (0.62 ± 0.10) with SPECT, which was significantly better than the correlations achieved with the CTVI_{HU} (0.33 ± 0.14, $p < 0.05$) and CTVI_{Jac} (0.23 ± 0.11, $p < 0.05$) methods. For the region-wise evaluation, the Dice similarity coefficient of the high functional region for CTVI_{SVD} (0.63 ± 0.07) was significantly higher than the corresponding values for the CTVI_{HU} (0.43 ± 0.08, $p < 0.05$) and CTVI_{Jac} (0.42 ± 0.05, $p < 0.05$) methods.

Conclusion: The strong correlation between CTVI_{SVD} and SPECT demonstrates the potential usefulness of this novel method of ventilation estimation for surrogate ventilation imaging.

KEYWORDS

ventilation, 4DCT, super-voxel, radiotherapy, lung cancer

1 Background

Lung cancer is the most common cause of cancer-related death in both men and women (Wild et al., 2020). Radiotherapy (RT) is an important treatment modality for lung cancer, especially in patients in whom surgical resection is contraindicated or those with mid- or late-stage lung cancers (Gadgeel et al., 2012). The functional lung volume that can be irradiated in such patients is limited, as irradiation of functioning tissue can lead to radiation pneumonitis (RP) and respiratory failure. Currently, the percentage of the lung volume receiving at least 20 Gy ($V20$) and the mean lung dose (MLD) are used to predict the risk of pulmonary injury (Lee et al., 2003) or the maximum acceptable dose to deliver to a lesion (Baisden et al., 2007). However, these parameters are evaluated across the whole lung volume and do not account for functional differences between lung regions. Recently, regional lung functionality assessment has been shown to enable highly functional lung areas to be spared from irradiation and thus can be used to design treatment plans that reduce the risk of injury (Hoover et al., 2014; Bucknell et al., 2018; Lee and Park, 2020; Vinogradskiy et al., 2022).

Lung ventilation images can provide regional functional information. Clinical-standard lung ventilation imaging techniques require radioactive gases or aerosols; for example, single-photon emission computed tomography (SPECT) uses Technetium-99 m (Tc-99 m) (Suga et al., 2004) and positron emission tomography (PET) uses Gallium-68 (Ga-68) (Ament et al., 2013). However, not all hospitals can perform PET or SPECT scans, and the radiopharmaceuticals used for imaging expose patients to additional radiation doses. Hyperpolarized noble gas magnetic resonance imaging (MRI) ventilation (Cai et al., 2007; Cai et al., 2009; Tustison et al., 2010; Roos et al., 2015) is another non-invasive imaging technique used to generate ionizing radiation-free ventilation images for lung function assessment. However, MRI ventilation requires a tracer gas and specialized equipment, which may limit the availability of this modality in clinical practice. CT-derived ventilation imaging (CTVI) is another method of generating ventilation images. Moreover, as CT scans of patients undergoing RT are routinely performed, CTVI methods could potentially help patients avoid unnecessary radiation doses and medical costs.

Current CTVI methods are mainly based on volume changes (Jacobian-based, $\mathrm{CTVI_{Jac}}$) or density changes ($\mathrm{CTVI_{HU}}$) and use four-dimensional CT (4DCT) and deformable image registration (DIR) (Vinogradskiy, 2019). In 4DCT-based methods, the peak-inhale phase CT ($\mathrm{CT_{in}}$) and peak-exhale phase CT ($\mathrm{CT_{ex}}$) are selected from 4DCT data to represent the largest regional volume differences and changes in HU values. The rationale underlying density change-based methods is that each lung CT voxel represents a combination of water-like and air-like tissues (Simon, 2000), so the density of the lung voxel in the $\mathrm{CT_{in}}$ decreases when air is inhaled. The density change in each voxel then can be calculated by applying DIR to map the voxels between CT images of inhalation and exhalation. The Jacobian-based methods use the volume change in a given lung voxel due to inhaled air. The volume change can be calculated as the Jacobian of the generated DIR (Reinhardt et al., 2008). However, because these methods are performed at the voxel level, their results are substantially affected by image artifacts and DIR accuracy. Therefore, sub-regional level analysis methods have been developed to improve the accuracy robustness of CTVI (Szmul et al., 2019; Castillo et al., 2020). These methods have yielded some improvements but they also are DIR-based, which means that their accuracy depends on DIR algorithms; thus, they are affected by the parameters of DIR algorithms and the sensitivity of DIR to 4DCT image artifacts. Other CTVI methods that do not use DIR have been devised. For example, Kipritidis et al. (2016) devised a modified Hounsfield unit (HU)-based method that generates robust ventilation images without DIR. However, this method may overestimate areas with edges between solid tissue and normal parenchyma within the lung, such as the peritumoral lung and the pleural space. Some deep learning-based methods can generate highly accurate functional lung images (Zhong et al., 2019; Liu et al., 2020; Ren et al., 2021a; Ren et al., 2021b), but these results lack anatomical explanations.

Current DIR-based CTVI methods are sensitive to both CT image quality and DIR algorithms, so the images they generate have a limited correlation with the gold-standard ventilation images generated using SPECT and PET (Vinogradskiy, 2019). Consequently, the results of CTVI are complicated and difficult to interpret, meaning they may be unsuitable for clinical application. The super-pixel concept was first proposed and developed as an image segmentation technology in 2003 (Ren and Malik, 2003). It uses pixel blocks that form specific patterns with adjacent pixels that have a similar texture, color, and other features. Images can be represented by a small number of super-pixels, which significantly reduces the complexity of image post-processing. A similar concept, the super-voxel, is used for three-dimensional (3D) image analysis. An air exchange unit is evaluated using a volume of approximately 2 $\mathrm{cm^3}$ (Levin et al., 2017) that contains a cluster of CT voxels with a resolution of approximately 1 mm × 1 mm × 3 mm. The CT image of a patient with lung cancer can be pre-processed by segmentation into a small number of super-voxels, where each super-voxel contains a cluster of voxels with similar features and forms perceptually meaningful anatomic features. Drawing on this principle, the current study devised a super-voxel-based method for generating robust lung ventilation images from the mean CT density value (D_{mean}) of super-voxels. The ventilation images generated are based on CT image features in the absence of DIR. The results are robust and expected to be directly interpretable and meaningful for predicting the outcomes of patients with lung cancer.

2 Materials and methods

2.1 Workflow of the study

Figure 1 shows the main workflow of this study. The $\mathrm{CT_{ex}}$ and $\mathrm{CT_{in}}$ were used to calculate the ventilation images. A clustering method was used to generate super-voxels, and the D_{mean} of each super-voxel was used to calculate the ventilation images $\mathrm{CTVI_{SVD}}$. The results of $\mathrm{CTVI_{SVD}}$ and the DIR-based CTVIs ($\mathrm{CTVI_{HU}}$;

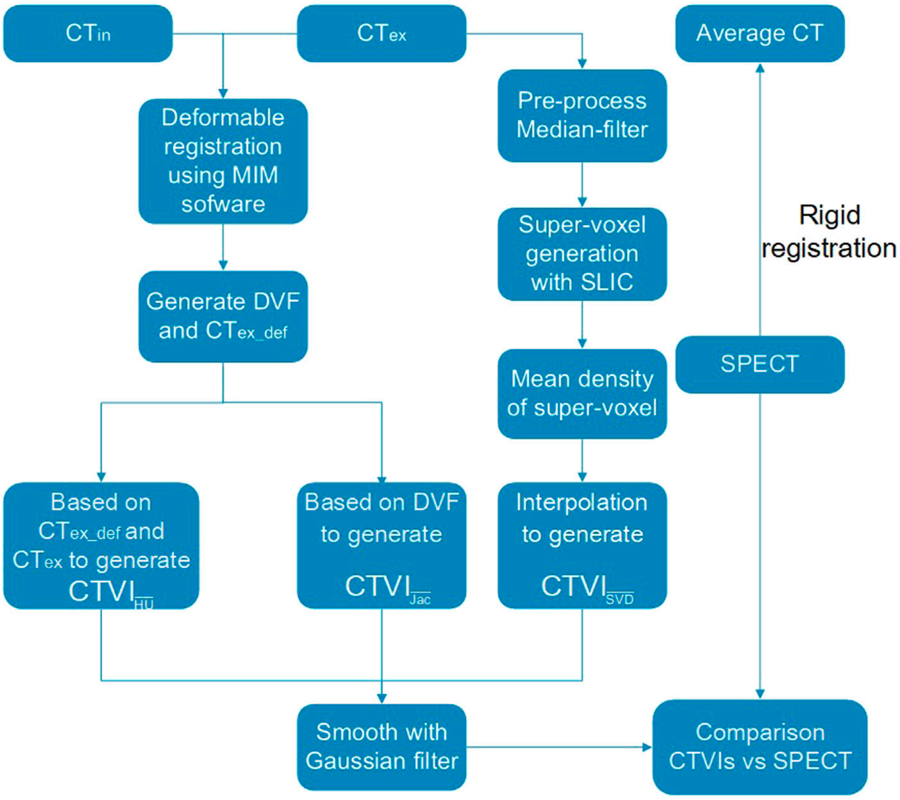

FIGURE 1
Flowchart of this study for comparing the $CTVI_{SVD}$, $CTVI_{HU}$, and $CTVI_{Jac}$ with SPECT.

$CTVI_{Jac}$) were compared with SPECT images. The details are presented in the following sections.

2.2 Image data

The data of 21 patients with lung cancer were acquired from the Ventilation And Medical Pulmonary Image Registration Evaluation (VAMPIRE) dataset (Kipritidis et al., 2019). All of the patients underwent 4DCT and diethylenetriamine pentaacetate (DTPA)-SPECT scans at Stanford University, United States (Yamamoto et al., 2014). All of the patients provided written informed consent to participate in a clinical trial of 4DCT ventilation imaging approved by the institutional review board for a study by Yamamoto (Yamamoto et al., 2014). Ten breathing phase CT images and a time-average CT with a slice thickness of 2.0, 2.5, or 3.0 mm were available for each patient. The average interval between the 4DCT and subsequent DTPA-SPECT (including low-dose attenuation correction CT) scans was 4 (±5) days. Rigid registration was performed between each SPECT image and the time-average CT image using Mattes mutual information rigid registration in Plastimatch. The DTPA-SPECT scans were linearly interpolated to match the dimensions of the time-average CT image (Kipritidis et al., 2019). The lung masks for all of the CT images (4DCT and attenuation correction CT) were also acquired from the VAMPIRE dataset, which used a region-growing method. The lung masks of the attenuation correction CT images were also used as the masks of the SPECT images. The CT values were converted to density values using Eq. 1, as follows:

$$Density = \frac{HU + 1000}{1000} \tag{1}$$

2.3 DIR-based CTVI methods

The two main conventional DIR-based methods are $CTVI_{HU}$ and $CTVI_{Jac}$. Both methods require DIR between the CT_{in} and CT_{ex}. In $CTVI_{HU}$, a voxel at spatial position x of the CT_{ex} is mapped toward a voxel at spatial position x' of the CT_{in} by DIR. The ventilation value at position x can be directly calculated using Eq. 2 (Kipritidis et al., 2019), as follows:

$$Vent(x) = \frac{-1000 \times \left(HU_{ex}(x) - HU_{in}(x')\right)}{HU_{ex}(x) \times \left(HU_{in}(x') + 1000\right)} \tag{2}$$

In $CTVI_{Jac}$, the volume change of a voxel at position x is calculated using the determinant of the Jacobian of the deformation field at position x. This process is performed using Eq. 3, as follows:

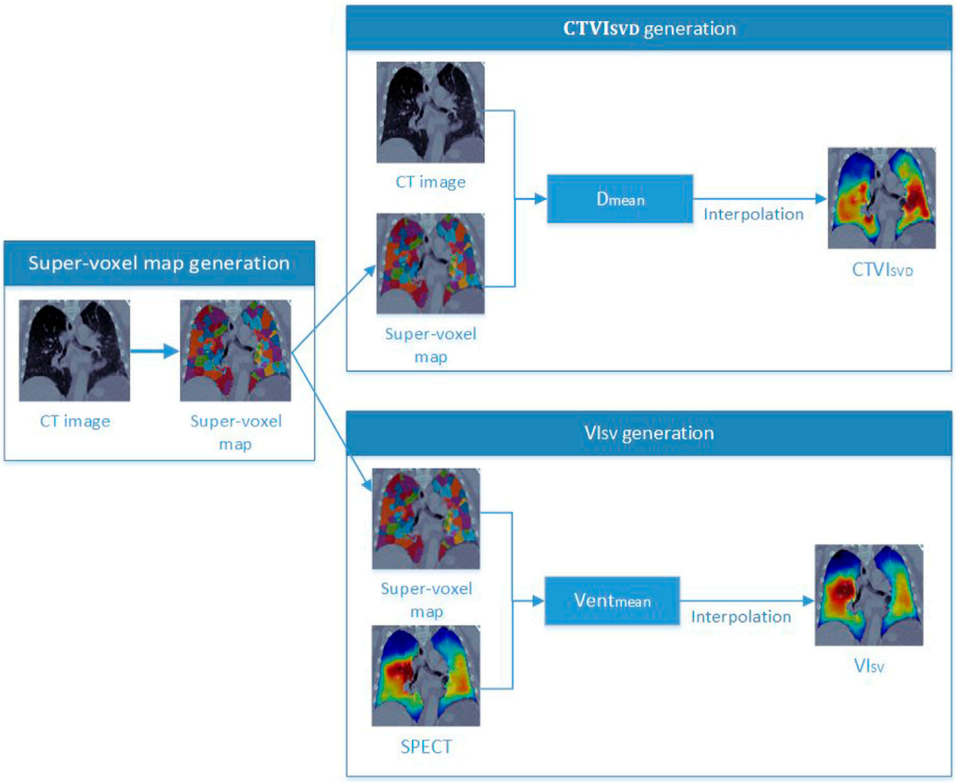

FIGURE 2
The workflow of the generations of the $CTVI_{SVD}$ and VI_{SV}.

$$Vent(\boldsymbol{x}) = \begin{vmatrix} 1+\frac{\partial u_x(\mathbf{x})}{\partial x} & \frac{\partial u_x(\mathbf{x})}{\partial y} & \frac{\partial u_x(\mathbf{x})}{\partial z} \\ \frac{\partial u_y(\mathbf{x})}{\partial x} & 1+\frac{\partial u_y(\mathbf{x})}{\partial y} & \frac{\partial u_y(\mathbf{x})}{\partial z} \\ \frac{\partial u_z(\mathbf{x})}{\partial x} & \frac{\partial u_z(\mathbf{x})}{\partial y} & 1+\frac{\partial u_z(\mathbf{x})}{\partial z} \end{vmatrix} - 1 \tag{3}$$

Both $CTVI_{HU}$ and $CTVI_{Jac}$ images were calculated in this study and used for comparison. DIR between the CT_{in} and CT_{ex} was performed using MIMvista 6.3.4 (MIM Software Inc., Cleveland, OH, United States) with a default spacing resolution of 3 mm.

2.4 Super-voxel segmentation

Simple linear iterative clustering (SLIC) (Achanta et al., 2012) is a clustering method applied to lung CT 3D images to generate super-voxels with low computational power requirements. The SLIC algorithm first initializes the K_{init} seeds by resampling pixels on a regular grid. Then, it assigns each voxel to the closest seed point to generate K_{init} clusters based on the distance (D), as described by Eq. 4:

$$D = \sqrt{{d_c}^2 + \left(\frac{d_s}{S}\right)^2 \times m^2} \tag{4}$$

where d_c is the HU value difference, d_s is the Euclidean distance, S is the initial sampling interval $S = \sqrt{\frac{N}{K_{init}}}$, N is the total voxel number in the lung volume, and m is a weighting value used to control the compactness of the super-voxel. Next, the positions of the centers are moved to the point with the smallest gradient to prevent placement on the edges of an image or at a noisy voxel. The above steps are repeated until the result converges. Only the super-voxels in the lung mask were used in this study. An in-house tool based on Matlab (MathWorks Inc., Natick, MA, United States) was used, and K_{init} was set as 1,500 for all of the patients (refer to the Discussion section for commentary). The number of super-voxels generated varied between the patients according to their lung anatomy. All of the CT and SPECT images were interpolated into images of the same size and with a pixel size of with 2 mm × 2 mm × 2 mm, and a 3D median filter with dimensions of 5 voxels × 5 voxels × 5 voxels was applied to the images to reduce noise.

2.5 Super-voxel-based ventilation image $CTVI_{SVD}$ calculation

As shown in Figure 2, a super-voxel map was generated on CT_{ex} images (as described in Section 2.4), and the D_{mean} of each super-voxel was calculated. Other studies have used fixed threshold intervals of −1,024 to −400 HU to generate the lung parenchyma (Kemerink et al., 1998; Kuhnigk et al., 2005). In the current study, the same fixed threshold interval was applied to identify the non-lung region; a super-voxel with a D_{mean} greater than 0.6 according to Eq. 1 was assigned a value of 0 to remove clearly false results from consolidation of the tumor and abnormal tissues, which have a high density but should have a low ventilation value. The super-voxel segmentation results were then directly mapped on the SPECT images, as both the SPECT and time-average CT data were registered according to the VAMPIRE challenge, and the time-average CT and CT$_{\text{ex}}$ images shared the same position. The mean ventilation value ($Vent_{mean}$) was calculated using SPECT image data. The correlation between the D_{mean} and $Vent_{mean}$ of the super-voxels was determined using Spearman's correlation analysis.

Figure 2 shows the workflow for generating the CTVI$_{\text{SVD}}$ images and the ventilation images based on SPECT (VI$_{\text{SV}}$). CTVI$_{\text{SVD}}$ image generation requires only a CT$_{\text{ex}}$ image, while VI$_{\text{SV}}$ images require both CT$_{\text{ex}}$ and SPECT images. To demonstrate the feasibility of generating a reasonable ventilation image using hundreds of super-voxels, we generated the VI$_{\text{SV}}$ image and compared it with a SPECT image. The details of CTVI$_{\text{SVD}}$ are presented as follows. To perform CTVI$_{\text{SVD}}$ of the whole lung volume, we used the geometric center of a super-voxel to represent the position of the super-voxel, and the D_{mean} value as the ventilation value of the center positions of the super-voxels. The ventilation values of all of the voxels in a lung were then calculated via interpolation with the D_{mean} of the super-voxels, as follows (Eq. 5):

$$V = WV_{sup} \tag{5}$$

$$w_{ij} = e^{-\left(\frac{r_{ij}}{r_{mean}}\right)^2} \tag{6}$$

where V is the vector of the ventilation value of all voxels in a lungs; V_{sup} is the vector calculated only using the D_{mean} of the super-voxel; W is the interpolation weight matrix; w_{ij} is the element of the W matrix, which is calculated based on the distance between voxel i and the center position of super-voxel j, as shown in Eq. 6; r_{mean} is the mean distance between the super-voxels; and r_{ij} is the distance between voxel i and super-voxel j. The lung volume was divided into the left and right lungs. For each voxel, the ventilation value was interpolated using only the super-voxels from the ipsilateral lung. To smooth the final CTVIs, we applied a 3D Gaussian filter with a kernel size of three voxels to each lung voxel. The same post-processing steps were applied to all CTVIs. The $Vent_{mean}$ of the super-voxels from SPECT was used to generate the VI$_{\text{SV}}$ according to the above-stated interpolation method and the correlation between VI$_{\text{SV}}$ and SPECT was evaluated. Two more super-voxels-based ventilation images were also generated for comparison. The $Vent_{mean}$ of the super-voxels from CTVI$_{\text{HU}}$ and CTVI$_{\text{Jac}}$ was used to generate the CTVI$_{\text{SVHU}}$ and CTVI$_{\text{SVJac}}$ with a similar method as VI$_{\text{SV}}$, respectively. Their correlations with SPECT were also evaluated.

2.6 Comparison of CTVI$_{\text{SVD}}$, CTVI$_{\text{HU}}$, CTVI$_{\text{Jac}}$, CTVI$_{\text{SVHU}}$, and CTVI$_{\text{SVJac}}$ with SPECT

The CTVI$_{\text{SVD}}$ images generated in this study were evaluated with the corresponding SPECT images using voxel-wise Spearman correlation analysis. Spearman correlation analysis was also used to compare SPECT images with CT$_{\text{ex}}$, CTVI$_{\text{HU}}$, CTVI$_{\text{Jac}}$, CTVI$_{\text{SVHU}}$, and CTVI$_{\text{SVJac}}$ images. The comparison between the CT$_{\text{ex}}$ and SPECT was used to show the advantages of analysis at the super-voxel level compared to the voxel level. To assess the concordance of high-functioning regions between CTVI and SPECT, SPECT and CTVI$_{\text{SVD}}$ images from each patient were divided into two volumes by the 66th percentile ventilation value in the lung, which is used to distinguish high- and low-functioning lung regions. This value has been used by other studies (Yamamoto et al., 2011; Ren et al., 2021b). The Dice similarity coefficient index (DSC) was used to assess the accuracy of CTVI$_{\text{SVD}}$ in segmenting the high- and low-functioning lung regions. The DSC was also used to compare the high- and low-functioning lung regions segmented by SPECT with those segmented by CTVI$_{\text{HU}}$, CTVI$_{\text{Jac}}$, CTVI$_{\text{SVHU}}$, and CTVI$_{\text{SVJac}}$. Only the intersection between the CT and SPECT lung masks was analyzed in this study.

2.7 Impact of the super-voxel number on CTVI$_{\text{SVD}}$ experiments

The size of the super-voxels may influence the results of CTVI$_{\text{SVD}}$. On the one hand, super-voxels that are too large may not be able to identify small defects. On the other hand, super-voxels that are too small may lose their structure-oriented properties. A particular clustering may influence the results of CTVI$_{\text{SVD}}$. For example, by increasing the number of super-voxels, the size of clusters is reduced. To investigate how the size of the super-voxels influences the results, we measured the correlation of CTVI$_{\text{SVD}}$ with SPECT for different numbers of super-voxels. Performance was evaluated at various values of K_{init} (300, 500, 800, 1,000, 1,500, 2,000, 2,500, 3,000, 4,000, 8,000, 12,000, and 15,000) to cover an extensive range. A large value of K_{init} increases the calculation time and depletes the memory needed to calculate the interpolation matrix W, as described in Section 2.5. The computer used for this analysis was equipped with an Intel® Core™ i9-11900K 3.50-GHz processor and 64.0 GB of RAM.

3 Results

3.1 Super-voxel segmentation

The SLIC method was used to divide the lung volumes of the 21 patients into 380–715 super-voxels at a K_{init} of 1,500. Figure 3 shows an example of super-voxel segmentation of the lung volume. Different colors indicate different super-voxel regions. The mean correlation between VI$_{\text{SV}}$ and SPECT was 0.91 (range: 0.84–0.96). Figures 4B, C show a comparison between SPECT and VI$_{\text{SV}}$ images. The two images have a similar function distribution. The strong correlation between VI$_{\text{SV}}$ and SPECT suggests that a reasonable CTVI image of the whole lung volume can be generated by analyzing hundreds of super-voxels.

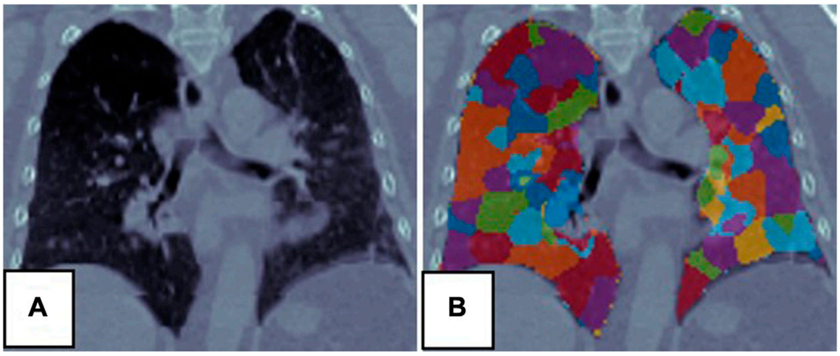

FIGURE 3
Super-voxel segmentation in the lungs of a patient. **(A)** Is the CT, **(B)** is the result of the super-voxel segmentation in the lung region.

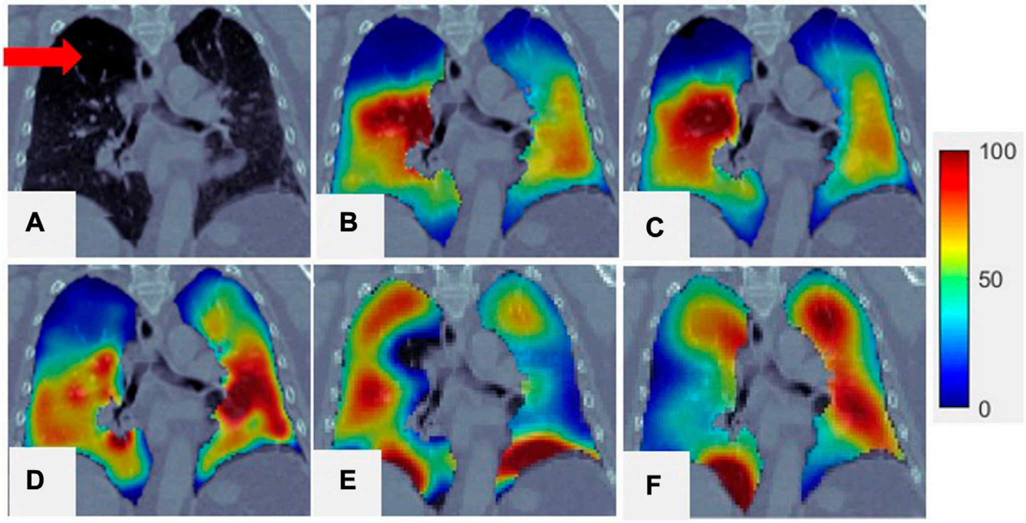

FIGURE 4
Comparison of SPECT image and $CTVI_{SVD}$ images for a representative case. **(A)** Is CT; **(B)** is the SPECT of the lung region superimposed onto the CT; **(C)** is the VI_{SV} of the lung region superimposed onto the CT; **(D)** is the $CTVI_{SVD}$ of the lung region superimposed onto the CT; **(E)** is the $CTVI_{Jac}$ of the lung region superimposed onto the CT; **(F)** is the $CTVI_{HU}$ of the lung region superimposed onto the CT. For all the figures, their 99th percentile and higher values were scaled to 100 (to reduce the artifact effect caused by the tracer deposited at airways in SPECT for visual inspection), and the minimum value was scaled to 0.

3.2 Comparison of $CTVI_{SVD}$, $CTVI_{HU}$, $CTVI_{Jac}$, $CTVI_{SVHU}$, and $CTVI_{SVJac}$ with SPECT

The correlation between the D_{mean} from CT and the $Vent_{mean}$ for the super-voxel volume from SPECT was 0.59 ± 0.09, indicating that super-voxels with a lower mean density tend to have a lower function value than super-voxels with a higher mean density. This moderate-to-strong correlation means that the D_{mean} of a super-voxel can be used as a surrogate for $Vent_{mean}$ when generating $CTVI_{SVD}$, as mentioned in Section 2.5. Figure 4 presents a comparison of SPECT with $CTVI_{SVD}$. The low-functioning lung region, indicated by the red arrow in the CT image and by the blue and black-blue area in the ventilation image (Figure 4B), can be identified using $CTVI_{SVD}$ (dark blue area in Figure 4D). The mean correlation coefficient between $CTVI_{SVD}$ and SPECT was 0.62 (range: 0.37–0.77). The mean correlation coefficients of SPECT with CT_{ex}, $CTVI_{HU}$; $CTVI_{Jac}$; $CTVI_{SVHU}$,; $CTVI_{SVJac}$ were 0.16 ± 0.16, 0.33 ± 0.14, 0.23 ± 0.10, 0.39 ± 0.18, and 0.33 ± 0.15 respectively. These results indicate that $CTVI_{SVD}$ is closer to SPECT than conventional DIR-based methods. The super-voxel based method can improve the correlations of the DIR-based CTVIs by 0.06 and 0.10 for $CTVI_{HU}$; $CTVI_{Jac}$, respectively. A similar improvement was also reported by Szmul's study (Szmul et al., 2019).

The mean *DSC* values of the high-functioning (DSC_h) and low-functioning regions (DSC_l) on $CTVI_{SVD}$ images were 0.63 ± 0.07 and 0.81 ± 0.03, respectively. Because the criterion for

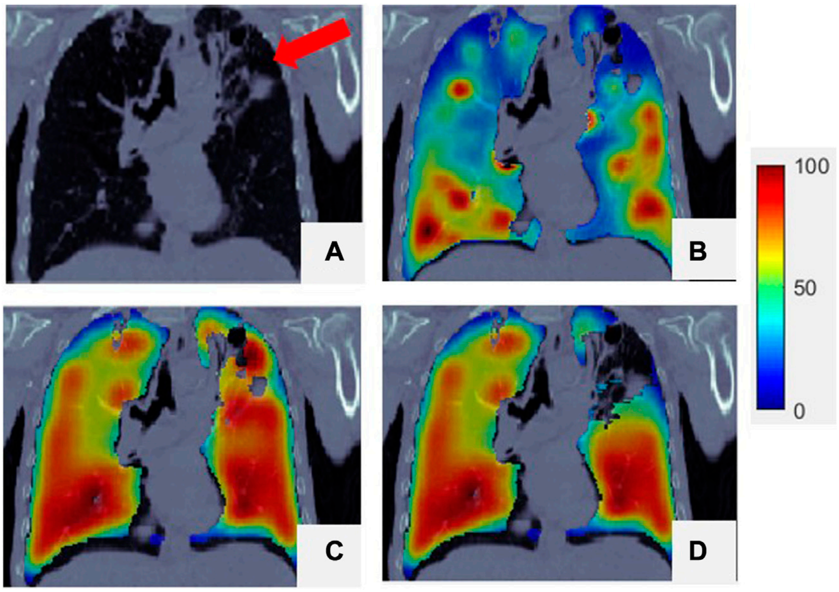

FIGURE 5
Comparison of SPECT image and $\mathrm{CTVI}_{\mathrm{SVD}}$ images for a representative case. **(A)** Is CT; **(B)** is the SPECT of the lung region superimposed onto the CT; **(C)** is the origin $\mathrm{CTVI}_{\mathrm{SVD}}$ of the lung region superimposed onto the CT; **(D)** is the corrected $\mathrm{CTVI}_{\mathrm{SVD}}$ of the lung region superimposed onto the CT. For all the figures, their 99th percentile and higher values were scaled to 100, and the minimum value was scaled to 0.

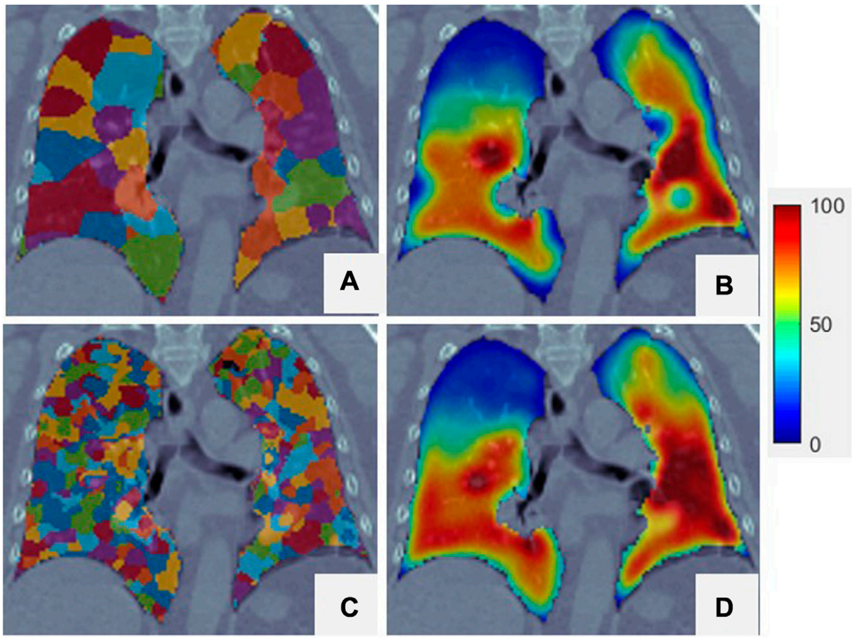

FIGURE 6
Two different super-voxel segmentations with different K_{init} and the corresponding $\mathrm{CTVI}_{\mathrm{SVD}}$. The K_{init} of the top row is 500, and the bottom row is 120000. **(A,C)** are the results of the super-voxel segmentation in the lung region. **(B,D)** are the $\mathrm{CTVI}_{\mathrm{SVD}}$ of the lung region superimposed onto the CT.

dividing the lung is the 66th, the low-functioning region is larger than the high-functioning region, and DSC_l is higher than DSC_h. As shown in Figure 4, the locations of the low-functioning regions on the $\mathrm{CTVI}_{\mathrm{SVD}}$ images matched those on the SPECT images, but the highest-functioning regions (dark red area) just exhibited a certain amount of overlap. The mean DSC_h values of $\mathrm{CTVI}_{\mathrm{HU}}$, $\mathrm{CTVI}_{\mathrm{Jac}}$, $\mathrm{CTVI}_{\mathrm{SVHU}}$, and $\mathrm{CTVI}_{\mathrm{SVJac}}$ were 0.43 ± 0.08 and 0.42 ± 0.05, 0.49 ± 0.11, and 0.48 ± 0.07, respectively, and the corresponding mean

TABLE 1 The influence of the different numbers of the super-voxel. K_{init} means the initial setting of the super-voxel number for the CT image, and K_{final} means the final extracted super-voxel number in the lung volume. The mean correlation value is the mean Spearman correlation value of all the patients. D_{mean} is the mean density of the super-voxel, and $Vent_{mean}$ is the mean ventilation value of the super-voxel. The *p*-values are obtained from the paired-samples *t*-test of the K_{init} of other value with the K_{init} of 1,500.

K_{init}	K_{final}	Mean correlation value			
		D_{mean} vs. $Vent_{mean}$	*p*-value	$CTVI_{SVD}$ vs. SPECT	*p*-value
300	193	0.49	0.0001	0.57	0.0002
500	280	0.50	0.0002	0.58	0.0003
800	373	0.57	0.0146	0.61	0.0915
1,000	413	0.57	0.0207	0.60	0.0012
1,500	520	0.59	—	0.62	—
2,000	615	0.57	0.0739	0.62	0.2733
2,500	713	0.58	0.2508	0.63	0.0606
3,000	802	0.57	0.0948	0.63	0.0738
4,000	1,018	0.54	0.0120	0.63	0.1480
8,000	1,788	0.48	0.0005	0.62	0.3097
12,000	2,550	0.46	0.0004	0.62	0.3142
15,000	3,108	0.45	0.0001	0.62	0.3376

DSC_l values were 0.70 ± 0.04, 0.70 ± 0.03, 0.74 ± 0.06, and 0.73 ± 0.04, respectively.

For some patients, $CTVI_{SVD}$ yielded low correlation with SPECT. However, this could be improved. As indicated by the red arrow in Figure 5A, a defective lung region with a high density at the top of the left lung caused a falsely high ventilation value, as shown in Figure 5C. Such errors can be corrected by manually contouring the defect regions via assignment to a low ventilation value. In this case, the final correlation coefficient increased to 0.52, as shown in Figure 5D.

3.3 Evaluation of the impact of the super-voxel number on $CTVI_{SVD}$

Figure 6 shows super-voxel segmentation using two values of K_{init}. As the number of super-voxels increased, the size of the super-voxels decreased. The generated $CTVI_{SVD}$ images show high similarity in highly ventilated regions. As shown in the bottom left row of Figure 6, as the volume of the super-voxel decreased, it became more difficult to contain the whole texture of the sub-region; this presents an obstacle to analysis of the $Vent_{mean}$ with other features of such a super-voxel. Table 1 shows the experimental results obtained with different numbers of super-voxels. On average, approximately 193, 280, 373, 413, 520, 615, 713, 802, 1,018, 1,788, 2,550, and 3,108 super-voxels were extracted from the lung volumes of the 21 patients when K_{init} was set as 300, 500, 800, 1,000, 1,500, 2,000, 2,500, 3,000, 4,000, 8,000, 12,000, and 15,000, respectively. The correlation of D_{mean} with $Vent_{mean}$ was strongest when approximately 520 super-voxels were extracted from the lung volume and decreased as the number of super-voxels continued to increase. A paired-samples *t*-test to compare the D_{mean} and $Vent_{mean}$ obtained at a K_{init} of 1,500 with those obtained at other K_{init} values revealed that a K_{init} of 1,500 generated the most reasonable number of super-voxels inside the lungs. The D_{mean} exhibited a stronger correlation with $Vent_{mean}$ at a K_{init} of 1,500 than at K_{init} values lower than 1,500 and higher than 3,000. The correlation of $CTVI_{SVD}$ with SPECT reached a plateau at approximately 520 super-voxels and remained stable as the number of super-voxels increased. Thus, K_{init} was set as 1,500 to retain as many structure-oriented properties as possible for each super-voxel.

4 Discussion

In this study, a super-voxel-based method was developed to generate surrogate ventilation images directly from CT images. The SLIC method was employed to generate super-voxels inside the lung volume, and the D_{mean} of the super-voxels was used as a surrogate for the mean ventilation value to calculate a whole-lung ventilation image through interpolation. This novel $CTVI_{SVD}$ method achieved a mean Spearman's correlation coefficient of 0.62 (range: 0.37–0.77) with the ground-truth SPECT, which was significantly higher than the correlation coefficients of SPECT with the DIR-based methods $CTVI_{HU}$ (0.33 ± 0.14, $p < 0.05$), $CTVI_{Jac}$ (0.23 ± 0.10, $p < 0.05$), $CTVI_{SVHU}$ (0.39 ± 0.18, $p < 0.05$), and $CTVI_{SVJac}$ (0.33 ± 0.15, $p < 0.05$). The DSC_h of $CTVI_{SVD}$ was 0.63 ± 0.07, which was also significantly higher than those of $CTVI_{HU}$ (0.43 ± 0.08, $p < 0.05$), $CTVI_{Jac}$ (0.42 ± 0.05, $p < 0.05$), $CTVI_{SVHU}$ (0.49 ± 0.11, $p < 0.05$) and $CTVI_{SVJac}$ (0.48 ± 0.07, $p < 0.05$), and the DSC_l of $CTVI_{SVD}$ (0.81 ± 0.03) was higher than those of $CTVI_{HU}$ (0.70 ± 0.04, $p < 0.05$), $CTVI_{Jac}$ (0.70 ± 0.03, $p < 0.05$), $CTVI_{SVHU}$ (0.74 ± 0.06, $p < 0.05$) and $CTVI_{SVJac}$ (0.73 ± 0.04, $p < 0.05$). By using this novel method, the complexity of a ventilation imaging problem can be reduced from calculating millions of ventilation values for all voxels to only calculating hundreds of $Vent_{mean}$ values for super-voxels. The $Vent_{mean}$ of a super-voxel can be directly derived from super-voxel features. Thus, $\mathrm{CTVI_{SVD}}$ can be generated without DIR, so the novel method is simpler and more robust than DIR-based methods.

This study shows that the D_{mean} of a super-voxel is strongly correlated with the $Vent_{mean}$ of a super-voxel, which means that a lower super-voxel density is usually associated with less functional ventilation than a higher super-voxel density. Similar results have been shown in other studies (Lafata et al., 2019; Yang et al., 2021). As shown in Figure 4, the region with low ventilation function (indicated by arrows) is darker than the region with normal function. The low-functioning region may correspond to a defective lung region caused by emphysema, where healthy pulmonary tissue has been replaced increasingly by air due to alveolar damage and weakening and rupture of the inner walls of the air sacs. This was a preliminary study of the use of the D_{mean} of super-voxels to generate ventilation images, and only 21 patients were included. Other super-voxel features can be analyzed and combined with Dmean to build a more accurate and robust model for future CTVI studies involving more patient data.

According to Eq. 4, the total super-voxel number and compactness value affect segmentation of the super-voxels. The SLIC algorithm used in this study can refine the compactness value adaptively to reduce the influence of this variable without requiring pre-assignment. The only variable required for SLIC is the total number of super-voxels. The correlation between D_{mean} and $Vent_{mean}$ is strongest when approximately 520 super-voxels are extracted from the lung volume and decreases as the number of super-voxels increases. Meanwhile, as the number of super-voxel increases, the mean correlation between $\mathrm{CTVI_{SVD}}$ and SPECT increases and then plateaus. A reasonable explanation for this observation is that as the number of super-voxels increases, the size of the super-voxels decreases, and some of the densities of these small super-voxels are then affected by the bronchi, noise, or artifacts with high-density values. The mean correlation between the D_{mean} and $Vent_{mean}$ of the super-voxels decreases to tend to be the pixel level results, which had the same value, 0.40 ± 0.19, as the correlation between the $\mathrm{CT_{ex}}$ (after interpolation and denoising with a median filter) and SPECT. However, these discrepancies can be reduced by the smoothness of the Gaussian filter in the final image processing. The correlation between $\mathrm{CTVI_{SVD}}$ and SPECT remains stable. Accordingly, in this study, the K_{init} setting that yielded the strongest correlation between the D_{mean} and $Vent_{mean}$ was selected to maintain the structure-oriented properties of the super-voxels to the greatest extent possible. The correlation between the $\mathrm{CT_{ex}}$ and SPECT was 0.16 ± 0.16, significantly lower than the result obtained with $\mathrm{CTVI_{SVD}}$ method. This outcome is probably mainly attributable to the technical limitations associated with SPECT imaging. SPECT has an original resolution of 8 mm. We resampled the SPECT image with a resolution of 2 mm in the data process, so it could serve as a data smoothing process. This process was similar to our method, wherein we calculated the mean density of the super-voxel and then used interpolation to calculate the value of each voxel.

This study has some limitations. Pulmonary ventilation refers to the air exchange between the atmosphere and the lungs. It involves the inflow of air through the airway to the alveoli, where the air exchange occurs, followed by outflow through the airway. Our results show that lung regions with lower density values exhibit lower ventilation values than those with higher density values. As previously mentioned, the damaged alveoli in a patient with emphysema lost their ability to expel air, leading to decreased intensity. However, in some cases, abnormal lung regions associated with pulmonary diseases can exhibit increased density, known as opacities, and fall into four patterns: consolidation, interstitial, nodules or masses, and atelectasis (L ung-disease, 2023). These diseases can also obstruct the airway or damage to the parenchyma, leading to a loss of air exchange capability. Consequently, some pulmonary diseases may affect the CTVI results in this study. However, the clinical presentation of pulmonary diseases on CT images can vary. Raju et al. categorized the signs of the lung disease into 22 groups (Raju et al., 2017). These signs can increase the difficulty of automatically recognizing defect regions. In this study, the super-voxel was the smallest unit of analysis and its features can be used directly to classify it as a defect or normal region. In future work, we will create a super-voxel-based model to automatically identify defect regions and correct the ventilation value to increase the accuracy of our method.

Moreover, some regions may have a low ventilation value due to pressure placed by the tumor on the central airway and blood vessels; this pressure can be recovered after radiotherapy (Yuan et al., 2012). Such regions need to be carefully protected during the treatment, and the dose should be as low as possible as normal lung regions. In cases with such regions, the patient's dyspnea may be reduced and the lung function may increase if the tumor shrinks after treatment. From this perspective, CTVI can provide more information than SPECT. More investigation is needed to identify these regions and thus guide treatment planning.

5 Conclusion

In this study, we developed a super-voxel-based method to generate surrogate ventilation images from CT data. The observed correlation between $\mathrm{CTVI_{SVD}}$ and SPECT indicates that $\mathrm{CTVI_{SVD}}$ has high similarity with SPECT. Our results also show that the D_{mean} can be used as a surrogate for the $Vent_{mean}$ in the context of generating ventilation images.

Data availability statement

The original contributions presented in the study are included in the article/supplementary material, further inquiries can be directed to the corresponding authors.

Ethics statement

The studies involving human participants were reviewed and approved by Departmental Research Committee Department of

Health Technology and Informatics. Written informed consent for participation was not required for this study in accordance with the national legislation and the institutional requirements.

Author contributions

ZC: data analysis, methodology, writing—original draft. Y-HH: data acquisition and analysis, writing—editing. F-MK and WH: result checking, writing—review. GR and JC: supervision, writing—review and editing.

Funding

This work was partly supported by the General Research Fund (GRF 15103520) from The University Grants Committee, and Health and Medical Research Fund (HMRF 07183266, HMRF 09200576) from The Health Bureau, The Government of the Hong Kong Special Administrative Regions.

Acknowledgments

We would like to acknowledge the data provided by the VAMPIRE challenge.

Conflict of interest

The authors declare that the research was conducted in the absence of any commercial or financial relationships that could be construed as a potential conflict of interest.

Publisher's note

References

Achanta, R., Shaji, A., Smith, K., Lucchi, A., Fua, P., and Süsstrunk, S. (2012). SLIC superpixels compared to state-of-the-art superpixel methods. *IEEE Trans. pattern analysis Mach. Intell.* 34 (11), 2274–2282. doi:10.1109/TPAMI.2012.120

Ament, S. J., Maus, S., Reber, H., Buchholz, H. G., Bausbacher, N., Brochhausen, C., et al. (2013). PET lung ventilation/perfusion imaging using 68 Ga aerosol (Galligas) and 68 Ga-labeled macroaggregated albumin. *Recent Results Cancer Res.* 2013, 395–423. doi:10.1007/978-3-642-27994-2_22

Baisden, J. M., Romney, D. A., Reish, A. G., Cai, J., Sheng, K., Jones, D. R., et al. (2007). Dose as a function of lung volume and planned treatment volume in helical tomotherapy intensity-modulated radiation therapy-based stereotactic body radiation therapy for small lung tumors. *Int. J. Radiat. Oncology* Biology* Phys.* 68 (4), 1229–1237. doi:10.1016/j.ijrobp.2007.03.024

Bucknell, N. W., Hardcastle, N., Bressel, M., Hofman, M. S., Kron, T., Ball, D., et al. (2018). Functional lung imaging in radiation therapy for lung cancer: A systematic review and meta-analysis. *Radiotherapy Oncol.* 129 (2), 196–208. doi:10.1016/j.radonc.2018.07.014

Cai, J., Altes, T. A., Miller, G. W., Sheng, K., Read, P. W., Mata, J. F., et al. (2007). MR grid-tagging using hyperpolarized helium-3 for regional quantitative assessment of pulmonary biomechanics and ventilation. *Magnetic Reson. Med.* 58 (2), 373–380. doi:10.1002/mrm.21288

Cai, J., Sheng, K., Benedict, S. H., Read, P. W., Larner, J. M., Mugler, J. P., et al. (2009). Dynamic MRI of grid-tagged hyperpolarized helium-3 for the assessment of lung motion during breathing. *Int. J. Radiat. Oncology* Biology* Phys.* 75 (1), 276–284. doi:10.1016/j.ijrobp.2009.03.051

Castillo, E., Castillo, R., Vinogradskiy, Y., Nair, G., Grills, I., Guerrero, T., et al. (2020). Technical Note: On the spatial correlation between robust CT-ventilation methods and SPECT ventilation. *Med. Phys.* 47 (11), 5731–5738. doi:10.1002/mp.14511

Gadgeel, S. M., Ramalingam, S. S., and Kalemkerian, G. P. (2012). Treatment of lung cancer. *Radiol. Clin.* 50 (5), 961–974. doi:10.1016/j.rcl.2012.06.003

Hoover, D. A., Reid, R. H., Wong, E., Stitt, L., Sabondjian, E., Rodrigues, G. B., et al. (2014). SPECT-Based functional lung imaging for the prediction of radiation pneumonitis: A clinical and dosimetric correlation. *J. Med. Imaging Radiat. Oncol.* 58 (2), 214–222. doi:10.1111/1754-9485.12145

Kemerink, G. J., Lamers, R. J., Pellis, B. J., Kruize, H. H., and van Engelshoven, J. M. (1998). On segmentation of lung parenchyma in quantitative computed tomography of the lung. *Med. Phys.* 25 (12), 2432–2439. doi:10.1118/1.598454

Kipritidis, J., Hofman, M. S., Siva, S., Callahan, J., Le Roux, P. Y., Woodruff, H. C., et al. (2016). Estimating lung ventilation directly from 4D CT Hounsfield unit values. *Med. Phys.* 43 (1), 33–43. doi:10.1118/1.4937599

Kipritidis, J., Tahir, B. A., Cazoulat, G., Hofman, M. S., Siva, S., Callahan, J., et al. (2019). The VAMPIRE challenge: A multi-institutional validation study of CT ventilation imaging. *Med. Phys.* 46 (3), 1198–1217. doi:10.1002/mp.13346

Kuhnigk, J.-M., Dicken, V., Zidowitz, S., Bornemann, L., Kuemmerlen, B., Krass, S., et al. (2005). Informatics in radiology (infoRAD): New tools for computer assistance in thoracic CT. Part 1. Functional analysis of lungs, lung lobes, and bronchopulmonary segments. *Radiographics* 25 (2), 525–536. doi:10.1148/rg.252045070

Lung-disease (2023). Lung diseases four-pattern approach. Available from: https://radiologyassistant.nl/chest/chest-x-ray/lung-disease.

Lafata, K. J., Zhou, Z., Liu, J. G., Hong, J., and Kelsey, C. R. (2019). An exploratory radiomics approach to quantifying pulmonary function in CT images. *Sci. Rep.* 9 (1), 11509–9. doi:10.1038/s41598-019-48023-5

Lee, H. K., Vaporciyan, A. A., Cox, J. D., Tucker, S. L., Putnam, J. B., Ajani, J. A., et al. (2003). Postoperative pulmonary complications after preoperative chemoradiation for esophageal carcinoma: Correlation with pulmonary dose-volume histogram parameters. *Int. J. Radiat. Oncol. Biol. Phys.* 57 (5), 1317–1322. doi:10.1016/s0360-3016(03)01373-7

Lee, S. J., and Park, H. J. (2020). Single-photon emission computed tomography (SPECT) or positron emission tomography (PET) imaging for radiotherapy planning in patients with lung cancer: A meta-analysis. *Sci. Rep.* 10 (1), 14864–14911. doi:10.1038/s41598-020-71445-5

Levin, D. L., Schiebler, M. L., and Hopkins, S. R. (2017). Physiology for the pulmonary functional imager. *Eur. J. radiology* 86, 308–312. doi:10.1016/j.ejrad.2016.09.027

Liu, Z., Miao, J., Huang, P., Wang, W., Wang, X., Zhai, Y., et al. (2020). A deep learning method for producing ventilation images from 4DCT: First comparison with technegas SPECT ventilation. *Med. Phys.* 47 (3), 1249–1257. doi:10.1002/mp.14004

Raju, S., Ghosh, S., and Mehta, A. C. (2017). Chest CT signs in pulmonary disease: A pictorial review. *Chest* 151 (6), 1356–1374. doi:10.1016/j.chest.2016.12.033

Reinhardt, J. M., Ding, K., Cao, K., Christensen, G. E., Hoffman, E. A., and Bodas, S. V. (2008). Registration-based estimates of local lung tissue expansion compared to xenon CT measures of specific ventilation. *Med. image Anal.* 12 (6), 752–763. doi:10.1016/j.media.2008.03.007

Ren, G., Lam, S. K., Zhang, J., Xiao, H., Cheung, A. L. Y., Ho, W. Y., et al. (2021). Investigation of a novel deep Learning-Based computed tomography perfusion mapping framework for functional lung avoidance radiotherapy. *Front. Oncol.* 11, 644703. doi:10.3389/fonc.2021.644703

Ren, G., Zhang, J., Li, T., Xiao, H., Cheung, L. Y., Ho, W. Y., et al. (2021). Deep learning-based computed tomography perfusion mapping (DL-CTPM) for pulmonary CT-to-perfusion translation. *Int. J. Radiat. Oncology* Biology* Phys.* 110 (5), 1508–1518. doi:10.1016/j.ijrobp.2021.02.032

Ren, X., and Malik, J. (2003). "Learning a classification model for segmentation," in IEEE International Conference on Computer Vision, Nice, France, 13-16 October 2003.

Roos, J. E., McAdams, H. P., Kaushik, S. S., and Driehuys, B. (2015). Hyperpolarized gas MR imaging: Technique and applications. *Magn. Reson. Imaging Clin.* 23 (2), 217–229. doi:10.1016/j.mric.2015.01.003

Simon, B. A. (2000). Non-invasive imaging of regional lung function using x-ray computed tomography. *J. Clin. Monit. Comput.* 16 (5), 433–442. doi:10.1023/a:1011444826908

Suga, K., Kawakami, Y., Zaki, M., Yamashita, T., Shimizu, K., and Matsunaga, N. (2004). Clinical utility of co-registered respiratory-gated 99mTc-Technegas/MAA SPECT-CT images in the assessment of regional lung functional impairment in patients with lung cancer. *Eur. J. Nucl. Med. Mol. imaging* 31 (9), 1280–1290. doi:10.1007/s00259-004-1558-1

Szmul, A., Matin, T., Gleeson, F. V., Schnabel, J. A., Grau, V., and Papież, B. W. (2019). Patch-based lung ventilation estimation using multi-layer supervoxels. *Comput. Med. Imaging Graph.* 74, 49–60. doi:10.1016/j.compmedimag.2019.04.002

Tustison, N. J., Awate, S. P., Cai, J., Altes, T. A., Miller, G. W., de Lange, E. E., et al. (2010). Pulmonary kinematics from tagged hyperpolarized helium-3 MRI. *J. Magnetic Reson. Imaging* 31 (5), 1236–1241. doi:10.1002/jmri.22137

Vinogradskiy, Y., Castillo, R., Castillo, E., Schubert, L., Jones, B. L., Faught, A., et al. (2022). Results of a multi-institutional phase 2 clinical trial for 4DCT-ventilation functional avoidance thoracic radiation therapy. *Int. J. Radiat. Oncology* Biology* Phys.* 112 (4), 986–995. doi:10.1016/j.ijrobp.2021.10.147

Vinogradskiy, Y. (2019). CT-based ventilation imaging in radiation oncology. *BJR|Open* 1, 20180035. doi:10.1259/bjro.20180035

Wild, C., Weiderpass, E., and Stewart, B. W. (2020). *World cancer report: Cancer research for cancer prevention*. France: IARC Press.

Yamamoto, T., Kabus, S., Lorenz, C., Mittra, E., Hong, J. C., Chung, M., et al. (2014). Pulmonary ventilation imaging based on 4-dimensional computed tomography: Comparison with pulmonary function tests and SPECT ventilation images. *Int. J. Radiat. Oncology* Biology* Phys.* 90 (2), 414–422. doi:10.1016/j.ijrobp.2014.06.006

Yamamoto, T., Kabus, S., von Berg, J., Lorenz, C., and Keall, P. J. (2011). Impact of four-dimensional computed tomography pulmonary ventilation imaging-based functional avoidance for lung cancer radiotherapy. *Int. J. Radiat. Oncology* Biology* Phys.* 79 (1), 279–288. doi:10.1016/j.ijrobp.2010.02.008

Yang, Z., Lafata, K. J., Chen, X., Bowsher, J., Chang, Y., Wang, C., et al. (2021). Quantification of lung function on CT images based on pulmonary radiomic filtering. *Med. Phys.* 49, 7278. doi:10.1002/mp.15837

Yuan, S. T., Frey, K. A., Gross, M. D., Hayman, J. A., Arenberg, D., Cai, X. W., et al. (2012). Changes in global function and regional ventilation and perfusion on SPECT during the course of radiotherapy in patients with non-small-cell lung cancer. *Int. J. Radiat. Oncology* Biology* Phys.* 82 (4), e631–e638. doi:10.1016/j.ijrobp.2011.07.044

Zhong, Y., Vinogradskiy, Y., Chen, L., Myziuk, N., Castillo, R., Castillo, E., et al. (2019). Technical Note: Deriving ventilation imaging from 4DCT by deep convolutional neural network. *Med. Phys.* 46 (5), 2323–2329. doi:10.1002/mp.13421

frontiers | Frontiers in Physiology

TYPE Original Research
PUBLISHED 28 April 2023
DOI 10.3389/fphys.2023.1133334

OPEN ACCESS

EDITED BY
Sam Bayat,
Université Grenoble Alpes, France

REVIEWED BY
Helen Marshall,
The University of Sheffield,
United Kingdom
G. Kim Prisk,
University of California, San Diego,
United States

*CORRESPONDENCE
Sarah Svenningsen,
✉ svennins@mcmaster.ca

RECEIVED 28 December 2022
ACCEPTED 03 April 2023
PUBLISHED 28 April 2023

CITATION
Radadia N, Friedlander Y, Priel E, Konyer NB, Huang C, Jamal M, Farncombe T, Marriott C, Finley C, Agzarian J, Dolovich M, Noseworthy MD, Nair P, Shargall Y and Svenningsen S (2023), Comparison of ventilation defects quantified by Technegas SPECT and hyperpolarized ^{129}Xe MRI.
Front. Physiol. 14:1133334.
doi: 10.3389/fphys.2023.1133334

Comparison of ventilation defects quantified by Technegas SPECT and hyperpolarized ^{129}Xe MRI

Nisarg Radadia[1], Yonni Friedlander[2,3], Eldar Priel[2,4,5], Norman B. Konyer[3], Chynna Huang[2], Mobin Jamal[1], Troy Farncombe[6,7], Christopher Marriott[6,7], Christian Finley[2,4,5], John Agzarian[2,4,5], Myrna Dolovich[1,2,3], Michael D. Noseworthy[3,6,8], Parameswaran Nair[1,2], Yaron Shargall[2,4,5] and Sarah Svenningsen[1,2,3]*

[1]Division of Respirology, Department of Medicine, McMaster University, Hamilton, ON, Canada, [2]Firestone Institute for Respiratory Health, St. Joseph's Healthcare Hamilton, Hamilton, ON, Canada, [3]Imaging Research Centre, St. Joseph's Healthcare Hamilton, Hamilton, ON, Canada, [4]Division of Thoracic Surgery, St. Joseph's Healthcare Hamilton, Hamilton, ON, Canada, [5]Division of Thoracic Surgery, Department of Surgery, McMaster University, Hamilton, ON, Canada, [6]Department of Radiology, McMaster University, Hamilton, ON, Canada, [7]Department of Nuclear Medicine, St. Joseph's Healthcare Hamilton, Hamilton, ON, Canada, [8]Department of Electrical and Computer Engineering, McMaster University, Hamilton, ON, Canada

Introduction: The ideal contrast agents for ventilation SPECT and MRI are Technegas and ^{129}Xe gas, respectively. Despite increasing interest in the clinical utility of ventilation imaging, these modalities have not been directly compared. Therefore, our objective was to compare the ventilation defect percent (VDP) assessed by Technegas SPECT and hyperpolarized ^{129}Xe MRI in patients scheduled to undergo lung cancer resection with and without pre-existing obstructive lung disease.

Methods: Forty-one adults scheduled to undergo lung cancer resection performed same-day Technegas SPECT, hyperpolarized ^{129}Xe MRI, spirometry, and diffusing capacity of the lung for carbon monoxide (DL_{CO}). Ventilation abnormalities were quantified as the VDP using two different methods: adaptive thresholding (VDP_T) and k-means clustering (VDP_K). Correlation and agreement between VDP quantified by Technegas SPECT and ^{129}Xe MRI were determined by Spearman correlation and Bland-Altman analysis, respectively.

Results: VDP measured by Technegas SPECT and ^{129}Xe MRI were correlated (VDP_T: $r = 0.48$, $p = 0.001$; VDP_K: $r = 0.63$, $p < 0.0001$). A 2.0% and 1.6% bias towards higher Technegas SPECT VDP was measured using the adaptive threshold method (VDP_T: 23.0% ± 14.0% vs. 21.0% ± 5.2%, $p = 0.81$) and k-means method (VDP_K: 9.4% ± 9.4% vs. 7.8% ± 10.0%, $p = 0.02$), respectively. For both modalities, higher VDP was correlated with lower FEV_1/FVC (SPECT VDP_T: $r = -0.38$, $p = 0.01$; MRI VDP_K: $r = -0.46$, $p = 0.002$) and DL_{CO} (SPECT VDP_T: $r = -0.61$, $p < 0.0001$; MRI VDP_K: $r = -0.68$, $p < 0.0001$). Subgroup analysis revealed that VDP measured by both modalities was significantly higher for participants with COPD ($n = 13$) than those with asthma ($n = 6$; SPECT VDP_T: $p = 0.007$, MRI VDP_K: $p = 0.006$) and those with no history of obstructive lung disease ($n = 21$; SPECT VDP_T: $p = 0.0003$, MRI VDP_K: $p = 0.0003$).

Discussion: The burden of ventilation defects quantified by Technegas SPECT and ^{129}Xe MRI VDP was correlated and greater in participants with COPD when compared to those without. Our observations indicate that, despite substantial differences between the imaging modalities, quantitative assessment of ventilation defects by Technegas SPECT and ^{129}Xe MRI is comparable.

KEYWORDS

ventilation imaging, Technegas SPECT, hyperpolarized xenon-129, MRI, airflow obstruction, ventilation defects, functional lung imaging

1 Introduction

Pulmonary ventilation imaging modalities have been developed to provide a regional evaluation of airflow obstruction at high-resolution and thus ultimately improve the clinical management of a variety of lung diseases. Nuclear medicine (Jögi et al., 2011; Bajc et al., 2017; Farrow et al., 2017), magnetic resonance imaging (MRI) (Kruger et al., 2016; Ohno et al., 2022; Sharma et al., 2022) and computed tomography (CT) (Park et al., 2010; Kim et al., 2012) based methods have all demonstrated abnormal and heterogeneous ventilation in patients with obstructive lung diseases, including chronic obstructive pulmonary disease (COPD) and asthma. While the potential added value of ventilation imaging modalities over conventional global measures of lung function made by breathing tests is recognized, few are widely available or used in the routine management of obstructive lung disease.

The most clinically established and widely used ventilation imaging modality is single photon emission computed tomography (SPECT) using a range of ventilation agents including krypton-81 m gas (^{81m}Kr) and ^{99m}Tc-labelled aerosols (e.g., diethylene-triamine-pentaacetate [DTPA] and Technegas) (Roach et al., 2013; Bajc et al., 2019). Beyond its primary use in conjunction with perfusion SPECT for the diagnosis of pulmonary embolism, ventilation SPECT is rarely utilized for other indications such as pre-operative quantification of lung function (Genseke et al., 2018) and functional lung avoidance in radiation therapy planning (Munawar et al., 2010; Yuan et al., 2011). Alternatively, inhaled hyperpolarized gas MRI, using either helium-3 (^{3}He) or xenon-129 (^{129}Xe), has undergone extensive research and development for obstructive lung disease applications (Kirby et al., 2012; Svenningsen et al., 2013; Ebner et al., 2017; Shammi et al., 2022; Stewart et al., 2022). Compared to SPECT, hyperpolarized gas MRI offers higher spatial and temporal resolution without exposure to ionizing radiation. However, its availability is currently limited to specialized academic centers. Previous cross-modality investigations have demonstrated the comparability of ^{81m}Kr SPECT with ^{3}He MRI in 23 patients with COPD and 9 healthy volunteers (Stavngaard et al., 2005), and ^{99m}Tc-DTPA SPECT with ^{129}Xe MRI in 11 patients with COPD (Doganay et al., 2019; Kim et al., 2019). While these preliminary investigations report good comparability, they were limited by the small number of patients and disease populations evaluated. Most importantly, the current ideal contrast agents for ventilation SPECT and MRI are generally accepted to be Technegas (Bajc et al., 2019) and ^{129}Xe gas (Niedbalski et al., 2021), respectively, and they have not been directly compared to each other.

With broadening interest in the clinical utility of ventilation imaging, and recent approval of ^{129}Xe MRI and impending approval of Technegas SPECT by the U.S. Food and Drug Administration, a direct quantitative comparison of the modalities is needed. Therefore, the primary objective of this study was to compare the ventilation defect percent (VDP) assessed by Technegas SPECT and ^{129}Xe MRI obtained the same day in a convenient sample of patients scheduled to undergo lung cancer resection with and without pre-existing obstructive lung disease. The secondary objective was to evaluate and compare the relationship of VDP assessed by both modalities with clinical history and standard lung function measures of obstructive lung diseases. To address these objectives, ventilation defects observed by Technegas SPECT and ^{129}Xe MRI were quantified as the whole-lung VDP using two previously published segmentation methods: adaptive thresholding (VDP_T), previously optimized for Technegas SPECT (Farrow et al., 2012); and, k-means clustering (VDP_K), previously optimized for ^{129}Xe MRI (Kirby et al., 2012).

2 Materials and methods

2.1 Participants and study design

This was a prospectively planned sub-study of patients scheduled to undergo first-time lung cancer resection at the division of Thoracic Surgery, McMaster University, Hamilton, Ontario as part of their clinical care who were enrolled into a single-center, prospective, 5-week observational study designed to evaluate the prevalence and clinical relevance of abnormal ventilation in lung cancer patients prior to lung resection. Eligible patients were greater than 18 years of age, first-time lung resection candidates in accordance with the British Thoracic Society guidelines (Callister et al., 2015), and they could not have had previous lung resection, previous chest radiation, or MRI contraindications. All participants provided written informed consent to an ethics-board approved (Hamilton Integrated Research Ethics Board #7770) and registered (ClinicalTrials.gov #NCT04191174) protocol. We report data acquired at a single pre-operative study visit, at which time baseline demographic data and clinical history were collected, and participants performed standard-of-care pulmonary function testing (spirometry and diffusing capacity of the lung for carbon monoxide (DL_{CO})), Technegas SPECT-CT and ^{129}Xe MRI. Image session order was randomized.

2.2 Technegas SPECT-CT acquisition

Technegas (Cyclomedica Australia, Sydney) was prepared with a Technegas Generator (Cyclomedica Australia, Sydney) according to the manufacturer recommendations and a 40 MBq dose was administered to the participant in the supine position via inhalation. The participant was coached to inhale Technegas, starting at functional residual capacity, until 40 µSv/h was measured by a hand-held Geiger counter positioned over the chest. Technegas SPECT was then acquired while supine, during 15-min of tidal breathing using an Optima™ Nuclear Medicine (NM)/Computed Tomography (CT) 640 hybrid imaging system (GE Healthcare, Milwaukee, United States) and in accordance with The Canadian Association of Nuclear Medicine guidelines using the following acquisition parameters: LEHR collimator, energy window: 140 keV ± 20%, zoom factor of 1.0, 128 × 128 matrix and 4.42 mm isotropic voxels, step and shoot, 25 s/image, 60 images per acquisition (30 images per camera head), 360° rotation, 6° steps, body contour. A low dose non-contrast chest CT was subsequently acquired on the same NM/CT system during free breathing for attenuation correction and to allow for delineation of the thoracic cavity volume using the following acquisition and reconstruction parameters: 120 kVp, 20 mA, 1 s tube rotation time, 1.25 pitch, 512 × 512 matrix, 2.5 mm slice thickness, 2.5 mm slice spacing, standard reconstruction kernel, and 50 cm display field of view. Technegas SPECT reconstruction was performed using a Hermes Workstation (Hermes Medical Solutions, Stockholm, Sweden) with the following settings: OSEM reconstruction (2 iterations, 10 subsets), 3D Gaussian filter with 1.20 cm FWHM with corrections for attenuation, scatter, and collimator resolution recovery.

2.3 MRI acquisition

^{129}Xe ventilation MRI and ^{1}H MRI were acquired using a Discovery™ MR750 3T system (General Electric Healthcare; Milwaukee, United States) as previously described (Svenningsen et al., 2021). Participants were instructed to inhale 1 L of gas (N_2 for ^{1}H MRI and a hyperpolarized ^{129}Xe/N_2 mixture for ^{129}Xe MRI) from functional residual capacity, and coronal slices were acquired under breath-hold conditions. Spin-exchange polarizer systems (Polarean 9800 or 9820, Polarean, Durham, United States) were used to polarize isotopically enriched ^{129}Xe gas (86%; ~600 mL) that was dispensed into a pre-filled mixing syringe (~400 mL of N_2) to achieve a fixed dose of 1 L that was transferred to a Tedlar bag (Jensen Inert Products, Coral Springs, United States) for participant delivery. ^{129}Xe polarization was measured using a polarization measurement station (Polarean Inc., Durham, United States) and the dose-equivalent (DE) volume of 100% enriched, 100% polarized ^{129}Xe was calculated as previously described (He et al., 2015). Following inhalation of the 1 L dose from functional residual capacity, hyperpolarized ^{129}Xe static ventilation MRI was performed using a custom-built, unshielded quadrature-asymmetric bird-cage coil and a 3D fast gradient recalled echo sequence (acquisition time = 10 s, TE = 1.5 ms, TR = 5.1 ms, variable flip angle, initial flip angle = 1.3°, receive bandwidth = 16 kHz, field of view = 40 × 40 × 24 cm^3, reconstructed matrix size = 128 × 128 × 16, voxel size = 3.125 × 3.125 × 15 mm^3). A matching ^{1}H MRI was performed using the whole-body radiofrequency coil and a fast-spoiled gradient echo sequence (acquisition time = 9 s, TE = 1.2 ms, TR = 4.3 ms, flip angle = 20°, FOV = 40 × 40 cm, matrix size = 128 × 128, 16 slices, voxel size = 3.125 × 3.125 × 15 mm^3).

2.4 VDP quantification

Ventilation defects observed by Technegas SPECT and ^{129}Xe MRI were quantified as the whole-lung VDP using two different segmentation methods: adaptive thresholding (VDP_T) and k-means clustering (VDP_K), which have been optimized and validated for Technegas SPECT (Farrow et al., 2012) and ^{129}Xe MRI (Kirby et al., 2012), respectively. For the adaptive thresholding method (Farrow et al., 2012), voxels within the thoracic cavity were defined as "ventilation defect" if they were below a threshold determined as 0.5 x $Mean_{5\text{-}80}$, where $Mean_{5\text{-}80}$ is the mean intensity of all voxels in the thoracic cavity that fall between the 5th and 80th percentile of voxel intensities. The k-means method (Kirby et al., 2012) used an iterative algorithm to bin the voxel intensities into five clusters, with the lowest signal cluster being considered "ventilation defect." For both segmentation methods, the whole-lung VDP was calculated as the volume of ventilation defects normalized to the thoracic cavity volume.

2.4.1 SPECT segmentation

The thoracic cavity was delineated by registering the CT to the Technegas SPECT and then segmenting the CT using semi-automated segmentation and registration software implemented on a HERMES workstation. Technegas SPECT ventilation segmentation using the threshold method was implemented on a HERMES workstation and the k-means method was implemented using the Image Processing Toolbox provided by MATLAB R2022b (The MathWorks Inc., Natick, MA, United States).

2.4.2 MRI segmentation

The thoracic cavity was delineated by registering the ^{1}H MRI to the ^{129}Xe MRI and then segmenting the ^{1}H MRI using a previously described semi-automated pipeline implemented in MATLAB (Kirby et al., 2012). ^{129}Xe MRI ventilation segmentation using the threshold method was implemented in MATLAB and the k-means method was performed using the previously described MATLAB pipeline (Kirby et al., 2012).

2.5 Statistical analysis

Data were tested for normality using the Shapiro-Wilk normality test and, when data were not normal, non-parametric tests were performed. Differences in demographic and clinical characteristics between participants with no history of lung disease, asthma, and COPD were determined using a one-way ANOVA with Tukey's multiple comparisons test for parametric data or Kruskal Wallis with Dunn's multiple comparisons test for non-parametric data. The correlation and agreement between VDP measured by Technegas SPECT and ^{129}Xe MRI were evaluated by Spearman (ρ) correlation coefficients and Bland-Altman analysis, respectively. The relationship of VDP measured by Technegas SPECT and ^{129}Xe MRI with age, pack-year smoking history, spirometry, and DL_{CO} were evaluated by Pearson (r) or Spearman (ρ) correlation coefficients. Statistical analyses were performed using GraphPad Prism 8.0 (GraphPad Software, San Diego, CA, United States) and all results were considered significant when the probability of making a Type I error was less than 5% ($p < 0.05$).

3 Results

Forty-four patients scheduled for resection of lung cancer were enrolled, and 41 who completed same-day Technegas SPECT and

TABLE 1 Participant demographics and clinical characteristics.

		History of obstructive lung disease			
	All (n = 41)	None (n = 21)	Asthma (n = 6)	COPD (n = 13)	*p*-value*
Age years	68 ± 7	69 ± 9	64 ± 6	68 ± 6	0.41
Female sex n (%)	25 (61)	14 (67)	5 (83)	6 (46)	--
BMI kg/m^2	27 ± 6	27 ± 6	31 ± 6	24 ± 7	0.08
Smoking history					
Never n (%)	8 (20)	7 (33)	1 (17)	0 (0)	--
Past n (%)	24 (59)	10 (48)	5 (83)	8 (62)	--
Current n (%)	9 (22)	4(19)	0 (0)	5 (38)	--
Pack-years	27[0–100]	20[0–66]	9[0–25]	50[14–100]	**0.005†**
Pulmonary function tests					
FEV$_1$%$_{pred}$	84 ± 23	94 ± 19	83 ± 16	69 ± 27	**0.007‡**
FVC%$_{pred}$	98 ± 18	104 ± 20	97 ± 12	92 ± 15	0.17
FEV$_1$/FVC %	67 ± 13	72 ± 10	69 ± 6	57 ± 16	**0.003‡**
DL$_{CO}$%$_{pred}$	93 ± 31	107 ± 24	111 ± 24	62 ± 22	**<0.0001†**
Primary tumor characteristics					
NSCLC n (%)	33 (80)	16 (76)	4 (66)	12 (92)	--
SCLC n (%)	1 (2)	--	1 (17)	--	--
Other n (%)	3 (7)	2 (10)	1 (17)	--	--
Stage n (%)#					
Stage I	25 (61)	12 (57)	5 (83)	8 (62)	--
Stage II	7 (17)	4 (19)	--	2 (15)	--
Stage III	3 (7)	--	1 (17)	2 (15)	--
Stage IV	2 (5)	2 (10)	--	--	--
T-classification n (%)#					
T$_1$ (≤3 cm)	19 (46)	8 (38)	3 (50)	8 (62)	--
T$_2$ (>3 to ≤5 cm)	11 (27)	8 (38)	2 (33)	1 (8)	--
T$_3$ (>5 to ≤7 cm)	4 (10)	1 (5)	1 (17)	1 (8)	--
T$_4$ (>7 cm)	3 (7)	1 (5)	--	2 (15)	--

Values are mean ± standard deviation or median [minimum-maximum] except when indicated otherwise. BMI = body mass index; COPD = chronic obstructive pulmonary disease; FEV$_1$ = forced expiratory volume in one second; FVC = forced vital capacity; DL$_{CO}$ = diffusion capacity for carbon monoxide; NSCLC = non-small cell lung cancer; SCLC = small cell lung cancer; %$_{pred}$ = percent of predicted value. #As per TNM-staging 8th edition. *Significance of difference between groups was determined using a one-way ANOVA, with Tukey's multiple comparisons test (parametric data) or Kruskal Wallis with Dunn's multiple comparisons test (non-parametric data). Multiple comparisons revealed †COPD, different from asthma and none, ‡COPD, different from none. Bold values denote statistical significance at the $p < 0.05$ level.

^{129}Xe MRI were included in our analysis. Three of the enrolled participants were excluded from our analysis because ^{129}Xe MRI was not performed; two participants had an MRI contraindication (brain aneurism clip), and one was unable to accommodate MRI scheduling. Of the 41 participants evaluated, 21 (51%) had no concomitant history of lung disease, while 6 (15%) had a history of asthma, 13 (32%) had COPD, and 1 (2%) had interstitial lung disease (ILD). Participant demographics, clinical characteristics, and primary tumor characteristics are summarized in Table 1. Participants with no history of lung disease, asthma, and COPD were well-balanced with respect to age ($p = 0.41$) and BMI ($p = 0.08$). Participants with COPD had a higher pack-year smoking history and lower DL$_{CO}$%$_{pred}$ than participants with asthma ($p = 0.01$ and $p = 0.0004$) and those with no history of lung disease ($p = 0.02$ and $p < 0.0001$). FEV$_1$%$_{pred}$ and FEV$_1$/FVC were also lower for participants with COPD than those with no history of lung disease ($p = 0.005$ and $p = 0.002$).

Technegas SPECT and ^{129}Xe MRI were well-tolerated by all participants, with no occurrence of adverse events. The scanning sessions were performed 90 ± 30 min apart [minimum of 12 min, maximum of 120 min]. Dosing and measurements of image quality are provided in the online supplement (Supplementary Table S1). Figure 1 shows coronal Technegas SPECT, ^{129}Xe MRI, and corresponding structural ^{1}H MRI slices for four representative participants. For participant A, a never-smoker with no history of lung disease, both modalities revealed relatively normal ventilation. For participant B, an ex-smoker with no history of lung disease, both modalities revealed peripheral ventilation defects despite normal lung function assessed by spirometry. For participants C and D, past smokers with COPD, large and spatially concordant ventilation defects were observed by both modalities. While most ventilation defects, such as those highlighted by yellow arrows, were spatially concordant across

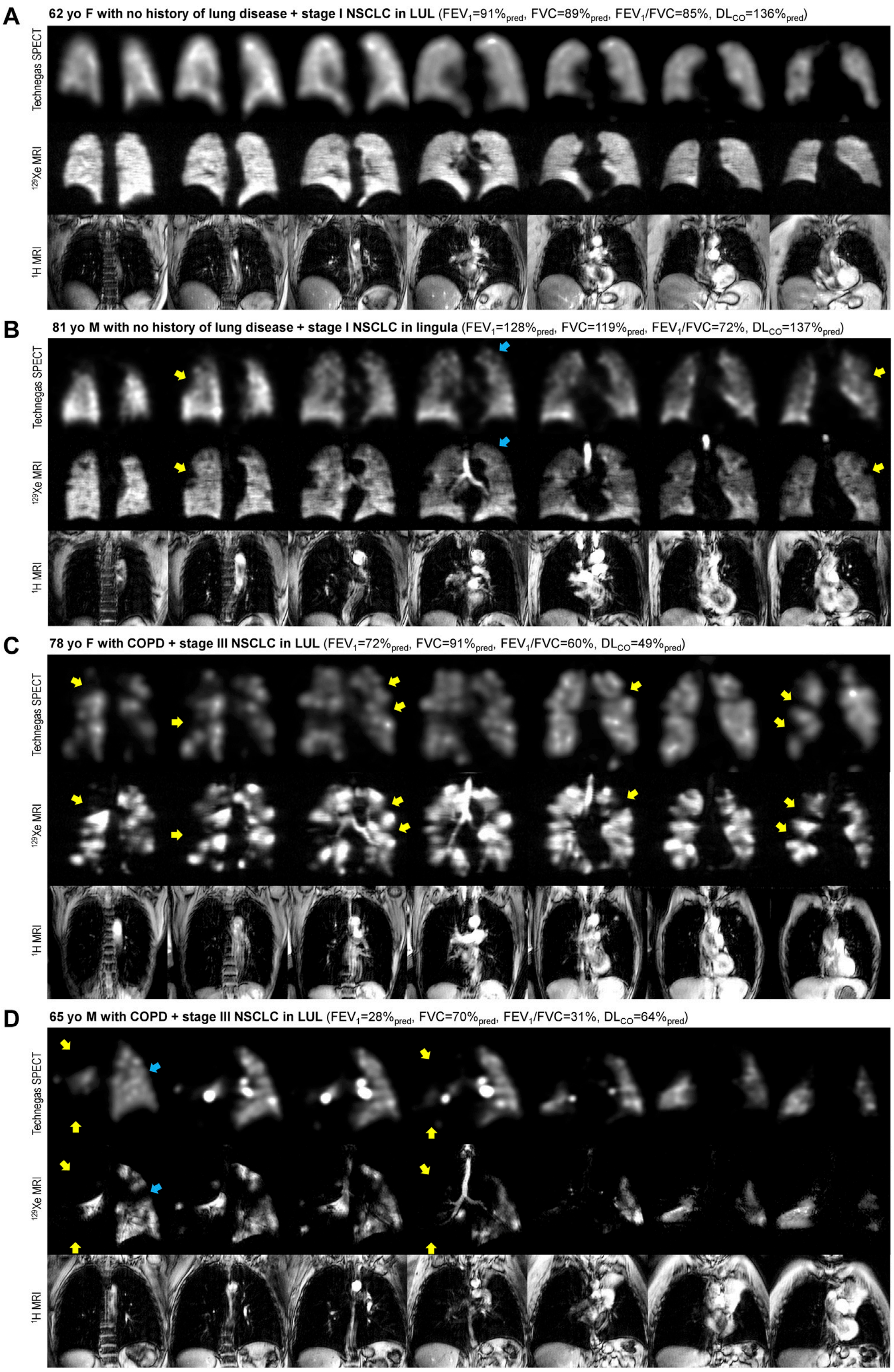

62 yo F with no history of lung disease + stage I NSCLC in LUL (FEV$_1$=91%$_{pred}$, FVC=89%$_{pred}$, FEV$_1$/FVC=85%, DL$_{CO}$=136%$_{pred}$)

81 yo M with no history of lung disease + stage I NSCLC in lingula (FEV$_1$=128%$_{pred}$, FVC=119%$_{pred}$, FEV$_1$/FVC=72%, DL$_{CO}$=137%$_{pred}$)

78 yo F with COPD + stage III NSCLC in LUL (FEV$_1$=72%$_{pred}$, FVC=91%$_{pred}$, FEV$_1$/FVC=60%, DL$_{CO}$=49%$_{pred}$)

65 yo M with COPD + stage III NSCLC in LUL (FEV$_1$=28%$_{pred}$, FVC=70%$_{pred}$, FEV$_1$/FVC=31%, DL$_{CO}$=64%$_{pred}$)

FIGURE 1
Comparison of ventilation visualized by Technegas SPECT and hyperpolarized ^{129}Xe MRI. Anatomically matched coronal Technegas SPECT, ^{129}Xe MRI, and ^{1}H MRI slices for four representative participants. Select examples of spatially concordant and discordant ventilation defects are highlighted by yellow and blue arrows, respectively. **(A)** 62-year-old female with necrotizing granuloma in left upper lobe and no history of lung disease. Technegas SPECT: VDP$_T$ = 12%*, VDP$_K$ = 5%; ^{129}Xe MRI: VDP$_T$ = 22%, VDP$_K$ = 1%*; FEV$_1$ = 91%$_{pred}$, FVC = 89%$_{pred}$, FEV$_1$/FVC = 85%, DL$_{CO}$ = 136%$_{pred}$. **(B)** 81-year-old male with stage I NSCLC in lingula and no history of lung disease. Technegas SPECT: VDP$_T$ = 28%*, VDP$_K$ = 14%; ^{129}Xe MRI: VDP$_T$ = 18%, VDP$_K$ = 4%*; FEV$_1$ = 128%$_{pred}$, FVC = 119%$_{pred}$, FEV$_1$/FVC = 72%, DL$_{CO}$ = 137%$_{pred}$. **(C)** 78-year-old female with stage III NSCLC in left upper lobe and concomitant COPD. Technegas SPECT: VDP$_T$ = 47%*, VDP$_K$ = 20%; ^{129}Xe MRI: VDP$_T$ = 31%, VDP$_K$ = 19%*; FEV$_1$ = 72%$_{pred}$, FVC = 91%$_{pred}$, FEV$_1$/FVC = 60%, DL$_{CO}$ = 49%$_{pred}$. **(D)** 65-year-old male with stage III NSCLC in left upper lobe and concomitant COPD. Technegas SPECT: VDP$_T$ = 84%*, VDP$_K$ = 52%; ^{129}Xe MRI:

(Continued)

FIGURE 1 (Continued)
VDP_T = 37%, VDP_K = 48%*; FEV_1 = 28%$_{pred}$, FVC = 70%$_{pred}$, FEV_1/FVC = 31%, DL_{CO} = 64%$_{pred}$. COPD = chronic obstructive pulmonary disease; FEV_1 = forced expiratory volume in one second; FVC = forced vital capacity; DL_{CO} = diffusing capacity for carbon monoxide; LUL = left upper lobe; NSCLC = non-small cell lung cancer; %$_{pred}$ = percent of predicted value. *Thresholding (VDP_T) and k-means clustering (VDP_K) methods previously optimized and validated for Technegas SPECT and ^{129}Xe MRI, respectively.

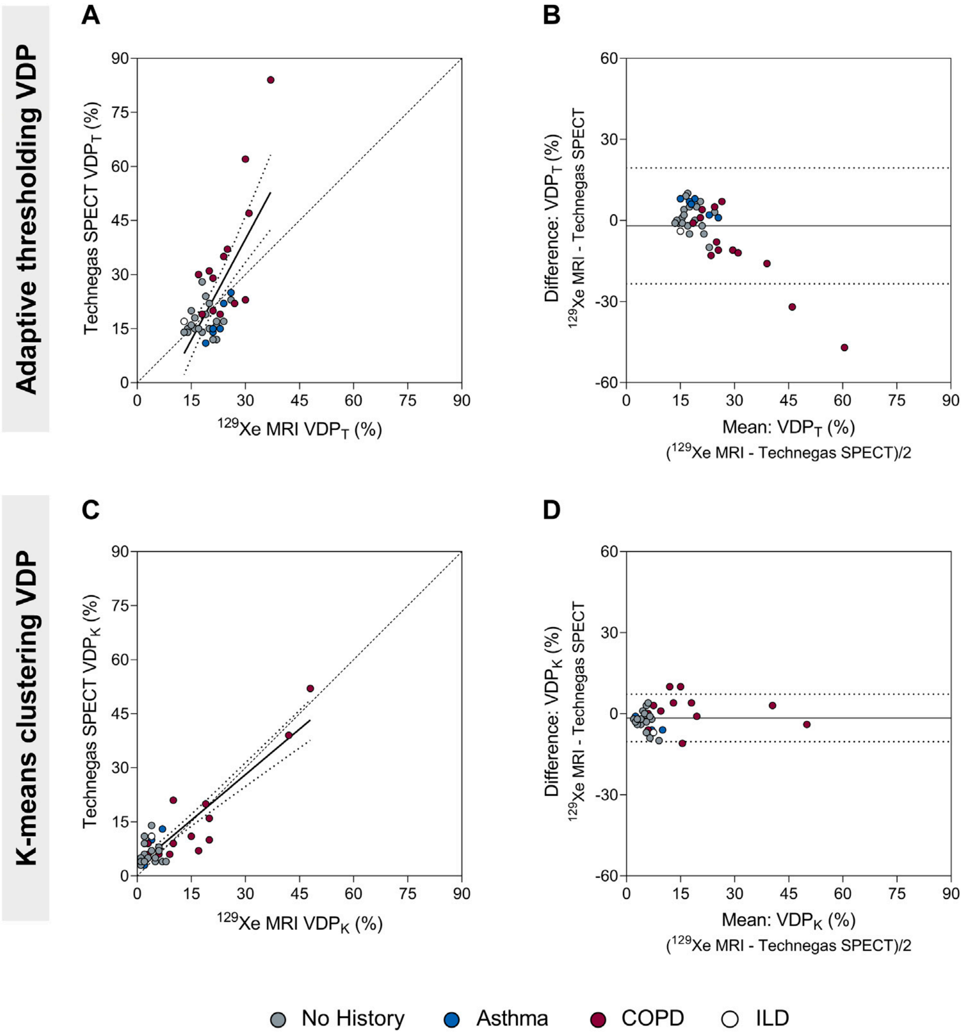

FIGURE 2
Comparison of the ventilation defect percent (adaptive thresholding (VDP_T) and k-means clustering (VDP_K)) quantified by Technegas SPECT and ^{129}Xe MRI. **(A)** Positive relationship between Technegas SPECT and ^{129}Xe MRI VDP_T quantified using the adaptive threshold method ($r = 0.48$, $r^2 = 0.49$, $p = 0.001$, $y = 1.86x-16.11$). **(B)** Bland-Altman plot of the difference between Technegas SPECT and ^{129}Xe MRI VDP_T quantified using the adaptive threshold method. Bias = −2.0% (95% limits of agreement, −23.4% to 19.4%). **(C)** Positive relationship between Technegas SPECT and ^{129}Xe MRI VDP_K quantified using the k-means clustering method ($r = 0.63$, $r^2 = 0.80$, $p < 0.0001$, $y = 0.84x+2.83$). **(D)** Bland-Altman plot of the difference between Technegas SPECT and ^{129}Xe MRI VDP_K quantified using the k-means clustering method. Bias = −1.6% (95% limits of agreement, −10.4% to 7.2%). For correlation plots, the dashed line represents the line of identity ($y = x$) and the dotted lines represent the 95% confidence intervals of the linear regression line. For Bland-Altman plots, the solid line represents the mean of the paired differences, and the dotted lines represent the 95% limits of agreement. Colored data points represent history of lung disease (no history, n = 21; asthma, n = 6; COPD, n = 13; ILD: n = 1). *Thresholding (VDP_T) and k-means clustering (VDP_K) methods previously optimized and validated for Technegas SPECT and ^{129}Xe MRI, respectively.

modalities, focal discordances were also observed, such as those highlighted by blue arrows for participants B and D.

The VDP for Technegas SPECT and ^{129}Xe MRI were quantified using adaptive thresholding (VDP_T) and k-means clustering (VDP_K) methods. The VDP was higher when determined using the threshold method compared to the k-means method for both Technegas SPECT ($VDP_T = 23.0 \pm 14.0\%$ vs. $VDP_K = 9.4 \pm 9.4\%$, $p < 0.0001$) and ^{129}Xe MRI ($VDP_T = 21.0 \pm 5.2\%$ vs. $VDP_K = 7.8 \pm$

TABLE 2 Univariate relationships of Technegas SPECT VDP and ^{129}Xe MRI VDP with participant demographics and clinical characteristics.

	Technegas SPECT				^{129}Xe MRI			
	VDP_T, %*		VDP_K, %		VDP_T, %		VDP_K, %*	
	r	p	r	p	r	p	r	p
Age years	0.02	0.91	0.04	0.80	−0.24	0.13	0.28	0.07
Pack-year smoking history	0.25	0.10	0.21	0.18	−0.02	0.89	0.56	**0.0002**
$FEV_1\%_{pred}$	−0.26	0.12	−0.26	0.09	−0.55	**0.0002**	−0.35	**0.03**
$FVC\%_{pred}$	−0.08	0.60	−0.16	0.31	−0.26	0.10	−0.19	0.24
FEV_1/FVC, %	−0.38	**0.01**	−0.28	0.07	−0.43	**0.005**	−0.46	**0.002**
$DL_{CO}\%_{pred}$	−0.61	**<0.0001**	−0.52	**0.0005**	−0.37	**0.02**	−0.68	**<0.0001**

Relationships were evaluated with Pearson correlation coefficients for parametric data and Spearman's correlation coefficients for non-parametric data. VDP = ventilation defect percent; VDP_T = VDP, determined by thresholding method; VDP_K = VDP, determined by k-means method; FEV_1 = forced expiratory volume in one second; FVC = forced vital capacity; DL_{CO} = diffusion capacity for carbon monoxide. *Thresholding (VDP_T) and k-means clustering (VDP_K) methods previously optimized and validated for Technegas SPECT, and ^{129}Xe MRI, respectively. Bold values denote statistical significance at the p <0.05 level.

10.0%, $p < 0.0001$). Figure 2 summarizes the correlation and agreement of VDP_T and VDP_K measured by Technegas SPECT and ^{129}Xe MRI. For both quantification methods, VDP measured by Technegas SPECT and ^{129}Xe MRI were correlated (Figure 2A: VDP_T, r = 0.48, $p = 0.001$; Figure 2C: VDP_K, r = 0.63, $p < 0.0001$). Using the threshold method, Bland-Altman analysis (Figure 2B) indicated a 2.0% bias (95% limit of agreement: −23.4% to 19.4%) for higher VDP_T measured by Technegas SPECT (Technegas SPECT VDP_T = 23.0 ± 14.0% vs. ^{129}Xe MRI VDP_T = 21.0 ± 5.2%, $p = 0.81$). Using the k-means method, Bland-Altman analysis (Figure 2D) indicated a similar 1.6% bias (95% limit of agreement: −10.4% to 7.2%) for higher VDP_K measured by Technegas SPECT (Technegas SPECT VDP_K = 9.4 ± 9.4% vs. ^{129}Xe MRI VDP_K = 7.8 ± 10.0%, $p = 0.02$).

Univariate relationships of Technegas SPECT VDP and ^{129}Xe MRI VDP with age, pack-year smoking history, spirometry and DL_{CO} are summarized in Table 2. Using the threshold method, Technegas SPECT VDP_T and ^{129}Xe MRI VDP_T were negatively correlated with $DL_{CO}\%_{pred}$ (r = −0.61, $p < 0.0001$; and r = −0.37, p = 0.02) and FEV_1/FVC (r = −0.38, $p = 0.01$; and r = −0.43, $p = 0.005$). ^{129}Xe MRI VDP_T, but not Technegas SPECT VDP_T, was correlated with $FEV_1\%_{pred}$ (r = −0.55, $p = 0.0002$). Using the k-means method, Technegas SPECT VDP_K and ^{129}Xe MRI VDP_K were negatively correlated with $DL_{CO}\%_{pred}$ (r = −0.52, $p = 0.0005$; and r = −0.68, $p <$ 0.0001). ^{129}Xe MRI VDP_K, but not Technegas SPECT VDP_K, was correlated with pack-year smoking history (r = 0.56, $p = 0.0002$), $FEV_1\%_{pred}$ (r = −0.35, $p = 0.03$) and FEV_1/FVC (r = −0.46, p = 0.002). For both modalities, VDP_T and VDP_K were not different for participants classified by tumor stage or tumor size (Supplementary Table S2). Additionally, for both modalities, VDP_T and VDP_K of the ipsilateral lung (lung with tumor) was not different than the VDP_T and VDP_K of the contralateral lung (lung without tumor) (Supplementary Figure S1).

Figure 3 summarizes VDP for 21 (51%) participants with no concomitant obstructive lung disease, 6 (15%) with a history of asthma, and 13 (32%) with COPD. The one (2%) participant with interstitial lung disease was excluded from this cross-sectional comparison. Using the threshold method (Figures 3A, B), Technegas SPECT VDP_T and ^{129}Xe MRI VDP_T were significantly higher for participants with COPD than with those with no history of lung disease ($p = 0.0003$ and $p = 0.0004$). Technegas SPECT VDP_T, but not ^{129}Xe MRI VDP_T, was significantly higher for participants with COPD than with those with asthma (p = 0.007 and $p = 0.45$). There was no difference in Technegas SPECT VDP_T or ^{129}Xe MRI VDP_T between participants with asthma and those with no history of lung disease ($p > 0.99$ and $p = 0.15$). Using the k-means method (Figures 3C, D), Technegas SPECT VDP_K and ^{129}Xe MRI VDP_K were significantly higher for participants with COPD than with those with asthma ($p = 0.04$ and $p = 0.006$) and no history of lung disease ($p = 0.002$ and $p = 0.0003$). There was no difference in Technegas SPECT VDP_K or ^{129}Xe MRI VDP_K between participants with asthma and those with no history of lung disease ($p > 0.99$ and $p > 0.99$).

4 Discussion

We prospectively compared ventilation defects assessed by same-day Technegas SPECT and ^{129}Xe MRI in 41 patients scheduled to undergo first-time lung cancer resection, a subset of whom had concomitant asthma or COPD. We report that ventilation defects quantified by Technegas SPECT and ^{129}Xe MRI VDP (determined using both adaptive thresholding and k-means clustering segmentation methods) were 1) correlated with one another, 2) similarly correlated with standard measures of airflow limitation (FEV_1/FVC) and diffusing capacity ($DL_{CO}\%_{pred}$), and 3) significantly higher for participants with COPD than those with asthma and no history of obstructive lung disease.

Many segmentation methods have been developed and optimized to quantify ventilation defects as the VDP, including linear binning, thresholding, and k-means clustering. In this study, VDP was determined for both Technegas SPECT and ^{129}Xe MRI using adaptive thresholding and k-means segmentation methods. The basis for this decision was that the adaptive thresholding quantification method has been previously optimized and

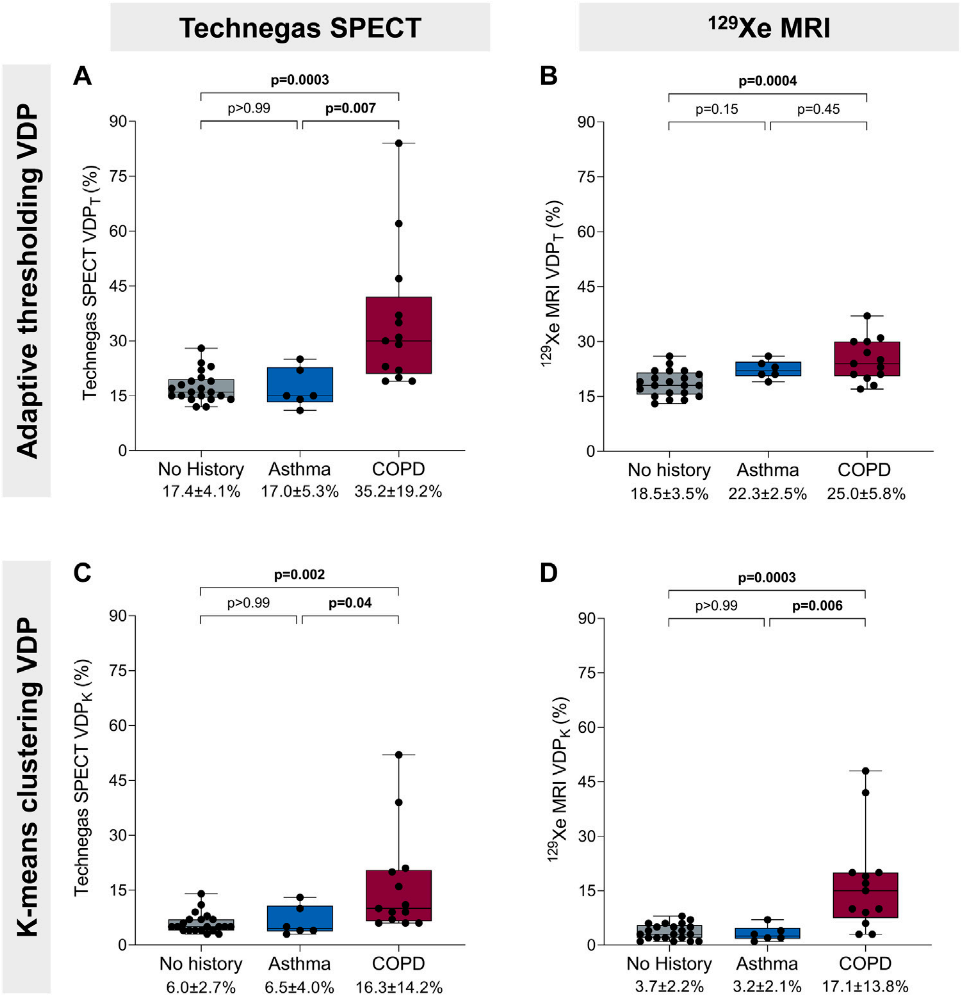

FIGURE 3
Ventilation defect percent and history of obstructive lung disease. **(A)** Technegas SPECT VDP$_T$* was higher in participants with COPD than participants with asthma (35.2% ± 19.2% vs. 17.0 ± 5.3, p = 0.007) and those with no history of lung disease (35.2% ± 19.2% vs. 17.4 ± 4.1, p = 0.0003). **(B)** ^{129}Xe MRI VDP$_T$ was higher for participants with COPD than those with no history of lung disease (25.0% ± 5.8% vs. 18.5% ± 3.5%, p = 0.0004). **(C)** Technegas SPECT VDP$_K$ was significantly higher for participants with COPD than those with asthma (16.3% ± 14.2% vs. 6.5% ± 4.0%, p = 0.04) and no history of lung disease (16.3% ± 14.2% vs. 6.0% ± 2.7%, p = 0.002). **(D)** ^{129}Xe MRI VDP$_K$* was higher in participants with COPD than participants with asthma (17.1% ± 13.8% vs. 3.2% ± 2.1%, p = 0.006) and those with no history of lung disease (17.1% ± 13.8% vs. 3.7% ± 2.2%, p = 0.0003). Box plots show minimum, first quartile, median, third quartile, and maximum VDP with individual values for all participants superimposed on the plot. Difference between groups was determined using one-way ANOVA with Tukey's multiple comparisons test or Kruskal Wallis with Dunn's multiple comparisons test. *Thresholding (VDP$_T$) and k-means clustering (VDP$_K$) methods previously optimized and validated for Technegas SPECT and ^{129}Xe MRI, respectively.

validated for Technegas SPECT by Farrow et al., (2012), and the k-means method for ^{129}Xe MRI by Kirby et al., (2012). Using both segmentation approaches, we observed that the burden of ventilation defects quantified by Technegas SPECT and ^{129}Xe MRI VDP acquired on the same day were correlated. While this is the first comparison of ventilation defects assessed by Technegas SPECT and ^{129}Xe MRI, our observations are consistent with previous investigations demonstrating the comparability of ventilation assessed by SPECT and MRI when utilizing alternative ventilation agents. Stavngaard and colleagues previously reported a good correlation between ^{81m}Kr SPECT and ^{3}He MRI for both visual and quantitative assessments of ventilation defect scores in a cohort of 23 COPD and 9 healthy participants (Stavngaard et al., 2005). In a smaller study of 11 COPD patients, Doganay et al. demonstrated a good correlation between ^{99m}Tc-DTPA SPECT and ^{129}Xe MRI relative lobar percentage ventilation (Doganay et al., 2019). For ventilation SPECT, international guidelines now recommend Technegas as the preferred ventilation agent in patients with obstructive lung disease (Roach et al., 2013; Bajc et al., 2019) limiting the clinical relevance of previous comparisons that used ^{81m}Kr and ^{99m}Tc-DTPA. Additionally, for hyperpolarized gas ventilation MRI, ^{129}Xe gas is now preferred over ^{3}He gas due to its greater availability, lower cost, and higher solubility that permits dissolved-phase imaging (Niedbalski et al., 2021).

In most participants, visual assessment showed spatial agreement between focal ventilation defects observed by both modalities. However, as highlighted in Figure 1 by the blue arrows, some discordance was also observed. We also report a mean bias, 2.0% and 1.6%, towards higher VDP measured by Technegas SPECT than ^{129}Xe MRI, which was observed using the adaptive threshold and k-means method, respectively. This inter-modality bias and lack of absolute agreement in ventilation defects were not unexpected and may be explained by several factors. First, fundamental differences in the physical properties of the ventilation agents may contribute to differences in lung distribution. Technegas is an ultrafine aerosolized particle (0.005–0.2 μm (Lemb et al., 1993)) whose distribution in the lungs, unlike that of ^{129}Xe gas, is impacted by aerosol deposition mechanics. While Technegas behaves in a gas-like manner, permitting peripheral penetration and alveolar deposition (Bajc et al., 2019), it has been previously shown to aggregate at sites of severe obstruction leading to "hot-spots" (De Nijs et al., 2021). Shown in Figure 1D, we observed this effect in a 65-year-old male with severe COPD (FEV_1 = 28%$_{pred}$, FEV_1/FVC = 31%). Bilateral hotspots are observed on Technegas SPECT in the left and right main bronchi. Greater ventilation is observed distal to the right main bronchi hotspot by ^{129}Xe MRI than Technegas SPECT. Second, the different acquisition conditions and spatial resolutions between modalities must be considered. Technegas SPECT is acquired during 15 min of tidal breathing, while ^{129}Xe MRI is acquired during a 10 s breath hold at functional residual capacity plus 1 L. As a result, respiratory and cardiac motion have greater influence on ventilation assessed by SPECT, contributing to blurring and fewer counts at the lung borders. Additionally, lung inflation during imaging affects ventilation defects, with increased ventilation defects observed at lower levels of lung inflation (Hughes et al., 2019). As SPECT is on average acquired at a lower lung inflation (average over tidal volume) than ^{129}Xe MRI (functional residual capacity plus 1 L), higher VDP is expected. Taken together, the aforementioned factors likely account for the higher VDP quantified by Technegas SPECT and the spatial discordances in focal ventilation defects that were observed upon visual inspection.

It is important to emphasize that this study did not intend to determine the optimal quantification approach for each modality, rather to determine if there was correlation and some equivalency between the two modalities using established quantification practices for each modality that are implemented in the literature. There are reasons why each modality may best be served by different segmentation methods, which is beyond the scope of this article. However, we do note that for both modalities, the adaptive threshold method resulted in significantly higher VDPs compared to the k-means clustering method, irrespective of history of obstructive lung disease. In the subgroup of patients with no history of lung disease, the majority of whom had well-ventilated lungs by visual inspection, the VDPs determined using the k-means method were much closer to zero than the threshold method (Technegas SPECT: VDP_K = 6.0% vs. VDP_T = 17.4%; ^{129}Xe MRI: VDP_K = 3.7% vs. VDP_T = 18.5%), which better reflects what the images show (e.g., Figure 1A). We also noticed that when the VDP was determined using the threshold method (but not the k-means method), the bias towards higher Technegas SPECT VDP_T increased with VDP_T, or greater airflow limitation (Figure 2C). This bias seems to be driven largely by a subset of patients with COPD in whom the Technegas SPECT VDP_T was considerably higher than the ^{129}Xe MRI VDP_T. Taken together, investigation of these cases reveals that the adaptive threshold classifies hypo-ventilated (or low ventilated) voxels as defect, leading to a significantly higher VDP_T, which can be misleading when interpreted in absolute terms. This effect, in combination with severe obstruction leading to "hot-spots," likely explains the exceptionally high Technegas SPECT VDP_T reported for two patients with COPD (62% and 84%).

Ventilation defect burden quantified by Technegas SPECT VDP_T and ^{129}Xe MRI VDP_K (VDPs determined using modality-specific approach) were similarly correlated to standard measures of airflow limitation (FEV_1/FVC) and diffusing capacity (DL_{CO}). For both modalities, the correlation with DL_{CO} was stronger than with FEV_1/FVC. One explanation for this may be that DL_{CO} is a direct measurement of the capacity of communicating lung volume to transfer gas from inhaled air to the bloodstream, whereas FEV_1/FVC is an indirect composite marker of the presence of airway obstruction with forced exhalation. Interestingly, ^{129}Xe MRI VDP_K but not SPECT VDP_T, was correlated with pack-year smoking history and FEV_1. The reason for this discrepancy is unclear. Consistent with these relationships, we also observed greater ventilation defect burden quantified by both modalities in participants with COPD compared to those with asthma and no history of obstructive disease. However, VDP assessed by both modalities was not higher in patients who reported a history of asthma compared to those without any known history of obstructive disease. This result may be considered unexpected as abnormal ventilation is a characteristic feature of asthma. We do note that the VDPs in our cohort of asthmatics are similar to what has been previously reported by others, using ^{129}Xe MRI VDP_K (Eddy et al., 2022) and Technegas SPECT VDP_T (Farrow et al., 2012; Farrow et al., 2017), respectively. When interpreting this result, it should be considered that most of our cohort of patients without any known history of obstructive lung disease were current smokers (4 of 21, 19%) or past smokers (10 of 21, 48%), 36% of whom had an FEV_1/FVC less than 0.70 and 7% had a DL_{CO} less than 80%$_{pred}$. As demonstrated by participant B in Figure 1, such patients may have subclinical or undiagnosed airways disease contributing to ventilation defects and increased VDP.

There are limitations to our study that should be considered. First, we evaluated a convenient sample of patients scheduled for lung cancer resection, in whom tumor burden may have influenced segmentation of the thoracic cavity and VDP quantification. However, in our cohort, tumor size was not associated with whole-lung VDP, and ipsilateral and contralateral VDP were not different (data provided online, Supplementary Figure S1; Table S2). These observations indicate that tumor burden did not significantly contribute to VDP assessed by either modality, which is not surprising given the small tumor sizes in our cohort (≤3 cm in 46%, >3 to ≤5 cm in 27%, >5 to ≤7 cm in 10%, and >7 cm in 7% of participants). Second, we did not quantitatively evaluate the spatial agreement of ventilation defects observed by Technegas SPECT and ^{129}Xe MRI. Such analysis is highly dependent on accurate registration and anatomical alignment of Technegas SPECT and ^{129}Xe MRI datasets, which was challenging due to differences in voxel size, acquisition conditions (tidal breathing vs. breath hold) and lung volume. Finally, our quantitative analysis distilled regional and voxel-wise measurements of ventilation down to a single whole-lung value, in this case the VDP. VDP is a binary whole-lung measurement that fails to characterize much of the information offered by ventilation imaging modalities. Furthermore, as our analysis demonstrates, different segmentation schemes yield different VDPs in the same individual.

In summary, using the current ideal contrast agents for ventilation SPECT and MRI, we imaged patients with and without obstructive lung disease prior to lung cancer resection to quantify and compare ventilation defects observed by both modalities. We report that the burden of ventilation defects quantified by Technegas SPECT and ^{129}Xe MRI are correlated and increased in participants with COPD. Our observations indicate that, despite substantial differences between the imaging modalities, assessment of ventilation defects using established quantification practices for Technegas SPECT and ^{129}Xe MRI are comparable, provided the same quantification approach is used. Future work is required to determine if superior and comparable improvements in patient outcomes are achieved by integrating ventilation assessment with Technegas SPECT and ^{129}Xe MRI into the clinical management of lung diseases and potential improvement in outcomes post-resection. For now, based on our findings, the selection of ventilation imaging modality can be guided by local availability and regulatory approval, contraindications, and concern of radiation burden.

Data availability statement

Data sharing requests will be considered from researchers that submit a proposal and an appropriate statistical analysis and dissemination plan. Data would be shared via a secure data access system by request to the corresponding author.

Ethics statement

The studies involving human participants were reviewed and approved by Hamilton Integrated Research Ethics Board. The patients/participants provided their written informed consent to participate in this study. Written informed consent was obtained from the individual(s) for the publication of any potentially identifiable images or data included in this article.

Author contributions

SS, YS, and PN were responsible for study conception and study design. YS, EP, CF, JA, and PN were responsible for identifying and characterizing the patients, and for clinical interpretation of the data. NR, MJ, and CH were responsible for recruiting study participants. CM, TF, and MD were responsible for ventilation SPECT-CT acquisition and/or interpretation. NBK and MDN were responsible for MRI acquisition and/or interpretation. NR, YF, and SS were responsible for data acquisition, analysis, and interpretation, and for preparing the first draft of the manuscript. All authors edited and reviewed the manuscript and approved the final version of the manuscript.

Funding

This was an investigator-initiated study funded by Cyclomedica Australia Pty Ltd. and The Lung Association. The funders had no role in the design of the study, the collection and analysis of the data, or the preparation of the manuscript.

Acknowledgments

The authors thank J. Lecomte, C. Awde, S. Weir, and S. Faseruk, the MRI technologists who performed the ^{129}Xe MRI, and L. Speziale, MJ, K. Fraser, and S. Fitzgerald, the nuclear medicine technologists who performed Technegas SPECT. We also thank C. Farrow for supporting the implementation of the adaptive threshold approach to quantify Technegas SPECT VDP at our center.

Conflict of interest

The authors declare that this was an investigator-initiated study that received funding from Cyclomedica Australia Pty Ltd. and The Lung Association. The funder was not involved in the study design, collection, analysis, interpretation of data, the writing of this article, or the decision to submit it for publication. SS reports a relationship with Polarean that includes: Speaking and lecture fees.

The remaining authors declare that the research was conducted in the absence of any commercial or financial relationships that could be construed as a potential conflict of interest.

Publisher's note

Supplementary material

The Supplementary Material for this article can be found online at: https://www.frontiersin.org/articles/10.3389/fphys.2023.1133334/full#supplementary-material

References

Bajc, M., Chen, Y., Wang, J., Li, X. Y., Shen, W. M., Wang, C. Z., et al. (2017). Identifying the heterogeneity of COPD by V/P SPECT: A new tool for improving the diagnosis of parenchymal defects and grading the severity of small airways disease. *Int. J. chronic Obstr. Pulm. Dis.* 12, 1579–1587. doi:10.2147/COPD.S131847

Bajc, M., Schümichen, C., Grüning, T., Lindqvist, A., Le Roux, P.-Y., Alatri, A., et al. (2019). EANM guideline for ventilation/perfusion single-photon emission computed tomography (SPECT) for diagnosis of pulmonary embolism and beyond. *Eur. J. Nucl. Med. Mol. Imaging* 46 (12), 2429–2451. doi:10.1007/s00259-019-04450-0

Callister, M. E. J., Baldwin, D. R., Akram, A. R., Barnard, S., Cane, P., Draffan, J., et al. (2015). British thoracic society guidelines for the investigation and management of pulmonary nodules: Accredited by NICE. *Thorax* 70 (2), 1–54. doi:10.1136/thoraxjnl-2015-207168

De Nijs, R., Sijtsema, N. D., Kruis, M. F., Jensen, C. V., Iversen, M., Perch, M., et al. (2021). Comparison of 81mKrypton and 99mTc-Technegas for ventilation single-photon emission computed tomography in severe chronic obstructive pulmonary disease. *Nucl. Med. Commun.* 42 (2), 160–168. doi:10.1097/MNM.0000000000001314

Doganay, O., Matin, T., Chen, M., Kim, M., McIntyre, A., McGowan, D. R., et al. (2019). Time-series hyperpolarized xenon-129 MRI of lobar lung ventilation of COPD in comparison to V/Q-SPECT/CT and CT. *Eur. Radiol.* 29 (8), 4058–4067. doi:10.1007/S00330-018-5888-Y

Ebner, L., He, M., Virgincar, R. S., Heacock, T., Kaushik, S. S., Freemann, M. S., et al. (2017). Hyperpolarized ^{129}Xenon magnetic resonance imaging to quantify regional ventilation differences in mild to moderate asthma: A prospective comparison between semiautomated ventilation defect percentage calculation and pulmonary function tests. *Investig. Radiol.* 52 (2), 120–127. doi:10.1097/rli.0000000000000322

Eddy, R. L., McIntosh, M. J., Matheson, A. M., McCormack, D. G., Licskai, C., and Parraga, G. (2022). Pulmonary MRI and cluster analysis help identify novel asthma phenotypes. *J. Magnetic Reson. Imaging* 56 (5), 1475–1486. doi:10.1002/jmri.28152

Farrow, C. E., Salome, C. M., Harris, B. E., Bailey, D. L., Bailey, E., Berend, N., et al. (2012). Airway closure on imaging relates to airway hyperresponsiveness and peripheral airway disease in asthma. *J. Appl. Physiology* 113 (6), 958–966. doi:10.1152/japplphysiol.01618.2011

Farrow, C. E., Salome, C. M., Harris, B. E., Bailey, D. L., Berend, N., and King, G. G. (2017). Peripheral ventilation heterogeneity determines the extent of bronchoconstriction in asthma. *J. Appl. Physiology* 123 (5), 1188–1194. doi:10.1152/JAPPLPHYSIOL.00640.2016

Genseke, P., Wetz, C., Wallbaum, T., Kreissl, M. C., Ghazzawi, S., Schreiber, J., et al. (2018). Pre-operative quantification of pulmonary function using hybrid-SPECT/low-dose-CT: A pilot study. *Lung Cancer* 118, 155–160. doi:10.1016/j.lungcan.2018.02.010

He, M., Robertson, S. H., Kaushik, S. S., Freeman, M. S., Virgincar, R. S., Davies, J., et al. (2015). Dose and pulse sequence considerations for hyperpolarized (129) Xe ventilation MRI. *Magn. Reson Imaging* 33 (7), 877–885. doi:10.1016/j.mri.2015.04.005

Hughes, P. J. C., Smith, L., Chan, H. F., Tahir, B. A., Norquay, G., Collier, G. J., et al. (2019). Assessment of the influence of lung inflation state on the quantitative parameters derived from hyperpolarized gas lung ventilation MRI in healthy volunteers. *J. Appl. Physiol.* 126 (1), 183–192. doi:10.1152/japplphysiol.00464.2018

Jögi, J., Ekberg, M., Jonson, B., Bozovic, G., and Bajc, M. (2011). Ventilation/perfusion SPECT in chronic obstructive pulmonary disease: An evaluation by reference to symptoms, spirometric lung function and emphysema, as assessed with HRCT. *Eur. J. Nucl. Med. Mol. Imaging* 38 (7), 1344–1352. doi:10.1007/s00259-011-1757-5

Kim, M., Doganay, O., Matin, T., Povey, T., and Gleeson, F. (2019). Comparison of the thoracic CT-based computational model with hyperpolarized Xenon-129 MRI and SPECT images to assess pulmonary ventilation in COPD patients. *Eur. Respir. J.* 54 (63), OA1931. doi:10.1183/13993003.CONGRESS-2019.OA1931

Kim, W. W., Lee, C. H., Goo, J. M., Park, S. J., Kim, J. H., Park, E. A., et al. (2012). Xenon-enhanced dual-energy CT of patients with asthma: Dynamic ventilation changes after methacholine and salbutamol inhalation. *AJR Am. J. Roentgenol.* 199 (5), 975–981. doi:10.2214/AJR.11.7624

Kirby, M., Svenningsen, S., Owrangi, A., Wheatley, A., Farag, A., Ouriadov, A., et al. (2012). Hyperpolarized 3He and ^{129}Xe MR imaging in healthy volunteers and patients with chronic obstructive pulmonary disease. *Radiology* 265 (2), 600–610. doi:10.1148/radiol.12120485

Kruger, S. J., Nagle, S. K., Couch, M. J., Ohno, Y., Albert, M., and Fain, S. B. (2016). Functional imaging of the lungs with gas agents. *J. Magn. Reson Imaging* 43 (2), 295–315. doi:10.1002/jmri.25002

Lemb, M., Oei, T. H., Eifert, H., and Gunther, B. (1993). Technegas: A study of particle structure, size and distribution. *Eur. J. Nucl. Med.* 20 (7), 576–579. doi:10.1007/BF00176550

Munawar, I., Yaremko, B. P., Craig, J., Oliver, M., Gaede, S., Rodrigues, G., et al. (2010). Intensity modulated radiotherapy of non-small-cell lung cancer incorporating SPECT ventilation imaging. *Med. Phys.* 37 (4), 1863–1872. doi:10.1118/1.3358128

Niedbalski, P. J., Hall, C. S., Castro, M., Eddy, R. L., Rayment, J. H., Svenningsen, S., et al. (2021). Protocols for multi-site trials using hyperpolarized ^{129}Xe MRI for imaging of ventilation, alveolar-airspace size, and gas exchange: A position paper from the ^{129}Xe MRI clinical trial. *Magnetic Reson. Med.* 86 (6), 2966–2986. doi:10.1002/mrm.28985

Ohno, Y., Hanamatsu, S., Obama, Y., Ueda, T., Ikeda, H., Hattori, H., et al. (2022). Overview of MRI for pulmonary functional imaging. *Br. J. Radiol.* 95 (1132), 20201053. doi:10.1259/bjr.20201053

Park, E. A., Goo, J. M., Park, S. J., Lee, H. J., Lee, C. H., Park, C. M., et al. (2010). Chronic obstructive pulmonary disease: Quantitative and visual ventilation pattern analysis at xenon ventilation CT performed by using a dual-energy technique. *Radiology* 256 (3), 985–997. doi:10.1148/radiol.10091502

Roach, P. J., Schembri, G. P., and Bailey, D. L. (2013). V/Q scanning using SPECT and SPECT/CT. *J. Nucl. Med.* 54 (9), 1588–1596. doi:10.2967/jnumed.113.124602

Shammi, U. A., D'Alessandro, M. F., Altes, T., Hersman, F. W., Ruset, I. C., Mugler, J., 3rd, et al. (2022). Comparison of hyperpolarized (3)He and (129)Xe MR imaging in cystic fibrosis patients. *Acad. Radiol.* 29 (2), S82–S90. doi:10.1016/j.acra.2021.01.007

Sharma, M., Wyszkiewicz, P. V., Desaigoudar, V., Guo, F., Capaldi, D. P., and Parraga, G. (2022). Quantification of pulmonary functional MRI: State-of-the-art and emerging image processing methods and measurements. *Phys. Med. Biol.* 67 (22), 22TR01. doi:10.1088/1361-6560/ac9510

Stavngaard, T., Søgaard, L. V., Mortensen, J., Hanson, L. G., Schmiedeskamp, J., Berthelsen, A. K., et al. (2005). Hyperpolarized 3He MRI and 81mKr SPECT in chronic obstructive pulmonary disease. *Eur. J. Nucl. Med. Mol. Imaging* 32 (4), 448–457. doi:10.1007/S00259-004-1691-X

Stewart, N. J., Smith, L. J., Chan, H. F., Eaden, J. A., Rajaram, S., Swift, A. J., et al. (2022). Lung MRI with hyperpolarised gases: Current & future clinical perspectives. *Br. J. Radiol.* 95 (1132), 20210207. doi:10.1259/bjr.20210207

Svenningsen, S., Kirby, M., Starr, D., Leary, D., Wheatley, A., Maksym, G. N., et al. (2013). Hyperpolarized ^{3}He and ^{129}Xe MRI: Differences in asthma before bronchodilation. *J. Magnetic Reson. Imaging* 38 (6), 1521–1530. doi:10.1002/jmri.24111

Svenningsen, S., McIntosh, M., Ouriadov, A., Matheson, A. M., Konyer, N. B., Eddy, R. L., et al. (2021). Reproducibility of hyperpolarized ^{129}Xe MRI ventilation defect percent in severe asthma to evaluate clinical trial feasibility. *Acad. Radiol.* 28 (6), 817–826. doi:10.1016/j.acra.2020.04.025

Yuan, S., Frey, K. A., Gross, M. D., Hayman, J. A., Arenberg, D., Curtis, J. L., et al. (2011). Semiquantification and classification of local pulmonary function by V/Q single photon emission computed tomography in patients with non-small cell lung cancer: Potential indication for radiotherapy planning. *J. Thorac. Oncol.* 6 (1), 71–78. doi:10.1097/jto.0b013e3181f77b40

Frontiers in Physiology

TYPE Mini Review
PUBLISHED 29 June 2023
DOI 10.3389/fphys.2023.1177717

OPEN ACCESS

EDITED BY
Joseph M. Reinhardt,
The University of Iowa, United States

REVIEWED BY
Alysson Roncally Silva Carvalho,
University of Porto, Portugal
Katerina Vaporidi,
University of Crete, Greece

*CORRESPONDENCE
Guido Musch,
guido.musch@umassmed.edu

RECEIVED 01 March 2023
ACCEPTED 30 May 2023
PUBLISHED 29 June 2023

CITATION
Musch G (2023), Molecular imaging of inflammation with PET in acute and ventilator-induced lung injury.
Front. Physiol. 14:1177717.
doi: 10.3389/fphys.2023.1177717

Molecular imaging of inflammation with PET in acute and ventilator-induced lung injury

Guido Musch *

Department of Anesthesiology and Perioperative Medicine, UMass Chan Medical School, Worcester, MA, United States

This review focuses on methods to image acute lung inflammation with Positron Emission Tomography (PET). Four approaches are discussed that differ for biologic function of the PET reporter probe, radiotracer employed, and the specific aspect of the inflammatory response that is targeted. 2-[^{18}F]fluoro-2-deoxy-D-glucose ([^{18}F]FDG) is an enzyme substrate whose uptake is used to measure the metabolic activation of inflammatory cells during acute lung injury in the noncancerous lung. $H_2{}^{15}O$ and radiolabeled plasma proteins are inert molecules with the same physical characteristics as their nonradioactive counterparts and are used to measure edema and vascular permeability. Tagged enzyme or receptor inhibitors are used to probe expression of these targets induced by inflammatory stimuli. Lastly, cell-specific tracers are being developed to differentiate the cell types that contribute to the inflammatory response. Taken together, these methods cast PET imaging as a versatile and quantitative tool to measure inflammation *in vivo* noninvasively during acute and ventilator-induced lung injury.

KEYWORDS

inflammation, positron-emission tomography, ventilator-induced lung injury, acute lung injury, respiratory distress syndrome, isotopes

1 Introduction

Pulmonary inflammation is a hallmark of acute lung injury and its form induced by mechanical ventilation (ventilator-induced lung injury, VILI). Because this inflammation is considered a driver of outcome and hence a target of therapeutic approaches, significant interest has developed around methods to detect, measure, and monitor it *in vivo* noninvasively in the lung as the inflammatory process develops. In this respect, Positron Emission Tomography (PET) has emerged as one of the favorite imaging methods because of its versatility. The possibility to label molecules that participate in the biochemical reactions of inflammatory processes with positron emitters, and follow their fate *in vivo*, noninvasively, and with 3-dimensional resolution without altering their chemical properties has led to an array of PET techniques that target various pathways of the inflammatory process. Not aiming to be an exhaustive review of this topic, the emphasis herein will be on examples of PET imaging methods that leverage different aspects of the inflammatory response.

2 Imaging inflammatory cell metabolic activity with 2-[^{18}F]fluoro-2-deoxy-D-glucose ([^{18}F]FDG)

Substantive experimental and clinical evidence has established PET measurement of [^{18}F]FDG uptake as a method to noninvasively assess activation of inflammatory cells, in particular neutrophils, in the noncancerous lung (Jones et al., 1994; Jones et al., 1997; Chen and Schuster, 2004). In this section, the molecular mechanisms underlying the [^{18}F]FDG signal, and its biologic significance, will be discussed first, followed by findings of studies that employed [^{18}F] FDG to gain insights into the pathophysiology of the acute respiratory distress syndrome (ARDS) and VILI and on the effect of interventions to ameliorate these conditions.

Cells activated by an inflammatory stimulus increase their glucose consumption to satisfy the ensuing energy requirement. Neutrophils do so to an exaggerated extent because they possess few mitochondria and rely primarily on glycolysis to sustain their functional responses (Bao et al., 2014). The low ATP yield of glycolysis implies that activated neutrophils consume much higher quantities of glucose than other cell types. This phenotypic trait can be leveraged by administering the positron emitting glucose analog [^{18}F]FDG, which is taken up by metabolically active cells through the facilitative glucose transporters, particularly Glut-1 and Glut-3 (Wang et al., 2016), and phosphorylated by hexokinase. Studies have shown that deoxyglucose uptake is related to plasma membrane levels of Glut-1 and to hexokinase activity (Haberkorn et al., 1994; Torizuka et al., 1995; Paik et al., 2005a; Paik et al., 2005b; Schuster et al., 2007). [^{18}F]FDG is thus an ideal tracer to measure neutrophil activation because it undergoes the two rate limiting steps of glycolytic metabolism, i.e., transport and phosphorylation (Torizuka et al., 1995; Paik et al., 2005b), on which the energy requirement for all of the activated neutrophil's functions rests. [^{18}F]FDG-6-phosphate, however, cannot proceed further along the glycolytic pathway nor leave the cell. It accumulates intracellularly in proportion to metabolic rate, yielding a signal that can be imaged by PET. Glut-1 translocation from the cytoplasm to the cell surface (Schuster et al., 2007) and increased transporter affinity (Tan et al., 1998) are the main mechanisms of increased deoxyglucose transport into activated neutrophils.

Tracer kinetic models have been developed to measure the rates of glucose transport and phosphorylation with PET (Phelps et al., 1979). Because some assumptions of those models may not be valid in the acutely injured lung, we developed a tracer kinetic model specific for acute lung injury that accounts for [^{18}F]FDG distribution in edematous tissue (Schroeder et al., 2008). This model allows estimation of the extravascular extracellular volume of distribution of [^{18}F]FDG and of the rates of glucose transport (k_1) and phosphorylation (k_3) in acutely injured lungs. Consequently, this model allows noninvasive quantitative assessment of the key molecular steps that control cellular utilization of glucose in a subject with acute lung injury. Using this model we showed that, under conditions of surfactant depletion and endotoxemia, two common causes of acute lung injury, [^{18}F]FDG PET-derived parameters correlated with biologically relevant effectors of inflammation, as the [^{18}F]FDG phosphorylation rate paralleled expression of IL-1β, IL-8, and IL-10, all cytokines implicated in VILI and acute lung injury, and the [^{18}F]FDG volume of distribution increased with the amount of infiltrating neutrophils. (de Prost et al., 2014).

The cellular events and signaling pathways responsible for increased glucose transport and phosphorylation in the activated neutrophil have been investigated *in vitro*. Such studies have shown that the increase in deoxyglucose uptake occurs during leukocyte priming (Tan et al., 1998; Jones et al., 2002a; Paik et al., 2004), for instance by TNF-α (Jones et al., 2002a). This finding supports the use of [^{18}F]FDG to measure neutrophil activation because priming is the first step in neutrophil activation and is critical for neutrophil-mediated tissue injury. Studies *in vitro* have shown that the molecular pathway for increased [^{18}F]FDG uptake involves several protein kinases, such as phosphatidylinositol-3 kinase (Paik et al., 2005a), tyrosine kinase, and protein kinase C (Tan et al., 1998; Paik et al., 2004), which affect the expression or activity of glucose transporters and hexokinase and are implicated in neutrophil priming.

In a unilateral model of VILI, we used PET of [^{18}F]FDG to demonstrate that tidal overdistension and end-expiratory alveolar derecruitment are accompanied by increased [^{18}F]FDG uptake (Musch et al., 2007), which could be significantly reduced by application of positive end-expiratory pressure (PEEP). The increase in [^{18}F]FDG uptake during VILI is largely attributable to neutrophils and, to a lesser extent, other cell populations such as macrophages and type 2 epithelial cells (Musch et al., 2007; Saha et al., 2013). Subsequent studies have employed this technique to demonstrate that, in VILI, the spatial distribution of [^{18}F]FDG uptake is related to that of lung mechanical strain (Retamal et al., 2018) and that an increase in regional pulmonary [^{18}F]FDG uptake is accompanied by overexpression of genes implicated in the pathogenesis of VILI, such as genes that encode for epithelial and endothelial stretch markers and genes involved in specific inflammatory pathways (Wellman et al., 2016; Motta-Ribeiro et al., 2018). The topographical heterogeneity of pulmonary [^{18}F] FDG uptake in VILI is enhanced by infusion of low-dose endotoxin during mechanical ventilation (Costa et al., 2010), a model for clinical sepsis, and reduced by protective ventilation with high PEEP and low tidal volume (de Prost et al., 2013). Specifically, endotoxin is synergistic with mechanical strain as lipopolysaccharide infusion amplified the effect of tidal strain on [^{18}F]FDG phosphorylation rate 3-fold (Wellman et al., 2014). This is consistent with a priming effect of endotoxin on the mechanically ventilated lung, acting as a "first hit" that renders the lung more vulnerable to the inflammatory effect of mechanical ventilation.

Inflammation imaging with PET of [^{18}F]FDG uptake has provided important insights also into the pathophysiology of acute lung injury due to causes other than mechanical ventilation, and of ARDS. In a sheep model of acute cotton smoke inhalation, we demonstrated that inflammatory cell metabolic activation occurs early and precedes impairment of pulmonary gas exchange (Musch et al., 2014). This finding is potentially clinically important because it implies that the therapeutic window for antiinflammatory therapies and application of protective mechanical ventilation might be soon after smoke inhalation and before the clinical picture of ARDS ensues. Chen et al. (Chen and Schuster, 2004) showed that when the acute injury was mainly characterized by alteration of pulmonary vascular permeability and edema, as in the oleic acid model, the increase of [^{18}F]FDG uptake was minor and not statistically significant. In contrast, the rate of [^{18}F]FDG uptake was

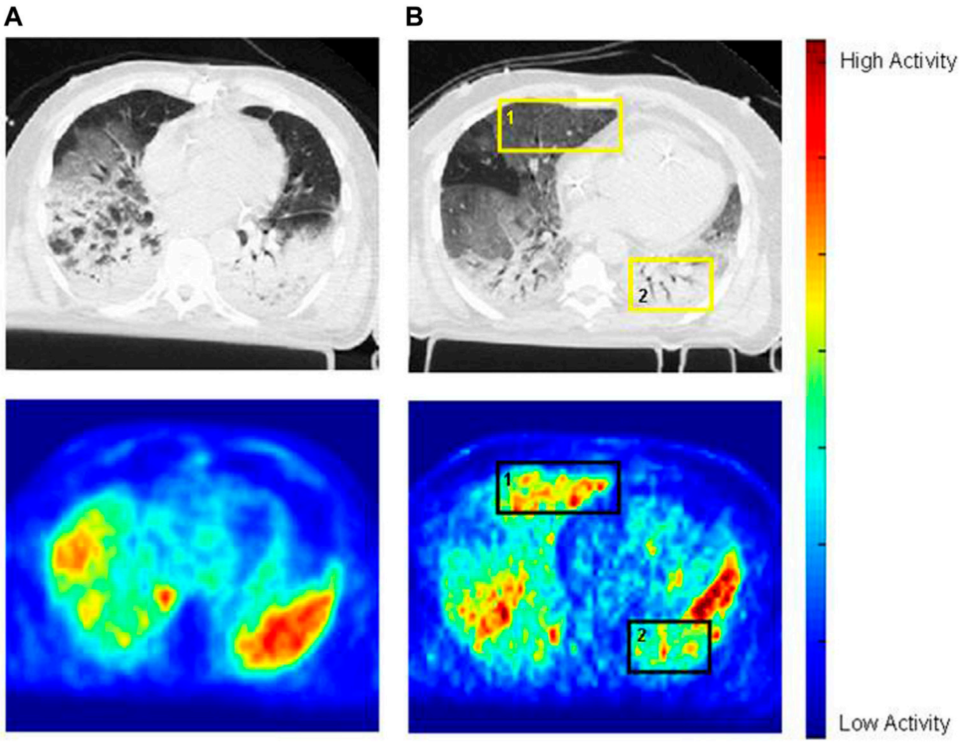

FIGURE 1
Images of cross-registered CT (top row) and [18]F]FDG PET (bottom row) in two mechanically ventilated patients with ARDS. In patient A (images on the left), [18]F]FDG distribution parallels that of the opacities on CT. In patient B (images on the right), [18]F]FDG uptake is higher in normally aerated regions than in dorsal opacified regions (e.g., square 1 *versus* square 2, or ventral half of the left lung *versus* its dorsal half−square 2). Reprinted from Bellani et al. (2009), with permission.

significantly elevated after a low dose infusion of endotoxin, both with and without concomitant oleic acid injury, even in the absence of alveolar neutrophilia. This finding is important because it established the specificity of [^{18}F]FDG PET for measuring neutrophil activity in acute lung injury.

[^{18}F]FDG PET imaging has been applied also to patients with ARDS. An early case report showed markedly increased and diffuse pulmonary [^{18}F]FDG uptake in a patient with ARDS (Jacene et al., 2004). The authors hypothesized that high rates of glucose utilization by the inflammatory cells involved in ARDS pathogenesis were responsible for the [^{18}F]FDG signal. A later study confirmed this finding in a larger cohort of patients and further showed that [^{18}F]FDG uptake was higher than in control subjects even in lung regions with normal density on computed tomography (Bellani et al., 2009). This finding is important because it implies that, in ARDS, also lung regions that appear normal radiographically are inflamed and, consequently, the functionally defined “baby lung” is not necessarily a healthy lung. A subsequent analysis shed further light on the cause of the elevated [^{18}F]FDG uptake in normally aerated lung regions of ARDS patients by reporting a direct correlation between [^{18}F]FDG uptake of these regions and their tidal mechanical strain (Bellani et al., 2011). This finding suggests that the inflammation of the baby lung is, at least in part, related to the strain imposed by mechanical ventilation, i.e., to VILI. This ability to topographically correlate the [^{18}F]FDG signal with regional density and mechanics, afforded by combined PET/CT imaging, can help differentiate when the inflammatory cell metabolic activation is due mainly to the primary insult causing ARDS or to the secondary insult from mechanical ventilation, even though neutrophil activation is a hallmark of both these processes. In this respect, Bellani et al. (Bellani et al., 2009) described distinct patterns of [^{18}F]FDG uptake in patients with ARDS. In some patients, uptake was highest in regions classified as nonaerated on CT, which are likely those most affected by the primary inflammatory process causing ARDS. In these patients, it is reasonable to assume that the [^{18}F]FDG signal primarily reflected neutrophil activation due to the primary insult. In other patients, instead, the [^{18}F]FDG uptake rate was higher in normally or mildly hypo aerated regions, suggesting that inflammatory cell activation in these patients could have been mainly due to the secondary insult from mechanical ventilation, as these are the regions distended by the tidal volume or that potentially undergo injurious cyclic tidal recruitment and derecruitment (Figure 1).

3 Imaging edema and pulmonary vascular permeability

A hallmark of any form of acute lung injury, including VILI and ARDS, is increased pulmonary vascular permeability, leading to interstitial and alveolar edema. One of the first applications of PET to functional lung imaging assessed these pathophysiological processes. That application relies on oxygen-15 labeled water ($H_2{}^{15}O$) as the radiotracer. $H_2{}^{15}O$ has the same physical properties as water. In particular, it diffuses freely across the pulmonary endothelium, so that the tracer rapidly reaches equilibrium with lung tissue. Regional lung water can be calculated by referencing lung tissue activity at equilibrium, measured with PET, to the activity of blood water, measured from blood samples collected during the scan. Regional lung water includes both intravascular (blood) and extravascular lung water. Because the pathophysiological variable of interest is edema, an additional measurement is necessary to parse out extravascular lung water. Intravascular lung water is computed by taking a PET scan after administration of a blood pool compartment label such as carbon monoxide, which binds to hemoglobin with high affinity and can be tagged with positron emitters carbon-11 (^{11}C) or oxygen-15 (^{15}O). Extravascular lung water is then obtained by subtracting intravascular water, measured with an inhalation PET scan of ^{11}CO or $C^{15}O$, from regional water measured with an intravenous infusion scan of $H_2{}^{15}O$ (Schuster et al., 1985; Schuster, 1989).

In acute and ventilator-induced lung injury, edema is a consequence of increased pulmonary vascular permeability. The possibility to label proteins that cross the alveolo-capillary membrane only in pathologic conditions of increased permeability with positron emitters enables PET to detect and measure this pathophysiologic alteration. A specific measure of pulmonary vascular permeability can thus be derived by measuring with PET the transport rate constant(s) (pulmonary transcapillary escape rate, PTCER) of a radiolabeled protein, such as ^{68}Ga-transferrin or ^{11}C-methylalbumin, between the intravascular and extravascular space (Schuster, 1989; Schuster et al., 1998).

Using these techniques, Sandiford et al. (Sandiford et al., 1995) reported that pulmonary vascular permeability, measured in ARDS patients *in vivo* from the PTCER of ^{68}Ga-transferrin, was higher than in normal subjects and, within the ARDS group, they did not find consistent differences in PTCER between ventral and dorsal lung regions. In contrast, they reported that extravascular lung water was significantly higher in dorsal, dependent regions, than in ventral, nondependent ones. These data are consistent with the subsequent findings of the [^{18}F]FDG studies mentioned above and further point to the fact that the functionally defined "baby lung" is not a healthy, normal lung. Instead, the lung in ARDS is globally inflamed even if the resulting increase in lung density may be heterogeneously distributed and edema predominantly dependent because of the effect of gravity.

4 Imaging enzymes and receptors involved in lung inflammation

Recently, PET techniques have been developed to image specific molecular targets involved in inflammation. Inducible nitric oxide synthase (iNOS) is expressed in pulmonary epithelium, increased by pulmonary inflammation, and associated with disease severity in ARDS. Because of the central role of iNOS in inflammation, efforts have been made to develop iNOS inhibitors as pharmaceutical agents, and radiolabeled iNOS inhibitors for probing iNOS expression *in vivo* using PET. One such radiotracer, named ^{18}F-NOS, was tested to detect pulmonary iNOS expression in murine models after intravenous or intratracheal endotoxin administration (Zhou et al., 2009). In that study (Zhou et al., 2009), there was a progressively higher *relative* uptake of ^{18}F-NOS in the lungs of mice pretreated with i.v. endotoxin compared with untreated controls up to 1 hour after administration of the tracer but this differential uptake almost entirely waned by 2 hours, pointing to the ideal kinetics of this tracer to image pulmonary inflammation. These biodistribution results paralleled the pulmonary levels of iNOS assessed by Western blot in the same mice, consistent with iNOS-specific uptake of ^{18}F-NOS, a conclusion confirmed by iNOS blocking studies. MicroPET images obtained over 1 hour in mice who had received intratracheal endotoxin confirmed higher pulmonary uptake of ^{18}F-NOS than in control mice. These animal studies were corroborated by a recent study in humans that showed a ~30% increase in ^{18}F-NOS uptake with PET 16 h after instillation of endotoxin in the right middle bronchus (Huang et al., 2015). This increased uptake was topographically associated with an increase in density on computed tomography of the area of endotoxin instillation and with positivity for iNOS of bronchoalveolar lavage cells recovered from that area and stained immunohistochemically. Taken together, these studies demonstrated the potential of ^{18}F-NOS to image iNOS activity in acute lung inflammation *in vivo*, including in humans.

Peroxisome proliferator-activated receptor gamma (PPARγ) has a role in metabolism and inflammation, and its agonists have been investigated in the treatment of a variety of diseases. PET ligands that bind to PPARγ have been developed to monitor receptor expression over time and potentially identify patients who would most likely benefit from PPARγ directed therapies (Lee et al., 2012).

5 PET imaging of lung macrophages

Although primed and activated neutrophils are the main source of the [^{18}F]FDG signal, other cell types also contribute to the uptake of [^{18}F]FDG. Specifically in relation to acute lung inflammation, Saha et al. (Saha et al., 2013) demonstrated that alveolar macrophages give an appreciable contribution to the [^{18}F]FDG signal both in VILI and in a model of acute lung injury caused by intranasal instillation of endotoxin. Consequently, there is considerable interest in PET tracers that can selectively tag macrophages. A class of these tracers is represented by translocator protein (TSPO) ligands. TSPO is a transmembrane mitochondrial channel overexpressed in macrophages and monocytes in various inflammatory states. Jones et al. (Jones et al., 2002b) showed that PET imaging of the TSPO ligand PK11195 labeled with ^{11}C revealed macrophage accumulation and trafficking in a rabbit model of lung injury induced by endobronchial instillation of silica particles. Radioactive counts from the challenged right upper lobe were elevated compared to control lung regions, and paralleled macrophage accumulation. With time, the signal increased also in regions along the lymphatic drainage path, consistent with macrophage trafficking through lymph ducts. In contrast, neither radioactivity nor macrophage numbers increased in lung regions challenged with endobronchial *S. pneumoniae*, despite marked neutrophilia on histology and demonstration in a prior study (Jones et al., 1994) that the *S. pneumoniae* model was associated with markedly increased [^{18}F]FDG uptake. A subsequent study in humans by the same group (Jones et al., 2003) corroborated the concept that ^{11}C- PK11195 and [^{18}F]FDG mostly target two different cell types, i.e., macrophages and neutrophils, respectively, which are involved to a different extent in asthma *versus* chronic obstructive pulmonary disease (COPD).

More recently, Chen et al. (Chen et al., 2021) reported on a newer TSPO PET ligand with greater affinity for TSPO and specificity for lung macrophages, N-acetyl-N-(2-[^{11}C]methoxybenzyl)-2-phenoxy-5-pyridinamine, which also can be labeled with ^{11}C ([^{11}C]PBR28). [^{11}C]PBR28 uptake increased concomitantly with the development of a M2 macrophage-dominant lung inflammatory response in a Sendai virus infection model. In contrast, [^{11}C]PBR28 uptake did not rise in an endotoxin instillation model characterized by neutrophilic inflammation. This differential uptake of [^{11}C]PBR28 between the two models contrasted with that of [^{18}F]FDG, which increased similarly in both. The increase in [^{11}C]PBR28 uptake, but not [^{18}F]FDG, was attenuated in transgenic mice heterozygous for a mutation that confers macrophage depletion ($Csf1^{wt/opT}$). Lung tissue immunohistochemical staining revealed that TSPO localized predominantly to macrophages rather than neutrophils.

Taken together, these results suggest that TSPO ligands, especially those of the later generation with higher affinity, may yield useful PET tracers to assess the pulmonary macrophage inflammatory response and complement the less specific metabolic information provided by [^{18}F]FDG.

6 Conclusion

Over the past several years, substantial advancements in PET technology, radiochemistry, and molecular biology have enabled development of an array of imaging methods to study inflammation in the acutely injured lung. These methods have yielded fundamental insights into the pathophysiology of VILI and ARDS.

Author contributions

The author confirms being the sole contributor of this work and has approved it for publication.

Funding

The funding for this article was provided by the Department of Anesthesiology and Perioperative Medicine at University of Massachusetts Chan Medical School and NIH R56HL161209.

Conflict of interest

The author declares that the research was conducted in the absence of any commercial or financial relationships that could be construed as a potential conflict of interest.

Publisher's note

References

Bao, Y., Ledderose, C., Seier, T., Graf, A. F., Brix, B., Chong, E., et al. (2014). Mitochondria regulate neutrophil activation by generating ATP for autocrine purinergic signaling. *J. Biol. Chem.* 289 (39), 26794–26803. doi:10.1074/jbc.M114.572495

Bellani, G., Guerra, L., Musch, G., Zanella, A., Patroniti, N., Mauri, T., et al. (2011). Lung regional metabolic activity and gas volume changes induced by tidal ventilation in patients with acute lung injury. *Am. J. Respir. Crit. Care Med.* 183 (9), 1193–1199. doi:10.1164/rccm.201008-1318OC

Bellani, G., Messa, C., Guerra, L., Spagnolli, E., Foti, G., Patroniti, N., et al. (2009). Lungs of patients with acute respiratory distress syndrome show diffuse inflammation in normally aerated regions: A [^{18}F]-fluoro-2-deoxy-D-glucose PET/CT study. *Crit. Care Med.* 37, 2216–2222. doi:10.1097/CCM.0b013e3181aab31f

Chen, D. L., Agapov, E., Wu, K., Engle, J. T., Solingapuram Sai, K. K., Arentson, E., et al. (2021). Selective imaging of lung macrophages using [^{11}C]PBR28-based Positron Emission Tomography. *Mol. Imaging Biol.* 23 (6), 905–913. doi:10.1007/s11307-021-01617-w

Chen, D. L., and Schuster, D. P. (2004). Positron emission tomography with [18F] fluorodeoxyglucose to evaluate neutrophil kinetics during acute lung injury. *Am. J. Physiol. Lung Cell. Mol. Physiol.* 286, L834–L840. doi:10.1152/ajplung.00339.2003

Costa, E. L., Musch, G., Winkler, T., Schroeder, T., Harris, R. S., Jones, H. A., et al. (2010). Mild endotoxemia during mechanical ventilation produces spatially heterogeneous pulmonary neutrophilic inflammation in sheep. *Anesthesiology* 112 (3), 658–669. doi:10.1097/ALN.0b013e3181cbd1d4

de Prost, N., Costa, E. L., Wellman, T., Musch, G., Tucci, M. R., Winkler, T., et al. (2013). Effects of ventilation strategy on distribution of lung inflammatory cell activity. *Crit. Care* 17 (4), R175. doi:10.1186/cc12854

de Prost, N., Feng, Y., Wellman, T., Tucci, M. R., Costa, E. L., Musch, G., et al. (2014). 18F-FDG kinetics parameters depend on the mechanism of injury in early experimental acute respiratory distress syndrome. *J. Nucl. Med.* 55 (11), 1871–1877. doi:10.2967/jnumed.114.140962

Haberkorn, U., Ziegler, S. I., Oberdorfer, F., Trojan, H., Haag, D., PeschkeBerger, P. M. R., et al. (1994). FDG uptake, tumor proliferation and expression of glycolysis associated genes in animal tumor models. *Nucl. Med. Biol.* 21, 827–834. doi:10.1016/0969-8051(94)90162-7

Huang, H. J., Isakow, W., Byers, D. E., Engle, J. T., Griffin, E. A., Kemp, D., et al. (2015). Imaging pulmonary inducible nitric oxide synthase expression with PET. *J. Nucl. Med.* 56 (1), 76–81. doi:10.2967/jnumed.114.146381

Jacene, H. A., Cohade, C., and Wahl, R. L. (2004). F-18 FDG PET/CT in acute respiratory distress syndrome: A case report. *Clin. Nucl. Med.* 29 (12), 786–788. doi:10.1097/00003072-200412000-00002

Jones, H. A., Cadwallader, K. A., White, J. F., Uddin, M., Peters, A. M., and Chilvers, E. R. (2002). Dissociation between respiratory burst activity and deoxyglucose uptake in human neutrophil granulocytes: Implications for interpretation of ^{18}F-FDG PET images. *J. Nucl. Med.* 43, 652–657.

Jones, H. A., Clark, R. J., Rhodes, C. G., Schofield, J. B., Krausz, T., and Haslett, C. (1994). *In vivo* measurement of neutrophil activity in experimental lung inflammation. *Am. J. Respir. Crit. Care Med.* 149, 1635–1639. doi:10.1164/ajrccm.149.6.7516252

Jones, H. A., Marino, P. S., Shakur, B. H., and Morrell, N. W. (2003). *In vivo* assessment of lung inflammatory cell activity in patients with COPD and asthma. *Eur. Respir. J.* 21 (4), 567–573. doi:10.1183/09031936.03.00048502

Jones, H. A., Sriskandan, S., Peters, A. M., Pride, N. B., Krausz, T., Boobis, A. R., et al. (1997). Dissociation of neutrophil emigration and metabolic activity in lobar pneumonia and bronchiectasis. *Eur. Respir. J.* 10, 795–803. doi:10.1183/09031936.97.10040795

Jones, H. A., Valind, S. O., Clark, I. C., Bolden, G. E., Krausz, T., Schofield, J. B., et al. (2002). Kinetics of lung macrophages monitored *in vivo* following particulate challenge in rabbits. *Toxicol. Appl. Pharmacol.* 183 (1), 46–54. doi:10.1006/taap.2002.9462

Lee, H., Chen, D. L., Rothfuss, J. M., Welch, M. J., Gropler, R. J., and Mach, R. H. (2012). Synthesis and evaluation of ^{18}F-labeled PPARγ antagonists. *Nucl. Med. Biol.* 39 (1), 77–87. doi:10.1016/j.nucmedbio.2011.07.002

Motta-Ribeiro, G. C., Hashimoto, S., Winkler, T., Baron, R. M., Grogg, K., Paula, L. F. S. C., et al. (2018). Deterioration of regional lung strain and inflammation during early lung injury. *Am. J. Respir. Crit. Care Med.* 198 (7), 891–902. doi:10.1164/rccm.201710-2038OC

Musch, G., Venegas, J. G., Bellani, G., Winkler, T., Schroeder, T., Petersen, B., et al. (2007). Regional gas exchange and cellular metabolic activity in ventilator-induced lung injury. *Anesthesiology* 106 (4), 723–735. doi:10.1097/01.anes.0000264748.86145.ac

Musch, G., Winkler, T., Harris, R. S., Vidal Melo, M. F., Wellman, T. J., de Prost, N., et al. (2014). Lung [^{18}F]fluorodeoxyglucose uptake and ventilation-perfusion mismatch in the early stage of experimental acute smoke inhalation. *Anesthesiology* 120 (3), 683–693. doi:10.1097/01.anes.0000435742.04859.e8

Paik, J. Y., Ko, B. H., Choe, Y. S., Choi, Y., Lee, K. H., and Kim, B. T. (2005). PMA-enhanced neutrophil [18F]FDG uptake is independent of integrin occupancy but requires PI3K activity. *Nucl. Med. Biol.* 32, 561–566. doi:10.1016/j.nucmedbio.2005.04.016

Paik, J. Y., Lee, K. H., Choe, Y. S., Choi, Y., and Kim, B. T. (2004). Augmented 18F-FDG uptake in activated monocytes occurs during the priming process and involves tyrosine kinases and protein kinase C. *J. Nucl. Med.* 45, 124–128.

Paik, J. Y., Lee, K. H., Ko, B. H., Choe, Y. S., Choi, Y., and Kim, B. T. (2005). Nitric oxide stimulates 18F-FDG uptake in human endothelial cells through increased hexokinase activity and GLUT1 expression. *J. Nucl. Med.* 46, 365–370.

Phelps, M. E., Huang, S. C., Hoffman, E. J., Selin, C., Sokoloff, L., and Kuhl, D. E. (1979). Tomographic measurement of local cerebral glucose metabolic rate in humans with (F-18)2-fluoro-2-deoxy-D-glucose: Validation of method. *Ann. Neurol.* 6, 371–388. doi:10.1002/ana.410060502

Retamal, J., Hurtado, D., Villarroel, N., Bruhn, A., Bugedo, G., Amato, M. B. P., et al. (2018). Does regional lung strain correlate with regional inflammation in acute respiratory distress syndrome during nonprotective ventilation? An experimental porcine study. *Crit. Care Med.* 46 (6), e591–e599. doi:10.1097/CCM.0000000000003072

Saha, D., Takahashi, K., de Prost, N., Winkler, T., Pinilla-Vera, M., Baron, R. M., et al. (2013). Micro-autoradiographic assessment of cell types contributing to 2-deoxy-2-[18F]fluoro-D-glucose uptake during ventilator-induced and endotoxemic lung injury. *Mol. Imaging Biol.* 15 (1), 19–27. doi:10.1007/s11307-012-0575-x

Sandiford, P., Province, M. A., and Schuster, D. P. (1995). Distribution of regional density and vascular permeability in the adult respiratory distress syndrome. *Am. J. Respir. Crit. Care Med.* 151, 737–742. doi:10.1164/ajrccm.151.3.7881664

Schroeder, T., Vidal Melo, M. F., Musch, G., Harris, R. S., Venegas, J. G., and Winkler, T. (2008). Modeling pulmonary kinetics of 2-deoxy-2-[^{18}F]fluoro-D-glucose during acute lung injury. *Acad. Radiol.* 15, 763–775. doi:10.1016/j.acra.2007.12.016

Schuster, D. P., Brody, S. L., Zhou, Z., Bernstein, M., Arch, R., Link, D., et al. (2007). Regulation of lipopolysaccharide-induced increases in neutrophil glucose uptake. *Am. J. Physiol. Lung Cell. Mol. Physiol.* 292, L845–L851. doi:10.1152/ajplung.00350.2006

Schuster, D. P., Markham, J., and Welch, M. J. (1998). Positron emission tomography measurements of pulmonary vascular permeability with ^{68}Ga-transferrin or ^{11}C-methylalbumin. *Crit. Care Med.* 26, 518–525. doi:10.1097/00003246-199803000-00026

Schuster, D. P., Mintun, M. A., Green, M. A., and Ter-Pogossian, M. M. (1985). Regional lung water and hematocrit determined by positron emission tomography. *J. Appl. Physiol.* 59 (3), 860–868. doi:10.1152/jappl.1985.59.3.860

Schuster, D. P. (1989). Positron emission tomography: Theory and its application to the study of lung disease. *Am. Rev. Respir. Dis.* 139, 818–840. doi:10.1164/ajrccm/139.3.818

Tan, A. S., Ahmed, N., and Berridge, M. V. (1998). Acute regulation of glucose transport after activation of human peripheral blood neutrophils by phorbol myristate acetate, fMLP, and granulocyte-macrophage colony-stimulating factor. *Blood* 91, 649–655. doi:10.1182/blood.v91.2.649

Torizuka, T., Tamaki, N., Inokuma, T., Magata, Y., Sasayama, S., Yonekura, Y., et al. (1995). *In vivo* assessment of glucose metabolism in hepatocellular carcinoma with FDG-PET. *J. Nucl. Med.* 36, 1811–1817.

Wang, Z. G., Yu, M. M., Han, Y., Wu, F. Y., Yang, G. J., Li, D. C., et al. (2016). Correlation of Glut-1 and Glut-3 expression with F-18 FDG uptake in pulmonary inflammatory lesions. *Med. Baltim.* 95 (48), e5462. doi:10.1097/MD.0000000000005462

Wellman, T. J., de Prost, N., Tucci, M., Winkler, T., Baron, R. M., Filipczak, P., et al. (2016). Lung metabolic activation as an early biomarker of Acute Respiratory Distress Syndrome and local gene expression heterogeneity. *Anesthesiology* 125 (5), 992–1004. doi:10.1097/ALN.0000000000001334

Wellman, T. J., Winkler, T., Costa, E. L., Musch, G., Harris, R. S., Zheng, H., et al. (2014). Effect of local tidal lung strain on inflammation in normal and lipopolysaccharide-exposed sheep. *Crit. Care Med.* 42 (7), e491–e500. doi:10.1097/CCM.0000000000000346

Zhou, D., Lee, H., Rothfuss, J. M., Chen, D. L., Ponde, D. E., Welch, M. J., et al. (2009). Design and synthesis of 2-amino-4-methylpyridine analogues as inhibitors for inducible nitric oxide synthase and *in vivo* evaluation of [18F]6-(2-fluoropropyl)-4-methyl-pyridin-2-amine as a potential PET tracer for inducible nitric oxide synthase. *J. Med. Chem.* 52, 2443–2453. doi:10.1021/jm801556h

frontiers | Frontiers in Physiology

TYPE Original Research
PUBLISHED 01 August 2023
DOI 10.3389/fphys.2023.1178339

OPEN ACCESS

EDITED BY
Sam Bayat,
Université Grenoble Alpes, France

REVIEWED BY
Sarah Svenningsen,
McMaster University, Canada
Sanghun Choi,
Kyungpook National University, Republic of Korea
Rui Carlos Sá,
University of California, San Diego, United States

*CORRESPONDENCE
Sean B. Fain,
✉ sean-fain@uiowa.edu

RECEIVED 02 March 2023
ACCEPTED 17 July 2023
PUBLISHED 01 August 2023

CITATION
Carey KJ, Hotvedt P, Mummy DG, Lee KE, Denlinger LC, Schiebler ML, Sorkness RL, Jarjour NN, Hatt CR, Galban CJ and Fain SB (2023), Comparison of hyperpolarized ^{3}He-MRI, CT based parametric response mapping, and mucus scores in asthmatics.
Front. Physiol. 14:1178339.
doi: 10.3389/fphys.2023.1178339

Comparison of hyperpolarized ^{3}He-MRI, CT based parametric response mapping, and mucus scores in asthmatics

Katherine J. Carey[1,2,3], Peter Hotvedt[4], David G. Mummy[5,6], Kristine E. Lee[7], Loren C. Denlinger[8], Mark L. Schiebler[2], Ronald L. Sorkness[9], Nizar N. Jarjour[8], Charles R. Hatt[3,10], Craig J. Galban[10] and Sean B. Fain[11]*

[1]Department of Medical Physics, University of Wisconsin—Madison, Madison, WI, United States, [2]Department of Radiology, University of Wisconsin—Madison, Madison, WI, United States, [3]Imbio LLC, Minneapolis, MN, United States, [4]Department of Nuclear Engineering, University of Michigan—Ann Arbor, Ann Arbor, MI, United States, [5]Center for In Vivo Microscopy, Department of Radiology, Duke University, Durham, NC, United States, [6]Center for In Vivo Microscopy, Duke University, Durham, NC, United States, [7]Department of Biostatistics, University of Wisconsin—Madison, Madison, WI, United States, [8]Division of Allergy, Pulmonary, and Critical Care Medicine, University of Wisconsin—Madison, Madison, WI, United States, [9]School of Pharmacy, University of Wisconsin—Madison, Madison, WI, United States, [10]Department of Radiology, University of Michigan, Ann Arbor, MI, United States, [11]Department of Radiology, University of Iowa, Iowa City, IA, United States

Purpose: The purpose of this study was to anatomically correlate ventilation defects with regions of air trapping by whole lung, lung lobe, and airway segment in the context of airway mucus plugging in asthma.

Methods: A total of 34 asthmatics [13M:21F, 13 mild/moderate, median age (range) of 49.5 (36.8—53.3) years and 21 severe, 56.1 (47.1—62.6) years] and 4 healthy subjects [1M:3F, 38.5 (26.6—52.2) years] underwent HP ^{3}He MRI and CT imaging. HP ^{3}He MRI was assessed for ventilation defects using a semi-automated k-means clustering algorithm. Inspiratory and expiratory CTs were analyzed using parametric response mapping (PRM) to quantify markers of emphysema and functional small airways disease (fSAD). Segmental and lobar lung masks were obtained from CT and registered to HP ^{3}He MRI in order to localize ventilation defect percent (VDP), at the lobar and segmental level, to regions of fSAD and mucus plugging. Spearman's correlation was utilized to compare biomarkers on a global and lobar level, and a multivariate analysis was conducted to predict segmental fSAD given segmental VDP (sVDP) and mucus score as variables in order to further understand the functional relationships between regional measures of obstruction.

Results: On a global level, fSAD was correlated with whole lung VDP ($r = 0.65$, $p < 0.001$), mucus score ($r = 0.55$, $p < 0.01$), and moderately correlated ($-0.60 \le r \le -0.56$, $p < 0.001$) to percent predicted (%p) FEV1, FEF25-75 and FEV1/FVC, and more weakly correlated to FVC%p ($-0.38 \le r \le -0.35$, $p < 0.001$) as expected from

---

Abbreviations: %P, Percent predicted; BD, Bronchodilator; BMI, Body mass index; COPD, Chronic obstructive pulmonary disease; CT, Computed Tomography; FEV_1, Forced expiratory volume in one second; FRC, Functional residual capacity; fSAD, Functional small airways disease; FVC, Forced vital capacity; HP ^{3}He MRI, Hyperpolarized helium-3 magnetic resonance imaging; PRM, Parametric Response Mapping; sVDP, segmental VDP; VDP, Ventilation defect percent.

previous work. On a regional level, lobar VDP, mucus scores, and fSAD were also moderately correlated (r from 0.45–0.66, $p < 0.01$). For segmental colocalization, the model of best fit was a piecewise quadratic model, which suggests that sVDP may be increasing due to local airway obstruction that does not manifest as fSAD until more extensive disease is present. sVDP was more sensitive to the presence of a mucus plugs overall, but the prediction of fSAD using multivariate regression showed an interaction in the presence of a mucus plugs when sVDP was between 4% and 10% ($p < 0.001$).

Conclusion: This multi-modality study in asthma confirmed that areas of ventilation defects are spatially correlated with air trapping at the level of the airway segment and suggests VDP and fSAD are sensitive to specific sources of airway obstruction in asthma, including mucus plugs.

KEYWORDS

asthma, MRI, CT, gas trapping, hyperpolarized He-3, parametric response mapping (PRM), ventilation

1 Introduction

Severe asthma exhibits considerable heterogeneity both across patients and within the lungs of an individual patient. Ventilation heterogeneity, or the non-uniform distribution of inspired gas within the lungs is a feature of asthma revealed by ventilation defects observed on HP gas MRI (Downie et al., 2007; Teague et al., 2014). Areas of ventilation defects have previously been shown to be associated with mucus plugging of the central airway as visualized on CT (Svenningsen et al., 2019; Mummy et al., 2022), areas of low density lung parenchyma on CT, thought to represent regions of air trapping (Fain et al., 2008), and local airway wall thickening presumably due to remodeling (Svenningsen et al., 2014). The ventilation defect percent, or VDP, has been established as a marker of asthma instability (Mummy et al., 2020). VDP has been extended to a regional measure using deformable registration to CT lobar and segmental structures, i.e., segmental VDP (sVDP), to guide bronchial ablation therapy (Thomen et al., 2015) and to better quantify regional association of VDP and mucus plugging (Mummy et al., 2022). However, the etiology of ventilation defects and air trapping in asthma are still under investigation.

Parametric response mapping (PRM) is a technique used to classify lung tissue based on densitometry at both inspiration and expiration (Galban et al., 2012) with the advantage of isolating inspiratory, i.e., emphysema, from expiratory low density lung parenchyma. The percent of low density lung parenchyma at expiratory lung volume from PRM corresponds to the functional small airways disease (fSAD) and has been shown to be associated with future spirometry decline in COPD (Bhatt et al., 2016) and asthma (Krings et al., 2021). fSAD is identical to air trapping measured using the −856 HU threshold (Lynch and Al-Qaisi, 2013) in asthma since emphysema is not a major component of the measurement.

The regional overlap of ventilation defects with air trapping is expected from previous work (Fain et al., 2008), but the anatomic co-localization at the lobar and airway segment level has not been directly studied. New measures of regional obstruction, including sVDP and mucus score, can provide anatomically precise co-localization of obstructive measures. This makes it possible to test spatial associations of ventilation defects with air trapping and their interaction with mucus plugging to gain insights into their functional significance in asthma. Here, we evaluate global and regional correlations between VDP and sVDP on HP ^{3}He MRI with mucus plugging and fSAD on quantitative CT after administration of four puffs of albuterol, a β-agonist bronchodilator (BD). The comparisons at the airway segment level in this work are the first quantitative co-localization of small airways and ventilation markers.

2 Materials and methods

2.1 Study population

Our study population was drawn from the National Heart, Lung, and Blood Institute (NHLBI) Severe Asthma Research Program III (SARP3) population (Teague et al., 2018) recruited and imaged between 2012 and 2016. The study was compliant with the Health Insurance Portability and Accountability Act (HIPAA) and approved by the Institutional Review Board (IRB). Written informed consent was obtained from all subjects. The population was divided into mild/moderate and severe asthma groups as defined by the SARP criteria (Jarjour et al., 2012). The HP ^{3}He MRI studies were conducted under Food and Drug Administration (FDA) investigational new drug (IND) protocol #064867. An overview of the study population and procedures is shown in Table 1.

CT, proton MRI, HP ^{3}He MRI, and spirometry were all acquired on the same day. To mitigate the effects of airway hyperresponsiveness, all imaging and spirometry were acquired after administration of four puffs of albuterol, a β-agonist BD. Percent Predicted (PP) values for forced expiratory volume in one second (FEV_1), forced vital capacity (FVC), and FEV_1/FVC were generated using the Global Lung Function Initiative reference values (Krings et al., 2021).

2.2 Imaging methods

Volumetric multidetector CT (MDCT) was acquired post-BD at both total lung capacity (TLC) and functional residual capacity

TABLE 1 Study population and image processing steps with number and percent of total participants at each stage. All imaging is post-bronchodilator. Percentages in the Healthy and Asthmatics columns are relative to the starting population; percentages in the Severe column are relative to the corresponding population at that stage.

Image acquisition and processing stages	Healthy N (%)	Total asthmatics (severe + moderate) N (%)	Severe N (%)
1. Total SARPIII asthmatic population at UW-Madison	5 (100%)	100 (100%)	62 (62.0%)
2. Subjects with HP ^{3}He MRI	5 (100%)	78 (78%)	48 (61.5%)
3. With inspiratory and expiratory CT	4 (80%)	34 (34%)	21 (61.7%)
4. With scored segmental mucus plugs	4 (80%)	34 (30%)	21 (61.7%)

(FRC) each during a breath hold of approximately 4 s using a GE Light Speed CT scanner with 64 detectors (0.625 mm^2 voxel size in-plane, 0.5 mm slice thickness). Images were reconstructed using a standard kernel. Specific acquisition parameters are presented in Supplementary Table S1.

MRI was acquired using a 1.5T Signa HDx GE scanner (GE Healthcare, Milwaukee, WI) with either a flexible (IGC Medical Advances, Milwaukee, WI) or a rigid-body (Rapid Biomedical, Columbus, OH) single-channel volume coil, depending on patient size. Both coils were tuned to operate at the resonant frequency of ^{3}He and decoupled from the body RF coil so that proton MRI and HP ^{3}He MRI could be acquired consecutively without moving the subject during matched breath-hold inflation volumes. The ^{3}He studies in this work were conducted using Polarean IGI.9600 polarizer (Polarean Imaging plc, Durham, NC) and using the SEOP method described previously (Lynch and Al-Qaisi, 2013).

A 4.5-mM dose of HP ^{3}He mixed with N_2 normalized to 14% of the subject's predicted total lung capacity (TLC) was prepared in a Tedlar™ bag (Jensen Inert Products, Coral Springs, FL) purged of oxygen to slow T1 relaxation. The subject was positioned supine in the scanner and inhaled the gas dose post-bronchodilator from functional residual capacity (FRC) through a short plastic tube attached to the bag. Subjects were instructed to hold their breath through a 16–20 s acquisition, and blood oxygen saturation was monitored continuously using a pulse oximeter to ensure safety during and after the anoxic breath-hold. Proton MRI was acquired to match volume and slice location after inhalation to an identical lung inflation volume. Specific MRI parameters are summarized in Supplementary Table S2.

2.3 Image analysis

2.3.1 MRI analysis

Ventilation defects were classified on HP ^{3}He MRI using a semi-automated algorithm to calculate whole lung VDP (Zha et al., 2016). Proton MRI was registered to HP ^{3}He MRI using a 3D rigid registration algorithm implemented using ANTs (http://stnava.github.io/ANTs/). The lung boundary was segmented on HP ^{3}He MRI with reference to the proton MRI. The whole lung VDP was then identified as a percentage of total lung volume using an adaptive k-means classifier (Zha et al., 2016). Adaptive k-means is similar to standard k-means except that it conducts two rounds of clustering. The first identifies the lowest signal intensities, and the second reclassifies the lowest cluster from the first round to identify the fully obstructed subset. We referenced the performance of this method to radiologist observers who manually identified defects and then tuned the threshold of the reclassification of the low signal voxels to match the manual result. See (Zha et al., 2016; He et al., 2019) for more details.

2.3.2 CT analysis

PRM analysis was applied to paired inspiratory and expiratory CT scans as previously described (Galban et al., 2012). Briefly, inspiratory CT was deformably registered to expiratory CT and voxel-wise changes in Hounsfield unit (HU) values of lung density were used to determine areas of normal lung parenchyma, non-emphysematous air trapping referred to as functional small airway disease (fSAD), emphysema (Emph), and parenchymal disease. Inspiratory CT images were processed through commercial package (VIDA Diagnostics, Coralville, IA) to generate a segmental anatomical mask. PRM percentages by bronchopulmonary lobe and segment (lobar and segmental PRM, respectively) were determined by applying the CT segmental mask to the PRM maps and calculating percent within the anatomical volume.

Mucus plug scoring was performed on CT by expert radiologists (B.M.E., D.S.G., J.D.N.,S.K.N., and M.L.S.) as part of a multisite effort within the SARP3 study, using the system developed by Dunican et al. (2018). Each individual bronchopulmonary segment was scored based on input from two readers and classified as having a mucus plug when at least one of the two readers scored a plug as present.

2.4 Image registration

As summarized in Figure 1, the CT lung boundary and segmental anatomical masks were generated using a commercial package (VIDA, Coralville, IA). To align to 3He MRI, the masks were then deformably registered to the anatomical proton MRI mask using the ANTs software package (http://stnava.github.io/ANTs/), and the resulting transformation was applied to the original CT images, thereby registering the segmental mask to the HP ^{3}He MRI. VDP by individual bronchopulmonary segment (sVDP) were determined using the registered CT segmental mask registered to the whole lung ventilation defect mask, a method based on the technique described by *Thomen et al* (Thomen et al., 2015). The segmental VDP (sVDP) was then compared to the corresponding segmental airway fSAD from the parametric response map of the CT scan at the expiratory (FRC) lung volume. Note that the PRM map is

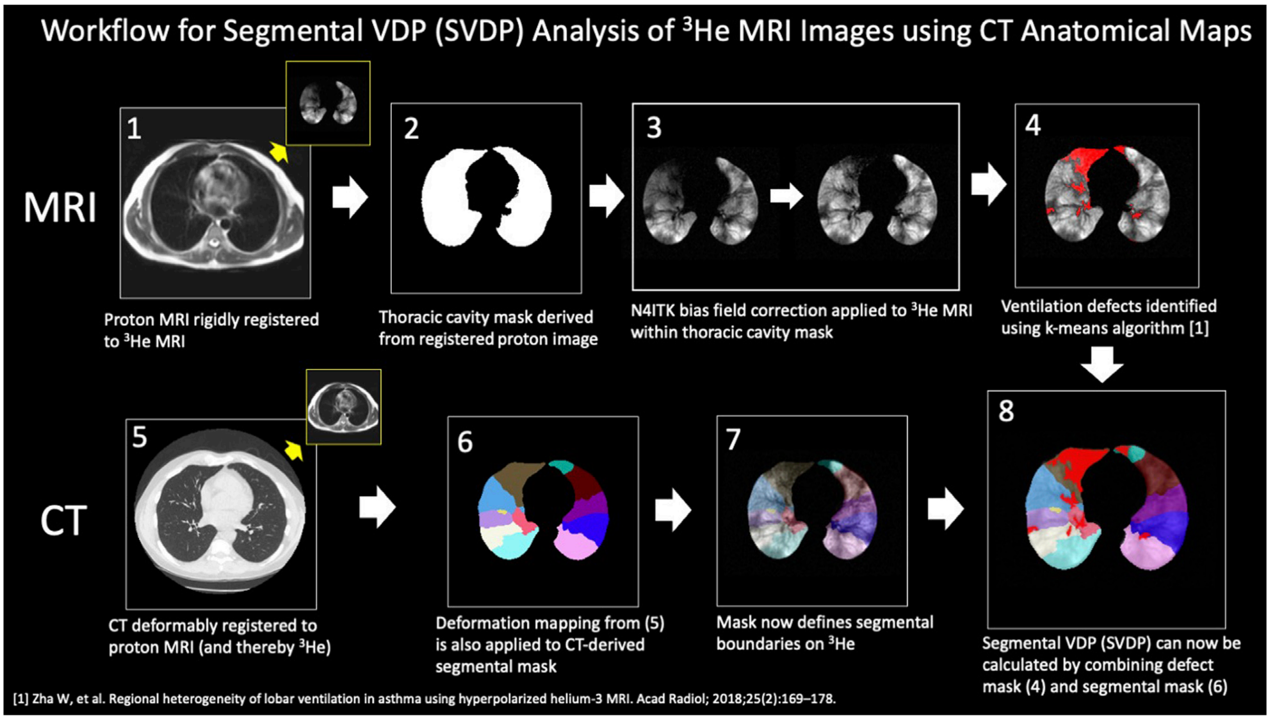

FIGURE 1
Steps in the analysis workflow to align segmental mask from CT to the ^{3}He MRI ventilation images. The steps are as described in the body of the figure. The segmental VDP (sVDP) was then compared to the corresponding segmental airway fSAD from the parametric response map of the CT scan at the expiratory (FRC) lung volume. Note that the PRM map is inherently registered to CT and so can be readily compared by airway segment with ^{3}He MRI after these analysis steps. Modified from Mummy et al. (2022). Used with permission.

inherently registered to CT and so can be readily compared by airway segment.

2.5 Statistical methods

Correlations between VDP, mucus plugging, and PRM measures on a whole lung and lobar level were calculated using the Spearman rank correlation. To further assess the spatial relationship between VDP, PRM_{fSAD}, and mucus plugs, logarithmic values of segmental VDP and PRM_{fSAD} were used to build a multivariate linear mixed model to best compare relationships accounting for the different lung regions. Piecewise linear mixed models were fit to allow for separate estimation of the effects when sVDP = 0. When sVDP is greater than 0, we evaluated curvilinear models and found the quadratic model provided the best fit. The best (most parsimonious) model was selected based on the Akaike Information Criterion (AIC) and Likelihood Ratio tests (for nested models). Tests for interactions between sVDP and segment region were significant for the intercept but not the quadratic form. Similarly, interactions with mucus plugs were significant for intercept shifts but not for the quadratic form. A mixed effects heterogenous compound symmetry covariance structure was used (for expected symmetry between left and right lung segments). A *p*-value of 0.05 was used for the threshold of statistical significance. Whole lung and lobar statistical comparisons and segmental modeling were completed by the statistician on the project (K.L.).

3 Results

3.1 Study population

The study population consisted of 38 participants, including 4 healthy non-asthmatics, with 13 participants classified as having mild/moderate asthmatics and 21 as having severe asthma per the SARP3 criteria (Dunican et al., 2018). Population statistics are represented in Table 2. There were significant differences between Severe and Mild/Moderate Asthmatics with respect to BMI, FEV1 PP, FVC PP and VDP. By contrast, there were no significant differences between Severe and Mild/Moderate Asthma for fSAD, Emph, or Mucus Score. Of the 34 asthma patients, nine had mucus plugs. Those nine subjects had 80 segments with mucus plugs (about 14% of all segments had a mucus plug).

3.2 Global analysis

Confirming previous results, whole lung VDP and fSAD correlated with each other (Supplementary Figure S1), spirometry and mucus score (Supplementary Table S3). Qualitatively, larger

TABLE 2 Population statistics split by asthma severity, and all subjects combined. Quantitative measures are presented as median [1st quartile—3rd quartile]. Whole lung mucus score presented is the sum of all segmental mucus scores. Measures are acquired after administration of four puffs of bronchodilator. All statistics were calculated using the Wilcoxon Rank Sum test with a significance threshold of $p < 0.05$. PP, percent predicted.

	Healthy	Mild/Moderate asthmatics	Severe asthmatics	All
N	4	13	21	38
Gender	1M:3F	5 M: 8F	8M: 13F	14M:24F
Age (years)	38.5 [26.6—52.2]	49.5 [36.8—53.3]	56.1 [47.1—62.6]	51.2 [45.6—61.0]
High Dose ICS	N/A	3	21	24
Daily OCS Dependent (Dose)	N/A	0	3 (4, 7, 8 mg)	3
Monoclonal Rx	N/A	1	4	5
BMI	25.4 ^ [24.0–27.0]	27.7 † [24.7—29.0]	32.4 ^† [282—34.5]	29.0 [26.3—34.1]
FEV1 PP	111 ^ [106—166]	87.8† [83.0—94.6]	77.8% ^† [69.1—97.7]	86.5% [75.4—105]
FVC PP	109 ^ [101—118]	101 † [86.6—109]	86.7 ^† [82.9—97.2]	93.6% [84.8—105]
FEV1/FVC PP	102 ^ [99.0—104]	96.2 [89.1—99.1]	91.1 ^ [82.3—98.5]	96.1% [85.5—99.0]
FEF25-75 PP	118 *^ [113—121]	79.5* [61.8—95.2]	55.8 ^ [38.7—90.8]	78.0 [51.1—105]
VDP	0.275% *^ [0.0750—0.629]	2.51% *† [1.17—4.30]	6.18% ^† [3.40—11.4]	3.43% [2.05—6.97]
fSAD	0.122% [0.0554–1.55]	0.620% [0.406—3.86]	1.36% [0.481—5.77]	1.19% [0.280—5.18]
Emph	0.0571% [0.0447—0.0816]	0.0875% [0.0613—0.124]	0.676% [0.0409—0.154]	0.0673% [0.0472—0.135]
Whole lung Mucus Score	0.0 [0.0—0.0]	0.0 [0.0—0.25]	0.0 [0.0—4.0]	0.0 [0.0—1.6]

*Significantly different between Healthy and Mild/Moderate Asthmatics.
^Significantly different between Healthy and Severe Asthmatics.
†Significantly Different between Mild/Moderate and Severe Asthmatics.

TABLE 3 Spearman correlation coefficients by lobe for lobar fSAD compared to lobar VDP (left). Spearman correlation coefficients by lobe for lobar VDP and fSAD when compared to lobar mucus score (right). LUL, left upper lobe; LLL, left lower lobe; RUL, right upper lobe; RML, right middle lobe; RLL, right lower lobe. PP, Percent Predicted. Significance Key: *$p < 0.05$, **$p < 0.01$, ***$p < 0.001$.

	VDP	Lobar mucus score	
Lobe	fSAD	fSAD	VDP
LUL	0.59 ***	0.38 **	0.54 **
LLL	0.66 ***	0.47 **	0.50 **
RUL	0.52 **	0.44 *	0.67 ***
RML	0.51 **	0.47 **	0.62 ***
RLL	0.45 **	0.30	0.57 **

areas of ventilation defect most commonly overlapped with areas of fSAD (Figure 2) but generally showed greater extent than fSAD (Figures 3A, B). More rarely, fSAD had greater extent, and in some participants, did not correspond to any local ventilation defect regions (Figures 3C, D).

3.3 Lobar analysis

Regional analysis comparing the extent of functional CT and MRI measures for the same lung lobe across all 38 participants (Table 3) showed that fSAD significantly correlated with lobar VDP in every lung lobe (r from 0.45–0.66, $p < 0.01$). Additionally, VDP correlated with mucus score in every lung lobe (r from 0.50–0.67, $p < 0.01$), while fSAD correlated with mucus score in 4 lobes ($r = 0.38–0.47$, $p < 0.05$) with the exception being the right lower lobe as shown in Table 3. A scatterplot comparing lobar fSAD and lobar VDP is shown in Figure 4.

3.4 Segmental analysis

The model of best fit for comparing segmental fSAD as a function of sVDP was a piecewise quadratic model with an interaction with the presence of mucus plugs (Figure 5A) and separate intercepts for each airway segment. The expected fSAD when sVDP values are at or near zero (the intercept) varies across segments (Figure 5B). Measures of fSAD were largely constant or modestly positive linear with increasing moderate sVDP values, but the dependence increased markedly for higher VDPs, typically starting at or near sVDP >4% after which segmental fSAD increased with sVDP at a growing rate. Details on the statistical model are in Appendix B. The three pieces of the model (VDP = 0, VDP > 0, and presence of mucus plugs) are all significantly different from each other ($p < 0.001$). The differences in the presence of mucus plugs on fSAD (red line, Figure 5) are largely for moderate levels of sVDP between 4% and 10%—note that by the time sVDP is >10%, the difference in fSAD when mucus plugs are present is less prominent. Plots of segmental fSAD and sVDP in airway segments with and without mucus from our study

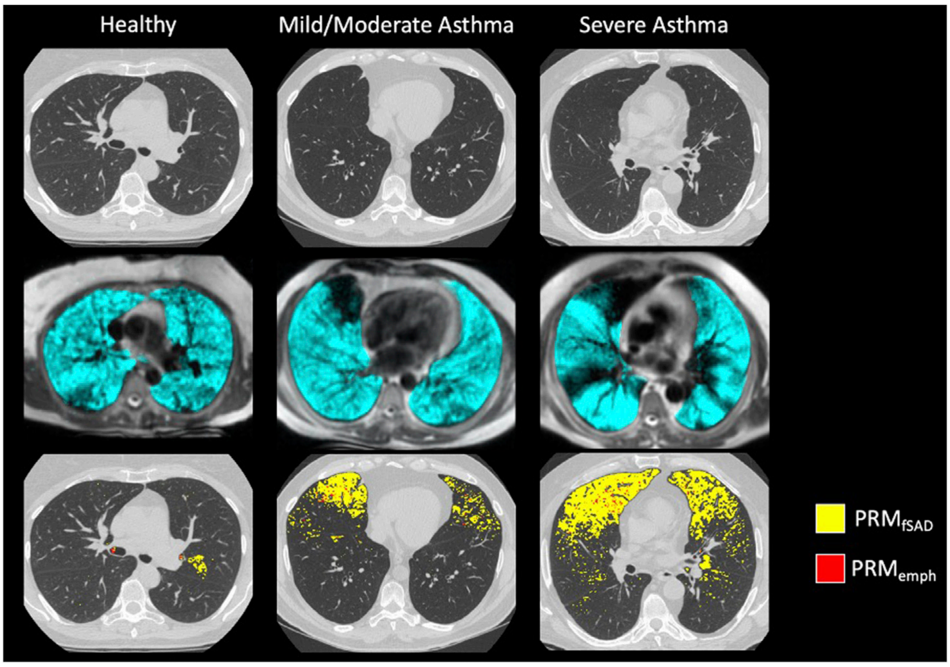

FIGURE 2
Example images of (from top to bottom): Inspiratory CT, HP 3He MRI overlaid on conventional MRI, and PRM maps overlaid on Inspiratory CT for a (from left to right) healthy subject, moderate asthmatic, and severe asthmatic.

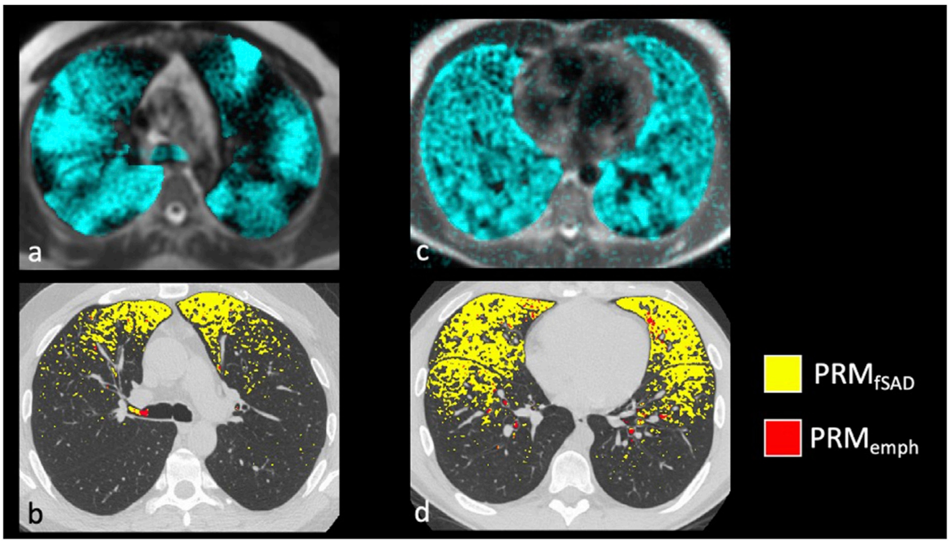

FIGURE 3
Examples of severe asthmatics where PRM and HP gas MRI are discordant. The most common discordant pattern is **(A,B)** HP 3He MRI ventilation > fSAD with whole lung VDP of 18.4% and PRMfSAD of 5.8%, and the least common is in **(C,D)** HP 3He MRI ventilation << fSAD with a whole lung VDP of 6.3% and PRMfSAD of 23.7%.

cohort further support this finding, suggesting better contrast for detecting obstruction due to mucus on a per segment basis (Figures 6B vs. 6A) overall. To further illustrate, a qualitative example of this result is shown in Figure 7 where a mucus plug is visualized in a moderate asthmatic comparing the resulting HP gas MRI sVDP with the corresponding fSAD from PRM. The typical pattern shown is that sVDP is much greater than fSAD in the vicinity of the mucus plug.

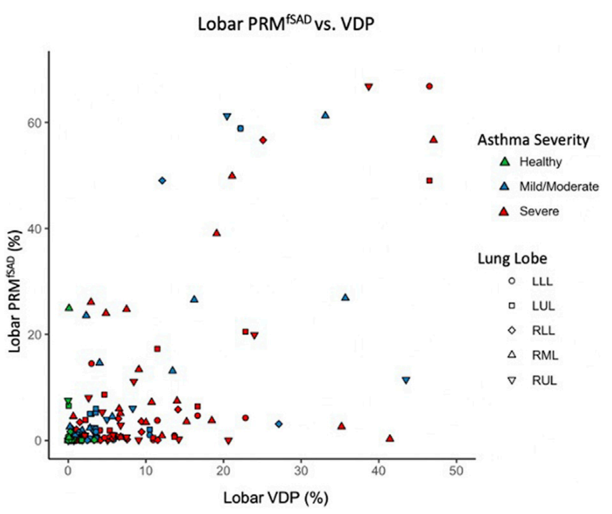

FIGURE 4
Scatter plot comparing lobar VDP to average whole lung and lobar fSAD. Points are colored based on disease severity and their shapes classify what lobe the datapoint is from. LLL, left lower lobe; LUL, left upper lobe; RLL, right lower lobe; RML, right middle lobe; RUL, right upper lobe.

4 Discussion

This is the first multimodality imaging study in patients with asthma to compare ventilation defects measured using the ventilation defect percent (VDP) with HP 3He MRI at the global, lobar and segmental level with functional small airways disease (fSAD) and airway mucus plugging after administration of four puffs of albuterol of BD. The fSAD is higher in segments with ventilation defects on HP 3He MRI. The fSAD measure, derived from parametric response mapping, identifies low density lung (−856 HU) on expiratory CT, and in asthma is synonymous with air trapping. The results corroborate previous work (Fain et al., 2008; Capaldi et al., 2016; Bell et al., 2019) showing correlation between ventilation heterogeneity and air trapping at the whole lung and qualitative regional levels (upper, middle, and lower and anterior/posterior). By comparing the measurements within physiologically defined anatomy of the lung, we show that VDP and fSAD are directly related at the lobar and segmental levels. The specific relationship was best described by a piecewise quadratic model with an interaction in the presence of airway mucus plugging suggesting fSAD responds to the presence of mucus plugging. Specifically, the interaction of fSAD with mucus plugs over a limited range of segmental VDP highlights potential differences in the sensitivity of these measures.

Importantly, the relationships between VDP and fSAD and their interactions with mucus plugs highlight potential differences in the measures that could be useful for interpretation. It was directly shown that fSAD is higher in segmental airway regions that also have ventilation defects, suggesting that the airway ventilation defects and air trapping likely share a similar etiology at the segmental level. However, it should be noted that spatial overlap was assumed in this analysis because the same segmental airway regions are shared but overlap was not directly measured. The interaction of fSAD's dependence on VDP in the presence of a mucus plug shown in Figure 5 argues for a difference in degree of response that supports the idea that fSAD is emphasizing more distal vs. central airway obstruction. That is, the impact of mucus on fSAD is most pronounced at

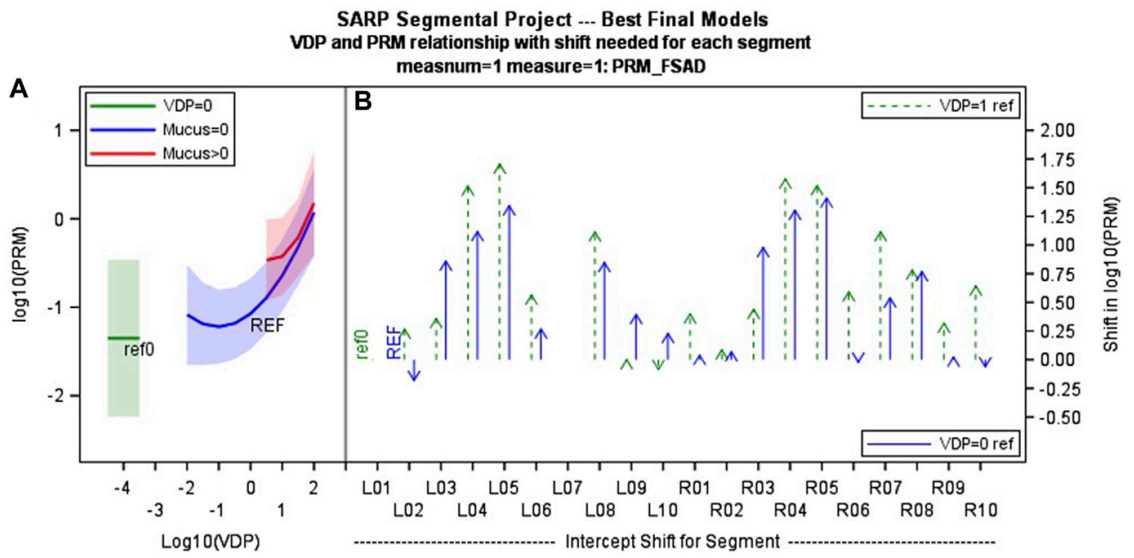

FIGURE 5
(A) shows the mixed effects piecewise multi-variate model showing how PRM fSAD changes with segmental VDP (with and without presence of mucus plug blue vs. red line). This functional relationship is common across all airway segments, but with **(B)** different intercepts for each segment (offsets relative to segmental VDP = 1 and segmental VDP = 0 are shown). These differences may relate to airway geometry, propensity for disease and/or inconsistency in lung inflation at functional residual capacity lung volume. **(C)** Segmental labels are defined as shown at far right. LB1 = Left bronchus segment 1, RB1 = right bronchus segment 1 etc.,. . . with index increasing from lung apex to base.

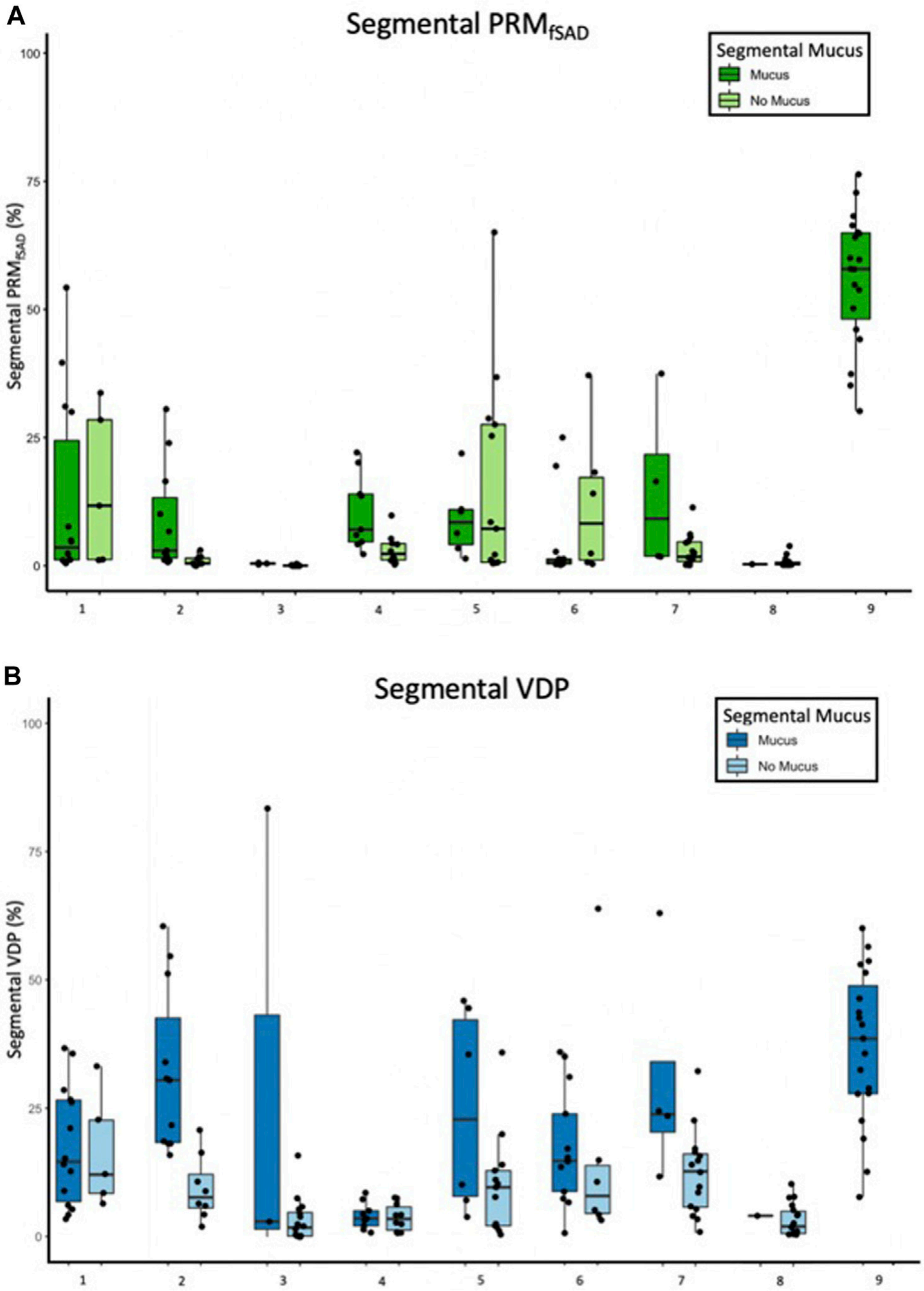

FIGURE 6
Box and whisker plots of **(A)** fSAD and **(B)** segmental VDP separated by segments with and without mucus plugs for each of 9 participants with non-zero mucus scores. Each data point is one bronchopulmonary segment and sums over both categories to the 19 segments analyzed.

moderate levels of sVDP between 4% and 10%; this observation is consistent with fSAD being more sensitive to mucus plugging in the more distal small airways than sVDP since ventilation is only modestly reduced locally. By the time sVDP is >10%, the interaction with mucus between fSAD and sVDP is no longer apparent, which likely reflects the shared mechanisms of reduced gas delivery to the airway and its corresponding impact on gas retention leading to air trapping in that segment. Moreover, we are comparing a relatively low-resolution imaging modality, HP gas MRI, with results from a high-resolution imaging modality. fSAD derived from CT is likely more sensitive to changes on the scale of millimeters whereas HP gas MRI resolution is on the scale of a centimeter.

Despite the sensitivity of fSAD to early disease processes, we found that empirically, the sVDP better delineates visible mucus plugged segments on a per subject basis than fSAD. This is likely due to stochastic and inconsistency in lung inflation impacting lung density and airway closure, especially at functional residual

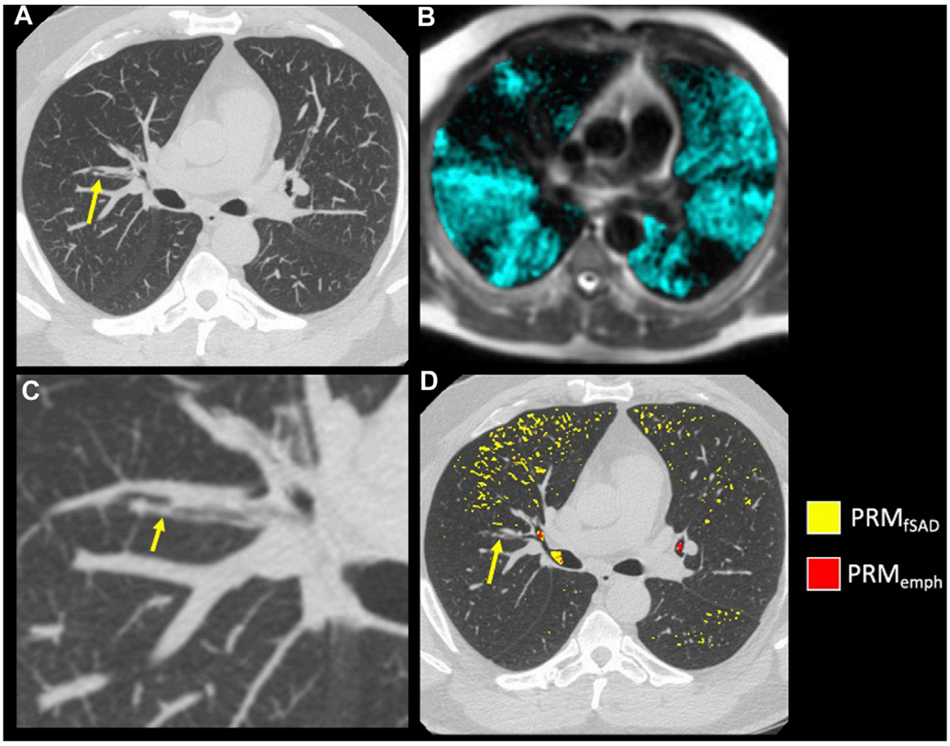

FIGURE 7
Example of mucus plugging within a moderate asthmatic. **(A)** A mucus plug (arrow) visualized on inspiratory CT using a MIP of 7 slices. **(B)** A close-up of the mucus plug (arrow) in **(A)** **(C)** HP 3He MRI overlaid on conventional MRI with ventilation defects occurring near and downstream of the mucus plug visualized in **(A)**. **(D)** PRM maps overlaid on Inspiratory CT in the axial slice of the mucus plug (arrow).

capacity lung volume on the expiratory CT due to dose limitations (Appendix A) and inconsistencies in lung inflation that more greatly impact fSAD measurements (Boes et al., 2015). In our study CT scans were performed at functional residual capacity (FRC) rather than residual volume (RV), which may also contribute to physiologic variability in fSAD (Comellas et al., 2023). An advantage of VDP is that the signal is solely from direct gas filling of the airways from inhalation of the HP gas, which is more directly affected by central airway obstruction with consequent downstream opacification of the airway tree and is therefore less dependent on the lung inflation than densitometry on CT, although this needs further investigation.

Both fSAD and VDP are associated with future lung function decline and exacerbations in severe asthma (Mummy et al., 2020; Krings et al., 2021). To further establish the understanding of VDP and fSAD in asthma, additional studies are needed to investigate longitudinal changes in these metrics with special focus on regional measures and reducing sources of variability. VDP was highly correlated with measures of fSAD with similar functional dependence over each segment, but each segment had a different intercept. This suggests that airway anatomy is possibly predisposing each airway segment to more or less inconsistency in lung inflation at functional residual capacity lung volume and/or different levels of disease due to airway geometry or gravity dependence. An important area for future investigation is airway dysanapsis which may be an important factor in predisposing individuals and specific airway segments to more obstruction in asthma (Smith et al., 2020).

There are important limitations to this study. First, this study is small and representative of a single center. As asthma is a highly heterogenous disease, the relationship we observe between fSAD, mucus, and VDP may not be reflective of asthma in general. Second, the mucus score was performed independently by multiple radiologists involved in the SARP3 study and do not reflect a consensus read to resolve discordant scores. Similarly, the mucus score (Dunican et al., 2018) gives only a presence or absence measure in each segment so it is impossible to assess VDP and fSAD with respect to location or size of the mucus plug within a given airway segment. Third, the version of the parametric response mapping algorithm used in this work occasionally failed to fully remove airway regions from analysis, often near branch points of the central airways. These errors are a negligible fraction of the lobar and segmental lung regions analyzed in this work and are unlikely to substantively affect the results and conclusions. Finally, for legacy reasons this study was performed with hyperpolarized ^{3}He gas, while hyperpolarized 129Xe gas is far more common in clinical research at present. We anticipate a similar functional relationship between VDP, fSAD, and airway mucus using HP ^{129}Xe MRI (McIntosh et al., 2022). Studies directly comparing the two gases in the same patients show qualitatively larger VDP using HP ^{129}Xe MRI presumably due to increased density of the gas mixture (Kirby et al., 2013). It is therefore conceivable that VDP measured with HP 129Xe MRI will have improved sensitivity to obstruction compared to fSAD, but testing of this hypothesis is left to future studies.

5 Conclusion

In conclusion, areas of ventilation defect as found on HP ^{3}He MRI in asthma are spatially and globally correlated with areas of fSAD on CT, as determined using PRM. On the segmental level, our model predicting fSAD showed a quadratic relationship with VDP, and potentially improved sensitivity to mucus plugs for fSAD when obstruction is mild, i.e., sVDP is within 4%–10%. Overall, mucus plugs were more consistently associated with large sVDP than with large fSAD in the corresponding airway segment, possibly because of the larger response from the absence of airways distal to the obstruction.

Data availability statement

The original contributions presented in the study are included in the article/Supplementary Materials, further inquiries can be directed to the corresponding author.

Ethics statement

The studies involving human participants were reviewed and approved by the Health Sciences IRB of the University of Wisconsin—Madison. The patients/participants provided their written informed consent to participate in this study.

Author contributions

All coauthors made substantial contributions to the conception or design of the work under guidance of SF and CG. KC and PH contributed to the CT image acquisition and analysis, KC and KL contributed to the statistical analysis, and all co-authors to the interpretation of data for the work. All co-authors contributed to the drafting of the work and revising it critically for important intellectual content. All co-authors provided approval for publication of the content. Corresponding author SF and co-authors are accountable for all aspects of the work and ensuring that questions related to the accuracy or integrity of any part of the work are appropriately investigated and resolved. All authors contributed to the article and approved the submitted version.

Funding

The Funding for this study was provided by NIH/NHLBI grant U10 HL109168, NIH/CTSA grant UL/TR000427, The American Lung Association, NIH/NHLBI R01HL126771, S10 OD016394, S10 OD026960, R01HL139690, R01HL150023 and a Wisconsin Alumni Research Foundation (WARF) technology transfer training grant. Funding sources had no involvement in study design, the collection, analysis, or interpretation of data, the writing of this report, or the decision to submit this article for publication.

Conflict of interest

SF receives research support from GE Healthcare and serves on the scientific advisory board of Polarean PLC. KC and CH are currently employees of Imbio LLC. LD and NJ are Principal Investigators in the NHLBI PrecISE Trial network that has relationships with the following companies for drug support and equipment contracts: Glaxo Smith Kline, Laurel, Sun Pharma, Vifor/OM Pharm, Vitaeris/CSL Behring, Vitaflo, Vyaire, Caire Diagnostics, MIR, Propeller Health, ZEPHYRx. NJ reports grants and personal fees from AstraZeneca, and personal fees from GSK and Boehringer Ingelheim for consultations outside the submitted work. LD has consulted with Glaxo Smith Kline, AstraZeneca, Sanofi and OM Pharma during the course of this study.

The remaining authors declare that the research was conducted in the absence of any commercial or financial relationships that could be construed as a potential conflict of interest.

Publisher's note

Supplementary material

The Supplementary Material for this article can be found online at: https://www.frontiersin.org/articles/10.3389/fphys.2023.1178339/full#supplementary-material

References

Bell, A. J., Foy, B. H., Richardson, M., Singapuri, A., Mirkes, E., van den Berge, M., et al. (2019). Functional CT imaging for identification of the spatial determinants of small-airways disease in adults with asthma. *J. Allergy Clin. Immunol.* 144 (1), 83–93. doi:10.1016/j.jaci.2019.01.014

Bhatt, S. P., Soler, X., Wang, X., Murray, S., Anzueto, A. R., Beaty, T. H., et al. (2016). Association between functional small airway disease and FEV1 decline in chronic obstructive pulmonary disease. *Am. J. Respir. Crit. Care Med.* 194 (2), 178–184. doi:10.1164/rccm.201511-2219OC

Boes, J. L., Bule, M., Hoff, B. A., Chamberlain, R., Lynch, D. A., Stojanovska, J., et al. (2015). The impact of sources of variability on parametric response mapping of lung CT scans. *Tomography* 1 (1), 69–77. doi:10.18383/j.tom.2015.00148

Capaldi, D. P., Zha, N., Guo, F., Pike, D., McCormack, D. G., Kirby, M., et al. (2016). Pulmonary imaging biomarkers of gas trapping and emphysema in COPD: (3)He MR imaging and CT parametric response maps. *Radiology* 279 (2), 597–608. doi:10.1148/radiol.2015151484

Comellas, A. P., Newell, J. D., Jr, Kirby, M., Sieren, J. P., Peterson, S., Hatt, C., et al. (2023). Residual volume versus FRC computed tomography assessment of functional small airway disease in smokers with and without chronic obstructive pulmonary disease. *Am. J. Respir. Crit. Care Med.* 207 (11), 1536–1539. doi:10.1164/rccm.202210-1852LE

Downie, S. R., Salome, C. M., Verbanck, S., Thompson, B., Berend, N., and King, G. G. (2007). Ventilation heterogeneity is a major determinant of airway hyperresponsiveness in asthma, independent of airway inflammation. *Thorax* 62 (8), 684–689. doi:10.1136/thx.2006.069682

Dunican, E. M., Elicker, B. M., Gierada, D. S., Nagle, S. K., Schiebler, M. L., Newell, J. D., et al. (2018). Mucus plugs in patients with asthma linked to eosinophilia and airflow obstruction. *J. Clin. Invest.* 128 (3), 997–1009. doi:10.1172/JCI95693

Fain, S. B., Gonzalez-Fernandez, G., Peterson, E. T., Evans, M. D., Sorkness, R. L., Jarjour, N. N., et al. (2008). Evaluation of structure-function relationships in asthma using multidetector CT and hyperpolarized He-3 MRI. *Acad. Radiol.* 15 (6), 753–762. doi:10.1016/j.acra.2007.10.019

Galban, C. J., Han, M. K., Boes, J. L., Chughtai, K. A., Meyer, C. R., Johnson, T. D., et al. (2012). Computed tomography-based biomarker provides unique signature for diagnosis of COPD phenotypes and disease progression. *Nat. Med.* 18 (11), 1711–1715. doi:10.1038/nm.2971

He, M., Zha, W., Tan, F., Rankine, L., Fain, S., and Driehuys, B. (2019). A comparison of two hyperpolarized (129)Xe MRI ventilation quantification pipelines: The effect of signal to noise Ratio. *Acad. Radiol.* 26 (7), 949–959. doi:10.1016/j.acra.2018.08.015

Jarjour, N. N., Erzurum, S. C., Bleecker, E. R., Calhoun, W. J., Castro, M., Comhair, S. A. A., et al. (2012). Severe asthma: Lessons learned from the national Heart, lung, and blood Institute severe asthma research Program. *Am. J. Respir. Crit. Care Med.* 185 (4), 356–362. doi:10.1164/rccm.201107-1317PP

Kirby, M., Svenningsen, S., Kanhere, N., Owrangi, A., Wheatley, A., Coxson, H. O., et al. (2013). Pulmonary ventilation visualized using hyperpolarized helium-3 and xenon-129 magnetic resonance imaging: Differences in COPD and relationship to emphysema. *J. Appl. Physiol.* 114 (6), 707–715. doi:10.1152/japplphysiol.01206.2012

Krings, J. G., Goss, C. W., Lew, D., Samant, M., McGregor, M. C., Boomer, J., et al. (2021). Quantitative CT metrics are associated with longitudinal lung function decline and future asthma exacerbations: Results from SARP-3. *J. Allergy Clin. Immunol.* 148 (3), 752–762. doi:10.1016/j.jaci.2021.01.029

Lynch, D. A., and Al-Qaisi, M. A. (2013). Quantitative computed tomography in chronic obstructive pulmonary disease. *J. Thorac. Imaging* 28 (5), 284–290. doi:10.1097/RTI.0b013e318298733c

McIntosh, M. J., Kooner, H. K., Eddy, R. L., Jeimy, S., Licskai, C., Mackenzie, C. A., et al. (2022). Asthma control, airway mucus, and (129)Xe MRI ventilation after a single benralizumab dose. *Chest* 162 (3), 520–533. doi:10.1016/j.chest.2022.03.003

Mummy, D. G., Carey, K. J., Evans, M. D., Denlinger, L. C., Schiebler, M. L., Sorkness, R. L., et al. (2020). Ventilation defects on hyperpolarized helium-3 MRI in asthma are predictive of 2-year exacerbation frequency. *J. Allergy Clin. Immunol.* 146 (4), 831–839 e6. doi:10.1016/j.jaci.2020.02.029

Mummy, D. G., Dunican, E. M., Carey, K. J., Evans, M. D., Elicker, B. M., Newell, J. D., Jr, et al. (2022). Mucus plugs in asthma at CT associated with regional ventilation defects at (3)He MRI. *Radiology* 303 (1), 184–190. doi:10.1148/radiol.2021204616

Smith, B. M., Hoffman, E. A., and Barr, R. G. (2020). Dysanapsis and COPD-reply. *JAMA* 324 (15), 1572. doi:10.1001/jama.2020.15654

Svenningsen, S., Haider, E., Boylan, C., Mukherjee, M., Eddy, R. L., Capaldi, D. P. I., et al. (2019). CT and functional MRI to evaluate airway mucus in severe asthma. *Chest* 155 (6), 1178–1189. doi:10.1016/j.chest.2019.02.403

Svenningsen, S., Kirby, M., Starr, D., Coxson, H. O., Paterson, N. A. M., McCormack, D. G., et al. (2014). What are ventilation defects in asthma? *Thorax* 69 (1), 63–71. doi:10.1136/thoraxjnl-2013-203711

Teague, W. G., Tustison, N. J., and Altes, T. A. (2014). Ventilation heterogeneity in asthma. *J. Asthma* 51 (7), 677–684. doi:10.3109/02770903.2014.914535

Teague, W. G., Phillips, B. R., Fahy, J. V., Wenzel, S. E., Fitzpatrick, A. M., Moore, W. C., et al. (2018). Baseline features of the severe asthma research program (SARP III) cohort: differences with age. *J. Allergy Clin. Immunol. Pract.* 6 (2), 545–554. doi:10.1016/j.jaip.2017.05.032

Thomen, R. P., Sheshadri, A., Quirk, J. D., Kozlowski, J., Ellison, H. D., Szczesniak, R. D., et al. (2015). Regional ventilation changes in severe asthma after bronchial thermoplasty with (3)He MR imaging and CT. *Radiology* 274 (1), 250–259. doi:10.1148/radiol.14140080

Zha, W., Niles, D. J., Kruger, S. J., Dardzinski, B. J., Cadman, R. V., Mummy, D. G., et al. (2016). Semiautomated ventilation defect quantification in exercise-induced bronchoconstriction using hyperpolarized helium-3 magnetic resonance imaging: A repeatability study. *Acad. Radiol.* 23 (9), 1104–1114. doi:10.1016/j.acra.2016.04.005

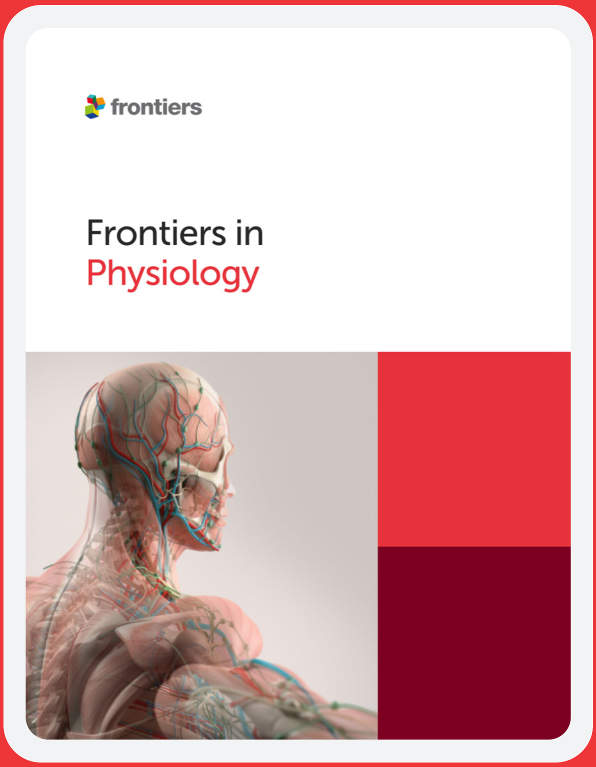

frontiers

Frontiers in Physiology